Digital Processing for an Analogue Subcarrier Multiplexed Mobile Fronthaul

A Thesis Submitted to The University of Kent

For the Degree of Doctor Of Philosophy In Electronic Engineering

By

Shabnam Noor

March, 2019

Abstract

In order to meet the demands of the fifth generation of mobile communication networks (5G), such as very high bit-rates, very low latency and massive machine connectivity, there is a need for a flexible, dynamic, scalable and versatile mobile fronthaul. Current industry fronthaul standards employing sampled radio waveforms for digital transport suffer from spectral inefficiency, making this type of transport impractical for the wide channel bandwidths and multi-antenna systems required by 5G. On the other hand, analogue transport does not suffer from these limitations. It is, however, prone to noise, non-linearity and poor dynamic range. When combined with analogue domain signal aggregation/multiplexing, it also lacks flexibility and scalability, especially at millimetre wave frequencies.

Measurements (matched in simulation) of analogue transport at millimetre wave frequencies demonstrate some of these issues. High data rates are demonstrated employing wide bandwidth channels combined using traditional subcarrier multiplexing techniques. However, only a limited number of channels can be multiplexed in this manner, with poor spectral efficiency, as analogue filter limitations do not allow narrow gaps between channels.

To this end, over the last few years, there has been significant investigation of analogue transport schemes combined with digital channel aggregation/ de-aggregation (combining/ separating multiple radio waveforms in the digital domain). This work explores such a technique.

Digital processing is used at the transmitter to flexibly multiplex a large number of channels in a subcarrier multiplex, without the use of combiners, mixers/ up-converters or Hilbert transforms. Orthogonal Frequency Division Multiplexing (OFDM) – derived Discrete Multi-Tone (DMT) and Single Sideband (SSB) modulated channels are integrated within a single Inverse Fast Fourier Transform (IFFT) operation. Channels or channel groups are mapped systematically into Nyquist zones by using, for example, a single IFFT (for a single 5G mobile numerology) or multiple IFFTs (for multiple 5G mobile numerologies).

The analogue transport signal generated in this manner is digitally filtered and band-pass sampled at the receiver such that each corresponding channel (e.g. channels destined to the same radio frequency (RF)/ millimetre wave (mmW) frequency) in the multiplex is presented at the same intermediate frequency, due to the mapping employed at the transmitter. Analogue or digital domain mixers/ down-converters are not required with this technique. Furthermore,

each corresponding channel can be readily up-converted to their respective RF/mmW channels with minimal per-signal processing. Measurement results, matched in simulation, for large signal multiplexes with both generic and 5G mobile numerologies show error-vector magnitude performance well within specifications, validating the proposed system.

For even larger multiplexes and/or multiplexes residing on a higher IF exceeding the analogue bandwidth and sampling rate specifications of the ADCs at the receiver, the use of a bandwidth-extension device is proposed to extend the mapping to a mapping hierarchy and relax the analogue bandwidth and sampling rate requirements of the ADCs. This allows the receiver to still use digital processing, with only minimal analogue processing, to band-pass sample smaller blocks of channels from the larger multiplex, down to the same intermediate frequency. This ensures that each block of channels is within the analogue bandwidth specification of the ADCs. Performance predictions via simulation (based on a system model matched to the measurements) show promising results for very large multiplexes and large channel bandwidths.

The multiplexing technique presented in this work thus allows reductions in per-channel processing for heterogeneous networking (or multi-radio access technologies) and multi-antenna configurations. It also creates a re-configurable and adaptable system based on available processing resources, irrespective of changes to the number of channels and channel groups, channel bandwidths and modulation formats.

Acknowledgements

I am deeply grateful to my supervisor Prof Nathan Gomes, for giving me the life-changing opportunity to work in this field, for his patient and valuable guidance and support in this work and for his many important lessons regarding career, work ethic and life in general.

I am also very grateful to my colleague and best friend, Dr Philippos Assimakopoulos, for being a dependable collaborator and for being there every step of the way.

I would like to thank Dr Anthony Nkansah and Dr Jeanne James, for all their help and guidance. I would also like to thank everyone that I have collaborated with so far, especially Minqi Wang (from Orange Labs, France).

I would like to give a big thank you to all my friends and colleagues at this University, for their constant support and encouragement and a special thank you to Kenan and Tara, for always being there for me.

I am very grateful to this School for offering me a Graduate Teaching Assistantship, without which none of this would have been possible. I would also like to express my gratitude to the academic and administration staff in EDA, for their guidance and support during all these years. I feel very proud to have been a part of this School.

Finally, I would like to thank my family and especially my parents, for their constant support and for always believing in me.

List of Publications

[P1] S. Noor, P. Assimakopoulos, N. J. Gomes, “A Flexible Subcarrier Multiplexing System with Analog Transport and Digital Processing for 5G (and beyond) Fronthaul,” Journal of Lightwave Technology [*accepted for publication*].

[P2] P. Assimakopoulos, S. Noor, N. J. Gomes, “A method of generating and processing a transport signal for carrying channels in a radio access network,” U.K. Patent P47636GB [*Filed: 10 January, 2019*].

[P3] M. Almoteriy, M. Sobhy, J. Batchelor, S. Noor, N. Gomes, “Antenna Simulation and Effects in Digital Communication Systems,” in *The Loughborough Antennas & Propagation Conference (LAPC 2018)*, Loughborough, UK, 2018, pp. 1-6.

[P4] N. J. Gomes, U. Habib, S. Noor, A. E. Aighobahi, P. Assimakopoulos, “Support of Multi-Antenna and Multi-User Systems using Radio Over Fiber,” in *Asia Communications and Photonics Conference (ACP)*, Guangzhou, China, 2017.

[P5] T. Yamaguchi, H. Morimoto, U. Habib, S. Noor, N. Gomes, H. Toda, “Output Power Enhancement by Optical Pulse Compression in Photonic-based RF generation – Laser Linewidth and Phase Noise of the RF Output,” in *The Institute of Electronics, Information and Communication Engineers*, 2017.

[P6] N. J. Gomes, P. Assimakopoulos, M. K. Al-Hares, U. Habib, S. Noor, “The New Flexible Mobile Fronthaul: Digital or Analog, or Both?,” in *18th International Conference on Transparent Optical Networks (ICTON)*, Trento, Italy, 2016.

[P7] RAPID deliverable D423, “Photonic processing of mm-wave signals” European Horizon 2020 Programme Project: RAPID, 2016 [Confidential report].

[P8] RAPID, “Periodic Technical Report Part B”, 2016 [Confidential report].

[P9] RAPID deliverable D221, “Subsystem and component specifications”, 2015 [Confidential report].

TABLE OF CONTENTS

List of abbreviations

1G	First Generation of Mobile Communication Networks
2G	Second Generation of Mobile Communication Networks
3G	Third Generation of Mobile Communication Networks
3GPP	Third Generation Partnership Project
4G	Fourth Generation of Mobile Communication Networks
5G	Fifth Generation of Mobile Communication Networks
AC	Alternating Current
ADC	Analogue-to-Digital Converter
AWG	Arbitrary Waveform Generator
b2b	Back-to-Back
BER	Bit Error Rate
BBU	Baseband Unit
BPSK	Binary Phase Shift Keying
CA	Carrier Aggregation
CDMA	Code Division Multiple Access
CF	Crest Factor
CoMP	Co-ordinated Multipoint
CP	Cyclic Prefix
CP-OFDM	Cyclic Prefix Orthogonal Frequency Division Multiplexing
CPRI	Common Public Radio Interface
C-RAN	Centralised or Cloud Radio Access Network
CS	Cyclic Suffix
CU	Central Unit
CWL	Continuous Wave Laser
D2D	Device-to-Device
DAS	Distributed Antenna System
DAC	Digital-to-Analogue Converter
DC	Direct Current
DFB	Distributed Feedback
DFT	Discrete Fourier Transform
DL	Downlink
DML	Directly Modulated Laser
DMT	Discrete Multi-Tone
DPD	Digital Pre-Distortion
DSB	Double Sideband

DSP	Digital Signal Processing
DU	Distributed Unit
DVB-T	Digital Video Broadcasting – Terrestrial
DVB-T2	Digital Video Broadcasting – Second Generation Terrestrial
DWDM	Dense Wavelength Division Multiplexing
E/O	Electrical-to-Optical
EAM	Electro-Absorption Modulator
EDFA	Erbium Doped Fibre Amplifier
eMBB	Enhanced Mobile Broadband
ECL	External Cavity Laser
eNodeB	Enhanced Base Station in UMTS (Universal Mobile Telecommunications Service) Standard
EVM	Error Vector Magnitude
FBG	Fibre Bragg Gratings
FDD	Frequency Division Duplex
FDM	Frequency Division Multiplexing
FFT	Fast Fourier Transform
FP	Fabry–Pérot
FPGA	Field-Programmable Gate Array
FSR	Full-Scale Range
Gbps	Gigabits-per-second
gNB	5G Next Generation Base Station supporting 5G New Radio
GSM	Groupe Speciale Mobile or Global System of Mobile Communications
GSMA	Global System of Mobile Communications Association
HetNet	Heterogeneous Networking
HLS	Higher Layer Split
ICI	Inter-Carrier Interference
IDFT	Inverse Discrete Fourier Transform
IF	Intermediate Frequency
IFFT	Inverse Fast Fourier Transform
IFoF	Intermediate Frequency over Fibre
IIR	Infinite Impulse Response
IM/DD	Internet of Things
IMD	Intermodulation Distortion
IoT	Intensity Modulation and Direct Detection
IQ	In-phase/ Quadrature Phase
IS-95	Interim Standard 95
ISI	Inter-Symbol Interference

ITU	International Telecommunication Union
LO	Local Oscillator
LOS	Line of Sight
LTE	Long-Term Evolution
LTE-A	Long-Term Evolution Advanced
MAC	Media Access Control
Mbps	Megabits-per-second
MeNB	Master Enhanced Base Station in UMTS
METIS	Mobile and wireless communications Enablers for the Twenty-twenty Information Society
MIMO	Multiple-Input Multiple-Output
mMIMO	Massive Multiple-Input Multiple-Output
mMTC	Massive Machine Type Communications
mmW	Millimetre Wave
multi-RAT	Multi Radio Access Technology
MZM	Mach-Zehnder Modulator
NF	Noise Figure
NGMN	Next Generation Mobile Networks
NG-RAN	Next Generation Radio Access Network
NodeB	Base Station in UMTS
NR	New Radio
NZ	Nyquist Zone
O/E	Optical-to-Electrical
OCS	Optical Carrier Suppression
ODSB	Optical Double Sideband
OFCG	Optical Frequency Comb Generation
OFDM	Orthogonal Frequency Division Multiplexing (same as CP-OFDM)
OFDMA	Orthogonal Frequency Division Multiplexing Access
OSC	Oscilloscope
OSSB	Optical Single Sideband Modulation
OWC	Optical-Wireless Communication
PAN	Personal Area Network
PHY	Physical Layer
PM	Phase Modulation
P1dB	1-dB Compression Point
P/S	Parallel-to-Serial
PAPR	Peak-to-Average Power Ratio
PDCP	Packet Data Convergence Protocol

PDM	Polarisation Division Multiplexing
PIN PD	PIN Photodiode
PM	Phase Modulation
PRBS	Pseudo Random Binary Sequence
PSD	Power Spectral Density
PSAM	Pilot Symbol Assisted Modulation
QAM	Quadrature Amplitude Modulation
QPSK	Quadrature Phase Shift Keying
RAN	Radio Access Network
RAPID	Radio Technologies for 5G Using Advanced Photonic Infrastructure for Dense User Environments
RCE	Receiver Constellation Error
RAT	Radio Access Technology
RAU	Remote Access Unit
RF	Radio Frequency
RIN	Relative Intensity Noise
RLC	Radio Link Control
RMS	Root-Mean-Square
RoF	Radio-over-Fibre
RRC	Radio Resource Control
RRH	Remote Radio Head
RRU	Remote Radio Unit
RSOA	Reflective Semiconductor Optical Amplifier
SC-FDMA	Single-Carrier Frequency Division Multiple Access
S/P	Serial-to-Parallel
SCM	Sub-Carrier Multiplexing
SDAP	Service Data Adaptation Protocol
SDR	Software Defined Radio
SeNB	Secondary Enhanced Base Station in UMTS
SFDR	Spurious Free Dynamic Range
SMF	Single-Mode Fibre
SNR	Signal-to-Noise Ratio
SSB	Single Sideband
TDMA	Time Division Multiple Access
THA	Track-and-Hold Amplifier
UDN	Ultra Dense Network
URLLC	Ultra-Reliable Low-Latency Communication
VCSEL	Vertical Cavity Surface Emitting Laser
WDM	Wavelength Division Multiplexing

Wi-Fi	Wireless Fidelity
WiMAX	Worldwide Interoperability for Microwave Access
WLAN	Wireless Local Area Network
UDWDM	Ultra-Dense Wavelength Division Multiplexing
V2X	Vehicle-to-Everything
VLC	Visible Light Communication
VNA	Vector Network Analyser
VPI	Virtual Photonics Inc.
ZP	Zero Prefix

List of Figures

List of Tables

1 Introduction

1.1 The 5G Mobile Fronthaul

5G is the next step in the evolution of wireless technologies. In order to meet projected demands of new services, targets such as high bit-rates (otherwise known as Enhanced Mobile Broadband, eMBB), reliability and very low latency and massive machine connectivity have been identified [1], [2], and a 5G New Radio (NR) air interface has been standardised [3]. 5G NR will support a wide range of frequency bands and technologies to support such targets. These will include heterogeneous networking (HetNet), including 60 GHz (5G) mobile access and legacy services such as Long Term Evolution (LTE) [4] and massive Multiple Input Multiple Output (mMIMO) multi-antenna systems. To fulfil projected service requirements and support these technologies, there is a need for a flexible, dynamic, scalable and versatile 5G (and beyond) mobile fronthaul.

The fronthaul is a section of the radio access mobile communication network consisting of a Distributed Unit (DU) and Remote Radio Unit (RRU). In conventional (or legacy) fronthaul networks, all the complex signal-processing operations are performed at the DU (this has traditionally been called the Baseband Processing Unit, BBU) while the RRU (this has traditionally been called the Remote Radio Head, RRH) does little more than transmitting and receiving Radio Frequency (RF) signals to and from mobile users (i.e. radio frequency processing). Legacy fronthauls employ the transport of time domain in-phase and quadrature (IQ) quantised samples in the access network, resulting in very high data rates over the fronthaul section of the current fourth generation radio access network (4G) [5], [6]. These data rates scale with number of antennas and signal bandwidths so are expected to increase further with 5G. Moving more of the functionality to the RRU through functional decompositions helps to reduce these data rates. However, this may be at the cost of exceeding the end-to-end latency limits imposed by co-ordinated techniques, such as those used in distributed MIMO systems [7]. As a result, the wider channel bandwidths and mMIMO techniques required by 5G pose a significant challenge for digital transport.

Therefore, there is renewed interest in the use of analogue transport in next generation mobile networks. Analogue transport can provide high spectral efficiency and reduced latency, allowing joint processing of signals at the DU. However, analogue transport has been restricted to niche

applications such as Distributed Antenna Systems (DAS), due to limitations including poor dynamic range and susceptibility to non-linearities [8]. Traditionally, a DAS system consists of Remote Antenna Units (RAUs) connected to a Central Unit (CU) via a Radio-over-Fibre (RoF) link (employing a functional hierarchy similar to the DU and RRU). A concept diagram of an analogue RoF fronthaul is shown in Figure 1-1.

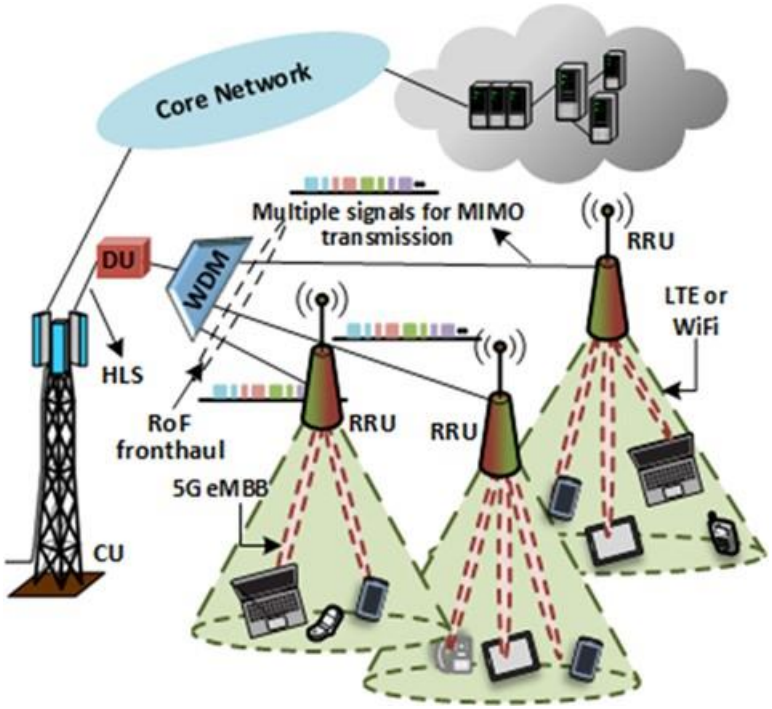

Figure 1-1 5G heterogeneous network configuration employing an analogue RoF fronthaul.

In the diagram, the Central Unit (CU), which employs a High Layer Split (HLS) of the 5G protocol layer stack to a DU, receives signals from a core network. Following this, the DU performs all the processing for different numerologies (i.e. Orthogonal Frequency Division Multiplexing (OFDM) signals with different generation characteristics). The signals are then combined in the electrical domain (following placement to different Intermediate Frequencies, IFs) through Subcarrier Multiplexing (SCM) for analogue transport, while different RRUs are addressed through different wavelengths of light using a Wavelength Division Multiplexing (WDM) scheme. LTE signals can be used to provide wider area coverage while 5G millimetre-wave (mmW) signals use narrow beams through beamforming.

SCM, which traditionally multiplexes signals using low-cost analogue components (local oscillators, mixers, band-pass filters etc.), in conjunction with WDM schemes, can lead to very

high capacity links [9]. However, analogue domain multiplexing lacks flexibility and scalability, especially at mmW frequencies. Applications such as mMIMO would require a large number of signals (e.g. 128 or higher per antenna array in the case of full-digital mMIMO or fewer per array in the case of hybrid mMIMO) to be multiplexed and transmitted over a fibre link. As the number of signals increases (especially within the subcarrier multiplex), an equally large number of components is required, as well as fine control of these components, resulting in high complexity and cost [10], [11]. Furthermore, these components need to be customisable for each signal and thus lead to reduced flexibility in deployment. Therefore, a new approach involving digital domain SCM combined with analogue transport, also referred to as digital channel aggregation/ de-aggregation [12], Intermediate Frequency over Fibre (IFoF) or multi-IFoF [13], has been investigated extensively in the past few years. This approach has the potential to meet the differing requirements of the 5G mobile fronthaul in terms of high data rates and spectral efficiency, flexibility, scalability, low latency and reduced system complexity and cost.

In this thesis, the terms “digital channel aggregation/ de-aggregation”, “digital SCM”, “digital domain SCM” and “IFoF”, have been used interchangeably. Moreover, the terms “signal” and “channel” have also been used interchangeably.

1.2 Motivation of this Work

There have been several promising demonstrations of digital channel aggregation/ de-aggregation, combined with analogue transport. Some of these demonstrations have reported very high data rates by combining different types of optical modulation and multiplexing techniques such as Phase Modulation (PM) and WDM [14], [15], [16], [17]. Others have shown the potential for mMIMO deployments [18]. Many of these demonstrations have employed a large number of channels, wide bandwidth channels [17] and up-conversion to mmW frequencies [14].

However, multiplexes consisting of a large number of wide-bandwidth channels occupy large bandwidths and require equally large sampling rates at the RRUs. Analogue-to-Digital Converters (ADCs) with sufficiently large analogue bandwidths (e.g. in excess of 10 GHz [18]) and high sampling rates are required for this operation. Moreover, for mMIMO systems, each channel has to be de-aggregated from these multiplexes and up-converted to the same

microwave and/ or mmW frequencies. These limitations pose a huge challenge in terms of cost and complexity at RRUs in 5G networks, especially for mmW frequencies, and are shown in Figure 1-2.

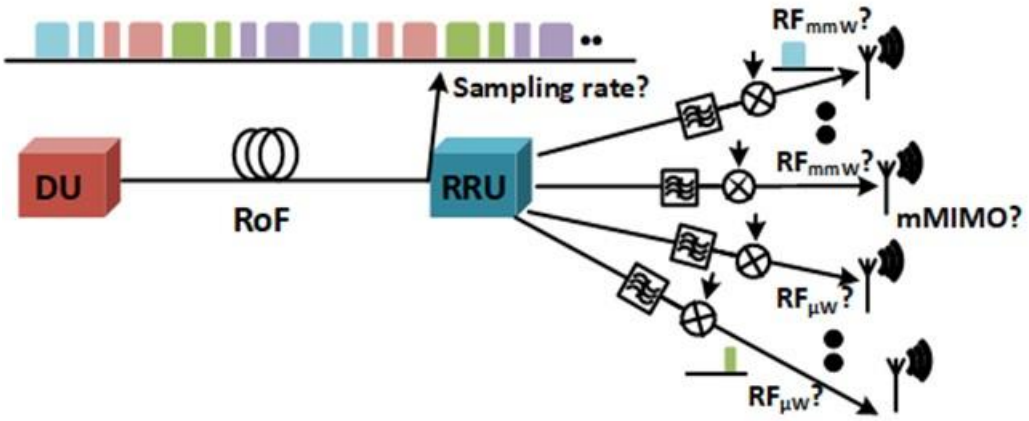

Figure 1-2 Limitations of current analogue transport techniques employing digital domain SCM techniques.

A traditional approach for reducing sampling rates is to employ band-pass sampling [19]. In [18] band-pass sampling has been used in conjunction with analogue domain filtering to de-multiplex a large number of signals, showing that low sampling rate ADC-induced aliasing effects can be rectified by MIMO processing. In [20] a low sampling rate ADC is used to frequency translate a mmW signal to RF in the uplink section of a digitised fronthaul. In [21], a track-and-hold amplifier (THA) is used in the transmitter side of a fronthaul to band-pass sample a signal down to baseband frequencies.

However, these approaches do not consider the signal placement in the RRU either in the digital or analogue domain, especially when large numbers of signals are transmitted for mMIMO and/or heterogeneous networking. Individual signals residing at different IFs will need to be frequency translated to the same frequency for mMIMO applications. Thus, up-conversion stages to RF/ mmW need to be adaptable for each signal, and frequency/phase synchronized. A flexible and scalable technique that is not affected by signal counts and facilitates the process of obtaining all signals at the same IF, reducing the amount of per-signal processing at the RRU, would be beneficial for the 5G fronthaul.

Furthermore, architectures such as the one presented in [18] employ band-pass sampling to keep sampling rates to a minimum for each channel at the RRU. However, for channels at a higher IF in the multiplex (e.g. at 9 GHz), ADCs with very large analogue bandwidths will still be required. As a result, even if each channel is sampled using a very low sampling rate, ADCs with very high sampling rate specifications (to match the high analogue bandwidths) will be required at the RRU with progressively higher IFs.

Moreover, employing analogue filters to de-aggregate the signals becomes problematic for high signal counts. A very large number of analogue filters is required (for e.g. in the architecture presented in by [18]), in order to filter individual or small groups of channels (e.g. 128 filters for 128 channels when each channel is filtered, or 64 filters when a pair of channels is filtered). As this filtering is carried out in the analogue domain, no flexibility is provided in adapting these filters and the number of channels they each filter.

1.3 Research Aims

In light of the very high bit-rates envisaged in 5G radio access networks, the use of wide channel bandwidths and large channel multiplexes will be of paramount importance in combination with HetNet and mMIMO techniques. Moreover, 5G mobile networks will have to be flexible, dynamic, versatile and scalable, in order to support different types of services with differing requirements. Since analogue transport over the fronthaul is able to offer higher spectral efficiency compared to digital transport, this work will investigate analogue and digital SCM techniques in an analogue RoF fronthaul, with emphasis on digital SCM schemes.

As the number of multiplexed channels increases, analogue SCM becomes increasingly complex and expensive (especially at mmW frequencies). This is because a greater number of analogue components such as filters and mixers is required for per-channel processing. In this work, an analogue SCM scheme employing variable wide bandwidth channels will be examined in detail, to confirm the limitations of such schemes, and will serve as a baseline for the digital SCM scheme.

A digital SCM scheme will be investigated as it has the potential to offer greater flexibility than analogue SCM schemes. This scheme should allow multiplexing/ de-multiplexing with the use of very few or no analogue components. It should also facilitate multiplexes of different sizes and

the combinations of different 5G signal bandwidths, numerologies and modulation schemes and formats. Thus, these attributes will allow the transport of signals of different types and generation characteristics via a single flexible platform, to be used for different 5G services.

For 5G networks and beyond, the digital SCM technique should be dynamic as well as flexible to allow for an adaptable/ re-configurable future fronthaul. One of the issues with analogue SCM techniques is their inability to adapt to changes in the number of channels, channel bandwidths and signal types (for example analogue filters cannot adapt/ scale well under such changes). The digital SCM technique should be able to accommodate such changes in the system in a dynamic and flexible manner.

Multi-Radio Access Technology (multi-RAT) applications require the transport and distribution of signals destined to different RATs such as LTE, Wi-Fi and mmW-5G [4]. For mMIMO, a very large number of channels have to be transported, individually processed and then placed at the same microwave and/or mmW frequencies for wireless transmission. This requires separate filtering and up-conversion stages for each channel, processes which are simply too complex and expensive (more so at mmW frequencies), especially using analogue components. The digital domain SCM technique should perform most of the processing in the digital domain and should be able to present each channel at the same IF at the receiver with limited use of further per-signal processing. Thus, channels destined for different microwave/mmW frequencies can be transported together and then readily up-converted to their respective frequencies, with reduced per-channel processing. This will be beneficial for multi-RAT and mMIMO networks.

Lastly, for large aggregate bandwidth multiplexes, methods for reducing receiver ADC sampling rates and analogue bandwidth requirements to arbitrary levels would be beneficial. However, such methods should not have a detrimental effect on the flexibility and scalability of the system. Current digital SCM schemes have limitations in these respects [22], [18].

1.4 Summary of Main Contributions of this Thesis

High data rates have been achieved using wide bandwidth OFDM channels multiplexed/ de-multiplexed using a low-complexity/ low-cost comb generation technique

- A mmW over fibre downlink system employing optical comb generation via a phase modulator and heterodyne detection has been used for transporting up to four channels

multiplexed using traditional analogue SCM techniques. Similar techniques have been demonstrated in [23] with up to three Quadrature Phase Shift Keying (QPSK) channels and very low data rates and in [24], employing a much lower data rate per optical sideband. In this work, up to four wide-bandwidth OFDM channels with 16-Quadrature Amplitude Modulation (QAM) subcarrier modulation have been transported at 25 GHz and 60 GHz. Channel bandwidths of 76 MHz, 152 MHz and 305 MHz have been used in these demonstrations. A maximum data rate of 2.13 Gbps has been achieved over a wireless distance of 4 metres using this technique of mmW up-conversion.

A flexible multiplexing technique using a single Inverse Fast Fourier Transform (IFFT) has been proposed/demonstrated

- A flexible approach for multiplexing a large number of OFDM signals with variable bandwidths, modulation levels and frequency guard-bands between them and seamlessly combining Single Sideband (SSB) - and Discrete Multi-Tone (DMT) - derived signals is presented for the first time. DMT can be employed to drive an optical modulator directly (i.e. without the need for up-conversion) and can be used in Optical-Wireless Communications (OWC) [25], [26] applications while SSB improves spectral efficiency. While large IFFTs are used by wireline standards such as Digital Video Broadcasting – Second Generation Terrestrial (DVB-T2) [27] these are only used for single channels. In [28] a single IFFT, albeit with a relatively small length combined with a propriety designed window function, was used to multiplex 32 LTE channels. However, this work did not incorporate variable bandwidths, DMT - and SSB - derived channels. As a result of the technique employed in this thesis, additional processing, e.g. via Hilbert transforms, digital up-converters etc., is not required for creating the multiplexes. Using a single IFFT length of 32768, up to 48 SSB channels have been demonstrated in this work, with 38.15 MHz channel bandwidths and 10.68 MHz gaps between channels, resulting in an aggregate data rate of 7.32 Gbps.
- Individual channels or groups of channels using the same or different numerologies (generic/5G), are transmitted together from the DU to the RRU through a common medium (fibre/ electrical connection). In the case of different numerologies, individual IFFTs are used to create Sub-Multiplexes, each employing a different sampling rate and numerology, which are then combined in the digital domain to form Multiplexes and/or Super-Multiplexes. This type of aggregation of very large size sub-multiplexes employing

different 5G numerologies has been presented for the first time. Good spectral efficiency and high data rates are demonstrated using 36 mixed-bandwidth DMT/ SSB-derived channels (16-QAM subcarrier modulation), two different 5G numerologies, gaps between channels as narrow as 3.7 MHz and an aggregate data rate of 3.3 Gbps. The highest aggregate data rate that has been demonstrated in this work is 8.3 Gbps, using 76 mixed-bandwidth channels (16-QAM subcarrier modulation), a single 5G numerology and gaps between channels as narrow as 1.83 MHz.

A novel Nyquist Zone (NZ) mapping technique for obtaining channels at the same IF at the RRU resulting in minimum per-signal processing has been proposed/demonstrated

- Past work, for example [18], has not considered the placement of signals in the RRU either in the digital or analogue domain, especially when large numbers of signals are transmitted for mMIMO and/or in multi-RAT applications. Individual signals may reside at different IFs, thus up-conversion stages to RF/mmW need to be bespoke, adaptable for each signal, and frequency/phase synchronized. The hierarchical NZ mapping technique presented here at the DU is used to create "Sub-Multiplexes", "Multiplexes" and "Super-Multiplexes" in any combination. The NZs are essentially frequency bands of pre-determined width, derived from the sampling or band-pass sampling process at the receiver side. Each of these NZs accommodates either a single channel or a channel set. When sampled at twice the pre-determined width at the RRU, each channel or channel set has the same centre frequency as corresponding channels of other channel sets. Thus, these corresponding channels can be readily up-converted to their respective RF/mmW frequency with minimal per-channel processing. This will be very important for mMIMO and HetNet applications.
- The receiver does most of the per-channel processing in the digital domain. This means that a very small number of mixers, up-/ down-converters, analogue filters etc. is used and a single RF and/ or mmW local oscillator (LO) stage, which reduces the amount of digital and/or analogue per-channel processing typically required in the receiver for placing channels at the same RF/mmW frequency. After channel de-aggregation, each corresponding channel across channel groups, can be up-converted to the same RF and/ or mmW frequency via a single LO stage. Since the composite radio waveform is generated at the DU with the Cyclic Prefix (CP) included, following de-multiplexing and down-sampling at the RRU side, each individual channel will directly have its own

decimated and appropriately sized CP and can thus be directly processed for transmission over a wireless channel.

The use of a THA at the receiver side of a fronthaul (RRU) has been proposed for the first time for minimising ADC sampling rates and enhancing scalability

- The THA can be used to extend the NZ mapping to a hierarchy for ever larger multiplexes and as a result, fits in well with NZ mapping, even though it requires a small amount of analogue domain processing. The THA provides flexibility in keeping ADC sampling rates and analogue bandwidth requirements to arbitrary low levels at the receiver. Receiving a very large multiplex at the RRU would normally require equivalently large ADC analogue bandwidth and sampling rate. Therefore, a THA can be used for multiplexes with aggregate bandwidths exceeding the ADC's sampling rate specifications and/or for multiplexes occupying sufficiently low aggregate bandwidths but placed at an RF such that their highest frequency component exceeds the ADC's analogue bandwidth specification. Flexibility in terms of IF placement of multiplexes, is beneficial for IFoF techniques [29], [30], [31].
- There have been limited proposed use of THAs in RoF applications, for example in [32], and here at the transmitter side of the digital link. In [21], a THA is used at the transmitter side of a fronthaul link to band-pass sample a signal down to baseband. In this work, up to 240 wide-bandwidth DMT/ SSB-derived channels occupying an aggregate analogue bandwidth of 16 GHz have been demonstrated in a simulation environment using an ADC sampling rate of only 3.93 GSps. An aggregate data rate of 49.7 Gbps has been achieved for this multiplex, using mixed bandwidths, 5G numerologies and subcarrier modulation (16-QAM and 64-QAM).

A flexible and scalable digital channel aggregation/ de-aggregation technique for the 5G (and beyond) network has been proposed and demonstrated

Traditional SCM techniques relying on analogue components to multiplex channels lack scalability (in terms of cost and complexity) for wide channel bandwidths and large size multiplexes. Analogue processing (for example analogue filters), cannot adapt or scale to changes in IFs, variable signal bandwidths and multiplex sizes. Past work on analogue fronthaul techniques, for example [9], [33], [34], has typically relied on a significant amount of analogue

processing. Operation within a 5G (and beyond) RAN means that multiplexes of different sizes, variable channel bandwidths (requiring variable filter passbands), different numerologies (i.e. sampling rates) and different RATs, need to be supported. The technique presented in this work multiplexes a large number of channels with different bandwidths and numerologies in a flexible and scalable manner. This is a result of the mapping method employed but also of processing carried out solely in the digital domain. Flexibility and scalability is thus achieved through multiple means (for example, a single large IFFT can be used per numerology but there is flexibility to employ separate IFFTs per numerology if reducing the size of the IFFT is desirable). Since most of the processing is performed in the digital domain, even when the THA is added as an extension to the fundamental technique, and analogue filters are used to select groups of channels, the addition of analogue processing has minimal effect on the flexibility of the system.

1.5 Structure of Thesis

The thesis is divided into 8 chapters, namely:

Chapter 2: The background theory for this thesis is presented, which includes the 5G physical interface, the theory of OFDM, error vector magnitude and sampling theory.

Chapter 3: RoF and its application in the modern fronthaul, as well as the different types of fronthaul architectures and their limitations are discussed in this chapter.

Chapter 4: This chapter discusses measurement results at microwave and millimetre wave frequencies employing channel aggregation (SCM) via analogue and digital techniques and channel de-aggregation via analogue techniques. It also includes characterisation and modelling of devices used in measurements within a VPI simulation environment, as well as simulation results of analogue SCM at mm-wave frequencies.

Chapter 5: This chapter presents the concept of a flexible SCM scheme employing Nyquist zone mapping and channel aggregation/ de-aggregation in the digital domain, with multiplexes of different sizes, employing different channel bandwidths and numerologies.

Chapter 6: Based on the concept introduced in the previous chapter, this chapter discusses the resulting system architecture and measurement results at microwave frequencies (with generic

and 5G numerologies), coupled with mmW generation and up-conversion via a remotely delivered mmW carrier.

Chapter 7: In this chapter, the system presented in the previous two chapters is modelled while the model is matched with measurement results employing generic and 5G numerologies. Following this, the model is extended and used to validate the performance predictions with a bandwidth-extension device through simulation.

Chapter 8: The conclusions and future work are presented in this chapter.

2 Background and Literature Review

2.1 Introduction

This chapter aims to provide the reader with the necessary background information for the specific concepts and technologies discussed in the rest of this thesis.

The chapter begins with a brief discussion of the different generations of mobile communication standards in Section 2.2. The frequency bands, technologies and services supported by each of these generations, as well as the expectations from 5G are discussed in this section. The introduction of a new 5G physical interface in order to address these expectations is discussed in Section 2.3. The discussions in both these sections are aimed at providing the reader with an understanding of the targets of 5G that form the foundation of this work.

The theory of OFDM, as well as DMT, is discussed in detail in Section 2.4. The different stages of OFDM signal generation and reception are examined, along with the role of the CP in the transmission of the signal through a channel and its effects on equalisation at the receiver. Moreover, performance issues with OFDM/ DMT such as Peak-to-Average Power Ratio (PAPR), timing and frequency offsets and the different methods that are employed to counteract these effects are discussed. This information is important, as both OFDM and DMT waveforms, as well as extensions of their transmitter and receiver structures to create multiplexes, have been used extensively in this thesis.

This is followed by a discussion on the Error Vector Magnitude (EVM) metric in Section 2.5. EVM has been used as the main performance metric for all results presented in this thesis. Finally, in Section 2.6, sampling theory is discussed, namely the difference between oversampling and under-sampling and the benefits and drawbacks of each of these techniques. These concepts are important as they are used extensively in the work presented in later chapters.

The chapter ends with Summary and Conclusions in Section 2.7.

2.2 Evolution of Wireless Technologies

In the past 30+ years, a new generation of mobile technologies has been introduced approximately every 10 years. The first generation of mobile communication networks, abbreviated “1G”, based on analogue voice communications, was introduced in the 1980s. However, as mobile telephony gained momentum, the limitations of 1G such as bulky devices, costly service, poor coverage and inefficient use of resources, became clear. 2G systems based on digital communications were introduced in the 1990s, which saw the advent of spectrum sharing schemes such as Time Division Multiple Access (TDMA) (employed by the Groupe Speciale Mobile or Global System of Mobile Communications (GSM) standard) and Code Division Multiple Access (CDMA) (employed by the Qualcomm Interim Standard 95 (IS-95)). These technologies became the foundation for 3G, which was introduced in the 2000s. By that time, the Internet had become widely accessible to the consumer community and the introduction of smartphones and other types of mobile devices meant that in addition to making voice calls, service users could navigate the Internet, download and stream movies and make video calls on the move, among many other applications [35], [36].

While 3G did increase voice capacity, the key changes were the optimisation of mobile networks for data services and the foundation of mobile broadband. 3G was succeeded by 4G and the Long Term Evolution/ Long Term Evolution-Advanced (LTE/ LTE-A) standard, which led to faster, better mobile broadband, along with a new, simplified all-Internet Protocol (IP) network architecture. A new air interface design was introduced, based on Orthogonal Frequency Division Multiplexing (OFDM) waveforms and multiple access (via Orthogonal Frequency Division Multiple Access (OFDMA) downlink and Single-Carrier Frequency Division Multiple Access (SC-FDMA) uplink). 4G-LTE has continued to evolve since then, introducing new technologies such as Multiple-Input Multiple-Output (MIMO), carrier-aggregation, higher modulation orders etc. in order to address the surge in data traffic, which has grown exponentially in the last decade [37].

A drastic upgrade of the entire communication infrastructure is required by the year 2020 in order to support the forecasted growth in the flow of information. As a result, frequencies higher than 3 GHz, where contiguous spectrum is available to accommodate wider communication channels, are required in order to support the demand for broader channel bandwidth associated with the forecasted growth.

The steady evolution of wireless technologies towards higher capacity and data rates is shown in Figure 2-1. The frequency bands shown in the figure will be discussed in Section 2.3.

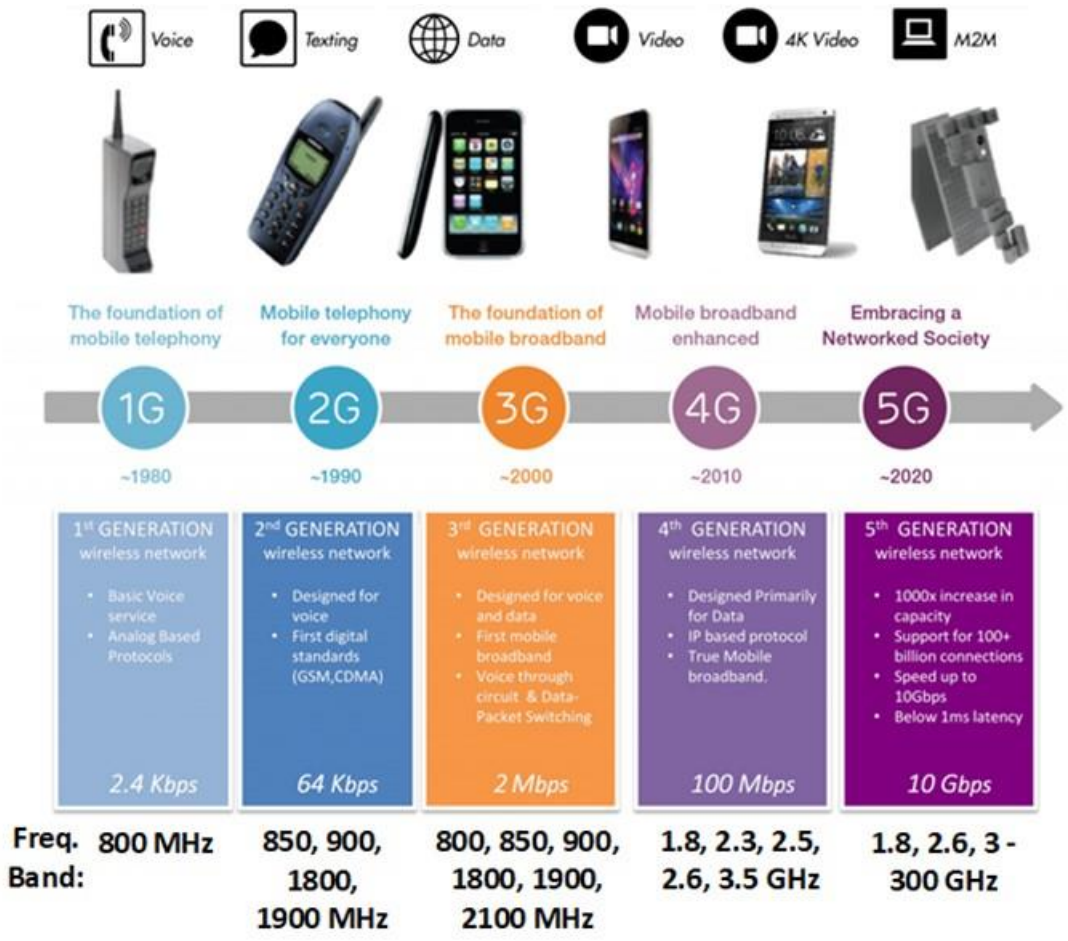

Figure 2-1 Evolution of Wireless Technologies [Source: SILIKA 2020 EU Project, 2017].

Fifth-generation wireless systems (5G) are the telecommunications standards that are set to succeed the current 4G standard. Compared to 4G, 5G aims to provide much higher data rates, reduced latency, ultra-reliability, energy efficiency, cost reduction, higher system capacity and massive device connectivity. The GSM Association (GSMA) [38], Next Generation Mobile Network (NGMN) [1] and the Mobile and wireless communications Enablers for the Twenty-twenty Information Society (METIS) project [2] have defined several use cases (or requirements), which can be narrowed down to three main categories:

- *Enhanced Mobile Broadband (eMBB)*
    - 10+ Gbps to users (100x typical data rate, even for high mobility; 1000x capacity/ km^2)
- *Ultra-Reliable, Low-Latency Communications (URLLC)*
    - Millisecond end-to-end latencies (<1ms Radio Access Network (RAN) latency)
- *Massive Machine-Type Communications (mMTC)*
    - Extremely large numbers of low data-rate devices (100x connected devices, even in crowded areas)

These use cases have been shown in Figure 2-2. GSMA also identifies fixed wireless access as a use case [38], which is the ability to offer fibre type speeds in both developed and developing markets using new wider frequency bands, massive MIMO (mMIMO) [39], [40] and beamforming technologies [41], [42], [43].

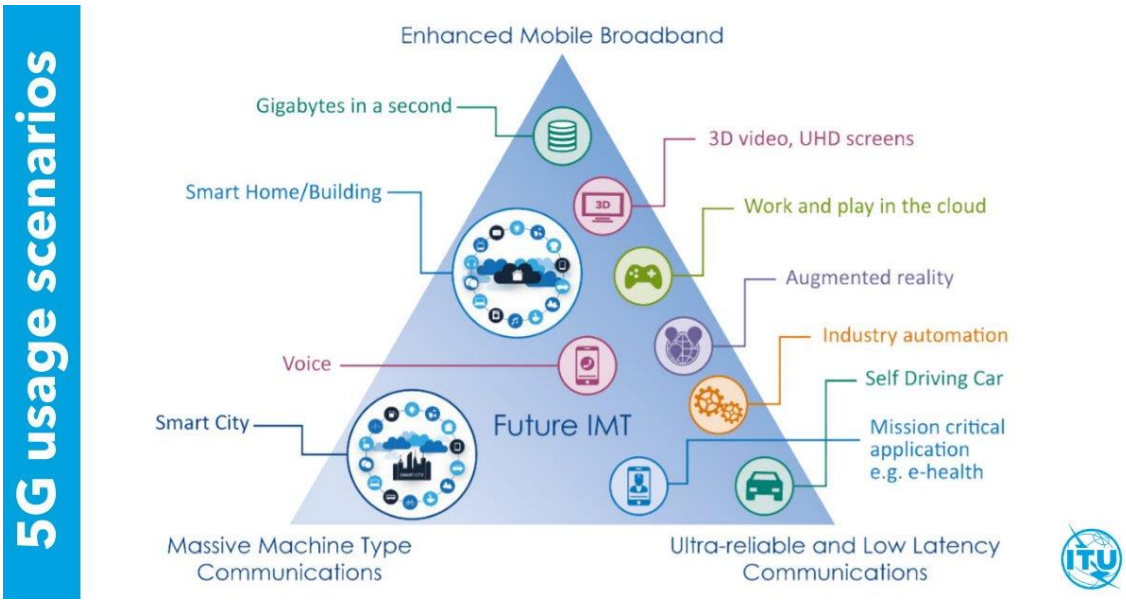

Figure 2-2 5G usage scenarios [Source: International Telecommunication Union (ITU), 2018].

The use cases will form the basis of radio technologies (or concepts) such as Device-to-Device (D2D), Moving Networks (MNs), Ultra-Dense Networks (UDNs) and mMIMO among others. Emerging applications and services enabled by 5G such as augmented/ virtual reality, Internet of Things (IoT) sensors and networks, embedded devices, advanced robotics, safety and lifeline systems, vehicle-to-Everything (V2X), cloud infrastructure, artificial intelligence etc. will be used by industry vertical service providers such as education, healthcare, smart grid and autonomous

transportation [36]. Some of these radio technologies and applications are shown in Figure 2-3 and will be covered in more detail in later sections.

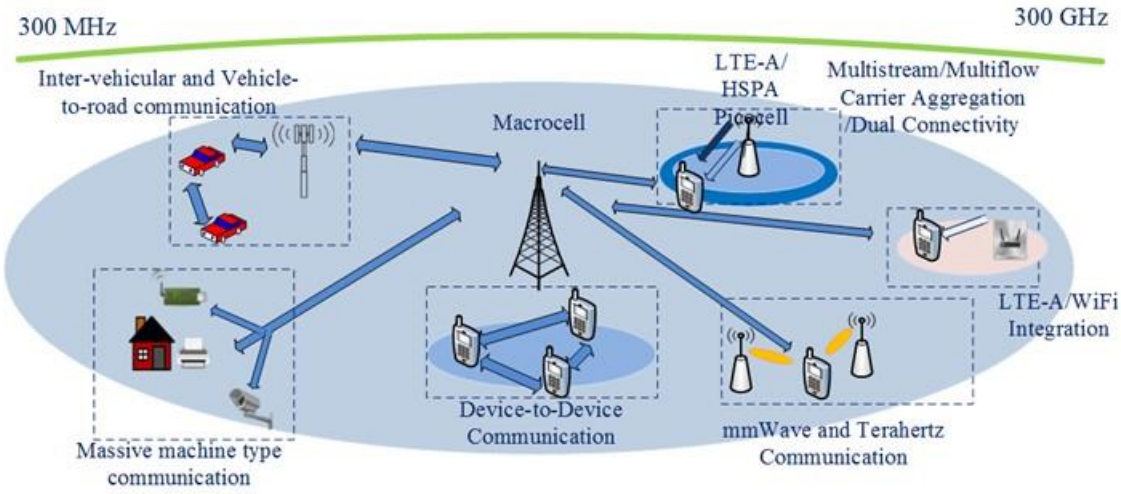

Figure 2-3 5G radio technologies and applications [Source: Georgia Institute of Technology, 2014].

2.3 The Fifth Generation of Mobile Communication Networks (5G) Physical Interface

Each new generation of mobile communication networks is assigned new frequency bands and wider spectral bandwidth per frequency channel (as depicted in Figure 2-1). 1G had a maximum per channel bandwidth of 30 kHz (frequency bands up to 800 MHz), 2G employed up to 200 kHz (frequency bands up to 1.9 GHz), 3G employed up to 5 MHz (frequency bands up to 2.1 GHz) and 4G, employed up to 20 MHz (frequency bands up to 3 GHz). For 5G, there is little room available for larger channel bandwidths while frequency bands suitable for land-mobile radio will overlap with K-band (18 - 27 GHz) transmissions of communication satellites [36]. The 3rd Generation Partnership Project (3GPP) is working to create system specifications for the unified 5G New Radio (NR) air interface, within the scope of the International Mobile Telecommunications 2020 (IMT-2020) project of the International Telecommunications Union (ITU). While previous generation networks primarily opted for licensed spectrum below 3 GHz, 5G NR will expand spectrum usage to licensed, shared and unlicensed spectrum, which will include existing mobile bands as well as new, wider 5G bands. These will include low-bands,

below 1 GHz, mid-bands between 1 and 6 GHz and high-bands above 24 GHz [3]. Channel bandwidths ranging from 5 MHz to 100 MHz will be supported for bands below 6 GHz while channel bandwidths from 50 MHz to 400 MHz will be supported for bands above 24 GHz [38].

The choice of radio waveform and multiple access technique are two of the most important decisions for designing the new 5G physical layer. To this end, many different candidate waveforms have been studied such as Universal-Filtered Multi-Carrier (UFMC), Resource Block Filtered Orthogonal Frequency Division Multiplexing (RB-F-OFDM) and Filtered-OFDM (F-OFDM), which are sub-band filtering waveforms and Filter-Bank Multi-Carrier (FBMC), which is a subcarrier filtering waveform [44], [45], [46], [47]. These waveforms have been mainly compared with standard OFDM, also known as Cyclic Prefix OFDM (CP-OFDM), with respect to out-of-band emissions and robustness against Carrier Frequency Offset (CFO) and Inter-Symbol Interference (ISI) [48]. However, 3GPP in its current release (release 15) has decided to adopt CP-OFDM with up to 256-QAM subcarrier modulation [49], [50] based on the most important performance indicators such as compatibility with multi-antenna technologies, high spectral efficiency, low implementation complexity, robustness to oscillator phase noise (crucial for operation at mm-wave frequencies) etc. [51]. Moreover, unlike 4G, where only Discrete Fourier Transform spread OFDM (DFT-s-OFDM, also known as SC-FDMA) was used in the uplink, 5G will employ both CP-OFDM and DFT-s-OFDM in the uplink, with CP-OFDM in the downlink [49].

Therefore, 5G radio access will comprise LTE evolution operating below 6 GHz while NR operates between 1 GHz to 100 GHz. In order to fulfil the requirements of the wide range of deployment options and services, a number of flexible OFDM numerologies have been proposed for 5G NR. These numerologies are defined by subcarrier spacing and cyclic prefix (normal/ extended) and the scalable subcarrier spacing (Δf) is defined by [49], [51], [50]:

$$\Delta f = 2^{\mu} \cdot 15 \quad , \quad \text{(kHz)} \tag{2-1}$$

where μ is the numerology factor and 15 kHz is the sub-carrier spacing of the base numerology (employed by LTE). Table 2-1 shows the different 5G numerologies and supported channels [50].

Table 2-1 5G numerology and supported channels. Sync signalling includes primary and secondary synchronisation signals while Broadcast includes the physical broadcast channel (PBCH)

Numerology factor	Subcarrier spacing (kHz)	CP type	Supported for Data/ Sync and Broadcast
0	15	Normal	Sync (< 6 GHz), Data (< 6 GHz)
1	30	Normal	Sync (< 6 GHz), Data (< 6 GHz)
2	60	Normal, extended	Data (< 6GHz and > 6 GHz)
3	120	Normal	Sync (> 6 GHz), Data (> 6 GHz)
4	240	Normal	Sync (> 6 GHz)

2.4 Orthogonal Frequency Division Multiplexing

Orthogonal Frequency Division Multiplexing (OFDM) [52], [53] (also known as CP-OFDM) is a special case of Frequency Division Multiplexing (FDM) that uses a large number of parallel, narrow-band subcarriers instead of a single wide-band carrier to transport information. Since adjacent subcarriers are orthogonal to each other, multiple subcarriers can be transmitted simultaneously in a tight frequency space without interference from one another. System standards using OFDM include [54], [55], [56], [57]:

- Wireless standards such as IEEE 802.11a, g, j, n (Wi-Fi) Wireless LAN; IEEE 802.15.3a Ultra Wideband (UWB) Wireless Personal Area Network (PAN); IEEE 802.16d/e (WiMAX); terrestrial digital TV systems, e.g. Digital Video Broadcasting – Terrestrial (DVB-T); 3GPP LTE/4G and now 5G
- Fixed/ wireline standards such as Asymmetric Digital Subscriber Line (ADSL), Very-high-bit-rate Digital Subscriber Line (VDSL), Power Line Communication (PLC) etc.

A simplified block diagram for the transmitter and receiver sections of an OFDM system is shown in Figure 2-4. Upper case characters denote frequency domain samples while lower case characters denote time domain samples.

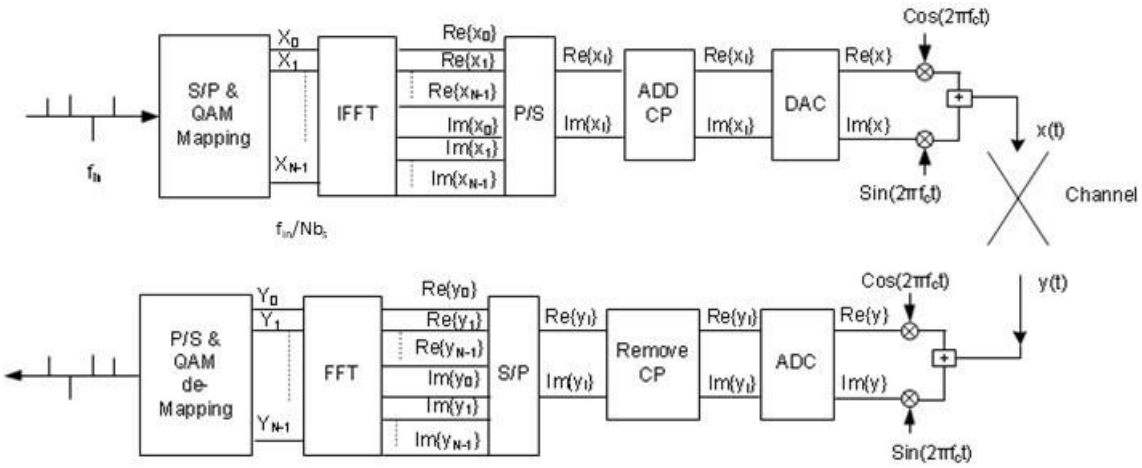

Figure 2-4 OFDM Transmitter and Receiver architectures [58].

The input data bits arrive at a rate, f_{in}, such that

$$f_{in} = \frac{b_s}{T_s} \ , \tag{2-2}$$

where, b_s is the bits per symbol and T_s is the input symbol time, with $1/T_s$ being the symbol rate. Following this stage, the bits go through Serial-to-Parallel (S/P) conversion and are mapped to Quadrature Amplitude Modulation (QAM) constellation points. The resulting QAM symbols create a vector of frequency domain samples $[X_0\ X_1 \ldots\ldots X_{N-1}]^T$, where N is the IFFT length. At this point, the rate of the samples, $r_{samples}$, is given by

$$r_{samples} = \frac{f_{in}}{N} \ . \tag{2-3}$$

The frequency domain samples then go through the IFFT block, which produces the vector of time domain samples $[x_0\ x_1 \ldots\ldots x_{N-1}]^T$.

The output of the IFFT modulator for a single symbol is given by [59]

$$x[n] = \frac{1}{\sqrt{N}} \sum_{k=0}^{N-1} X[k] e^{\frac{j2\pi kn}{N}} \ , \tag{2-4}$$

where the time domain samples at the output of the IFFT block are denoted by $x[n]$ while the frequency domain samples at the input of the IFFT block are denoted by $X[k]$.

After the IFFT stage and Parallel-to-Serial conversion (P/S), a CP is appended at the beginning of each OFDM symbol (the purpose of this step will be explained later). The OFDM symbol with a

CP (with a time duration of t_{CP}) appended to it will be referred to as a "frame". The baseband representation of the signal at this stage is given by

$$x_{CP}^{s}[n] = x^{s}[n].g[n] \ , \tag{2-5}$$

where *s* is the OFDM symbol index, $x^s[n]$ is the output of the IFFT for symbol *s* and *g[n]* is a window function. By default, a rectangular window function is used, with a span in time between $-t_{CP}$ and NT_s, with NT_s being the time duration of the OFDM symbol at the output of the IFFT (i.e. the OFDM symbol duration). This operation results in a sinc response for each subcarrier in the frequency domain, with nulls at intervals of the subcarrier spacing (neglecting the CP, this is equal to the OFDM symbol rate, $\Delta f = 1/NT_s$).

An example of the resulting frequency domain representation of the OFDM signal for a small number of subcarriers is show in Figure 2-5. At each sampling instant, the contribution of all other subcarriers except the one that is being sampled is at a zero crossing, resulting in orthogonality being maintained among the subcarriers. This also results in spectral efficiency as the spectrum is divided into overlapping orthogonal subcarriers (instead of individual subcarriers separated by frequency guard bands), due to the nature of the pulse shaping function *sin(x)/x*.

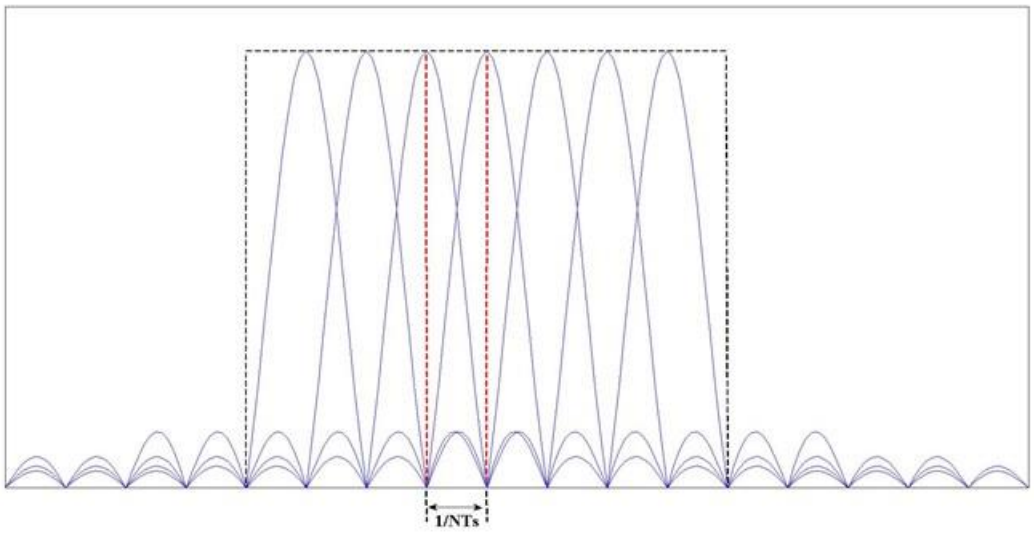

Figure 2-5 Frequency domain representation of an OFDM signal [58].

Generally, oversampling is applied to keep the filtering requirements at the output of the IFFT to a minimum. This operation can be represented by [60]

$$x\left[\frac{n}{Z}\right] = IFFT\sqrt{Z}\left(\left[X_0 \dots \dots X_{\frac{N}{2}-1}\ 0 \dots \dots 0\ X_{\frac{N}{2}} \dots \dots X_{N-1}\right]^T\right), \quad (2\text{-}6)$$

where *Z* is the oversampling factor and where there are *N(Z-1)* null subcarriers/ zeroes.

This stage is followed by a Digital-to-Analogue Converter (DAC) stage and up-conversion to pass-band (modulating the RF carrier), for transmission through a physical channel. After RF up-conversion, the RF output can be written as

$$x_{RF}(t) = \sum_{k=0}^{N-1}|X[k]|\cos\left[2\pi\left(f_c + \frac{k}{NT_s}\right)t + \Phi[k]\right], \quad (2\text{-}7)$$

where $|X[k]|$ and $\Phi[k]$ are the magnitude and phase of the complex symbols respectively. They are defined by the constellation of the chosen subcarrier modulation scheme (e.g. QAM, QPSK).

Discrete Multi-Tone (DMT) [54] is also a type of multicarrier modulation that like OFDM, divides a high-speed data stream into multiple parallel lower-speed streams and modulates them onto separate subcarriers of different frequencies. This type of waveform has been widely employed in copper-based wireline standards (such as ADSL) and more recently, in applications such as OWC or Visible Light Communications (VLC) [25], [26], [61]. Contrary to OFDM, the DMT output signal after the IFFT stage at the transmitter is real-valued and no in-phase and quadrature-phase (IQ) modulation onto an RF carrier is required [62]. As a result, broadband, high-frequency, analogue RF components required for IQ modulation are omitted from DMT transceivers and only a single DAC and ADC at the transmitter and receiver, respectively, are required to generate and capture the DMT sequence. Both these factors lead to a reduction in cost and complexity, making DMT a popular choice for OWC.

In order to generate a multicarrier sequence consisting of *N* subcarriers, DMT requires the use of an IFFT operation that is twice the length of the one needed for OFDM (and vice versa for the FFT stage at the receiver). To create a real-valued baseband DMT transmission sequence consisting of *N* subcarriers, a *2N*-point IFFT is required. For the *2N* inputs of the IFFT (frequency domain), indexed by *k = 0, 1, …, 2N-1*, the first half are assigned the values X_k while the second half have to be assigned the complex conjugate values of X_k^*. The Hermitian symmetry property is given by

$$X_{2N-k} = X_k^*, \quad (2\text{-}8)$$

for *k = 0, 1, …, 2N-1* and Im{X_0} = Im{X_N} = 0, such that there is no direct current (DC) value (the imaginary part is denoted by the Im{.} operator). Following this stage, the real-valued, time-domain output *x[n]* of the 2N-point IFFT, is given by [63]

$$x[n] = \frac{1}{\sqrt{2N}} \sum_{k=0}^{2N-1} X_k e^{j2\pi n \frac{k}{2N}} \quad . \tag{2-9}$$

Since the real-valued input and output sequences of the FFT and IFFT operations (respectively) are characterised by symmetry properties, these operations can be optimised for DMT modulation and half the number of computations can be saved. DMT and OFDM require approximately the same amount of complexity even though DMT employs a longer IFFT/ FFT length [63].

For both OFDM and DMT, the processes carried out at the transmitter are reversed at the receiver in order to retrieve the original QAM symbols.

2.4.1 Cyclic Prefix and Equalisation

2.4.1.1 Linear to Circular Convolution

In a linear time-invariant discrete-time channel with an impulse response *h[n]*, the output *y[n]* is the discrete-time convolution of the channel impulse response and the input data stream *x[n]* [59]. This can be expressed as

$$y[n] = h[n] * x[n] = x[n] * h[n] = \sum_k h[k]x[n-k] \ . \tag{2-10}$$

The *N*-point circular convolution of *x[n]* and *h[n]* is defined as

$$y[n] = x[n] \circledast h[n] = h[n] \circledast x[n] = \sum_k h[k]x[n-k]_N \ , \tag{2-11}$$

where *[n-k]$_N$* represents *[n-k]* modulo *N*. Therefore, *x[n-k]$_N$* is the periodic version of *x[n-k]* with period *N* and *y[n]* from (2-11) is also periodic with period *N*. Circular convolution in the time domain leads to multiplication in the frequency domain. In the absence of noise, this can be expressed as

$$DFT\{y[n] = x[n] \circledast h[n]\} = X[i]H[i] \ , \ 0 \le i \le N-1 \ , \tag{2-12}$$

where *H[i]* is the *N*-point Discrete Fourier Transform (DFT) of {*h[n]*}. When the sequence {*h[n]*} is of length *k*<*N*, it is padded with *N*-*k* zeros to obtain a length *N* for the *N*-point DFT. From (2-12), if the channel and input are circularly convolved, provided that *h[n]* is known at the receiver, the original data sequence *x[n]* can be recovered by taking the IDFT such that

$$x[n] = IDFT\left\{\frac{Y[i]}{H[i]}\right\} = IDFT\left\{\frac{DFT\{y[n]\}}{DFT\{h[n]\}}\right\} \ , 0 \le i, n \le N-1 \ . \quad (2\text{-}13)$$

2.4.1.2 Mitigation of Inter-Symbol Interference (ISI)

Linear convolution with a channel can cause energy from the previous and subsequent periodic extensions to leak into the current signal. A guard interval is required to accommodate the decaying transient of the previous symbol and prevent the initial transient from reaching the current symbol, an effect known as Inter-Symbol Interference (ISI). For OFDM, this guard interval can be inserted via two different methods. One method involves zero padding the guard interval and is known as zero prefix (ZP). The other method involves a cyclic extension of the OFDM symbol: a CP or Cyclic Suffix (CS) [64]. An advantage of using a zero prefix, which is a form of vector coding, is that no power is used to transmit it. However, for vector coding, the complexity scales quickly with *N* subcarriers in multichannel modulation schemes like OFDM and real-time channel knowledge is required at the transmitter, which is difficult to achieve in wireless systems [59]. In the case of OFDM, the standard method of CP insertion is making a copy of the last samples of the OFDM symbol and appending them to the beginning of the symbol. Therefore, the CP acts as a special time guard for an OFDM symbol transition to combat time dispersion. This is illustrated in Figure 2-6.

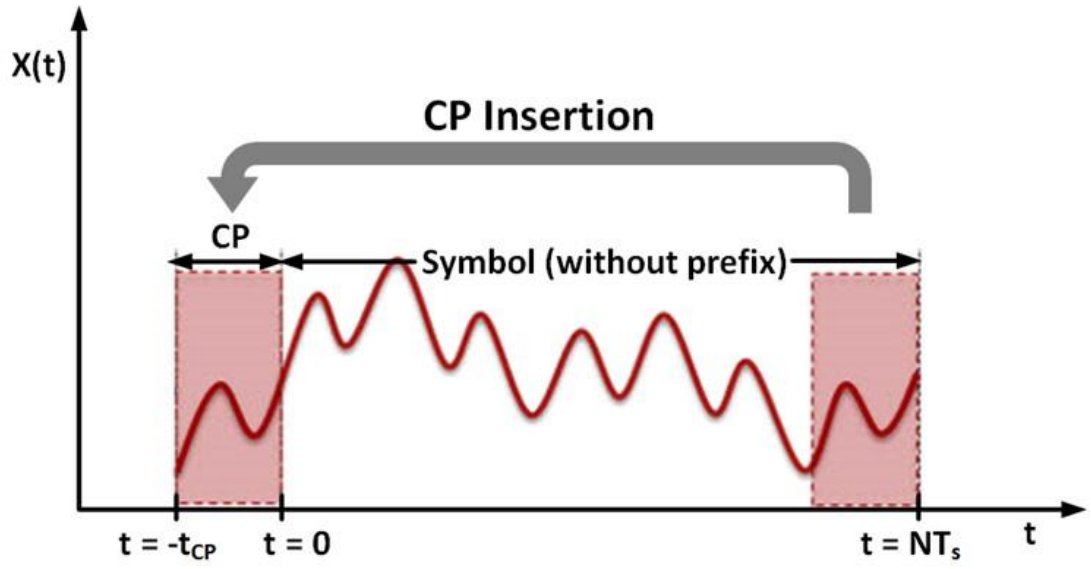

Figure 2-6 Example of CP insertion with time duration t_{CP}.

Upon CP addition, an OFDM symbol consisting of *N* samples in the discrete time domain obeys the following rule

$$x_{-\mu} = x_{N-\mu} \ , \tag{2-14}$$

where μ is the number of samples used to describe the CP and the total length of the new sequence of samples is $N+\mu$. This way, the first μ samples of the channel output affected by ISI can be discarded without any loss relative to the original information sequence. In continuous time, this is equivalent to using a guard band of duration T_m (the channel delay spread) after every block of *N* symbols of duration NT_s, in order to eliminate ISI between these data blocks. When the length of the CP is set longer than or equal to the maximum delay of a multipath channel, the ISI effect of an OFDM symbol on the next symbol is confined within the guard interval so that it may not affect the FFT of the next OFDM symbol (taken for the duration of the OFDM symbol without CP). As a result, a CP longer than the maximum delay of the multipath channel allows for maintaining the orthogonality among the subcarriers [64]. The CP can also be of different lengths depending on deployment scenario and can be categorised into normal and extended CP. Extended CP is generally used for larger coverage areas where the delay spread is longer.

CP insertion has its disadvantages as well as its obvious advantages. Since μ symbols are added to the input data blocks, there is an overhead of μ/N and a resulting data-rate reduction of

N/(μ+N). There is also a transmit power penalty by a factor of *(μ+N)/N*, associated with sending the CP as the prefix consists of redundant data [59].

2.4.1.3 Simplification of Equalisation

A continuous-time channel with a frequency response *H(f)* can be divided into orthogonal sub-channels without the knowledge of *H(f)* by splitting the total signal bandwidth into non-overlapping sub-bands. Similarly, knowledge of channel gains *H[i]*, *i = 0, …, N-1*, is not required in an OFDM system, which effectively decomposes the wideband channel into a set of narrowband orthogonal sub-channels with different QAM symbols. The demodulator can use the channel gains to recover the original QAM symbols by dividing these gains, such that

$$X[i] = Y[i]/H[i] \ . \tag{2-15}$$

This process is known as frequency equalisation [59]. However, for continuous-time OFDM, since the noise of the *i*th sub-channel is also scaled by *1/H[i]*, frequency equalisation leads to noise enhancement. As a result, even though the effect of flat fading on *X[i]* is removed by equalisation, the received SNR is unchanged.

The combined effect of the CP addition and the linear convolution of the OFDM signal results mathematically in circular convolution. Thus, the transmitted signal can be recovered from the received signal by multiplication with *1/H(i)*, where *H(i)* is the DFT of the channel response, meaning that the equalisation is carried out in the frequency domain. This type of equalization is known as zero-forcing equalisation.

Therefore, the CP being a guard interval mitigates ISI and in addition, simplifies the equalisation procedure at the receiver.

2.4.2 Issues with OFDM/ DMT

- *Peak-to-Average Power Ratio (PAPR)*

PAPR is an important factor in communication systems. For an analogue signal, PAPR is equal to the peak instantaneous power divided by the average power of the signal. PAPR is often given

as the square of the crest factor (CF), which is defined as the peak voltage over the RMS voltage of the signal.

Transmit power amplifiers operate more efficiently when the PAPR is low while they have to be operated with a large input power backoff to ensure linear amplification of the signal when the PAPR is high [59]. A typical power amplifier response is shown in Figure 2-7.

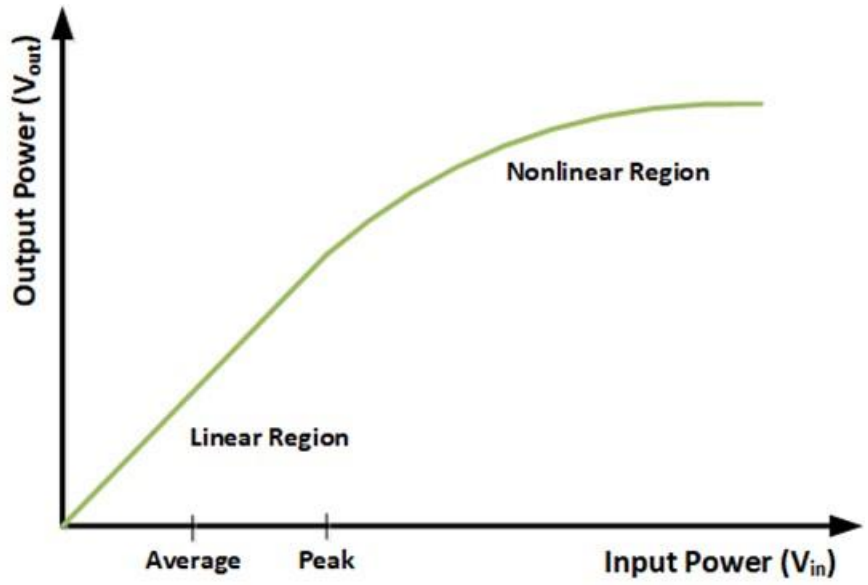

Figure 2-7 Typical power amplifier response.

In order to avoid signal distortion, operation in the linear region is desirable to keep the peak value constrained within this region and avoid signal distortion. Moreover, having the average value as close as possible to the peak value would ensure that the power amplifier operates at maximum efficiency.

High PAPR signals also possess large dynamic ranges necessitating the use of ADCs with high resolutions, which in turn places complexity and power penalty on receiver frontends.

PAPR is a considerable problem with multicarrier modulation schemes such as OFDM [59], [65], [66], as these signals possess high PAPR (peak PAPR increases approximately linearly with the number of subcarriers (N)). Techniques to reduce the effect of high PAPR include oversampling, clipping of the OFDM signal above some threshold, correction of nonlinear distortion from the power amplifier and special coding techniques [58], [59].

- *Timing and Frequency Offsets*

In OFDM, orthogonality among subcarriers is ensured by the subcarrier spacing, Δf,

$$\Delta f = \frac{1}{T_N} \ , \tag{2-16}$$

where, T_N (= NT_s) is the symbol time of the modulated signal in each subcarrier.

In practice, this frequency separation between the subcarriers is imperfect due to mismatched LOs (between transmitter and receiver), sampling frequency mismatches, Doppler frequency shifts or timing synchronisation errors, meaning that (2-16) does not hold. This results in inter-carrier interference (ICI), as the received FFT samples contain interference from adjacent subcarriers [59].

Time synchronisation can be obtained by cross-correlating the received signal $x_r(t)$ with the input signal $x_i(t)$, such that

$$R_{x_i x_r}(\tau) = \int_0^{NT} x_i^*(t) x_r(t+\tau) dt \ , \tag{2-17}$$

where * denotes the complex conjugate, and the received signal is given by

$$x_r(t) = x_i(t - t_d) + n(t) + d(t) \ , \tag{2-18}$$

where, t_d is the delay experienced by the signal through the link, $n(t)$ is additive noise and $d(t)$ is the distortion. The peak of the integral in (2-17) occurs at a delay value equal to the delay experienced by the signal through the channel and can thus be used to align the FFT window at the receiver.

The effects of timing offset are less compared to those from frequency offsets, if the full N-sample OFDM symbol is used at the receiver without interference from the previous or subsequent OFDM symbols. For this to happen, the cyclic prefix length, $\mu \gg \sigma_{Tm}/\mathrm{T_s}$ (T_m is the channel delay spread, T_s is the sampling time associated with the discrete time sequence and σ_{Tm} is the channel's rms delay spread). [59].

Error in frequency synchronisation due to LO frequency mismatches and sampling frequency (clock) mismatches between transmitter and receiver is a more serious issue in OFDM. This type of offset is illustrated in Figure 2-8. The frequency offset leads to a form of frequency modulation imposed on the time domain signal and a loss of orthogonality. This can be expressed as

$$\hat{X}(f) = X(f - \Delta f) \ . \tag{2-19}$$

A continuously rotating constellation is an indication of LO offset.

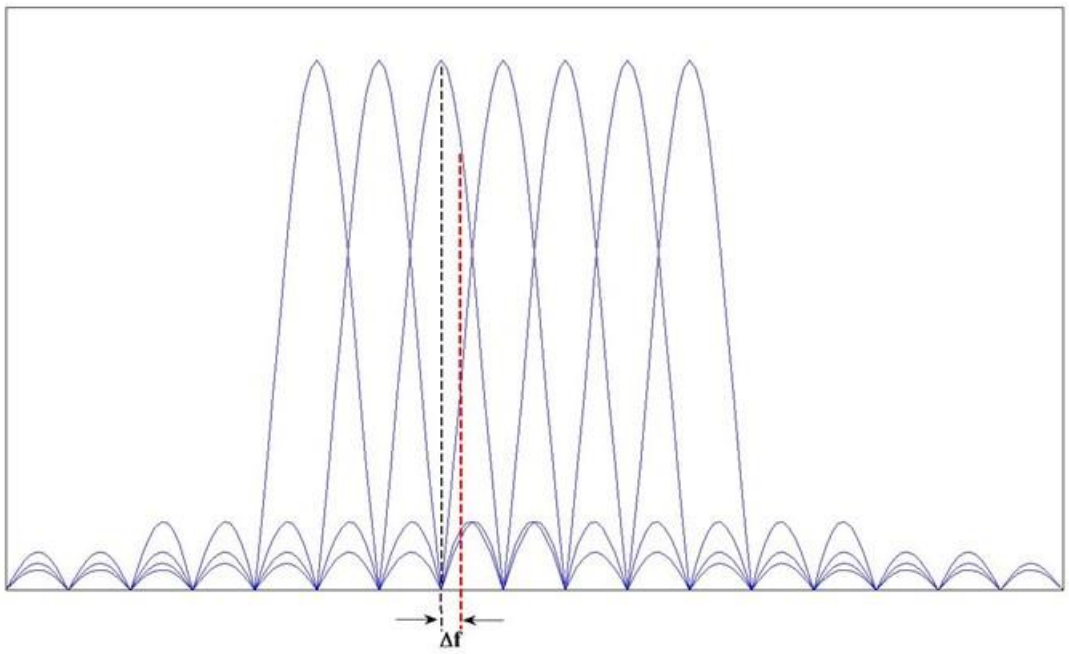

Figure 2-8 LO offsets causing incorrect sampling times [58].

Various methods exist that can provide information to the receiver, to provide some form of compensation for these offsets. These methods may be blind or non-blind (the non-blind method involves redundant information being sent from transmitter to receiver to track changes to the signal). For a timing offset, in practice, a similar procedure is carried out with a known sequence called a preamble that allows the receiver to synchronise the FFT window. The known sequence and the received one are applied to the integral in (2-17) to obtain the delay experienced by the signal due to the channel. A Pilot Symbol Assisted Modulation (PSAM) technique can also be used for time offset correction [67]. Known symbols are inserted periodically into the data sequence in the frequency domain so that the receiver can obtain information regarding the relative phase shifts of the subcarriers [68]. For correct estimation, the distance between adjacent pilot tones must be less than or equal to half the period of the channel transfer function [67]. Training sequences or pilot tones can also be used for both time and frequency synchronisation [69]. Moreover, redundancy of the CP can also be used for both frequency and time synchronisation [70], [71].

2.5 Error Vector Magnitude and other measures of link performance

EVM (similar to metrics such as Receiver Constellation Error (RCE)), is a metric used in advanced wireless system standards with complex modulation formats such as IEEE 802.11g wireless local area networks (WLANs) standards [72] and IEEE 802.16-2009 WiMAX standards [73], to measure the signal quality of a digital radio transmitter or receiver. Each of the different wireless standards specifies a maximum allowed EVM value and it is important that the measured EVM of the demodulated signal lies below this value, e.g. the 3GPP limits of 12.5% for 16-QAM, 8% for 64-QAM and 3.5% for 256-QAM for 5G [74]. EVM measurements are considered to be more useful than other measurements such as the often-used Bit Error Rate (BER), as they provide information about both amplitude and phase error in the signals [75].

EVM is a direct indication of modulation quality. It describes the vector difference or error (in terms of the Euclidean distance) between a received (measured) and an ideal point in a given QAM constellation, thus representing the noise and distortion in the transmission system. Figure 2-9 shows the 16-QAM constellation diagram containing all the ideal symbols (reference symbols) and one of the received symbols.

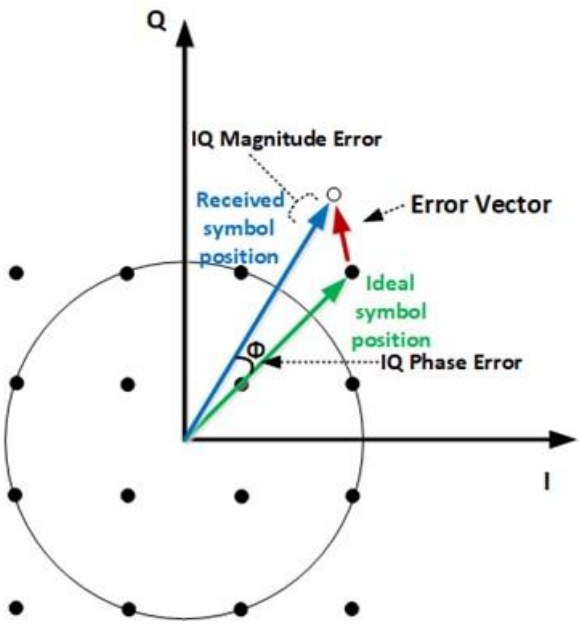

Figure 2-9 Error Vector Magnitude constellation diagram for 16-QAM [23]

The Error Vector (δ_{er}) can be calculated by

$$\delta_{er} = I(X_r - X_i) + Q(X_r - X_i) \ , \tag{2-20}$$

where $I(X_r)$ and $Q(X_r)$ are the In-phase (Real) and Quadrature phase (Imaginary) components of the received symbols while $I(X_i)$ and $Q(X_i)$ are the In-phase (Real) and Quadrature phase (Imaginary) components of the ideal symbols.

There are many definitions of EVM, depending on standard specifications [58]:

$$EVM(\%\, rms) = 100 \sqrt{\frac{\frac{1}{N}\sum_{n-1}^{N}([I\{X_r - X_i\}]^2 + [Q\{X_r - X_i\}]^2)}{\frac{1}{N}\sum_{n-1}^{N}([I\{X_i\}]^2 + [Q\{X_i\}]^2)}} \ , \tag{2-21}$$

$$EVM(\%\, peak) = 100 \sqrt{\frac{\frac{1}{N}\sum_{n-1}^{N}([I\{X_r - X_i\}]^2 + [Q\{X_r - X_i\}]^2)}{\max_{i}([I\{X_i\}]^2 + [Q\{X_i\}]^2)}} \ , \tag{2-22}$$

$$EVM(\%\, rms) = 100 \frac{1}{S}\sum_{1}^{S} \sqrt{\frac{\frac{1}{N}\sum_{n-1}^{N}([I\{X_r^s - X_i^s\}]^2 + [Q\{X_r^s - X_i^s\}]^2)}{\frac{1}{N}\sum_{n-1}^{N}([I\{X_i^s\}]^2 + [Q\{X_i^s\}]^2)}} \ , \tag{2-23}$$

where S is the number of OFDM symbols over which the EVM is calculated and s is the symbol index (such that, s = 1 to s = S). As shown in (2-21), the EVM is usually given as a percentage of the RMS value of the constellation. EVM can also be defined in terms of the peak constellation power, as shown in (2-22). The averaging method depends on the system under consideration. For simple QAM based systems (non-OFDM) the averaging is carried out over a certain number of QAM symbols. For OFDM based systems, it is generally carried out over all the data subcarriers within an OFDM symbol and depending on the standard, across a number of OFDM symbols as shown in (2-23).

From (2-21), the EVM can be expressed in terms of the SNR by the following

$$EVM = \sqrt{\frac{1}{SNR}} \ . \tag{2-24}$$

EVM can only provide a measure of the end-to-end quality of the link, meaning that for links that suffer from multiple impairments, the causes of EVM degradation can become difficult to pinpoint. However, a number of effects can be associated with the error statistics or with

observable effects in the constellation diagram (for example non-linear distortion in the link due to over-amplification or uncompensated frequency error [76]).

A signal transmitted through a link has to undergo a number of compensation processes at the receiver before any EVM estimates can be obtained correctly. The constellation has to be normalised so that a comparison can be made with the ideal reference constellation. A constellation will in general experience some phase rotation and gain from the link. Moreover, the frequency response of the link has to be equalised.

The particular design of a system determines exactly how these issues are rectified and Figure 2-10 shows a generalization of these processes. The received constellation is de-rotated and equalized, while the amounts of rotation and gain required to normalize it are determined by the reference constellation. The received constellation is normalised to some average power so that comparison with the reference constellation can be carried out. In this example, the received constellation is normalised to an average power of 1. The normalization process increases both the signal and noise amplitude by the same amount, leaving the SNR unchanged.

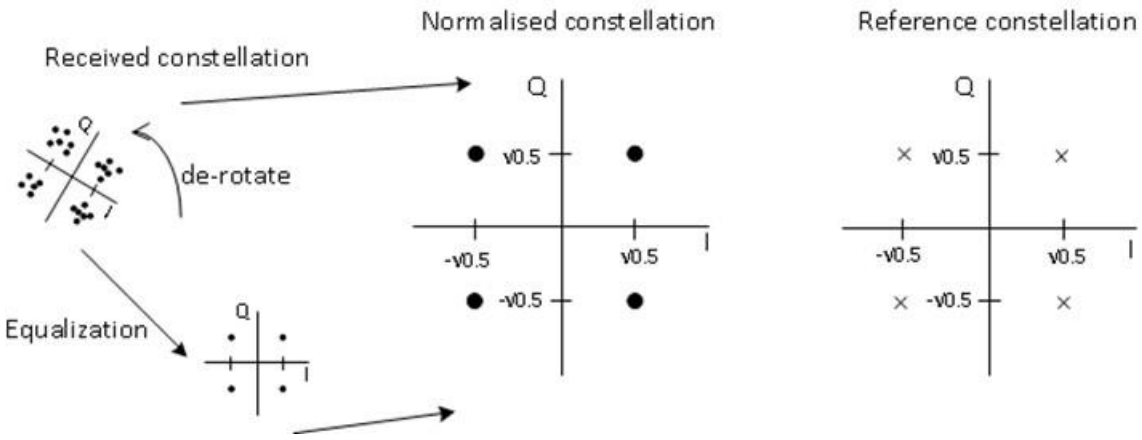

Figure 2-10 Normalization to an average power of 1 of a received constellation that has experienced some arbitrary gain and phase rotation from a link [58].

2.6 Oversampling and Under-sampling

2.6.1 Oversampling

According to the Nyquist criterion, a continuous analogue signal can be sampled such that $F_s > 2\Delta f_{in}$, in which F_s is the sampling frequency and Δf_{in} is the highest frequency component of the input signal. This means that the sampling frequency has to be at least twice the highest frequency component of a signal, to make sure that important information is not lost. Faster sampling (also known as oversampling) of a continuous analogue signal generally leads to a more accurate representation of the signal and is the norm. If fewer samples are taken, a point is reached when critical information of the signal is lost and the signal can no longer be accurately represented. If the sampling frequency is less than twice the maximum analogue signal frequency, a false (alias) frequency component is generated along with the correct one, leading to an effect called aliasing. It should be noted that the Nyquist bandwidth is defined to be the frequency spectrum from DC to $F_s/2$ and the frequency spectrum is divided into an infinite number of Nyquist zones, each having a width equal to 0.5 F_s. The first Nyquist zone is from DC to $F_s/2$, the second Nyquist zone is from $F_s/2$ to F_s and so on [77].

As demonstrated via example values in Figure 2-11, oversampling is sampling at a rate which is beyond twice the highest frequency component of the signal of interest. Since real-world signals are not perfectly filtered and often contain frequency components greater than the Nyquist freuquency, oversampling can increase the foldover frequency such that the unwanted components of the signal do not alias into the passband. As shown in the top part of the figure, for a signal with a carrier frequency of 70 MHz and a bandwidth of 20 MHz (60 MHz to 80 MHz), the maximum frequency component is 80 MHz and for an oversampling case, the minimum sampling rate is greater than 160 MSps . To keep the 60 MHz to 80 MHz band in the middle of the first Nyquist zone for flexible anti-aliasing analogue filter design, the sampling rate should be 280 MSps, which is 3.5 times the maximum frequency component of the signal.

To use a lower sampling rate as shown at the bottom of Figure 2-11, the signal bandwidth does not need to be in the middle of the first Nyquist zone and a minimum sampling rate of, e.g. 200 MSps. However in this case, band-pass filter design has more stringent requirements.

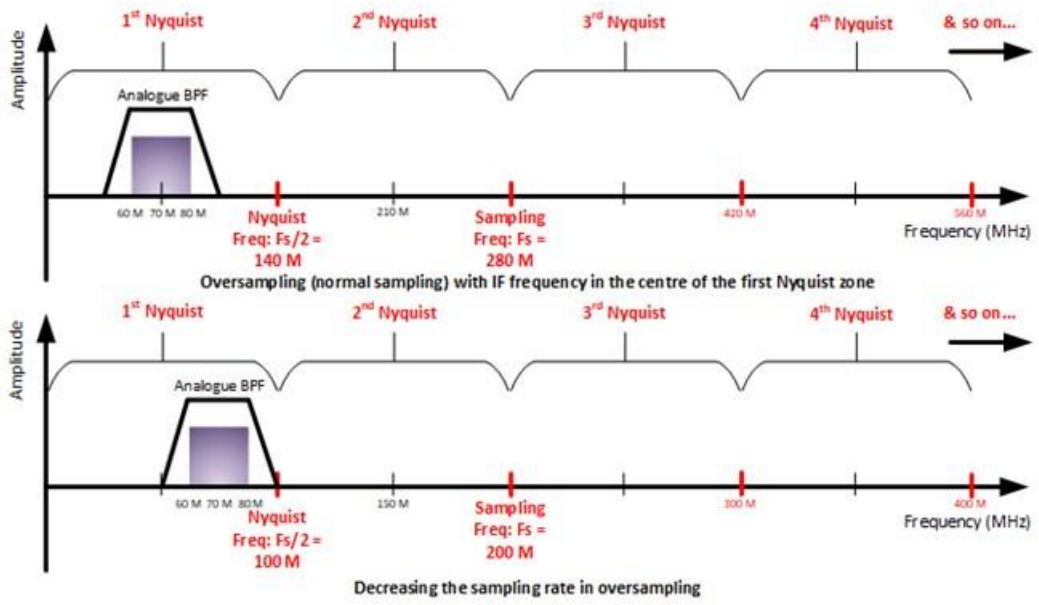

Figure 2-11 Example of oversampling.

2.6.2 Under-sampling

Under-sampling, also known as sub-sampling, band-pass sampling, harmonic sampling, sub-Nyquist sampling, IF sampling or direct IF-to-digital conversion [77], [19] is when a sampling frequency (F_s) less than twice the maximum frequency component in a signal is used. Under-sampling is when $F_s < 2\,f_{in}$, such that aliasing happens and mirror images around every multiple of F_s (F_s /2, F_s, 3 F_s /2 and so on) are produced. If F_s is slightly higher than f_{in}, an aliased signal at a lower frequency $F_s - f_{in}$ is produced. This effect can be used to good advantage, as the ADC can act as a mixer or downconverter in the receive chain.

As shown in Figure 2-12 (for the same example values), using under-sampling, a signal at a carrier frequency of 70 MHz and bandwidth of 20 MHz can be sampled at more than 40 MSps (56 MSps) for keeping the signal in the centre of the third Nyquist zone. This way the 20-MHz signal is aliased back to the first Nyquist zone, centred at 14 MHz. In this function, under-sampling techniques can be used to get rid of the entire analogue frequency down-conversion stage (thus reducing required board space, power consumption and cost of practical receiver design implementations) [78].

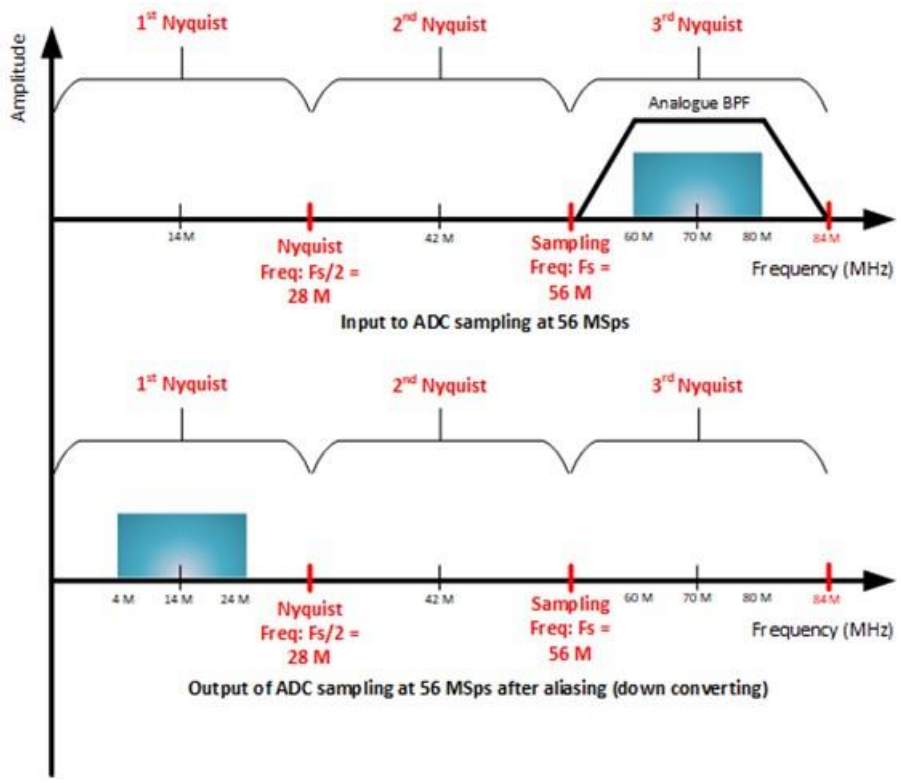

Figure 2-12 Example of under-sampling.

2.6.3 Comparison between Oversampling and Under-sampling for Passband Signals

- *Data rates*

For example, Field-Programmable Gate Arrays (FPGAs) are integrated circuits that are often used to capture the data output from ADCs. As the sampling rate of the ADC increases, the data rate to the FPGA also increases. This means that a sampling rate of 56 MSps used in under-sampling is more desirable than a sampling rate of 200 MSps used in oversampling. As data rates increase, greater care has to be taken when it comes to the layout of boards, signal routing and placement of the ADC and FPGA in the design [78]. As a result, cost and complexity increases.

- *Setup and hold time*

Setup and hold times become critical with high data rates. Under-sampling results in more relaxed setup and hold times due to lower data rates [78], [79].

- *Power consumption*

For most applications in defence and wireless infrastructure, pipeline ADCs are used, which consume a lot of power. The situation becomes worse when oversampling is employed [78].

- *Additional down-converter stage*

In order to convert the 70-MHz signal shown in the previous example to a lower IF frequency such as 14 MHz, under-sampling can be used. This helps to get rid of any additional down converter stage in front of the ADC, which is required when oversampling is used.

- *Cost of ADC*

For example, the cost of a 200 MSps ADC is at least twice the cost of a 56 MSps ADC. Thus, oversampling increases the cost of the ADC and by using under-sampling combined with proper filtering, the cost of the ADC can be reduced.

- *Processing gain*

When a signal is oversampled, a processing gain is achieved that can improve the the signal-to-noise (SNR). Processing gain, $G_{process}$, can be expressed by

$$G_{process} = 10\log((F_s/2)/BW) \ , \tag{2-25}$$

where *BW* is the bandwidth of the signal.

For the oversampling example discussed in Section 2.6.1, *BW* is 20 MHz and F_s is 200 MHz. Using (2-25), the processing gain is around 7 dB. The total SNR (SNR_{total}) can be calculated by

$$SNR_{total} = SNR_{ds} + G_{process} \ , \tag{2-26}$$

where SNR_{ds} is the SNR value typically provided in an ADC datasheet (processing gain not included). For as SNR_{ds} value of 72 dB (for a 12-bit ADC), SNR_{total} can be calculated to be 79 dBFS (decibels relative to full scale) [78] using (2-26). Processing gain is absent when under-sampling is used.

- *Frequency plan flexibility*

One of the biggest advantages of oversampling is the frequency plan. When a signal is oversampled, IF frequencies can be moved anywhere from DC to $F_s/2$ (the first Nyquist zone). The second and third harmonics fall outside this first Nyquist zone and can be filtered easily. When it comes to under-sampling, one of the key concerns is ADC filter design, which has to be planned such that the effects of the second and third order harmonics are minimal to avoid

distortion. An analogue filter (with a good 3-dB response) in front of the ADC can be helpful in reducing distortion. Moreover, for better Spurious-Free Dynamic Range (SFDR) performance, planning the ADC sampling rate based on the knowledge of aliased second and third order harmonics is also helpful when it comes to under-sampling.

- *Wide signal bandwidths*

Oversampling has the inherent capability of being able to handle wide signal bandwidths, as long as the entire signal is kept inside a single Nyquist zone (preferably in the middle of a Nyquist zone, for flexibility in filter design). When under-sampling wide bandwidth signals, care has to be taken to avoid aliasing.

- *Full-power bandwidth of the ADC*

The frequency of the ADC at which the input signal has a 3-dB loss is called the full-power bandwidth of the ADC. In order for under-sampling to work, it must be ensured that the ADC has adequate input bandwidth (not to be confused with input IF signal bandwidth).

- *Quantisation noise*

Noise in ADC conversions can be introduced from thermal noise, shot noise, variations in supply and reference voltage, phase noise due to sampling clock jitter and noise due to quantisation error, also known as quantisation noise. Under correct operating conditions, oversampling and averaging helps to reduce noise and improve SNR [80]. Sampling at a much higher rate normally spreads the quantisation noise over a larger bandwidth, resulting in less noise power per frequency. Thus, oversampling, followed by low-pass filtering, helps to average out more of the ADC noise [81].

In the measurements discussed later on in Sections 4.2 and 4.3 , this effect is observed when using higher sampling rates at the Oscilloscope to capture received samples. When low sampling rates are used, it can be seen that the noise floor rises leading to reduced SNRs. This is reflected by EVM performance for different sampling rates. For example, for the same signal, a sampling rate of 6.25 GSps leads to an EVM of 9.4%, for 50 GSps, the EVM is 8.3% while for 100 GSps, the EVM is 7.9%. Figure 2-13 shows the spectra of two 305 MHz channels (at 1.9 GHz and 2.5 GHz) multiplexed using SCM techniques, as seen on the oscilloscope. The snapshots show that the SNR is improved by approximately 2 dB when a sampling rate of 100 GSps is used compared to 6.25 GSps. Figure 2-14 shows similar effects when one out of the two channels is filtered for capturing.

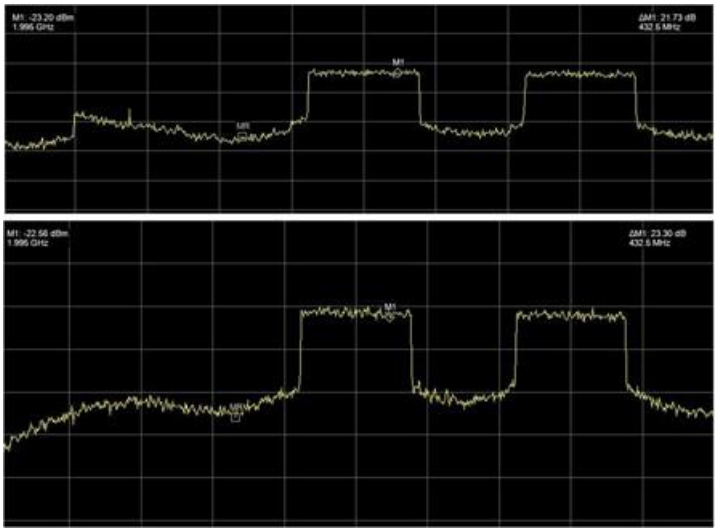

Figure 2-13 Spectra on oscilloscope for two SCM channels captured using 6.25 GSps (top) and 100 GSps (bottom) [10 dB per division; 0 dBm reference level; 1 MHz Resolution Bandwidth (RBW)].

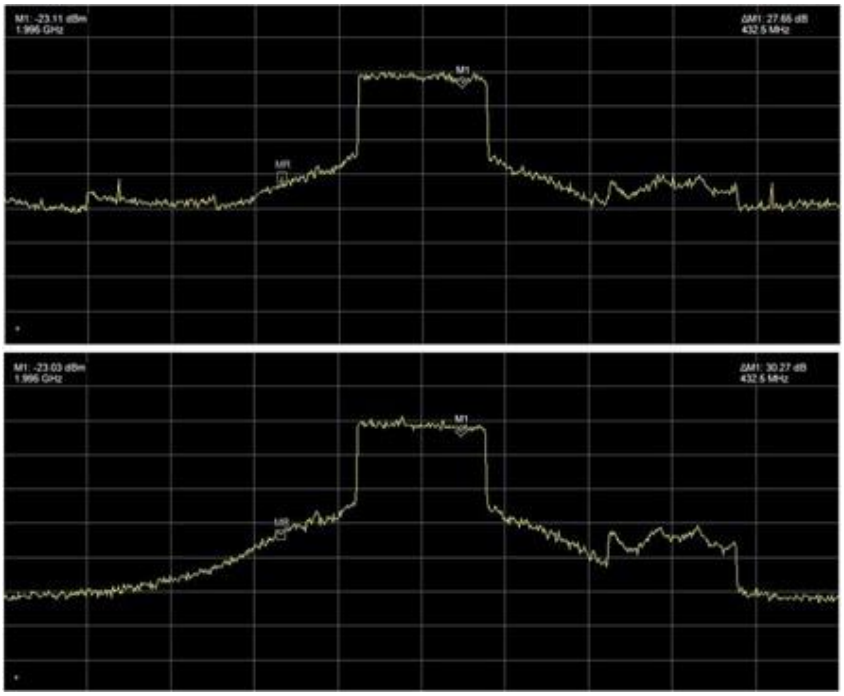

Figure 2-14 Spectra of Channel 1 (1.9 GHz) (out of two SCM channels) on the oscilloscope when captured with 6.25 GSps (top) and 100 GSps (bottom) [10 dB per division; 0 dBm reference level; 1 MHz Resolution Bandwidth (RBW)].

2.7 Summary and Conclusions

In order to support the predicted growth in the flow of information, 5G forms the new mobile communications standard that is set to succeed 4G by the year 2020. 5G aims to connect many different types of devices and support much higher data rate and low latency applications. 5G will include new deployment options and will enable new services in different industry verticals such as healthcare, manufacturing etc. To address these demands, the new 5G NR air interface will include bands operating below 6 GHz and higher bands above 24 GHz, wider channel bandwidths (e.g. 400 MHz) at these higher frequency bands and a flexible numerology design. In 3GPP release 15, it has been decided that standard OFDM (also termed CP-OFDM) with up to 256-QAM subcarrier modulation will be used for 5G.

CP-OFDM has been used extensively in many different telecommunication standards. It employs an IFFT, which is an efficient mathematical operation that converts frequency domain modulation samples to a complex sampled time domain waveform. DMT is an alternative modulation method to OFDM, whereby employing twice the IFFT length (compared to OFDM) can directly generate a real sampled waveform. As a result, it does not require modulation onto an RF carrier, making it a popular choice in OWC. Both waveforms suffer from issues such as high PAPR, timing and frequency offsets. However, there are established methods for counteracting these effects. EVM is a metric used to characterise noise and other types of distortion in a transmission system employing complex modulation formats and is thus very useful for OFDM/ DMT waveforms.

Oversampling involves sampling an analogue signal at a rate that is larger than the Nyquist rate (twice the highest frequency component of the signal) and leads to SNR improvements due to processing gain, and a reduction in quantisation noise. On the other hand, under-sampling, which involves sampling an analogue signal at a rate that is lower than the Nyquist rate, introduces a number of benefits such as the use of lower sampling rates, resulting in lower power consumption and lower cost of ADCs and reduction in the number of down-conversion stages at the receiver. Keeping in mind the problem of very high sampling rates required at the RRU in current IFoF demonstrations (discussed in Chapter 1), under-sampling can be a very useful technique.

3 Radio-over-Fibre for the 5G Fronthaul

3.1 Introduction

This chapter presents additional background theory, as well as related research, in order to provide the reader with a detailed overview of the area of research covered in this thesis.

Analogue and digital Radio-over-Fibre (RoF) technologies and their applications in the RAN over the years are discussed in Section 3.2. This section also explores typical RoF architectures and their building blocks, including a number of opto-electronic devices that are used in the work presented in this thesis.

Section 3.3 explores the current fronthaul section of the RAN that employs digital transport, and its limitations, especially in terms of its ability to cope with large signal bandwidths and multi-antenna techniques, that are required for 5G. It also discusses the role of functional splitting to mitigate some of these issues and the reasons for considering analogue transport via RoF schemes for the new 5G mobile fronthaul.

The section further explores the evolution of the analogue fronthaul, which has adopted new modulation and multiplexing techniques in the electrical and optical domain, as well as new techniques for mmW carrier generation. SCM and WDM, which are promising multiplexing techniques and have been used extensively used in this thesis, are also discussed in detail. The limitations of these techniques in terms of the flexibility and scalability, features that will be of prime importance for 5G, are discussed, especially those of traditional SCM. Finally, the benefits of a promising new technique that performs SCM in the digital domain but employs analogue transport, are discussed in detail. The main work presented in this thesis is based on this technique.

The chapter is summarised and concluded in Section 3.4.

3.2 Radio-over-Fibre

The concept of RoF was introduced in the 1980s following the introduction of microwave/ radio frequency (RF) subcarrier multiplexing (SCM), that rapidly gained popularity for the distribution of television channels [82], [83], [84]. Advantages such as low attenuation at RF frequencies, low cost and ease of installation make fibre the preferred option over co-axial cables in the distribution of RF signals. As a result, fibre links can also span much longer distances than co-axial links.

The fundamental principle of RoF transmission involves the transport of analogue radio signals via an optical fibre link. Analogue RoF has been a research interest for almost four decades, with commercial products available for mobile communications for almost three decades. However, it has been mostly limited to niche applications such as Distributed Antenna Systems (DAS) for in-building, shopping mall and sports venue coverage and base station hotels, which are of interest to mobile operators [85], [86]. One of the reasons for this is intrinsic link impairments. Analogue RoF is generally affected by distortion due to non-linearities, fibre chromatic dispersion, low signal-to-noise (SNR) and a narrow dynamic range, leading to limited transmission distance [8], [87], [88].

Traditionally, a DAS-RoF system consists of Remote Antenna Units (RAUs) connected to a Central Unit (CU) via a RoF link. The RAUs are simply a distributed set of antennas that transmit and receive RF signals from mobile users located in different geographical areas and have little or no processing capabilities. They exchange these RF signals with the CU, where all the signal processing such as modulation/ de-modulation, multiplexing/ de-multiplexing, handover, diversity etc. are carried out [8]. The advantage of such an architecture is that most of the complexity is concentrated in the CU, which means that only the low cost and low complexity RAUs need to be upgraded in order to make improvements in the coverage and capacity of the system. Processing signals from multiple RAUs at a single central location, rather than at separate entities, leads to savings for operators in terms of energy, space and shared equipment. It also allows joint processing of signals from multiple RAUs [8].

Typical analogue, as well as digital RoF systems have been shown in Figure 3-1. In the diagram, an analogue RoF link is shown in which the analogue signals are transmitted either at baseband (baseband over fibre) or up-converted to an RF or Intermediate Frequency (IF) (RF/ IF over fibre). RF over fibre has the advantage of requiring no frequency translation at the RAU/ RRU, but it

cannot accommodate multiple channels. This is because these channels may be mobile data channels with carrier frequencies that have been pre-determined by the current frequency allocation legislation.

The baseband/ IF/ RF analogue signal/s undergo electrical-to-optical (E/O) conversion at the CU and optical-to-electrical (O/E) conversion at the RAU. In the case of the digital RoF system employing the Common Public Radio Interface (CPRI) specification [89], In-phase/ Quadrature-phase (IQ) samples of radio channels (digitised radio), undergo E/O and O/E conversion for transmission between the Baseband Unit (BBU) and Remote Radio Head (RRH). This type of architecture is known as the Centralised or Cloud Radio Access Network (C-RAN), in which the RRHs are access nodes and the BBUs enable centralised processing, much like the analogue RoF architecture. These architectures are discussed further in Section 3.3, where it is also explained why the CU/ BBU and RAU/ RRH are now called Distributed Unit (DU) and Remote Radio Unit (RRU), respectively.

Note, that historically, there has been a general distinction made between DAS and centralised/cloud RAN – the latter have usually been put together for/ by an operator, whereas DAS was often put together by neutral host providers, who would just transparently transport many operators signals (and for many systems). There have been digitised RoF systems for DAS, but usually using proprietary techniques rather than CPRI.

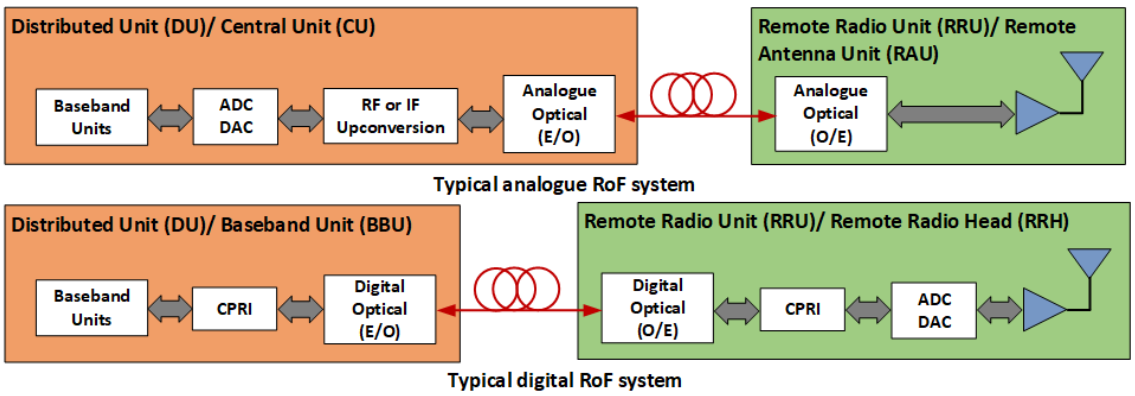

Figure 3-1 Typical RoF architectures.

A simple and cost-effective option for these links is the use of direct Intensity Modulation and Direct Detection (IM-DD). In such links, also called Directly Modulated Links (DMLs), RF signals directly modulate the intensity of the optical carrier from a semiconductor laser diode and are

directly detected via a photodiode (normally a PIN photodiode due to their superior linearity compared to other structures, such as avalanche photodiodes). In general, commercially available uncooled Distributed Feedback (DFB) lasers with high efficiency, low noise and low distortion are preferred over Fabry-Perot (FP) and vertical-cavity surface-emitting lasers [8], [90].

Links employing external modulation require a Mach-Zehnder Modulator (MZM), along with an unmodulated laser operating at a constant optical power (usually a Continuous Wave Laser (CWL)). External modulation with an MZM is thus more complex and expensive but offers improved performance in terms of noise and distortion, compared to a DML, especially if distortion compensation techniques are used. They can also be used at higher frequencies, than is the case with DML [91]. Moreover, since MZM links are not restricted by the availability of analogue lasers at specific wavelengths, they can be used with Dense Wavelength Division Multiplexing (DWDM) wavelengths to provide greater capacity per fibre. Other external modulator options include Electro-Absorption Modulators (EAMs) [92] and Reflective Semiconductor Optical Amplifiers (RSOAs) [93], [94] (RSOAs are mainly used in the uplink whereas MZMs are used in both the uplink and downlink). Other types of links include phase modulation (PM) with coherent detection [95], [96] or interferometric detection [97].

The MZM and PM are electro-optic modulators with interferometric structures that operate via the electro-optic effect, which involves applying an external electric field to modify the refractive index of the waveguide material. In the case of the MZM, the phase modulation induced by this electro-optic effect is converted to intensity modulation using an interferometric structure. The MZM consists of a PM (or two PMs, depending on the type of MZM, which is discussed later on in this section) that allows changing of the refractive index in proportion to a driving voltage. There are two types of mm-wave generation based on the MZM: the *2f* and *4f* methods. The optical field at the output of the MZM can be expressed by [23], [98]

$$E_{out} = E_i \cos[\varphi_{dc} + \beta_i \cos \omega_{RF} t] e^{j\omega_c t} \quad (\sqrt{W}) \tag{3-1}$$

where E_i and ω_c are the amplitude and angular frequency of the input optical carrier, respectively. φ_{dc} is the constant phase shift induced by the DC bias voltage applied to the MZM, β_i is the modulation index of the MZM and ω_{RF} is the angular frequency of the electrical driving signal applied to the MZM. β_i is given by

$$\beta_i = \pi \frac{V_m}{2V_\pi} \tag{3-2}$$

where V_m is the magnitude of the electrical signal to the MZM and V_π is the half-wave voltage to the MZM. The necessary driving voltage for achieving a phase shift of π radians is denoted as V_π.

Using Bessel functions, (3-1) can be expanded to [23]

$$E_{out} = \begin{Bmatrix} \cos\varphi_{dc} \cdot J_0(\beta) \cdot \cos\omega_c t \\ -J_1(\beta) \cdot \sin\varphi_{dc} \cdot \cos(\omega_c \pm \omega_{RF})t \\ +J_2(\beta) \cdot \cos\varphi_{dc} \cdot \cos(\omega_c \pm 2\omega_{RF})t \\ -J_3(\beta) \cdot \sin\varphi_{dc} \cdot \cos(\omega_c \pm 3\omega_{RF})t \end{Bmatrix} \quad (\sqrt{W}) \tag{3-3}$$

$J_n(\beta)$ is a solution to Bessel's second order differential equation and is thus referred to as the Bessel function of the first kind of order n and argument β. Note that n is shown up to the third order in (3-3). The choice of DC bias voltage to the MZM will supress either all the even (*cos*) or odd (*sin*) terms, as seen from (3-3). The transfer function with the minimum and maximum transmission points arising from the DC bias voltage setting is shown in Figure 3-2.

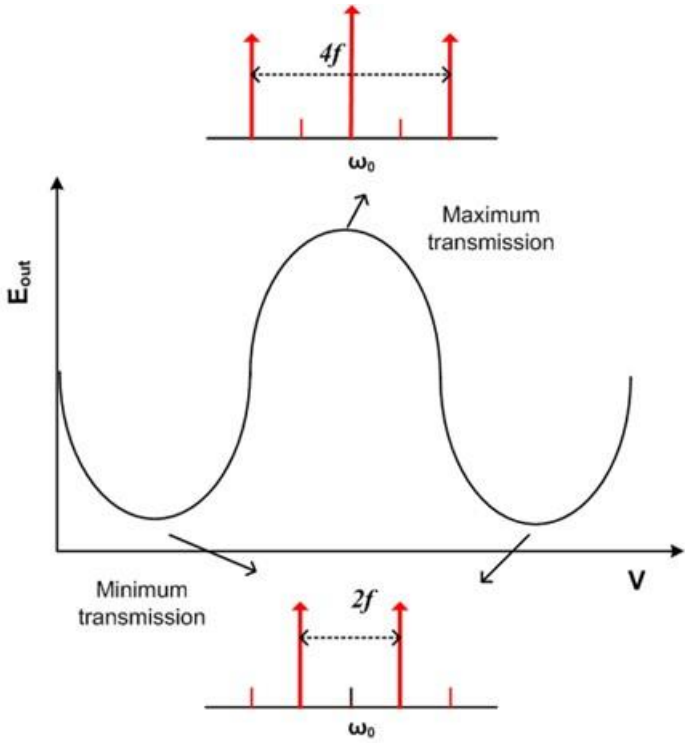

Figure 3-2 Transfer function of the MZM, with its minimum and maximum transmission points [23].

At the minimum transmission point, i.e. $\varphi_{dc} = \pi/2$, all even terms including the carrier are suppressed and the output of the MZM has two dominant optical components at $\omega_c \pm \omega_{RF}$, which are separated by twice the RF drive signal to the MZM. This is known as the *2f* method [23], [99]. For frequency quadrupling or the *4f* method [100], the MZM has to be biased at the maximum transmission point, i.e. $\varphi_{dc} = 0$. The MZM output consists of the carrier (ω_c), and the two optical components at $\omega_c \pm \omega_{RF}$, as well as other unwanted components that have much lower power levels compared to these three components. For frequency quadrupling, the optical carrier can be removed via an optical filter before heterodyning the two optical components at $\omega_c \pm \omega_{RF}$. Generally, the MZM is biased at its quadrature point ($\varphi_{dc} = \pi/4$ or $V_\pi/2$), which is at the centre of the linear zone, to minimise its non-linear effects [101] or at a point between minimum and quadrature [102]. As a result, the amplitude of the electrical modulation is limited to a very narrow window for linear operation.

Some of the important parameters associated with the MZM are insertion loss, which is essentially the loss of signal power introduced in the link by the MZM and the extinction ratio, which is the difference between the peak and trough of an MZM transfer function (a poor extinction ratio results in inter-modulation distortion and power penalty at the receiver) [103]. Another important parameter is residual frequency chirp, which is the modulation in the phase of the optical signal that is induced by the process of intensity modulation. This effect is more pronounced at higher frequencies and results in fibre chromatic dispersion [104].

There are mainly two types of MZM: single-drive and dual-drive (also known as differential). In the single-drive configuration, the modulating voltage is applied to one arm of the interferometer, with a phase change of π in the arm of the interferometer. In the dual-drive configuration, the modulating voltages are applied to both arms of the interferometer (the two PMs are driven independently), with phase changes of $\pm\pi/2$ in the arms of the interferometer. In the case of the single-drive MZM, the full V_π has to be applied in order to achieve the maximum extinction ratio while in the case of the dual-drive MZM, $\pm V_\pi/2$ has to be applied on the two arms to achieve maximum extinction ratio. There is generally some chirp (residual) in the output signal for a single-drive MZM while there is almost none for a dual-drive MZM. Two optical modulation techniques are employed using MZM structures. The first is Optical double sideband (ODSB) modulation, which suffers from the impact of chromatic dispersion and limits transmission distance. The second is Optical Single-Sideband (OSSB) modulation, which can overcome the effects of chromatic dispersion [105], [106]. To this end, the dual-drive MZM can

lead to better link performance as it performs OSSB [99] while the single-drive MZM performs only ODSB.

In contrast to intensity modulation (as in the case of the MZM), the amplitude of an angularly modulated signal (via frequency or phase modulation) always remains constant. When the required RF drive power is applied to the phase modulator, sidebands with a separation corresponding to the frequency of the RF signal are generated. However, the spectral components (sidebands) end up cancelling each other out upon direct detection via a photodiode due to the manner in which they are related in amplitude and phase. This means that no signal is generated at the output of the photodiode (PD). One way of generating a detectable signal at the PD is by altering the amplitude or phase relation between the sidebands of the phase modulated signal, e.g. by applying optical filtering. This is shown in Figure 3-3.

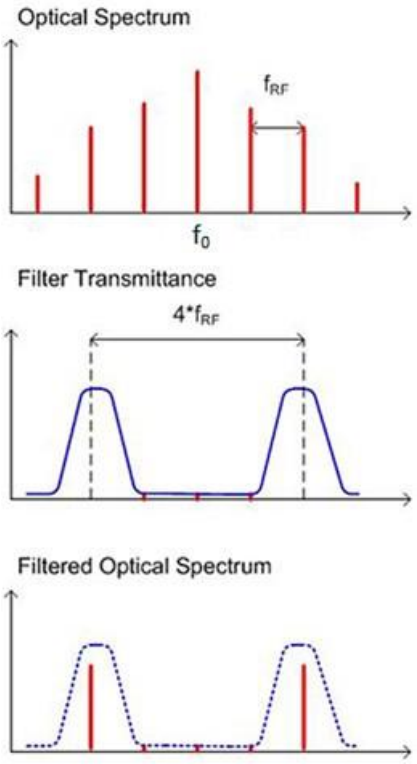

Figure 3-3 Effect of sideband filtering on a phase modulated signal (adapted from [23]).

The amplitude of the output optical signal from an optical phase modulator is given by [23]

$$E_p = E_o \sum_{n=-\infty}^{\infty} J_n(\beta_p) e^{j(\omega_0 + n\omega_{RF})t} \quad (\sqrt{W}) \tag{3-4}$$

where E_o is the amplitude of the input optical signal, β_p is the modulation index and J_n is the Bessel function of the first kind of order n with argument β_p. ω_0 and ω_{RF} are the angular frequencies of the input optical carrier (generated by the optical source) and of the electrical drive signal to the phase modulator, respectively. $J_n(\beta_p)$ is related to the modulation index of the phase modulator by

$$\beta_p = \pi \frac{V_m}{V_\pi} \tag{3-5}$$

where V_π is the half-wave voltage of the optical phase modulator and V_m is the amplitude of the RF drive signal. Note the similarity between (3-5) and (3-2). This alludes to the fact that the PM and MZM operate on the same principle. The difference (factor of ½) is just a normalisation based on the particular formalism used to express the optical signal amplitude or intensity (such as, in (3-4) and (3-1)).

Phase modulation spreads out the power of the optical signal among the carrier and the spectral components closest to it, with the amplitude distribution on the generated optical sidebands being governed by the corresponding Bessel functions parameterised by the term β_p. If the M^{th} and N^{th} order sidebands of the phase modulated signal are selected by optical filters, which are then combined and detected by the PD, the generated photocurrent (I) can be expressed as [23]

$$I = R(E_f * \overline{E_f}) \tag{3-6}$$

$$I_{dc} = RE_o^2(J_M(\beta_p)^2 + J_N(\beta_p)^2) \tag{3-7}$$

$$I_{ac} = 2RE_o^2 J_M(\beta_p) J_N(\beta_p)[\cos(M+N)\,\omega_{RF} t] \tag{3-8}$$

where R is the responsivity of the PD and E_f is the amplitude of the filter output signal when the M^{th} and N^{th} order sidebands are selected ($\overline{E_f}$ is the complex conjugate of E_f). The DC and Alternating Current (AC) terms, I_{dc} and I_{ac}, are expressed by (3-7) and (3-8), respectively, with the generated frequency equal to $M+N$ times the RF drive frequency to the PM. If M and N are the second order sidebands, the generated photocurrent is given by [23]

$$I = RE_o^2 J_2(\beta_p)^2 [4cos^2(2\omega_{RF})t] \tag{3-9}$$

$$I_{dc} = RE_o^2 J_2(\beta_p)^2 \tag{3-10}$$

$$I_{ac} = RE_o^2 J_2(\beta_p)^2 \cos(4\omega_{RF})\, t] \tag{3-11}$$

The AC term in (3-11) shows that the frequency obtained is four times the RF drive frequency. Some residual optical components from unwanted sidebands with limited power may fall in the filter passband region and have some effects on the phase and amplitude of the desired RF signal. This may be, e.g. distortion in the form of the residual components beating with the selected sidebands, generating signals at a number of different frequencies, including the same frequency as the desired RF signal. However, the power of these signals will be generally much lower than the power of the desired RF signal.

From (3-8), it can be seen that the power of the generated RF signal is defined by the term $2J_M(\beta_p)J_N(\beta_p)$ (provided E_o and R are ignored). When higher orders of sidebands are selected, increasing β_p, which involves increasing the power level of the RF drive signal to the PM, increases the power conversion efficiency [23].

Devices such as MZMs that perform intensity modulation are susceptible to DC bias drift, which results in the optical spectrum changing with time. In contrast, phase modulated signals are free from DC bias drift (they do not generally require a DC bias) and are tolerant to temperature change. Moreover, more power can be assigned to higher order sidebands by increasing the modulation index and sidebands can be filtered as required, which leads to power efficiency. An Optical Frequency Comb Generation (OFCG) [107] system has the advantage of being able to generate a broad and flat spectrum but phase modulation is a much simpler technique of optical comb generation.

3.3 Modern Fronthaul and its Limitations

3.3.1 The Digital Fronthaul

RoF transport based on digitisation of wireless signals was introduced in mid-2000, due to the limitations of analogue RoF (as discussed in Section 3.2). Currently, the fronthaul section of the RAN employs sampled radio waveform transport using industry standard specifications such as CPRI [89]. With 5G and beyond envisioned bandwidths and multi-antenna techniques (defined by 3GPP Release 14 [7] and 15 [74]), data rates over this type of transport will scale to impractical levels. Moreover, Ethernet has been suggested [5], [6], [108], as an alternative to CPRI, as it may lead to more efficient use of available resources through switching equipment

and reduction in costs due to the ubiquity of Ethernet equipment and the availability of standardised operations, administration and management (OAM) functions. However, whether CPRI or Ethernet is used, the data rate requirements do not change. As an example, using CPRI (which is operating at Option 8, shown in Figure 3-4 (b)), for 8 (8X8 MIMO) 100 MHz LTE signals, the projected line rate is appx. 49.152 Gbps (which can be reduced by removing some of the time-domain oversampling) [109]. In an equivalent analogue system, a bandwidth of 800 MHz is required (theoretically), assuming 100% efficiency.

Functional splitting has been proposed as a means of reducing the data rates over the future fronthaul. A 5G Next Generation Radio Access Network (NG-RAN) is shown in Figure 3-4 (a) while the LTE/ 5G protocol stack and its different split options relating to this architecture are shown in Figure 3-4 (b). The 5G system is divided into the 5G Core Network, the 5G RAN and User Equipment (UE) (not shown in diagram).

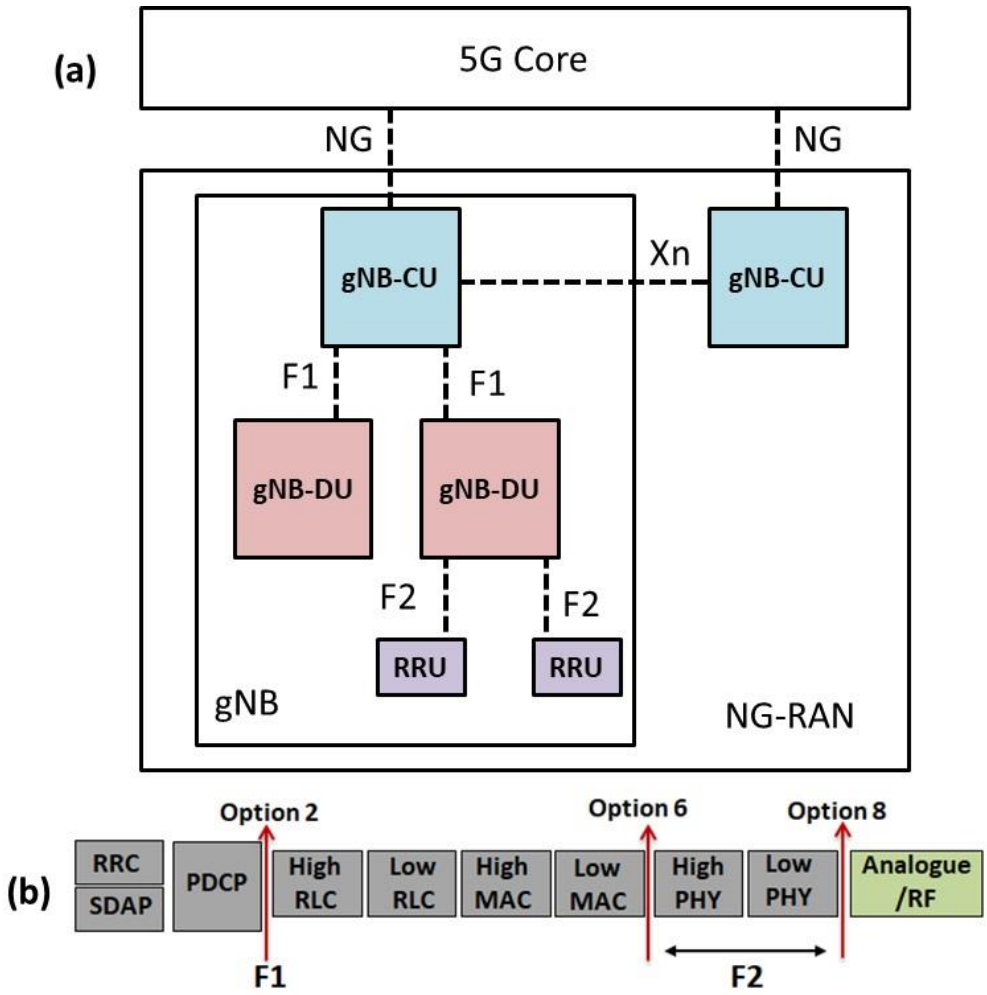

Figure 3-4 (a) 5G NG-RAN architecture (b) LTE/ 5G protocol stack and different split interfaces (including candidate split points).

As shown in Figure 3-4 (a), a set of gNBs are connected to the 5G Core through the NG logical interface and they can be interconnected via the Xn interface. The gNB, which is the 5G next generation base station supporting 5G NR, is divided into three units: Central Unit (CU), Distributed Unit (DU) and Remote Radio Unit (RRU). Operations that would otherwise be undertaken by a single base station are divided among these units through a de-composition of the 5G protocol stack. The protocol layers that form the stack (shown in Figure 3-4 (b)) are the Radio Resource Control (RRC, used for control-plane processing), Service Data Adaptation Protocol (SDAP, used for user-plane processing), Packet Data Convergence Protocol (PDCP), Radio Link Control (RLC), Media Access Control (MAC) and Physical (PHY). The functional split points determine how much of the different functions of the protocol stack are divided among the CU, DU and RRU (and the corresponding reduction in data rate over the fronthaul). The gNB

may consist of a gNB-CU, as well as one or more gNB-DUs while the gNB-CU and gNB-DUs are connected through the F1 interface. This interface supports signalling exchange and data transmission between the endpoints through a Higher Layer Split (HLS) [110]. The F2 interface supports signalling exchange and data transmission between the gNB-DU and multiple RRUs through a Lower Layer Split (split). These two interfaces define new network sections that are differentiated from the traditional backhaul (defined by the interface to the core) and are known as middle-haul (for the F1 interface) and fronthaul (for the F2 interface).

In a standalone configuration with independent CU, DU and RRU locations, Option 2 split for the F1 (between the PDCP and Higher RLC protocol layers) interface (shown in Figure 3-4 (b)) has already been standardised [111]. This is mainly because F1 had in essence been defined as dual connectivity Option 3C in LTE [112]. Dual connectivity was introduced as a means of increasing user throughput, enhance mobility robustness and support load-balancing among evolved Node Base Stations (eNodeBs), by allowing a UE to simultaneously transmit and receive data on multiple component carriers from two cell groups via a master eNodeB (MeNB) and secondary eNodeB (SeNB) [112], [113].

Heterogeneity will be a key feature of 5G networks, meaning that high-density but low-power small cell base stations will coexist with low-density large cell base stations [114]. Dual Connectivity will allow simultaneous connection to LTE and 5G within a macrocell (a radio access point with a long range optimised to provide greater coverage) and a small cell (a radio access point with a short range optimised to provide greater capacity) [115], [116], respectively. This is in contrast to the carrier aggregation (CA) scheme (another 4G/ 5G technology) [117], [112], which allows the network to increase user throughput and aggregate bandwidth by enabling a UE to transmit and receive data simultaneously on multiple component carriers from a single eNodeB/ gNB.

While the F1 interface has been defined, the F2 interface between the DU and the RRU is still under investigation. A range of potential intra-PHY split points for the F2 interface have been indicated in Figure 3-4 (b) (between Options 6 to 8). Depending on the final choice of the split point, the data rate required over the F2 interface will be reduced, albeit at the cost of more complex RRUs. Even with an intra-PHY split, data rate requirements will still impose significant demands on the transport network [118], [6] due to multiple antenna techniques such as mMIMO and 5G bandwidths (up to 400 MHz). Moreover, split points closer to the MAC/ PHY interface will impose restrictions in the deployment of joint processing/ co-operative base stations (e.g. in distributed MIMO scenarios, otherwise known as Coordinated Multi-Point

(CoMP)), due to increased latency [109]. As a result, analogue transport via RoF schemes has recently gained renewed interest [119].

3.3.2 The Analogue Fronthaul

In order to meet the projected demands of 5G and beyond mobile systems, many different analogue transport schemes have been investigated. Increased demand for wireless bandwidth has resulted in a move towards the mm-wave region of the radio frequency spectrum. There has been active exploration for a number of candidate mm-wave bands and in particular, the unlicensed 60 GHz frequency band [3], [120]. However, high propagation losses at these bands (resulting in Line-of-Sight (LOS) coverage and short transmission distances) [121], [122], as well as the inherent analogue link impairments makes the combination between wireless and wired connectivity challenging.

Investigations on the optical transport of mm-wave signals have resulted in many different modulation schemes. Even though RF over fibre has an advantage at microwave frequencies, this advantage is lost at mmW frequencies, as high-speed photodetectors and other high-speed equipment will lead to higher implementation cost while performance is impacted by fibre chromatic dispersion, which is worse at higher frequencies [123]. IF over fibre requires mmW LOs and high-speed mixers for frequency translation processes at the RRU but has been the most popular choice for mm-wave demonstrations in the uplink direction, due to the lack of low-cost optical mm-wave generators.

Since low modulation efficiency (optical-electrical-optical conversion) at high frequencies leads to weak modulation of mmW radio signal/s on to the optical carrier, the correct choice of modulation technique is very important [124]. Direct IM-DD is generally not used for mm-wave applications due to limitations in bandwidth and distortion due to non-linearity [125]. External modulation schemes are mostly used, such as external phase modulation [126] and intensity modulation schemes, such as optical double sideband (ODSB) [123], optical single sideband (OSSB) [127], [128], optical carrier suppression (OCS) and optical filtering of one of the unwanted sidebands [129]. Schemes for optical generation of mm-wave signals such as frequency doubling based on carrier suppression [129], frequency quadrupling [130], mode-locked lasers [131] and remote LO delivery [132], have also been investigated. In order to mitigate mm-wave analogue RoF link impairments such as inter-modulation distortion, linearization schemes, such as pre-

distortion [133], [134], the use of EAM [135] and also RSOAs, which reduce the distortion component of the MZM [136], [137], have been studied.

In order to achieve high data rates and spectral efficiency, many different transport and multiplexing techniques, based on different degrees of freedom (phase, amplitude, mode etc.), have been investigated. The most notable of these techniques is Polarisation Division Multiplexing (PDM) [138], [139], [140], which multiplexes based on the different polarisations of an optical signal. This technique is generally too complex and expensive for fronthaul and access networks but is important for long-distance, high-speed networks using many wavelength links, which are expensive anyway. Since the optical transport of mm-wave signals leads to the inefficient use of the optical bandwidth (the actual bandwidth of the wireless signal is relatively small compared to the total occupied bandwidth), wavelength-interleaving schemes [15], [124] incorporating SCM and WDM can be used to improve the spectral efficiency at relatively low cost and complexity.

An analogue fronthaul employing a traditional SCM scheme [82], [83], [84] is shown in Figure 3-5. *N* analogue signals (assumed to be at baseband) are up-converted to different IFs, combined in the electrical domain (using a power combiner) at the DU and transmitted over optical fibre following E/O conversion. At the RRU, the multiplex undergoes O/E conversion, before being separated (via appropriate RF filters and splitters or frequency de-multiplexers). The signals may undergo a different up-conversion process at the RRU (e.g. to place them at the same frequency for MIMO applications) or may be transmitted directly at the frequency they reside. These types of architectures can be built using low cost and readily available commercial equipment but are difficult to scale due to the complexity associated with the use of separate electrical amplifiers, LOs and electrical filters for the different channels. Precise control of LOs is required to avoid oscillator frequency offsets and good isolation and selectivity are required from splitters and filters, respectively. Techniques exist to reduce the number of mixer stages [33], [141] but are still not sufficient to reduce the overall system complexity especially for large multiplexes. Moreover, at mm-wave frequencies, the cost of amplifiers, mixers and RF filters makes traditional SCM techniques expensive and impractical. Analogue link impairments such as inter-modulation distortion and limitations in analogue filtering also make it difficult for channels to be placed close to each other, affecting spectral efficiency.

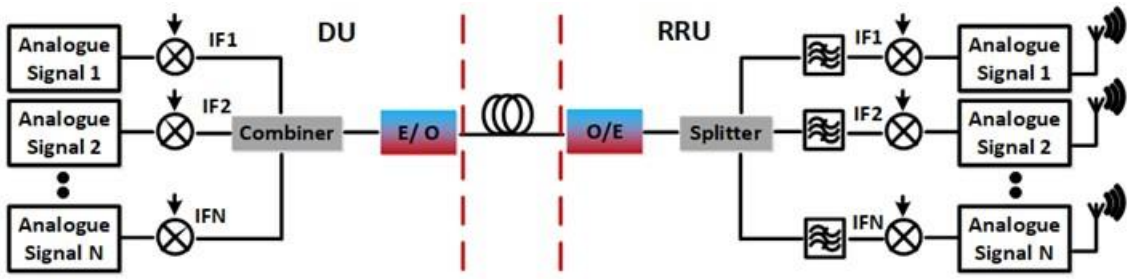

Figure 3-5 Traditional analogue fronthaul employing SCM.

WDM [12] is an optical multiplexing scheme that involves combining several modulated optical signals with different central frequencies to obtain a desired optical signal. DWDM is a WDM technology characterised by narrow channel spacing and a frequency grid, which is a reference set of frequencies used to denote allowed nominal central frequencies that may be used for defining applications. ITU-T defines this frequency grid as fixed, supporting a variety of channel spacing ranging from 12.5 GHz to 100 GHz and wider, based on a reference frequency of 193.1 THz or flexible, with a frequency granularity of 6.25 GHz [142]. A frequency granularity of 6.25 GHz (and lower) is also known as Ultra-Dense Wavelength Division Multiplexing (UDWDM) [143], [144], [16]. Arrayed Waveguide Gratings [145], optical interleavers [146] and optical circulators with Fibre Bragg Grating (FBG) filters [147] can be used for WDM techniques.

Accommodating a large number of signals by only utilising more wavelengths of light via WDM, may be an expensive and complex process that also leads to inefficient use of spectrum. Combining SCM with WDM may improve spectral efficiency. A simplified analogue fronthaul link employing wavelength-interleaving techniques via WDM and traditional SCM is shown in Figure 3-6. At the DU, multiple channels combined in the electrical domain via SCM are used to modulate optical carriers at different frequencies (IF over fibre). Generating the optical carriers via separate optical sources is expensive and difficult to scale [148]. As a result, techniques such as optical frequency comb generation [143], [149], [107] can be used to generate multiple frequency combs, which can be combined in the optical domain via WDM techniques, allowing efficient wavelength interleaving [150]. However, the architecture is still complex and lacks scalability, as the mm-wave channels combined in the electrical domain need to be de-multiplexed at the RRU [11]. These types of architectures lack flexibility as well, since changes in channel bandwidth (which would require adaptations to the RF filters being used in the architecture) or any form of signal manipulation (e.g. Hilbert transforms) are complex procedures in the analogue domain [34], [141], [9].

In order to address the high data rates and dense user environments in 5G, multiple-Radio Access Technologies (multi-RAT) mobile networks and mMIMO deployments will be very important. A multi-RAT network promotes heterogeneity by supporting both 60 GHz (5G) mobile access as well as legacy services such as LTE [4], [15] while mMIMO deployments, combined with beamforming technology, will utilise very large antenna arrays with targeted beams to provide high capacity and reliability via spatial multiplexing and diversity. One of the biggest challenges of MIMO deployments is that all MIMO channels must be at the same carrier frequency. While heterogeneity is feasible, approaches such as the one shown in Figure 3-6 will not be efficient for mMIMO.

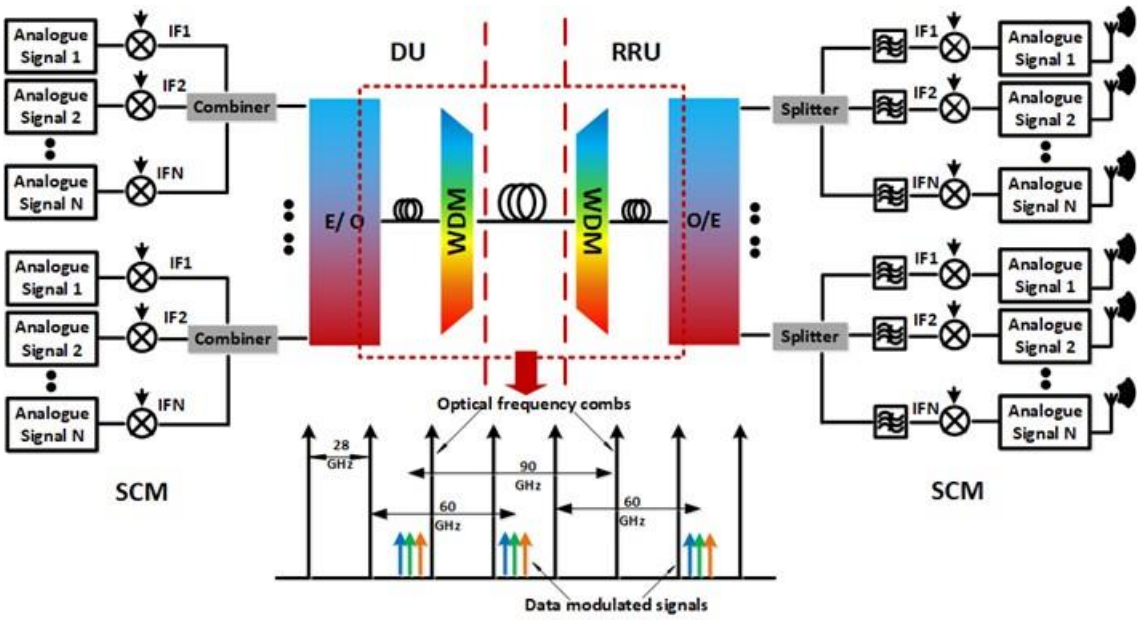

Figure 3-6 Analogue fronthaul employing SCM combined with DWDM and wavelength interleaving.

An alternative approach to transport wireless signals in the analogue fronthaul using digital instead of analogue SCM/ channel aggregation has been actively studied in recent years [12], [151], [152] and is shown in Figure 3-7. Channel aggregation at the DU can be implemented relatively simply via DSP by shifting the centre frequencies of the input wireless channels and combining them in the digital domain. After digital-to-analogue conversion, the block of channels is modulated onto an optical carrier and at the RRU, the reverse processes are applied for channel de-aggregation. This approach reduces the number of analogue components required at the DU and RRU, enhances flexibility (e.g. in varying filter parameters, multiplexing

signals from different RATs) and spectral efficiency and provides the benefit of analogue link impairment mitigation in the digital domain. This type of channel aggregation method may also be used for CA [117], [12].

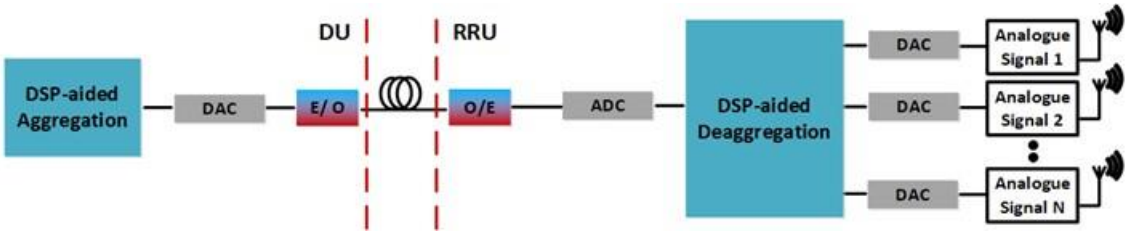

Figure 3-7 Analogue fronthaul with DSP-aided channel aggregation/ de-aggregation.

While channel aggregation at the DU can be realised in a relatively straightforward manner, the de-aggregation process at the RRU is more challenging, especially for a large number of multiplexed channels (e.g. in full-digital or hybrid MIMO applications). There have been a number of promising demonstrations using these DSP-assisted techniques [28], [153], [31], [29], [154], [155], [156] including using low cost, low sampling rate ADCs and bandpass-sampling techniques [18]. There have been several demonstrations with LTE signals and bandwidths [157], [158] and a few with wide bandwidth OFDM signals [13], [17]. Some of these demonstrations have used DMLs [157] and have investigated the effects of intermodulation distortion, as well as different mitigation approaches [157], [22]. A very large number of multiplexed signals and very high aggregate data rates have been demonstrated by IFoF techniques employing different modulation formats and 5G candidate waveforms and have been listed in [152], including one with a single OFDM channel with an aggregate data rate of 24.08 Gbps [159]. Other IFoF techniques have included WDM to achieve even higher data rates [14], [16] and some have also included mmW up-conversion [29], [160], [161].

However, most of these techniques employ very high sampling rates at the receiver [16], [22] and/ or very complex architectures [17]. For a very large number of aggregated channels occupying a large bandwidth, expensive RF filters and high sampling rate ADCs (with large analogue bandwidths) will be required for sampling the entire multiplex and de-aggregating the channels at a higher IF. This is an even bigger problem at mm-wave frequencies. Moreover, as each channel is at a different IF, a separate frequency conversion process will be required at the RRU for each channel in order to place them at the same carrier frequency for mMIMO transmission. Such issues will be addressed in this thesis.

3.4 Summary and Conclusions

The current fronthaul section of the RAN employs sampled radio waveform transport using industry specific standards such as CPRI. Data rates over this digital fronthaul will rise to impractical levels due to the wide channel bandwidths and multi-antenna systems required in 5G and beyond. Functional splitting has been proposed in order to reduce the data rate requirements over the fronthaul (e.g. through improvements in spectral efficiency). However, as split points move further away from the antenna and closer to the MAC-PHY interface, higher latency impairs joint processing of signals.

Analogue RoF, which involves the transmission of analogue radio signals over an optical fibre link, has been a research interest for many years. However, due to intrinsic link impairments (non-linear distortion, noise etc.) and the resulting SNR limitations, so far, analogue RoF has been limited to niche applications such as DAS. On the other hand, analogue RoF transport has a number of advantages compared to digital transport (namely improved spectral efficiency and reduced latency), and is thus being considered for the future fronthaul (5G and beyond mobile networks).

Over the years, several E/O and O/E conversion and multiplexing techniques have been investigated for the analogue RoF fronthaul. Increased demand for wireless bandwidth has resulted in a move towards mmW frequencies. However, low modulation efficiency of modulators at high frequencies means that the modulation technique has to be chosen carefully. Due to limitations in terms of modulation bandwidth and distortion, direct modulation is generally not used for mmW applications. External modulation schemes, e.g. via an MZM, are used instead. MZMs, as well as PMs, can also be used to produce optical frequency combs and can thus be used for mmW carrier generation.

Many different transport and multiplexing schemes have also been studied in order to achieve higher data rates and spectral efficiencies. These include traditional SCM schemes, which combine several analogue signals at the transmitter in the electrical domain by frequency translating each to a different IF, undergoing E/O and then O/E conversion at the receiver, after which analogue filters and down-converters are used to de-multiplex the signals. DWDM techniques can be used to multiplex signals via different wavelengths of light following E/O conversion of each signal. Rather than employing these multiplexing techniques independently, higher spectral efficiency can be achieved by combining both. However, when there are dynamic

variations in the multiplex creation process, such as in the number and bandwidth of individual signals, such analogue multiplexing techniques suffer from scalability issues. Scalability will be of prime importance in 5G (and beyond) mobile fronthauls, which have to be dynamic, versatile, flexible and scalable in order to be able to seamlessly support technologies such as mMIMO and heterogeneous networking. As a result, techniques employing SCM in the digital domain, coupled with analogue transport, have gained interest in recent years.

4 Analogue SCM at mm-Wave Frequencies

4.1 Introduction

This chapter begins with a discussion of traditional SCM techniques for a small count of multiplexed signals. Back-to-back (b2b) measurements (i.e. those that do not incorporate an optical link) are used to assess the performance of these multiplexing techniques. The first technique multiplexes the signal in the analogue domain while the second makes use of Arbitrary Waveform Generator (AWG) processing to multiplex signals in the digital domain. Both techniques de-multiplex the signals in the analogue domain.

Then, results are presented for optical links employing direct and external Intensity Modulation Direct Detection (IM-DD). These results aim to assess the performance of traditional SCM and can be used as a baseline for comparisons with the digital multiplexing technique that will be discussed in later chapters (starting with the concept Chapter 5).

Next, following a short introduction on the VPI simulator, the components used for these measurements as well as for measurements in Chapter 6 are characterized while modelling in VPI is carried out for these components with models matched to measured performances. A comparison between measured and simulated results for an external IM-DD link with mmW up-conversion is carried out.

Finally, a number of WDM techniques are discussed in conjunction with the SCM approaches, in terms of cost and complexity limitations.

Back-to-back measurements and measurements over an optical fibre link at RF frequencies for analogue SCM channels are discussed in Section 4.2. This is followed by experimental results at mmW frequencies using analogue SCM channels in Section 4.3. Characterisation and modelling of devices used in the experimental setup are discussed in Section 4.4. A comparison between measured and simulated results of analogue SCM at mmW frequencies is presented in Section 4.5. The chapter is concluded with a discussion regarding the issues with analogue SCM, SCM-WDM and SCM with MIMO/ mMIMO at mmW frequencies in Section 4.6.

4.2 Analogue SCM Experiments at RF Frequencies

This section presents measurement results at RF frequencies for two user-defined OFDM channels with 16-QAM subcarrier modulation, which are multiplexed in the electrical domain via SCM. The measurements include b2b, direct IM-DD and external IM-DD set-ups. The signal parameters used in these measurements (and in the measurements presented in later sections of this chapter) are as follows:

- Modulation: OFDM
- Subcarrier Modulation: 16-QAM
- Data subcarriers: 392
- Null subcarriers: 112
- Number of OFDM frames: 30
- Pilot tones: 8
- CP length: 0.125

Each OFDM signal is created in MATLAB (with a different random generator seed), downloaded to an AWG where it undergoes digital to analogue conversion and is transmitted via the link. The signal is then captured by a real-time Oscilloscope and processed offline in MATLAB. The two sampling rates that have been used to capture the signals at the oscilloscope for the measurements presented in this chapter are 100 GSps and 50 GSps (the effects of Oscilloscope sampling rates have been discussed in Chapter 2).

The devices and their parameters used for the measurements in this section are shown in the Appendix (Table 9-1). Some of these parameters are repeated in the descriptions of the different measurements in the following sub-sections.

4.2.1 Back-to-back SCM Measurement results

In Table 4-1, the results of back-to-back measurements using a single signal are shown. The EVM results in Table 4-1 show an increase in EVM each time the channel bandwidth is increased, due to the reduction in the SNR.

Table 4-1 Parameters corresponding to each channel bandwidth and back-to-back EVM results for a single channel (captured by the Oscilloscope using a sampling rate of 100 GSps)

Signal Bandwidth (MHz)	**Baseband Sampling Rate (MSps)**	**Data Rate per channel (Gbps)**	**EVM (% rms) (BTB) (OSC SR: 100GSps)**
76	97.656	0.266	1.9%
152	195.3125	0.532	2.2%
305	390.625	1.06	2.4%
610	781.25	2.13	2.7%

For the b2b measurements using two channels, two different approaches have been employed. The first approach comprises multiplexing in the analogue domain at the transmitter and analogue de-multiplexing at the receiver. The second approach comprises multiplexing in the digital domain at the transmitter and analogue de-multiplexing at the receiver.

Figure 4-1 shows the measurement setup for analogue multiplexing coupled with analogue de-multiplexing at RF. Two OFDM channels are created in MATLAB and using the AWG, Channel 1 is modulated onto a carrier frequency (f_1) of 1.9 GHz while Channel 2 is modulated onto a carrier frequency (f_2) of 2.5 GHz (the choice of carrier frequencies is a result of available RF filters). The two channels are generated using two different output ports of the AWG and combined in the analogue domain using an RF combiner/ splitter (in a completely analogue approach, the two channels would be generated at baseband and up-converted to their respected RF frequencies via LOs and mixers, resulting in higher losses and greater complexity). Note that the output signals from both output ports of the AWG have the same power. The combined channels are amplified (using RF Amplifier A, Appendix, Table 9-1) before being separated at the receiver, using an RF splitter and filters (even though the filter for Channel 2 is actually a high pass filter, it is called BPF2 for simplicity). They are then captured individually by the Oscilloscope to be processed offline in MATLAB. The sampling rate used at the Oscilloscope is set to 100 GSps. In Figure 4-1, the analogue and digital domains are indicated using different colours.

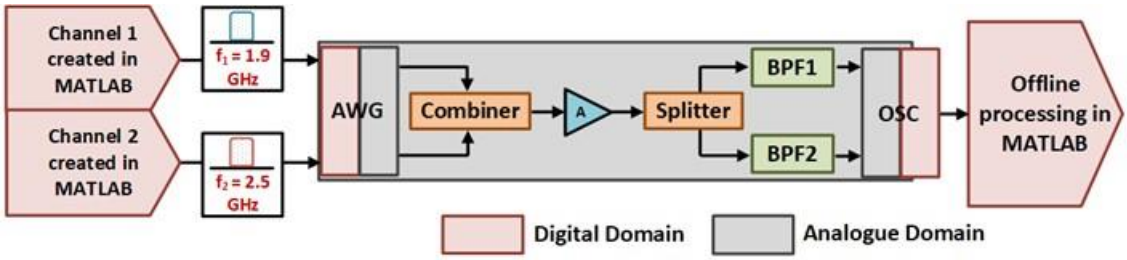

Figure 4-1 Approach I: Back-to-back measurements with two channels (analogue multiplexing at transmitter, analogue de-multiplexing at receiver).

The second approach employing digital multiplexing at the transmitter and analogue de-multiplexing at the receiver is shown in Figure 4-2. The two channels are downloaded to the AWG, placed at RFs of 1.9 GHz and 2.5 GHz and multiplexed using the multicarrier option of the AWG [162]. The subcarrier multiplex is then converted from a digital to an analogue signal, generated using a single channel/ output port of the AWG (the output power of the port is divided equally between the two channels), amplified and transmitted via an RF cable. At the receiving end, the channels are separated using a splitter and band-pass filters, before being captured by the oscilloscope for offline processing.

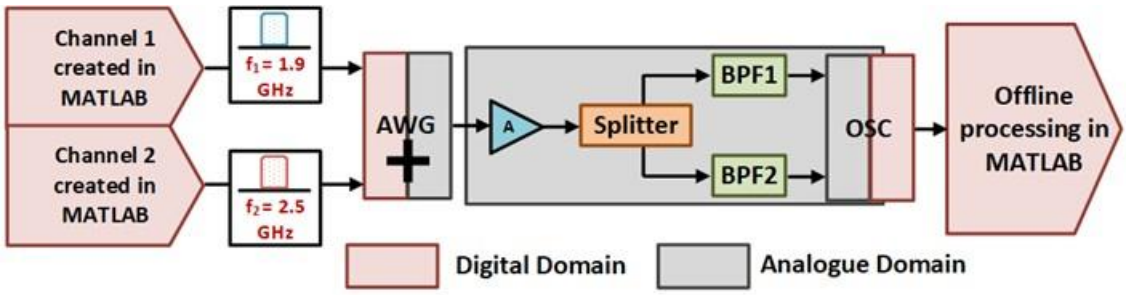

Figure 4-2 Approach II: Back-to-back measurements with two channels (digital multiplexing at transmitter, analogue de-multiplexing at receiver).

The results of these two measurements (for different channel bandwidths) are shown in Table 4-2. The results of only two channel bandwidths are shown as an example. Note that the same output power is used for the different channel bandwidths. However, for the larger bandwidth signals, the power is spread over a larger bandwidth, leading to a lower SNR.

Table 4-2 Back-to-back EVM performance of two SCM OFDM channels using Approaches I and II (captured by the Oscilloscope using a sampling rate of 100 GSps)

Approach	Channel Bandwidth (MHz)	Channel 1 EVM (% rms)	Channel 2 EVM (% rms)
I	305	2.6%	2.7%
	610	11.3%	11.4%
II	305	2.2%	2.3%
	610	11%	11.5%

As shown in the table, the EVM performance is much worse for 610 MHz. This is a result of the limited passband of the filter employed. For this reason, this bandwidth will not be used in experiments to follow. Moreover, the EVM performance of the second channel of the multiplex (which is at 2.5 GHz) is slightly worse, which may be due to a combination of the frequency response of the AWG [163] and filter response.

Approach I requires the use of two combiners/ splitters with a total insertion loss of approximately 10 dB and has higher cable loss compared to Approach II. It also requires the use of the 2-way power splitter/ combiner, which has limited isolation between its ports (approximately 16 dB). On the other hand, even though the 4-way power splitter/ combiner has 15 dB isolation between adjacent ports, it has approximately 35 dB isolation between ports 1 and 4 (which have been used in these experiments). Good isolation (as well as good selectivity of filters) is an important factor in these experiments due to the wide bandwidth of the signals and the inability to increase the frequency gap between the signals due to limitations of available filters. This results in worse EVM performance for Approach I (adding extra amplification or using a combination of the 2-way and 4-way combiner/ splitters leads to a slight improvement in the results). Lastly, since some of the SCM stages are moved from the analogue to the digital domain in Approach II, it has a lower number of analogue components and lower complexity compared to Approach I.

As a result, Approach II will be used for the rest of the measurements at RF and also for those at mmW frequencies. For simplicity, it will be called Analogue SCM from this point onwards.

4.2.2 Direct and External IM-DD Measurement Results

Figure 4-3 shows the measurement setup for direct IM-DD using two channels. At the CU, the two channels at 1.9 GHz and 2.5 GHz are multiplexed in the electrical domain via an SCM scheme using Approach II as described in Section 4.2.1. The SCM signal is amplified via Amplifier A (Appendix Table 9-1) and modulated onto an optical carrier using a Distributed Feedback (DFB) Laser (direct modulation). After transmission via a short length (1 metre) of single mode fibre (SMF), the channels are detected by a PIN Photodiode (PD) at the RAU, amplifed by Amplifier B (Appendix Table 9-1) and separated using the 4-way splitter and band-pass filters. They are then captured by the oscilloscope for offline processing in MATLAB.

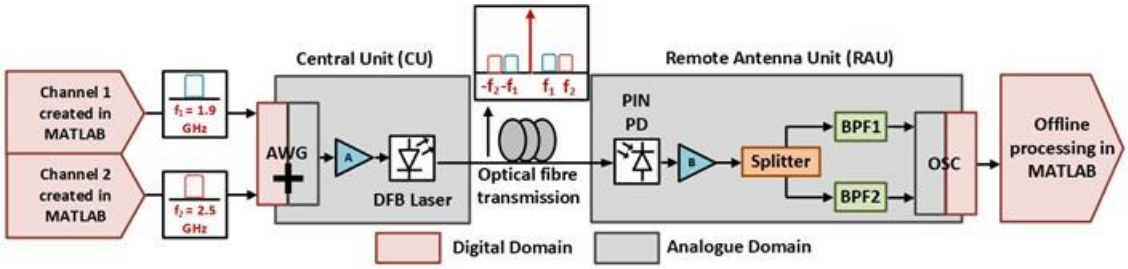

Figure 4-3 Measurements via a direct IM-DD link using two channels.

Figure 4-4 shows the measurement setup for external IM-DD using the same signals. Again, the two channels (at 1.9 GHz and 2.5 GHz) are multiplexed at the CU using Approach II. An optical carrier signal is supplied to the MZM by a Continuous Wave External Cavity Laser (denoted by CWL in the figure). The SCM signal is amplified via Amplifier A and modulated onto the optical carrier using the MZM. After transmission via a short length of optical fibre, the signals are amplified by two Erbium Doped Fibre Amplifiers (EDFAs) and detected by a mmW PD at the RAU. They are amplifed once more by Amplifier B and separated using the 4-way splitter and band-

pass filters, before being captured by the oscilloscope for offline processing in MATLAB. The MZM has been biased at point between quadrature and null in these experiments.

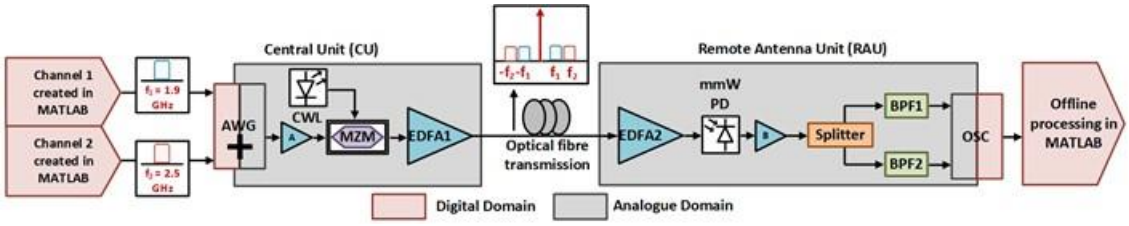

Figure 4-4 Measurements via an external IM-DD link using two channels.

The results of these two measurements are shown in Table 4-3, for a channel bandwidth of 305 MHz. Compared to the direct IM-DD link, the external IM-DD link shows better EVM performance due to improved RF gain and a flatter frequency response. As with the b2b measurements, the EVM performance for Channel 2 is slightly worse.

Table 4-3 Direct IM-DD and external IM-DD EVM performance of two channels at RF (captured by the Oscilloscope using a sampling rate of 100 GSps)

Measurement	**Channel Bandwidth (MHz)**	**Channel 1 EVM (% rms)**	**Channel 2 EVM (% rms)**
Direct IM-DD	305	6.8%	7.3%
External IM-DD	305	4.7%	5.2%

4.3 Analogue SCM Experiments at mm-Wave Frequencies

This section presents the analogue SCM measurements at mmW frequencies with up to four OFDM channels. Approach II (from Section 4.2.1) and external IM-DD are used, while the measurements are carried out at 60 GHz and 25 GHz mmW frequencies. Table 9-2 in the Appendix provides a list of devices and their parameters used in these experiments. Some of these are mentioned in the descriptions to follow. Note that the number of components shown

in this table is much higher compared to the number of components in Table 9-1 in the Appendix.

4.3.1 Analogue SCM Measurements at 60 GHz

Figure 4-5 shows the experimental setup for analogue SCM at 60 GHz. Two OFDM channels with 16-QAM subcarrier modulation and 305 MHz bandwidth each (data rate of 1.06 Gbps/ channel) are used in these experiments.

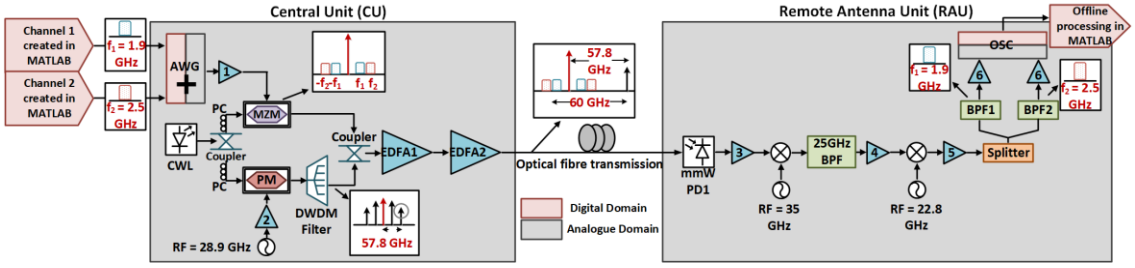

Figure 4-5 Experimental setup for analogue SCM at 60 GHz.

A 3-dB optical coupler splits the optical carrier signal from the CWL, with one output modulated by the SCM channels and the other used to generate an optical carrier 57.8 GHz away using a Phase Modulator (PM). In order to generate this carrier, an RF signal of 28.9 GHz drives the PM and a second order optical sideband is selected using a Dense Wavelength Division Multiplexing (DWDM) filter. Using the AWG, the two user-defined signals are combined at IFs of 1.9 GHz and 2.5 GHz, i.e. around 2.2 GHz, such that 57.8 GHz + 2.2 GHz = 60 GHz at the receiver. After amplification via Amplifier 1, the signals are modulated onto the optical carrier using the MZM. Polarisation controllers (PCs) have been used at the input of both the MZM and PM to maintain the polarisation of the optical carrier. The output of the MZM is combined with the filtered second order sideband and amplified by cascaded EDFAs before transmission over optical fibre.

At the RAU, a high bandwidth (70 GHz) PD (denoted by mmW PD1 in the figure) generates the 60 GHz band SCM signal. This is amplified by Amplifiers 3, 4 and 5, filtered by the 25 GHz band-pass filter and down-converted to IF (2.2 GHz) via two down-conversion stages (the choice of employing two down-conversion stages instead of one, was based on component availability). Finally, the SCM signal is filtered to individually obtain the 1.9 GHz and 2.5 GHz channels, which

are then amplified and captured using the oscilloscope for offline processing. A sampling rate of 50 GSps has been used to capture the signals.

The EVM performance for Channels 1 and 2 are 10.5 % and 10.8%, respectively and are within 3GPP limits [74]. The received constellations are shown in Figure 4-6.

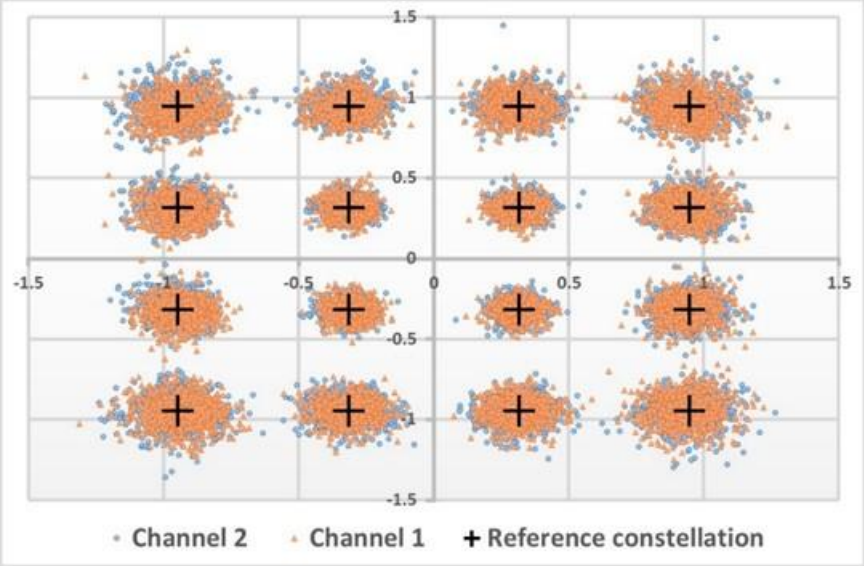

Figure 4-6 Received constellations of 60 GHz signals at 4.9 V MZM bias.

Note that these received constellations are for an MZM bias of 4.9 V, which was found to be the optimum working point. Figure 4-7 shows the effect of the MZM bias on the EVM performance of the two channels, with the bias varied between 3.3 V to 5.36 V. The best EVM performance for both channels is attained at a bias point of 4.9 V. The aggregate data rate for these experiments is 2.13 Gbps.

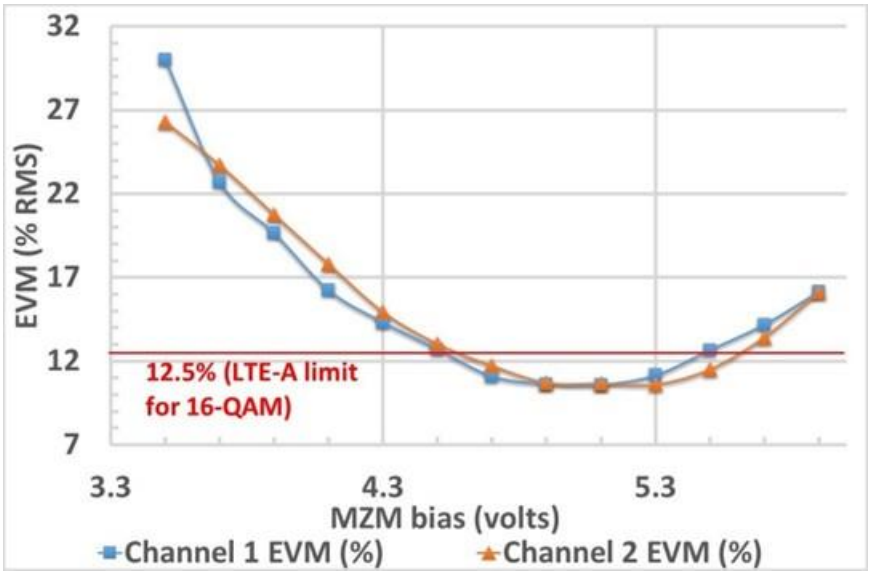

Figure 4-7 EVM versus MZM Bias for analogue SCM at 60 GHz.

In later experiments, the RF splitter, as well as the amplifier preceding it were removed and with further optimisation, the EVM performance was improved for Channels 1 and 2 to 9.6% and 9.8%, respectively. A sampling rate of 100 GSps was used for these results.

EVM performance could not be improved further for these measurements as a result of power limitations of the second order sideband from the PM, low responsivity of the 70 GHz mmW PD and high mixer loss due to two-stage down-conversion. Note that wireless transmission has not been attempted for these experiments, due to availability of components and the EVM performance being very close to 3GPP limits (more than two channels have not been attempted for the same reason).

4.3.2 Analogue SCM Measurements at 25 GHz

The experimental setup for analogue SCM at 25 GHz is shown in Figure 4-8. Two OFDM channels, each with a bandwidth of 305 MHz (a data rate of 1.06 Gbps/ channel), as well as up to four channels with bandwidths of 76 MHz (a data rate of 0.266 Gbps/ channel) and 152 MHz (a data rate of 0.532 Gbps/ channel) have been used in these experiments. As mentioned previously, the OFDM subcarrier modulation is 16-QAM, while parameters of components used in the setup are shown in the Appendix (Table 9-2).

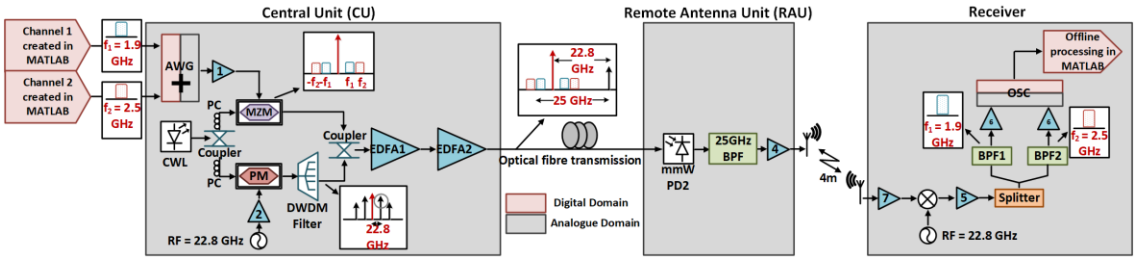

Figure 4-8 Experimental setup of analogue SCM at 25 GHz, with wireless transmission.

As with the 60 GHz measurements, a 3-dB optical coupler splits the optical carrier signal from the CWL, with one output modulated by the SCM channels and the other used to generate an optical carrier 22.8 GHz away using a PM. In order to generate this carrier, an RF signal of 22.8 GHz drives the PM and the first order optical sideband is filtered using a DWDM filter. Using the AWG, the user-defined signals are combined at different IFs around 2.2 GHz, such that 22.8 GHz + 2.2 GHz = 25 GHz. After amplification via Amplifier 1, the channels are modulated onto the optical carrier using an MZM. The output of the MZM is combined with the filtered first order sideband and amplified by cascaded EDFAs before transmission over optical fibre.

At the RAU, a high bandwidth (45 GHz) PD (denoted by mmW PD2 in the figure) generates the 25 GHz band SCM signal, which is filtered by the 25 GHz band-pass filter and amplified by Amplifier 4. Following that, the channels undergo wireless transmission over a distance of 4 metres.

At the receiver, the channels are amplified by Amplifier 7 to compensate for the loss due to wireless transmission. They are then down-converted to IF (2.2 GHz) via single-stage down-conversion stage and amplified by Amplifier 5. Finally, the SCM signal is filtered to individually obtain the channels, which are amplified and captured using the oscilloscope for offline processing. A sampling rate of 100 GSps has been used at the oscilloscope to capture the signals.

The EVM performance and aggregate data rates of the 25 GHz experiments with variable bandwidth SCM channels at different IFs are shown in Table 4-4. The best EVM performance is attained with the use of the 25 GHz band-pass filter, as it removes low frequency harmonics that interfere with the channels. Due to available filter limitations, the EVM performance of only two channels (out of each multiplex) are evaluated for each measurement and shown in the table.

Measurement 1 shows the EVM results for up to four 76-MHz channels, Measurement 2 shows EVM results for up to three 152 MHz channels and Measurement 3 is for up to two 305 MHz

channels. For comparison, the EVM results of both wired (just optical link) and wireless transmission are shown for these three measurements.

Table 4-4 EVM performance and aggregate data rates of 25 GHz experiments with different number of multiplexed channels and different channel bandwidths (filtered channels in red; captured using 100 GSps)

Measurement	**Channel Bandwidth (MHz)**	**Number of Channels**	**IF (GHz)**	**EVM for 2 filtered channels (% rms)**		**Aggregate Data Rate (Gbps)**
				With optical link	***Wireless***	
1	76	1	2.2	6.1	7.2	0.266
		2	1.9, 2.5	6.3, 6.5	7.4, 7.6	0.532
		3	1.9, 2.2, 2.5	6.5, 6.7	7.7, 7.9	0.798
		4	1.8, 2.23, 2.45, 2.61	6.9, 7.5	7.8, 8.1	1.06
2	152	1	2.2	7.2	8.3	0.532
		2	1.9, 2.5	7.3, 7.6	8.4, 8.8	1.06
		3	1.9, 2.2, 2.5	7.5, 8.0	8.8, 9.1	1.6
3	305	1	2.2	8	9.1	1.06
		2	1.9, 2.5	8.2, 8.5	9.4, 9.6	2.13
4	76 MHz and 152 MHz	4	1.9 (152 MHz), 2.25 (152 MHz), 2.45 (76 MHz), 2.6 (152 MHz)	7.6 (76 MHz), 8.6 (152 MHz @ 1.9 GHz IF)		1.87
5	152 MHz and 305 MHz	3	1.85 (152 MHz), 2.2 GHz (152 MHz), 2.5 (305 MHz)	8.8 (152 MHz @ 1.85 GHz), 9.5 (305 MHz)		2.13

The EVM performance becomes progressively worse as the channel bandwidth and number of multiplexed channels increase (resulting in narrower gaps between channels). The EVM performance for wireless transmission is around 1% higher than wired transmission.

Measurements 4 and 5 are for mixed channel bandwidths and do not include wireless transmission. The EVM performance for these measurements is slightly worse compared to the first three measurements. Among all the measurements, the smallest gap is used between the channels at 2.45 GHz and 2.6 GHz in Measurement 4, which are 76 MHz and 152 MHz bandwidth channels, respectively, leading to a gap of 36MHz.

All results shown in the table are within 3GPP limits [74].

4.4 Characterisation and Modelling of Devices

This section discusses the characterisation and modelling of devices, used in the experiments with analogue SCM at mmW frequencies. The modelling is carried out in VPI^{TM} (Virtual Photonics Inc), an optical communication simulation software package. Individual components (such as MZM, PM, RF amplifiers) have been modelled using available blocks and matched with experimental characterisation measurements. These simulated models allow for analysis of the effects that different component parameters have, both in the optical and electrical domains of the millimetre-wave over fibre system. Much of the characterisation and modelling done in this section will be re-used in Chapter 7.

This section is divided into three sub-sections. It begins with a short introduction on the VPI simulation environment in Section 4.4.1. Some of the important blocks and formulae used to model the devices used in measurements are shown in Section 4.4.2. Finally, Section 4.4.3 deals with component characterisation and matching to models. In order to analyse the system performance, it is important that the performance of components used in the simulations be similar to those used in the experiments.

4.4.1 Introduction to VPI Simulation Environment

The VPI™ [164] simulation hierarchy consists of three fundamental layers: Universe, Galaxy and Star, and is shown in Figure 4-9.

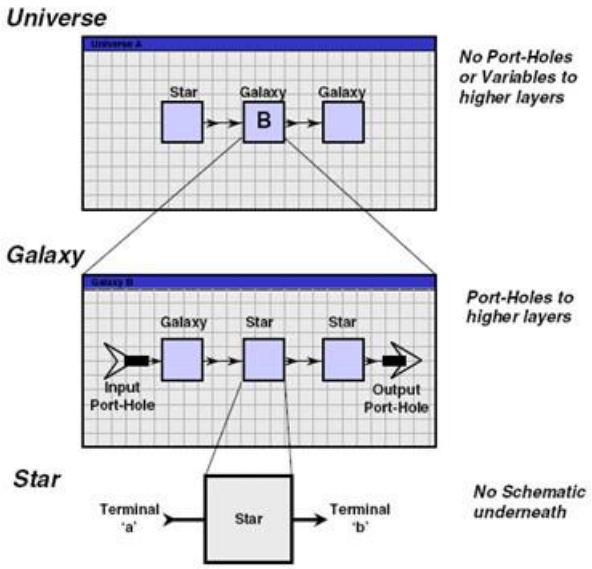

Figure 4-9 VPI^{TM} simulation hierarchy [from VPI™ simulation guide [165], pp. 34].

As shown in the figure, a universe (also referred to as a complete simulation application/ simulation setup/ schematic) consists of a network of stars and galaxies and is the top layer of the simulation. Galaxies contain stars and other galaxies while a star is the lowest level of simulation [165]. These three layers can be described as follows:

- ***Universe:*** It is the top layer of the hierarchy and it has no external connections. A big difference between this layer and the other two layers is that a universe can be run as a simulation but the galaxies and stars within it cannot be run on their own, as they require external connections
- ***Galaxy:*** It consists of interconnected stars and other galaxies. A galaxy can be simulated only if it lives within a universe. Galaxies can be interconnected as they have connections to other internal workings through input/ output ports (Port Holes) as shown in Figure 4-9. Galaxies can be used to interconnect several stars together in order to keep simulation setups clear and efficient and to make parameter handling easy. Galaxies will be explored further in Chapter 7

- ***Star:*** It is the lowest level in the simulation and represents optical or electrical models such as the PM, RF amplifiers etc. Most of the models supplied by VPI™ are stars. Stars cannot be subdivided and are sometimes referred to as atomic models.

4.4.2 Modelling of Devices

4.4.2.1 Laser Model

A datasheet model of the CW laser model ("*LaserCW_DSM"*) has been used in VPI. The parameters of this model are those commonly found on a manufacturer's data sheet. In the experimental set-up, the wavelength used was 1554.6 nm (corresponding to 194.8422 THz) and the output power was generally measured to be around 4.6 dBm (maximum output power of the laser at this wavelength was 5.3 dBm). Since the wavelength does not have any effect on the results in simulation, VPI's default wavelength or Emission Frequency has been used in the simulations. The parameters for modelling the CW Laser used in experiments have been shown in Table 4-5.

Table 4-5 Parameters of the datasheet model of a CW Laser set to model the experimental CW Laser

Parameter Name	**Parameter Value**
Emission Frequency	193.1 THz
Relative Intensity Noise (RIN)	-150 dB/ Hz
Linewidth of Laser	1 MHz
Average Power	4.6 dBm

4.4.2.2 DWDM Model

The DWDM filter has been modelled using an optical filter module ("*FilterOpt*") with the parameters shown in Table 4-6. It is a universal optical filter model for simulations of band-pass, bandstop and comb filters with standard transfer functions such as Butterworth, Chebyshev etc. [166]

Table 4-6 Parameters used to model the DWDM filter in VPI [23]

Parameter Name	Parameter Value
Filter Type	Band-pass
Transfer Function	Butterworth
Bandwidth	9 GHz
Filter Order	6
Filter Loss	6 dB
Centre Frequency	193.158 THz (60 GHz simulation); 193.123 THz (25 GHz simulation) [with reference to the emission frequency of 193.1 THz]

4.4.2.3 OFDM Transmitter

The theory of OFDM generation has already been covered in detail in Section 2.4 but is explained from the perspective of the VPI simulation environment here. The blocks used inside the OFDM transmitter module in VPI ("*Tx_El-OFDM"*) are shown in Figure 4-10. This module generates electrical signals corresponding to the real and imaginary parts of an OFDM signal. DMT and other modulation schemes can be implemented and the generated signal can be processed before and after IFFT using custom DSP procedures. Various bit and power loading schemes are also supported by this block and a cyclic prefix and pilot tones can be added via parameter setting [167].

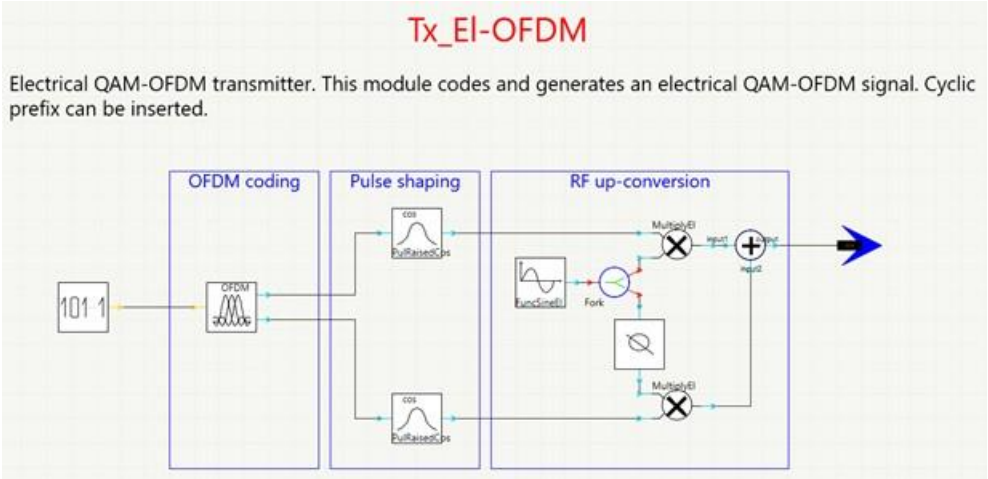

Figure 4-10 VPI implementation of the OFDM transmitter [167].

Data is generated randomly by a Pseudo Random Binary Sequence (PRBS) block, at a rate determined by the modulation level and the bit rate, e.g. if the bandwidth of a signal is 300 MHz and 16-QAM subcarrier modulation is being used, the bit rate will be 1.2 GHz (4*300 MHz). The raw digital binary bits are distributed into n_c data-streams, and each stream is then encoded according to the settings in the 'Subcarrier Modulation' parameters group of the "*Coder_OFDM*" block. The number of bits encoded in each symbol is given by the parameter "*BitsPerSymbolQAM*", which must be an integer value. Individual modulation formats can be specified for different subcarriers. An OFDM frame (note that the term "frame" is used within VPI, at this stage of signal generation) is then constructed by applying an n_c - point IFFT to the subcarriers' symbols. As in experiments, the number of subcarriers (IFFT length) is set to 512 and the CP length is set to 0.125.

The OFDM coding stage is followed by pulse shaping. In this stage, the rectangular input pulses are pulse-shaped by a filter with a raised cosine characteristic. Ideally at this stage, a linear low-pass filter would be used with a cut-off frequency or Nyquist Frequency of

$$F_n = B/2 \ , \tag{4-1}$$

where *B* is the symbol rate or baud rate at the subcarrier level and also determines the bandwidth of the OFDM signal (the addition of a CP increases this rate, as explained in Chapter 2). However, as this ideal low pass filter is not realizable, a practical odd-symmetric extension is the raised cosine characteristic fitted to the ideal low-pass filter. For an equalized channel and constant transmit power, the Nyquist characteristic is split equally between the transmitter filter and the receiver filter (matched filters), using a square-root Nyquist response. The roll-off factor, which is defined as the ratio of excess bandwidth above F_n, can be set using the "*squareRootRaisedCosine*" parameter and has been set to 0.25 for the simulations (as it is in experiments).

After the pulse shaping stage is the RF up-conversion stage, in which the In-phase channel data modulates a cosine wave carrier while the Quadrature channel data modulates the sine wave carrier via an RF phase shifter, sine wave generator and mixers. Finally, an OFDM signal up-converted to the chosen RF (specified by the "*Frequency*" parameter of the sine wave generator), with multilevel In-phase and Quadrature phase M-QAM coded symbols is generated.

Two other options of the OFDM transmitter module which have been used in these SCM simulations are "*RandomNumberSeed*" and "*ChannelLabel*". The first option provides a lookup index for bit sequence generation, which makes it easy to generate different data for the two

channels. The second option is for labelling the aggregate logical channel and is useful for distinguishing the two channels.

When setting up an OFDM simulation, it is very important to have the bit rate of the PRBS source set correctly. Otherwise the schematic iterates multiple times or produces erroneous results. The correct value of the bit rate or '*BitRateDefault*' in VPI, *R*, can be calculated from

$$R = \frac{b_f}{n_c} \times B \ , \tag{4-2}$$

where b_f is the bits per frame or the number of bits required for one frame encoding. This is equal to the sum of the number of bits per symbol for all subcarriers.

For most subcarrier level performance estimations, the simulated signal must contain an integer number of OFDM frames. As a result, the global parameter '*TimeWindow*' has to be set to an integer multiple of the OFDM frame duration that depends on the number of subcarriers, subcarriers' baud rate and cyclic prefix. This is given by

$$T = \left\lfloor \frac{(1+CP)\times n_c)}{B} \right\rfloor \ , \tag{4-3}$$

This means that VPI generally requires the number of symbols (ratio between time window and symbol rate) to be a power of two. This is specified by setting the global parameter '*GreatestPrimeFactorLimit*' or GPF limit to two (which is the default value). This factor ensures that the IFFT algorithm is used in simulations and VPI recommends setting it to any integer value between 2 to 13 (a setting of 2 leads to the highest processing speed, as an IFFT operation is employed). However, for some values of CP and number of carriers, a signal may be created with a non-power-of-two number of samples. In this case, the GPF should be set accordingly. The GPF can be deactivated by setting it to -1, which allows an arbitrary number of samples to be simulated.

4.4.2.4 Power Control and 50-ohm Conversion

An automatic gain control module combined with an electrical attenuator module have been used at the output of each OFDM transmitter module to vary the RF power of each SCM channel separately. This is shown in Figure 4-11. Note that these electrical and optical attenuator modules have also been used in other parts of the simulation to model losses in the

experimental setup. The RF power of the OFDM signal at the output of the automatic gain control block is referenced to 1Ω impedance. It is important to convert this impedance to 50Ω for modelling the input powers used in the experimental set-up (which is a 50Ω matched system). This has been done by placing an electrical amplifier module with the gain set to -17 dB (=*10*log(1/50)*).

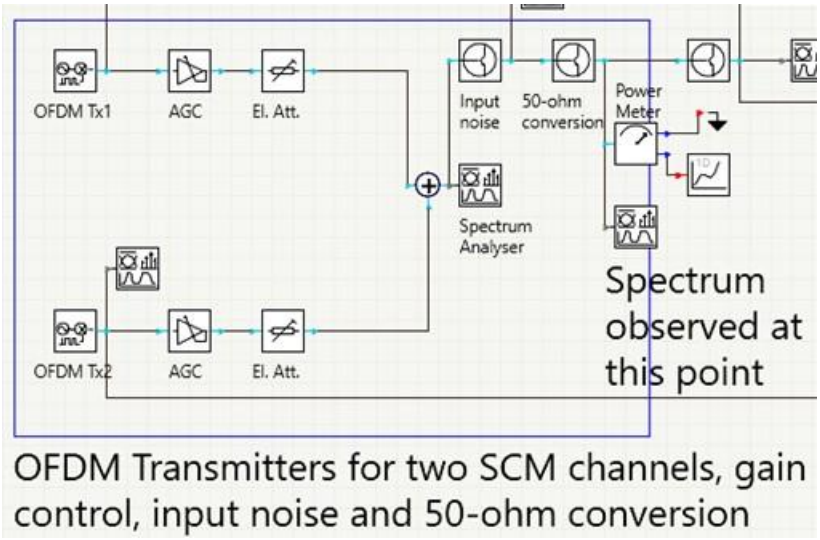

Figure 4-11 Gain Control, input noise and 50-ohm conversion of two OFDM SCM channels in VPI.

The "*AmpSysEl"* electrical amplifier block has been used for 50-ohm conversion and also to model input noise, which precedes the 50-ohm conversion. For modelling 50-ohm conversion, the gain is set to -17 dB and the "*CurrentNoiseSpectralDensity*" parameter is set to 0 while for modelling input noise, the gain is set to 0 while the *CurrentNoiseSpectralDensity* is set to the desired value. This module has been used to model the noise in the experimental setup in this manner and also to model the amplifiers used in the setup.

Figure 4-12 shows the spectrum of the two channels at the point shown in Figure 4-11 (after 50-ohm conversion). Both channels have an SNR of around 38 dB.

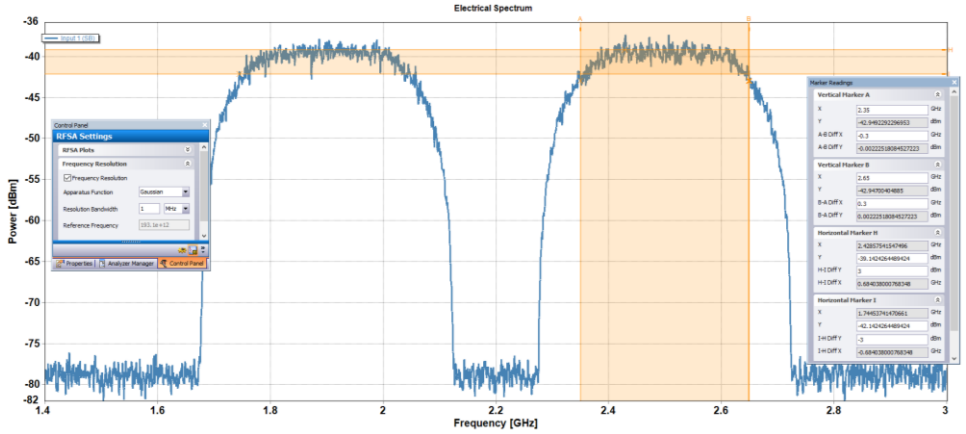

Figure 4-12 Spectrum of simulated SCM OFDM channels after 50-ohm conversion in VPI (Res. BW: 1 MHz, 300 MHz channels).

4.4.2.5 OFDM Receiver

The OFDM receiver has already been covered in detail in Section 2.4 but is explained from the perspective of the VPI simulation environment here. The blocks used inside the OFDM receiver module in VPI ("*Rx_El-OFDM_BER"*) are shown in Figure 4-13. This module decodes an electrical QAM-OFDM signal (preferably that generated by the *Tx_El-OFDM* module) by reversing the processes in the transmitter and evaluates the EVM and SER of the QAM signal.

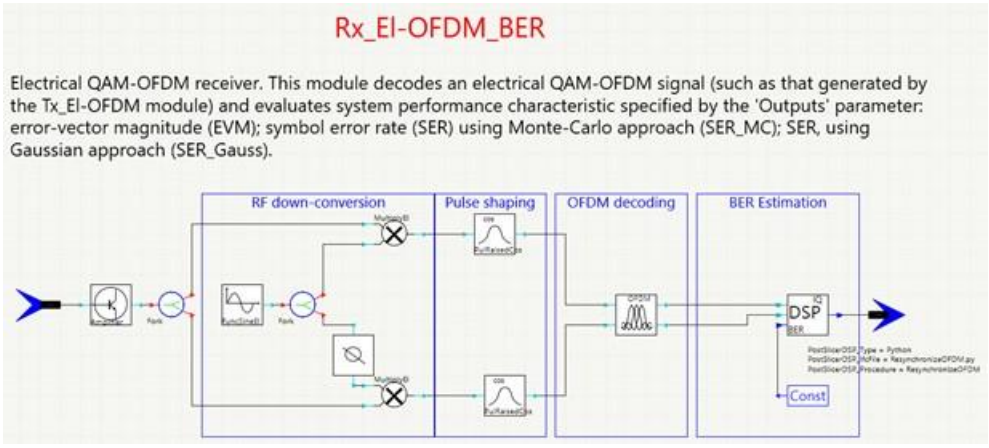

Figure 4-13 VPI implementation of OFDM receiver [168].

The demodulation process begins with the electrical signal first being down-converted to baseband. Following this, pulse shaping is applied and the signal is decoded in the "*Decoder_OFDM*" module. The obtained constellation is automatically corrected in amplitude

and phase for ideal signal detection and SER and EVM estimation. For optimal signal detection, the *NumberOfCarrier* (IFFT length), *BitsPerSymbolQAM* (subcarrier modulation level) and *CarrierFrequency* (IF) parameters (among other parameters such as Cyclic Prefix, Baud Rate etc.) in the receiver must have values identical to those in the transmitter. The Channel Label must be set to the correct value in order to detect the desired channel.

EVM will be used in the simulation results shown later on in Section 4.5 to estimate the transmission performance of the data modulated signal at the receiver. For EVM estimation, the "*Outputs*" parameter in the 'BER estimation' group must be set to "*EVM*". A one-dimensional numerical analyser at the output of the OFDM receiver module plots and displays the EVM. EVM calculation in VPI is carried out using equation (2-21) in Section 2.5.

In Section 4.5, a clock recovery module with a reference port will be used at the input of the OFDM receiver. This will be used to determine any time delay between the incoming transmitted signal and the original signal. The original signal is provided at the reference input from the OFDM transmitter output and module shifts the transmitted signal by the time delay.

4.4.2.6 RF Amplifiers and Noise calculations

In VPI, the electrical amplifier models use the '*CurrentNoiseSpectralDensity*' (Amps/$Hz^{0.5}$) parameter instead of the noise factor (*F*) (the noise figure, which is *F* in decibels, is a commonly given parameter in data sheets). Hence, the noise factor has to be converted to a current noise spectral density value. The noise factor is given by

$$F = \frac{SNR_{in}}{SNR_{out}} = \frac{S_{in} \times N_{out}}{N_{in} \times S_{out}} = \frac{G \times (N_{in} + N_{amp})}{G \times N_{in}} = 1 + \frac{N_{amp}}{N_{in}} \Rightarrow N_{amp} = (F - 1) \times N_{in} \,, \tag{4-4}$$

where

- S_{in}, S_{out} are the signals at the input and output of the amplifier, respectively.
- N_{in}, N_{out} are the noise at the input and output of the amplifier, respectively.
- N_{amp} is the excess (i.e. added) noise from the amplifier. [23]

The excess noise can be defined as

$$N_{amp} = I_n^2 \times R \Rightarrow I_n = \sqrt{\frac{N_{amp}}{R}} \,, \tag{4-5}$$

where,

- I_n is the noise current through the amplifier (current noise spectral density) and
- R is the test impedance (resistance) to measure the noise figure of the amplifier (50 Ω).

The input thermal noise density (Nin) of the amplifier is expressed as

$$N_{in} = kT \quad , \quad \text{(Watts/ Hz)} \tag{4-6}$$

where, k = 1.38E-23 J/K and T = 290 K. Finally, the relationship between noise factor and current noise spectral density is given by

$$I_n = \sqrt{\frac{(F-1)\times N_{in}}{R}} \quad , \qquad \text{(Amps/ } \sqrt{Hz}\text{)}. \tag{4-7}$$

The current noise spectral density calculations for the RF amplifiers used for the simulations (based on measured noise figure values, which are converted to noise factor) are shown in Table 4-7.

Table 4-7 Current noise spectral densities to be used in simulations for RF amplifiers used in experiments

RF Amplifier	**Noise Figure (dB)**	**Current Noise Spectral Density (Amps/ (Hz)$^{0.5}$**
SHF 824	3	8.925E-12
Norden Millimeter N07-1593	8	2.062E-11
Quinstar QPI-V02030-C1	5	1.316E-11
Quinstar QLW-24403536-JO	3.5	9.957E-12
SHF 100 AP	5.5	1.428E-11
Mini-circuits ZX60-2522M+	3	8.925E-12
Norden Millimeter N07-1725	3	8.925E-12

4.4.3 Component Characterisation and Matching to Models

4.4.3.1 RF Filters

An example of modelling an RF filter, specifically the one used for Channel 1 (1.9 GHz), is shown here, with the model matched in VPI to the filter's measured performance. A comparison between the measured filter parameters and those used to match them in simulation is shown in Table 4-8.

Table 4-8 Parameter comparison between measurement and simulation

Parameters	Measurement	Simulation
Filter model	Cascaded VLF-1800+ Low Pass Filter DC - 1800 MHz and Minicircuits VHF-1500+ High Pass Filter 1700 MHz - 4500 MHz	*"FilterEl"* electrical filter module; Filter type: Band-pass; Transfer function: Butterworth; Stop bandwidth: 1.66 GHz; Stopband attenuation: 50 dB
3-dB bandwidth	1.5 GHz - 2.16 GHz (660 MHz)	660 MHz
Insertion loss	1.5 dB	1.5 dB

The filter behaviour has been matched using the modules shown in Figure 4-14. The RF filter used in the experiments is a band-pass filter (created by cascading a low pass and high pass filter) with a 660 MHz 3-dB bandwidth and 1.5 dB insertion loss, as measured by an *Anritsu 37397C 40 MHz – 65 MHz Vector Network Analyzer (VNA)*. In VPI, an electrical sinewave generator has been used to generate a tone at the centre frequency (1.83 GHz) of the filter and the frequency has been swept from 0.8 to 2.8 GHz. The electrical attenuator models the insertion loss while the "*FilterEl*" electrical filter module is used to model the actual filter response. A power meter has been placed at the output of the sinewave generator to measure the input power to the filter while another power meter is used to measure the output power from the filter. The filter parameters are shown both in Figure 4-14 and in Table 4-8 while the comparison between the measured and simulated filter response is shown in Figure 4-15.

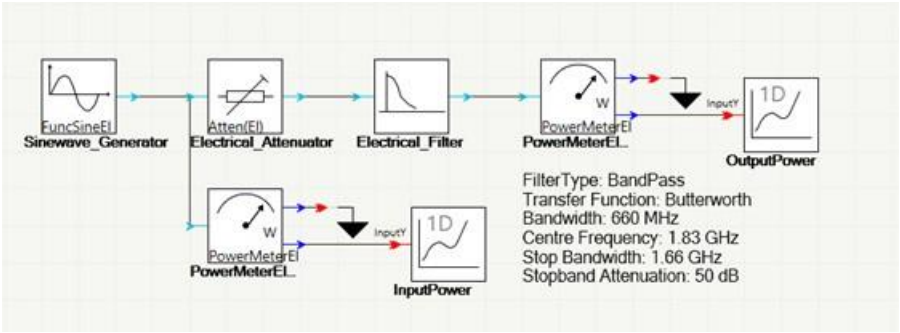

Figure 4-14 Characterisation of RF filter used for 1.9 GHz channel.

The passband ripple could not be modelled in VPI as the transfer function which matches the measured filter response is a Butterworth, which is inherently very flat in the passband. Moreover, the measured response has a different stopband attenuation beyond 2.4 GHz from the one below 1 GHz, a characteristic that has not been modelled.

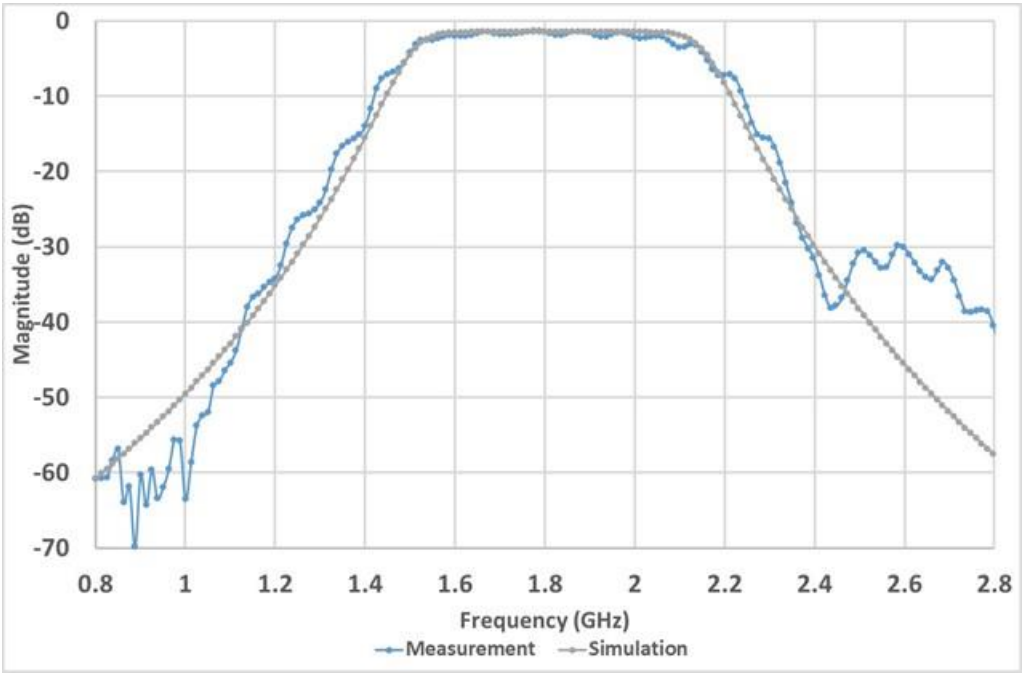

Figure 4-15 Comparison of measured and simulated filter response (used for the 1.9 GHz channel).

4.4.3.2 Phase Modulator (PM)

As already discussed in Section 3.2, a PM is an opto-electronic device that modulates the phase of an optical signal in proportion to the amplitude of an RF signal to produce phase modulated sidebands/ comb lines separated by the value of the RF signal frequency. Figure 4-16 shows how the behaviour of the PM used in measurements has been matched in VPI. As an example, only the results for the characterisation at 25 GHz have been presented.

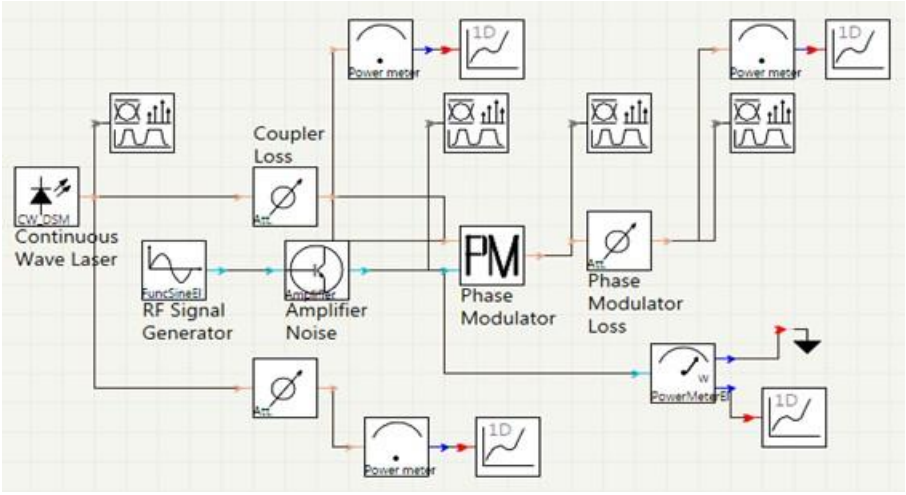

Figure 4-16 Matching measured behaviour of the Phase Modulator (PM) in VPI.

Similar to the simulation setup shown in the figure, the optical powers of the phase modulated sidebands have been measured for each RF power level and recorded, using a resolution bandwidth of 7.5 GHz (the maximum resolution bandwidth offered by an Agilent 86146B Optical Spectrum Analyzer). The output of the continuous wave laser module is connected to an optical attenuator to model coupler loss and the output port of the attenuator is connected to the optical input of the PM module ("*ModulatorPM*"). At the RF port of the PM, an RF signal of 23 GHz is applied (the RF signal frequency has been rounded up in simulations), along with the noise associated with the RF amplifier connected to the RF port. The output of the PM is connected to another optical attenuator, which models the PM insertion loss of 6.5 dB. The RF input power to the PM and the optical output power from the PM have been measured using RF and optical power meters respectively. The phase modulation can be adjusted by varying the "*PhaseDeviation*" parameter of the PM module, as well as the RF input power.

In both measurements and simulation, the RF input power to the PM and the optical power of the phase modulated sidebands have been related to the Bessel function graph to find the

modulation index using (3-5) in Section 3.2. With V_m being the amplitude of the RF signal and V_π being the half-wave voltage, the modulation index has been related to the *PhaseDeviation* parameter of the PM in simulations to model the correct spectrum. The modulation index used in the 25 GHz experimental setup is 1.4351 and the one used for the 60 GHz setup is 1.87. The optical power of the phase modulated sidebands/ comb lines versus the modulation index for the 25 GHz experiments and simulations have been shown in Figure 4-17 and Figure 4-18 respectively. The resulting PM optical spectrum with the 23 GHz separated phase modulated sidebands is shown in Figure 4-19.

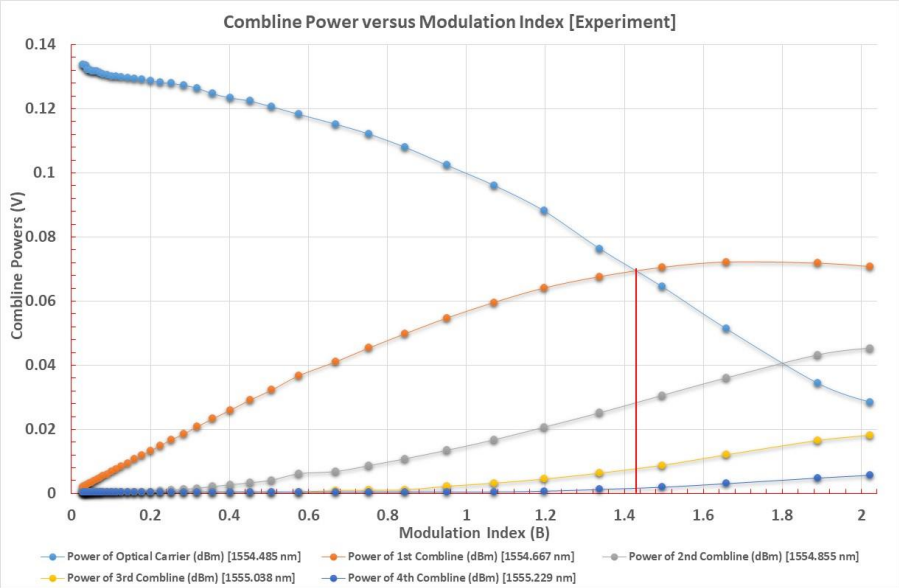

Figure 4-17 Phase modulated sideband/ comb line power versus modulation index in the 25 GHz experiments.

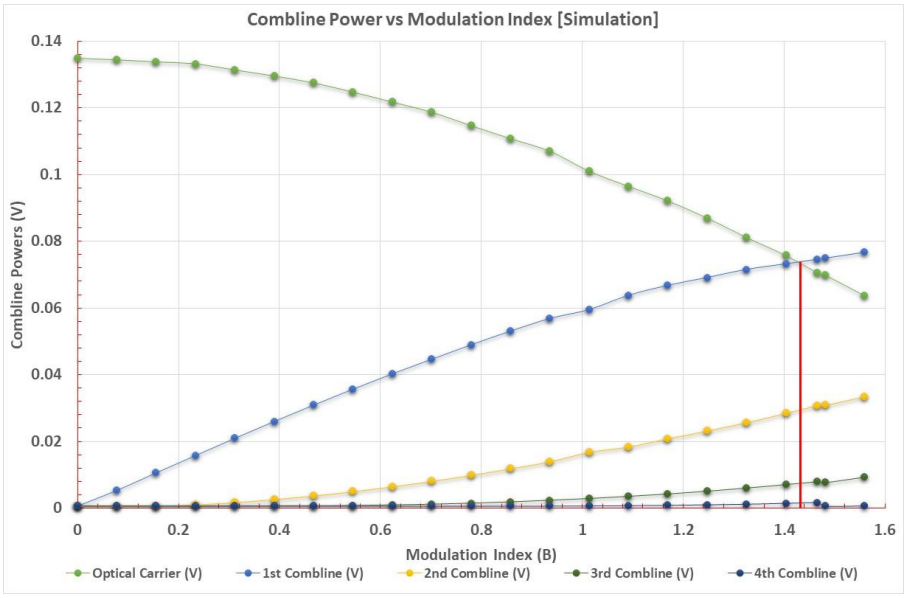

Figure 4-18 Phase modulated sideband/ comb line power versus modulation index in the 25 GHz simulations.

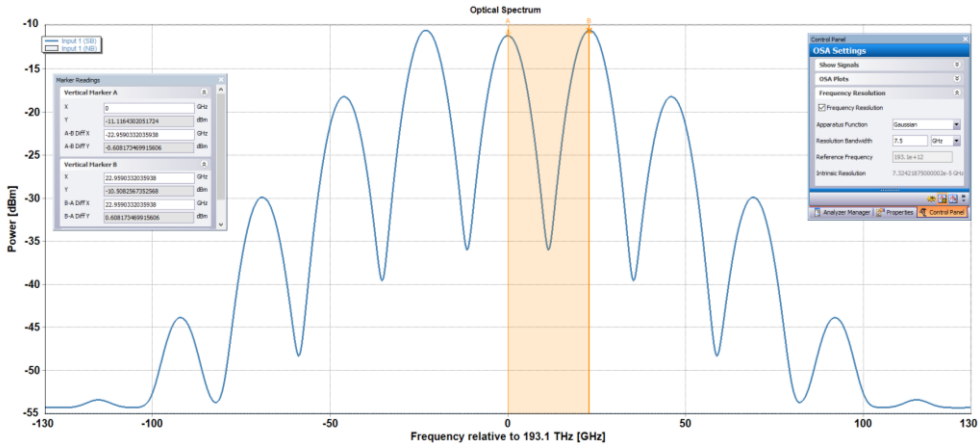

Figure 4-19 Optical spectrum of 23 GHz separated phase modulated sidebands, as seen in VPI. The first order sidebands have an optical power of approx. -11 dBm (Res. BW: 7.5 GHz).

4.4.3.3 Mach-Zehnder Modulator (MZM)

Figure 4-20 shows the process of matching the measured behaviour of the single-drive MZM in VPI.

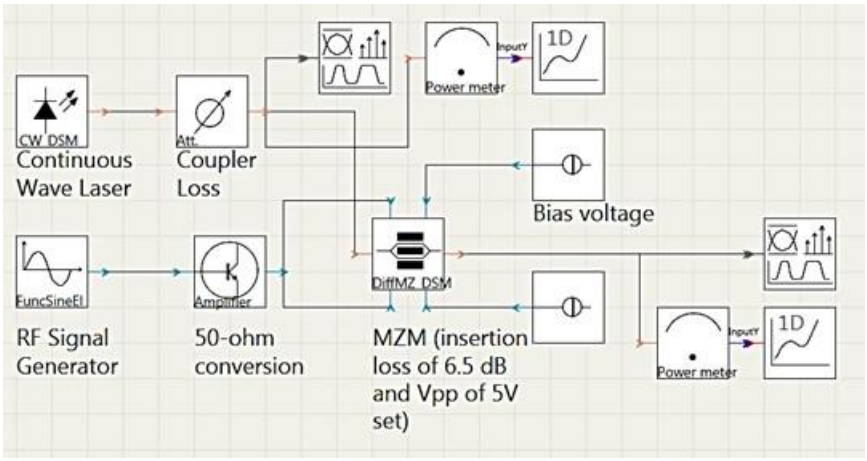

Figure 4-20 Matching measured behaviour of the Mach-Zehnder Modulator (MZM) in VPI.

The CWL is connected to the optical input port of the "*ModulatorDiffMZ_DSM*", which is a data sheet model of a differential MZM. This module has an optical input and output and four electrical input ports. The RF signal (with 50-ohm conversion) is applied to both the upper left and lower left RF input ports while the bias is applied via the upper right bias port using a DC source (the lower right bias port receives a bias voltage of 0 V). This arrangement causes the differential MZM model to function like a single-drive MZM (examples are shown in VPI manual [169]). The insertion loss has been set to the measured value of 6.5 dB.

The optical output power of the MZM in measurements and in simulation has been plotted against the bias voltage in Figure 4-21. The extinction ratio of the MZM is about 32 dB while the half-wave voltage is 5 V. It can be seen from the figure that the optimum working point is the null point. However, from further SCM experiments at 25 and 60 GHz, the operating point has been found to be between quadrature and the minimum transmission point, which keeps drifting between 4.8 V to 5.6 V due to thermal fluctuations. At this point, the optical carrier is almost completely suppressed and the first order sidebands (and the data modulated signals) gain maximum power. However, this operating point is not in the linear region of the MZM response and results in distortion due to non-linearities.

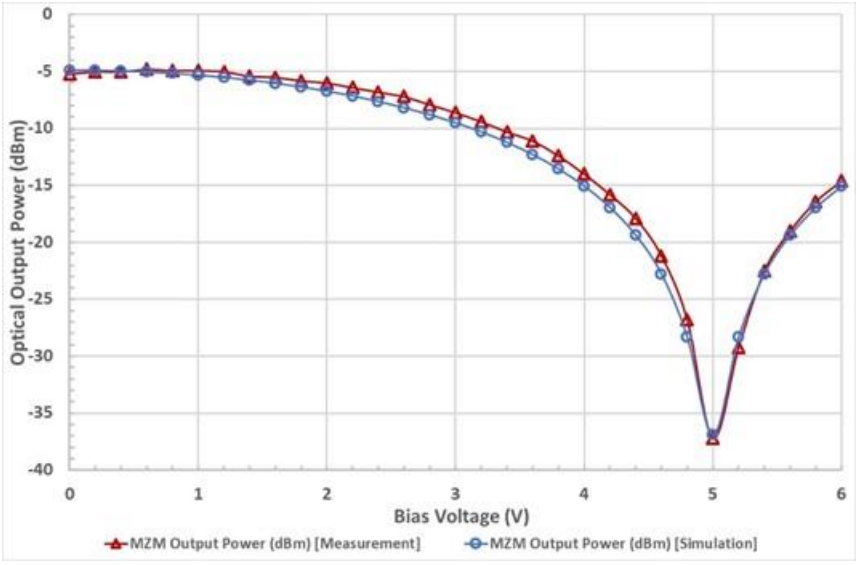

Figure 4-21 MZM optical output power versus bias voltage in experiments and in simulation.

4.5 Simulation Results of Analogue SCM at mmW Frequencies

Following the detailed descriptions of modelling and characterisation of the different devices used in the experimental set-up, simulation results for analogue SCM at 60 GHz are shown in this section. The analogue SCM setups for both 60 GHz and 25 GHz have been modelled in VPI (without wireless transmission). However, only the simulation setup for analogue SCM at 60 GHz is discussed here, as there are only a few differences between the two measurement setups: the RF signal to the PM and choice of phase modulated sideband, down-conversion stages (the 25 GHz setup has one) and amplification (the 60 GHz setup has more, due to the two down-conversion stages). The model is shown in two parts. The CU is presented in Figure 4-22 while the RAU is presented in Figure 4-23.

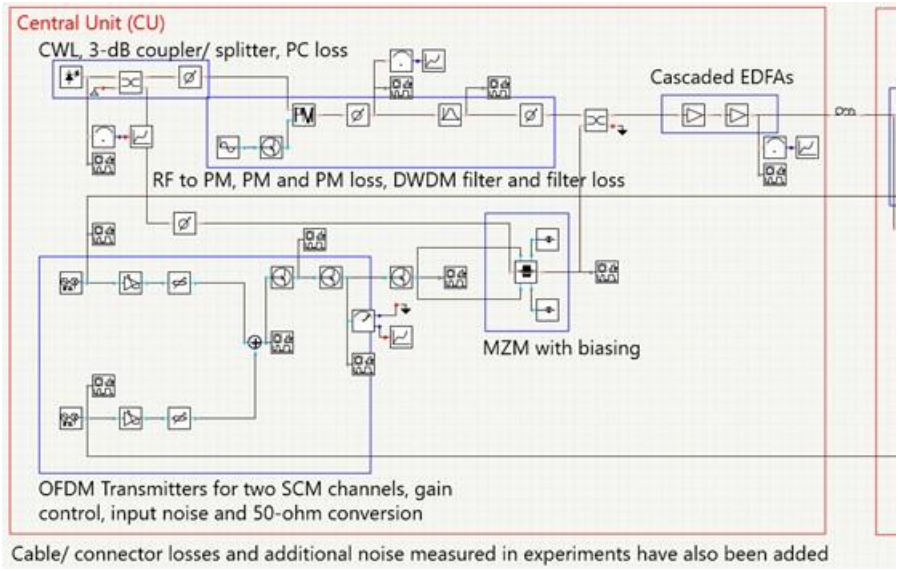

Figure 4-22 Central Unit in VPI (same for both 25 GHz and 60 GHz simulations).

The CU architecture is similar for both 60 GHz and 25 GHz simulations (and measurements). As shown in Figure 4-22, the optical carrier generated by the CWL is split into two parts by an optical 3-dB coupler and additional losses for the PCs (which are very small) have been included as well. OFDM transmitter modules have been used to generate two signals at centre frequencies of 1.9 GHz and 2.5 GHz, which are added in the electrical domain (the resulting spectrum was shown previously in Figure 4-12). Note that for simplicity, two 300 MHz OFDM channels (and not 305 MHz as in the measurements) with 16-QAM subcarrier modulation have been used in these simulations. The modelling of the PM and MZM has already been described in Section 4.4.3.2 and 4.4.3.3 respectively. The two cascaded EDFAs have been modelled using the "*AmpSysOpt*" optical amplifier module, with the "*OutputPowerMax*" parameter of each EDFA adjusted to match the measured power of 0 dBm at the PD input. Parameters such as gain and noise figure for each EDFA have been drawn from the Appendix, Table 9-1.

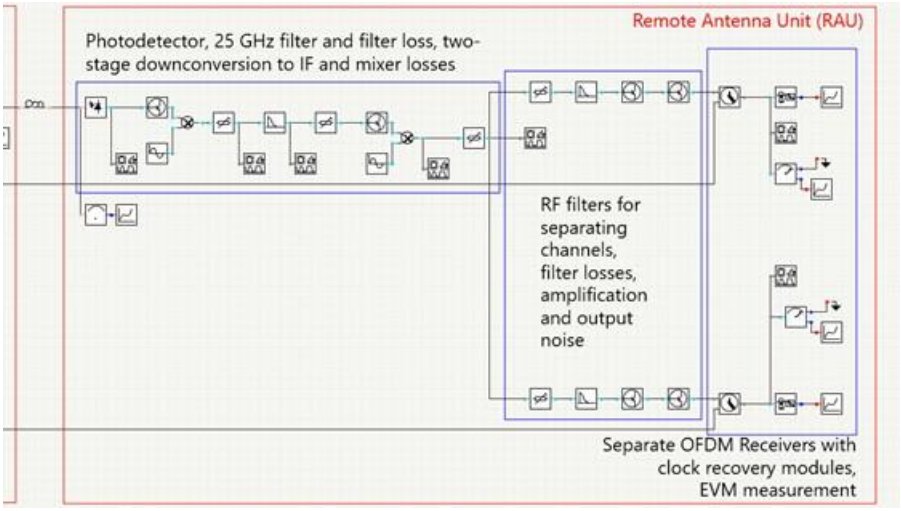

Figure 4-23 Remote Antenna Unit in VPI (60 GHz simulation).

Using the "*UniversalFiberFwd*" module, an optical fibre link with a length of 1 m and attenuation of 0.2 dB/km has been used to model the standard SMF patch-cord used in experiments. At the RAU shown in Figure 4-23, parameters for the two different mmW PDs used in the 60 GHz and 25 GHz measurements have been drawn from the Appendix, Table 9-2. The 25-GHz filter and other RF filters (and their corresponding losses) have been modelled as described in Section 4.4.3.1. The different mixer stages for 60 GHz and 25 GHz simulations (with their different losses at 58 GHz and 23 GHz) have been modelled using standard VPI mixer modules and electrical attenuators. Output noise is added before the two channels are received by their corresponding OFDM receiver modules.

In Figure 4-24, a comparison between measured and simulated EVM performance of the two channels for different MZM bias voltages at 60 GHz has been shown, with a particularly good match obtained at a bias voltage of 5.1 V. At this point, the EVM is 9.4% for Channel 1 and 9.8% for Channel 2, as also shown by the constellation diagrams in Figure 4-25. It has been observed that even though the two channels seem to have slightly different optimum bias points in measurements, they seem to have the same optimum bias point in simulations. Moreover, possibly due to larger inaccuracies in the model of the RF filter used for Channel 2, the difference between experiment and simulation is larger for Channel 2, compared to Channel 1.

For the 25 GHz model, the EVM of Channel 1 is 8.2% while the EVM of Channel 2 is 8.7% (not shown here).

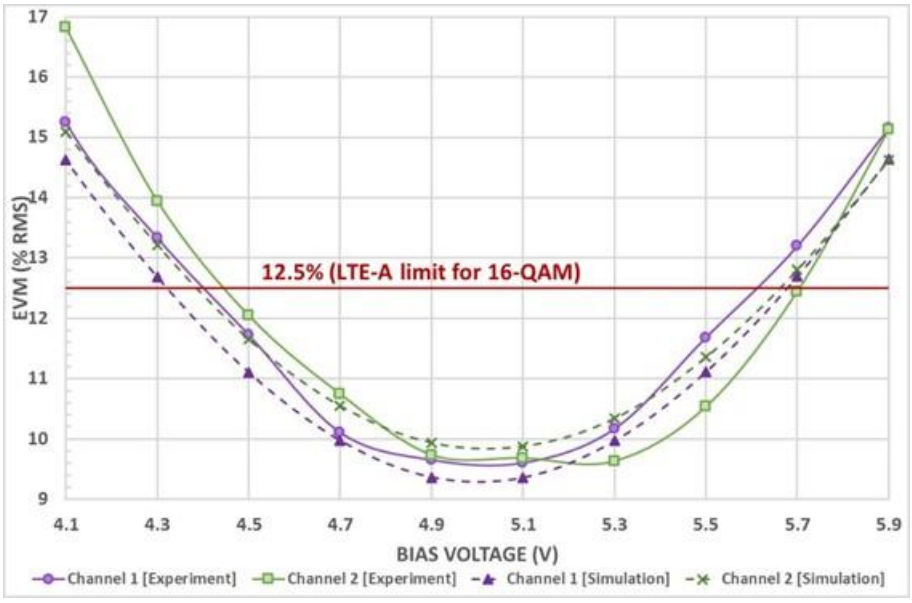

Figure 4-24 Channel 1 and 2 EVM (% RMS) versus MZM bias voltage comparison between 60 GHz experiment and simulation.

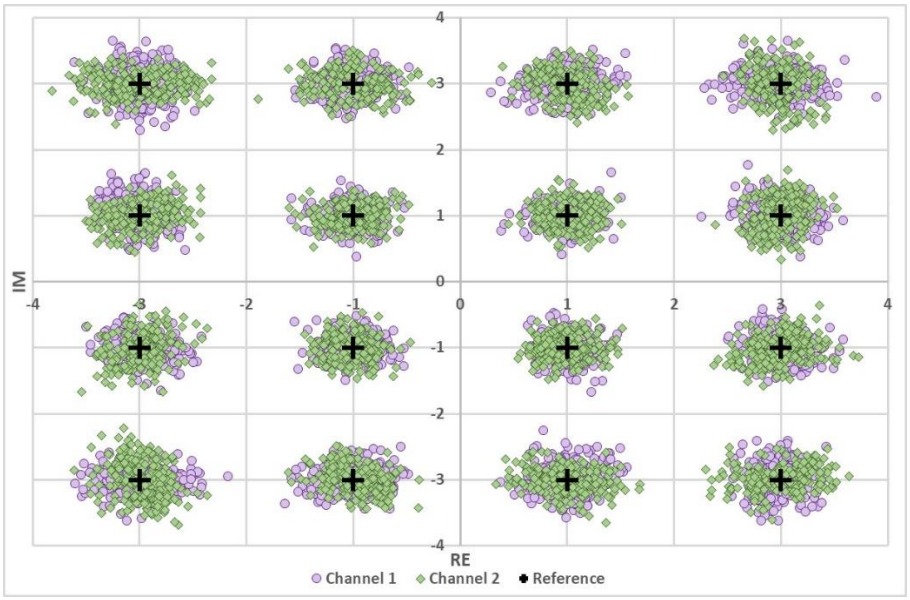

Figure 4-25 Received Constellations for Channel 1 and Channel 2 in 60 GHz simulations for an MZM bias voltage of 5.1 V (EVM: 9.4% and 9.8% respectively).

4.6 Summary and Discussion

Different measurement and simulation results on analogue SCM at RF and mmW frequencies have been discussed in this chapter. Experimental results for back-to-back, direct IM-DD and

external IM-DD at RF with two variable bandwidth SCM channels have been presented. These are followed by experimental results at 60 GHz and 25 GHz with up to four channels for a maximum aggregate data rate of approx. 2 Gbps. The 60 GHz and 25 GHz measurement setups have been modelled in a VPI^{TM} simulator. Components modelled in the simulation environment are verified against experimental component parameters with a good match, allowing the system to be studied in more detail to determine sources of performance limitations.

In order to meet the demands for high data rates and to accommodate multiple services envisaged for 5G communications [1], [170], it is necessary to be able to multiplex a large number of wideband signals in a spectrally efficient manner at the CU and transmit them to the RAU. Moreover, heterogeneous network architectures, where various signal types (for example 5G at mmW frequencies and 5G at RF frequencies and/ or Wireless Local Area Network (WLAN) signals can be jointly transmitted over a fibre fronthaul [132], [171], are also important for the future fronthaul. One of the simplest and most cost-effective ways of achieving both of these targets is to combine SCM with DWDM [142], [172], [173] and Ultra Dense Wavelength Division Multiplexing (UDWDM) [143], [174], [175]. However, it has been shown in this chapter that system complexity increases and component count rises as SCM architectures make the transition from RF to mmW frequencies and when even larger multiplexes need to be transmitted.

Complexity and component count issues are exacerbated with the inclusion of WDM. This is shown in Figure 4-26 in which the 60 GHz architecture (presented in Section 4.3.1) has been extended to accommodate more signals from different Radio Access Technologies (RATs) [176], [4], [15] using an SCM-DWDM approach. This architecture was presented in the Radio technologies for 5G using Advanced Photonic Infrastructure for Dense User Environments (RAPID) D423 deliverable [177].

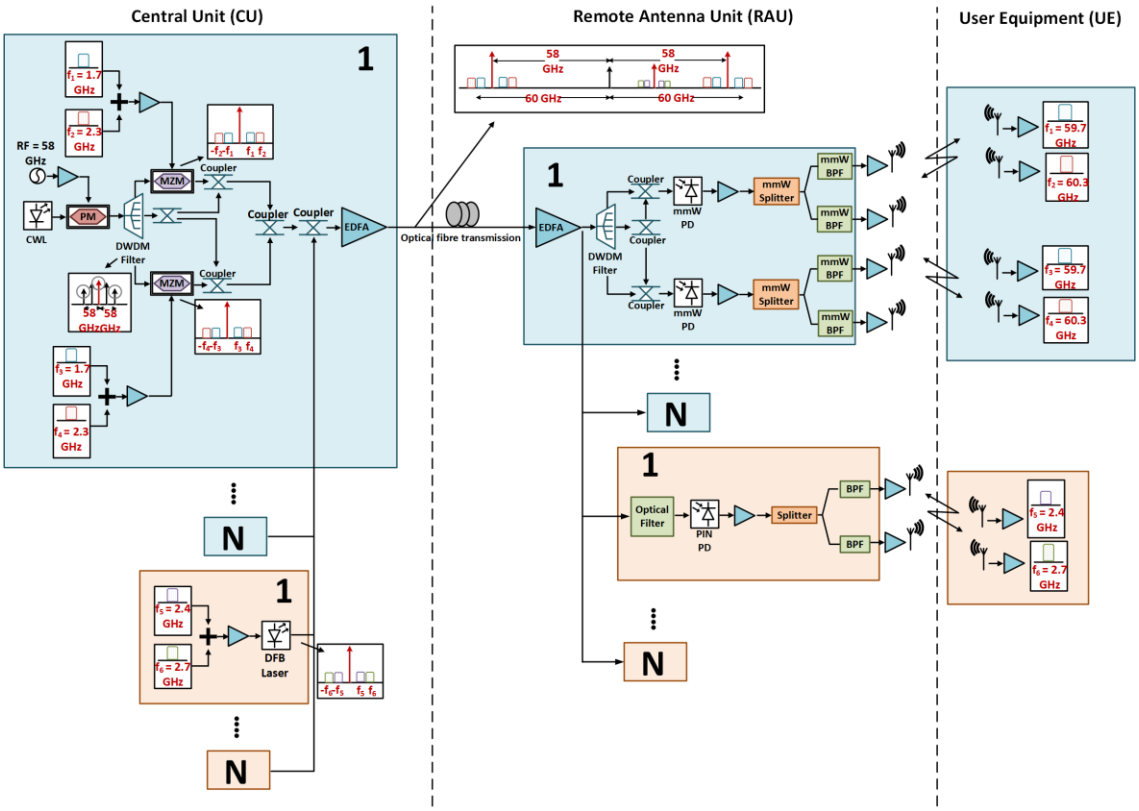

Figure 4-26 Heterogeneous architecture for transmitting mmW and WLAN signals using analogue SCM combined with DWDM.

As shown in the figure, at the CU, two phase modulated sidebands 58 GHz away from the optical carrier are data modulated with SCM signals in a dual wavelength modulation scheme [23]. These are combined with SCM WLAN signals modulating a DFB laser and transmitted across a single optical fibre link. In this architecture, there are *N* blocks of the setup for channels at mmW frequencies and *N* more blocks for channels at RF/ microwave frequencies. As SCM is used, the number of channels is much greater than *N* (for the mmW or microwave blocks) and channels at the same frequency can be destined for the same antenna array (e.g. the channels at 59.7 GHz or those at 2.4 GHz).

At the RAU, the 60 GHz signals are de-multiplexed using another DWDM filter or Arrayed Waveguide Gratings (AWG) while the WLAN signals are separated from the multiplex using an optical filter. After the mmW and WLAN signals are detected by their respective photodetectors, each of the SCM channels are de-multiplexed with the use of splitters and band-pass filters. The 60 GHz and WLAN signals are transmitted wirelessly and received by the User Equipment (UE), either via the use of standard antennas or leaky wave antennas in a Co-ordinated Multipoint (CoMP) scheme [178]. As shown in the figure, in order to accommodate more signals, the

architecture can be extended further but this also means that more optical sources will be required. More channels can be accommodated via SCM but this would mean that more RF power splitters and filters will be required, which are quite expensive at mmW frequencies. Moreover, simulation results of this system (not presented here), have shown the need for higher amplification in the optical and electrical domain and that preferably higher optical input power will be required as well in order to achieve acceptable EVM performance.

A novel concept of an SCM-UDWDM scheme, which was presented in the RAPID D221 deliverable [179] is shown in Figure 4-27 (includes both downlink and uplink transmission). Two different techniques of multiplexing wavelengths using UDWDM techniques incorporating 10 GHz channel spacing have been shown in this figure. The CU is quite similar to the one shown in Figure 4-26, although a flat, closely-spaced frequency comb will be beneficial in this case for mmW carrier generation and may be produced using a comb generation technique [143], [149], [107], [180].

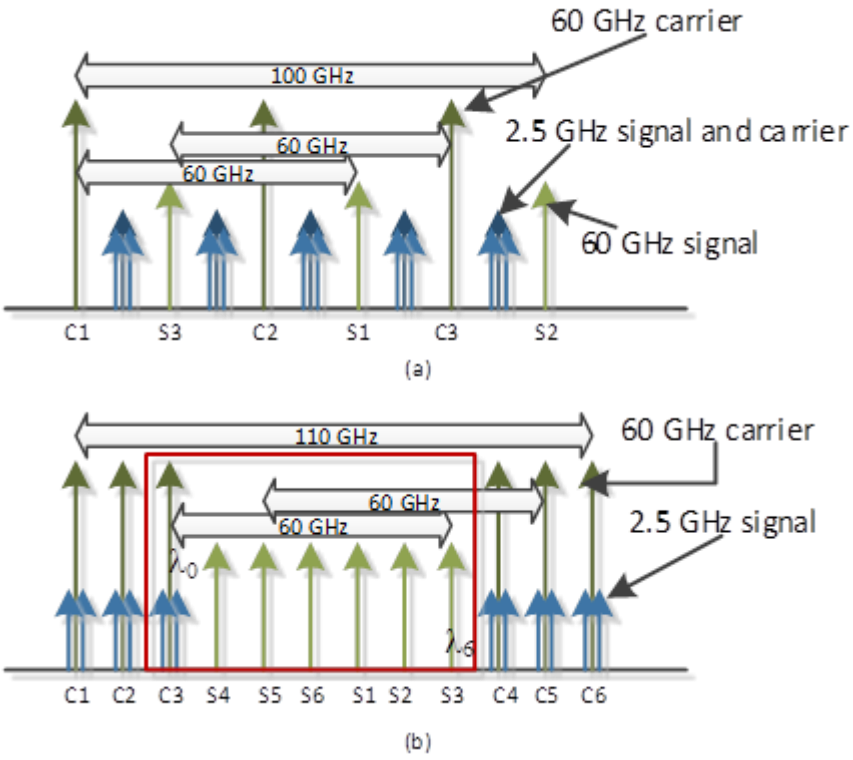

Figure 4-27 Wavelength interleaving for Ultra Dense Wavelength Division Multiplexing (UDWDM).

Figure 4-27 (a) shows a wavelength interleaving technique in which three 60 GHz signals and five 2.5 GHz signals fit within 100 GHz. Channel *S1* (light green arrow) corresponds to the carrier *C1* (dark green arrow) to produce a 60 GHz signal while the smaller arrows in the middle correspond to the 2.5 GHz signals (dark blue for carrier and light blue for sidebands). Similarly, Channel *S2* corresponds to *C2* and so on. Figure 4-27 (b) shows another technique in which 6 mm-wave signals and 6 microwave signals fit within 110 GHz. Again, *C1* corresponds to *S1*, *C2* to *S2* and so on. The signals are spaced at 10 GHz and the frequency of the laser corresponds to the frequency of *S6*. The frequency plan shown in Figure 4-27 (b) is the more bandwidth efficient one among the two, thus, the diagrams that follow are based on Figure 4-27 (b).

Figure 4-28 shows the receiver side of the setup. The combined signals are sent over fiber, to the receiver side (the RAU). Here, the de-multiplexer filters out each wavelength. λ_0 is passed to a 3-dB splitter. The signal from the upper arm is sent to a low speed photodiode to detect the 2.5 GHz microwave signal. The signal from the lower arm is filtered to obtain the carrier and sent to a coupler, along with λ_6. A mm-wave photodiode is then used to detect the 60 GHz signal.

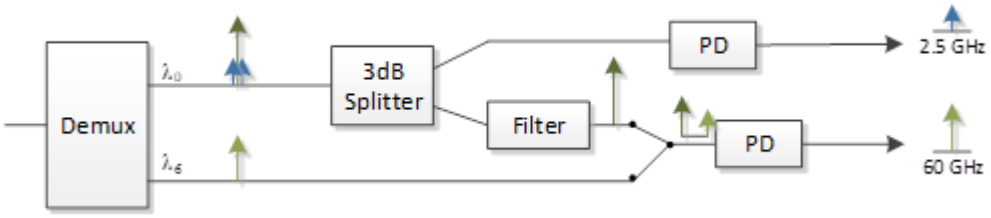

Figure 4-28 Receiver side of UDWDM setup.

Figure 4-29 shows the receiver side of the setup in greater detail for the downlink direction, as well as the setup for the uplink direction. The multiplexed signals (as shown at top left of the figure) are applied to the input of Circulator *A*. The circulator in combination with a Fibre Bragg Grating FBG1 drops λ_0 with the data, which gets passed on to the 3-dB power splitter (Power Splitter1). The signal on the left arm of the splitter is the 2.5 GHz RF data signal, which is detected by a photodiode (PD_1), amplified and radiated from an antenna to mobile units as a 2.5 GHz wireless signal. The signal from the other arm goes to *Circulator F*, from where λ_0 without the data gets reflected by FBG3 and is passed on to the input of the 3-port power splitter. All 3 output ports have the same signal (λ_0 without the data) and the signal from the first arm goes to Power Combiner 3, which receives the wavelength λ_6 (with data) on its other arm. The

combined signal is detected by PD_2, amplified and radiated from the antenna as a 60-GHz wireless signal. Both of these processes are for the downlink and have already been shown in Figure 4-28.

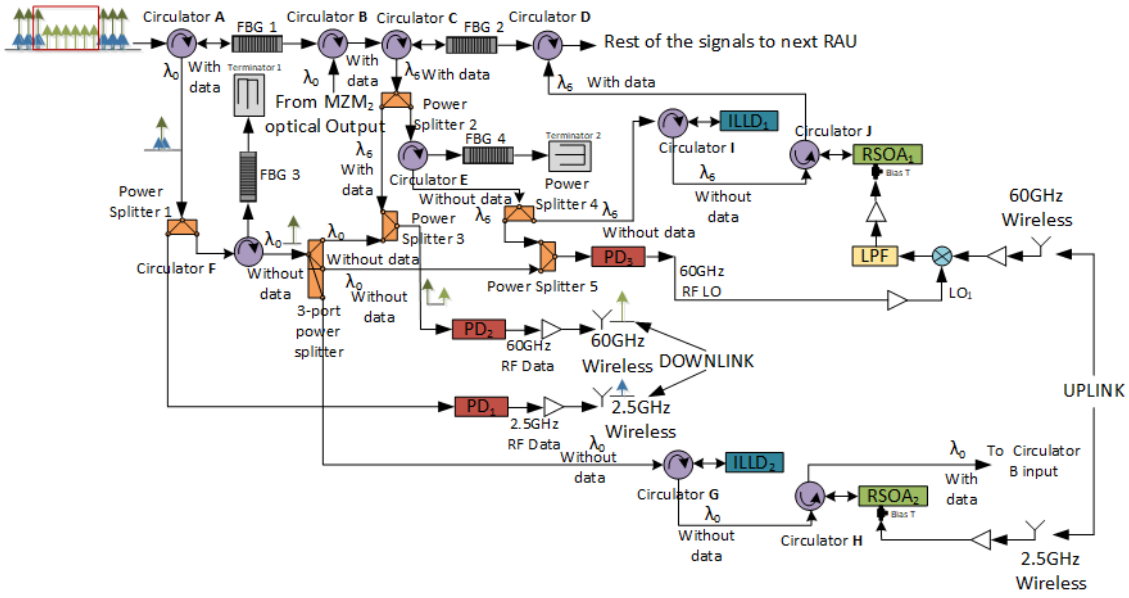

Figure 4-29 Downlink and Uplink of UDWDM setup.

The λ_0 without data signal from the third output of the 3-port power splitter is passed on to the input of Circulator G. From there, it goes to the Injection-Locked Semiconductor Laser Diode ($ILLD_2$), which locks on to the wavelength and the λ_0 without data signal is dropped to the input of Circulator H. This signal is then modulated by the 2.5 GHz wireless uplink signal from the Reflective Semiconductor Optical Amplifier ($RSOA_2$), producing λ_0 with data (the RSOAs are biased using a Bias-T, which combine the radio frequency signal with the DC bias). This is then sent to the input of Circulator B, which is already receiving all the wavelengths other than λ_0 with data from Circulator A. As there is no FBG between B and C to reflect any wavelengths, all the signals get passed on to Circulator C. λ_6 with data gets reflected by FBG2 and dropped to Power Splitter 2, while the rest of the signals get passed on to Circulator D and onto other RAUs in the topology. The λ_6 with data signal on the left arm of Power Combiner 3 is used in the downlink while the signal on the right arm goes to Circulator E. The without data λ_6 signal is reflected back from FBG4 and sent to Power Splitter 4. The signal on the left arm goes to the first input of Power Combiner 5 which is receiving the without data λ_0 signal at its second input from the middle arm of the 3-port power splitter. The signals get combined and are detected by

PD_3 as a 60-GHz RF LO signal. This is then amplified and sent to the mixer marked LO_1, to down-convert the 60-GHz uplink wireless signal. The Low Pass Filter (LPF) is used to obtain the down-converted 60-GHz baseband signal and this is then amplified and sent to $RSOA_1$, which performs data modulation with the λ_6 without data signal received from Circulator J. This circulator receives the λ_6 without data signal at its input after it is dropped by Circulator I. Finally, the λ_6 signal with data is sent to Circulator D.

An important advantage of this setup is that the 60-GHz optical reference signal can be transported from the CU to the RAU and reused in the uplink, instead of using an expensive 60-GHz LO or a tuneable laser source at the RAU. The use of the RSOAs and injection-locked lasers solves the problems of wavelength tune-ability and carrier extraction. One of the issues with this setup is the narrow band filtering necessary at FBG 4 which may be costly to implement and the stability of optical filters may be a cause for concern as well. The other issue is the use of several 3-dB splitters and combiners, which results in considerable power loss at each stage and requires proper planning regarding amplification at several stages.

Both the architectures discussed in this section are capable of transmitting a very large number of channels in a spectrally efficient manner, achieving very high data rates. However, as already discussed in Chapter 3, analogue systems suffer from non-linear distortion and techniques such as SCM are affected by fibre dispersion leading to low subcarrier power and low SNR. Moreover, channels in an analogue SCM technique cannot be placed very close to each other as this leads to inter-channel interference. This also means that there is limited flexibility, e.g. if the characteristics of the multiplexes change (channel bandwidth, number of channels etc.), filter characteristics have to be changed as well. Lastly, using such analogue SCM architectures in mMIMO applications will require multiple LOs and mixers at the RAU (one up-converter stage per antenna element for full-digital mMIMO or fewer per antenna array for hybrid mMIMO) in order to shift each channel to the same frequency. As a result, the overall cost and complexity of such architectures can be very high. Techniques such as the one reported in [33] can be used to slightly reduce the number of LOs required at the RAU. However, there is still a very small reduction in the overall complexity of the architecture.

With these issues in mind, the following chapter introduces an alternative technique for very flexible multiplexing of a large number of signals in the digital domain.

5 System Design of an Analogue Subcarrier Multiplexed Mobile Fronthaul with Digital Processing

5.1 Introduction

The aim of the work presented in this chapter is to describe a novel digital SCM approach that allows multiple channels using different modulation formats and numerologies to be subcarrier multiplexed at the DU (e.g. 5G eMBB mm-Wave and sub-6 GHz 5G/ Wi-Fi/ LTE signals). The approach reduces or entirely removes analogue domain processing. By employing appropriate channel mapping into available NZs and using band-pass sampling techniques [77], [19], [181], corresponding signals across NZs can be down-converted using a common down-sampling factor to the same IF. As a result, the channels can be readily up-converted to their respective RF/mmW frequencies. This feature of the proposed technique will be beneficial as part of a mMIMO or heterogeneous networking applications, with different radio-access technologies (RATs) at the RRU, or part of a system that is a mixture of both. A single IFFT stage is used to aid the mapping and to seamlessly aggregate both DMT - and SSB - derived channels with varying channel bandwidths and numerologies.

To relax sampling rate and analogue bandwidth requirements of RAU ADCs, a bandwidth extension device is employed at the RRU.

The main concepts of the proposed technique and an overview of its different aspects, which aim to solve many of the issues with analogue SCM (which were discussed in Chapter 4), are discussed in the following sections. Section 5.2 discusses how DMT and SSB-derived channels can be multiplexed seamlessly at the transmitter using single IFFT processing. Section 5.3 discusses how these multiplexes can be created using hierarchical NZ mapping. In addition to that, sampling rate and analogue bandwidth requirements of the ADCs in the receiver can be relaxed via the proposed use of bandwidth extension devices such as Track-and-Hold Amplifiers (THAs) [182], [183], [32]. The incorporation of this type of device, fits well within the mapping technique by extending the mapping to a mapping hierarchy and with only minimal analogue domain processing that does not affect the flexibility of the SCM approach. With the aim of efficient multiplexing and de-multiplexing of very large numbers of channels, “Sub-Multiplexes”, “Multiplexes” and “Super-Multiplexes” are created, utilising the available capacity of the link by

providing very high spectral efficiencies and flexible placement of the multiplexes in the frequency domain. This, in relation to the transmitter and receiver design, is discussed in Section 5.4. This is followed by the summary and conclusions of the chapter in Section 5.5.

5.2 Subcarrier Multiplexing using DMT and SSB Modulation

Figure 5-1 is an illustration of the technique of single large IFFT processing that would take place at the transmitter side, where there is a seamless combination of DMT and SSB-derived channels to create an arbitrary size multiplex. Note that large IFFTs are currently used by wireline standards such as DVB-T2 [187].

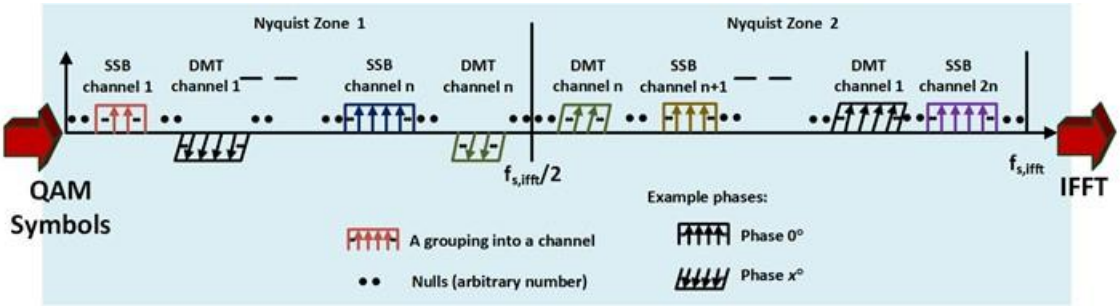

Figure 5-1 Seamless combination of DMT and SSB-derived channels for creating a multiplex using single IFFT processing at the transmitter.

As shown in the figure, the IFFT employs a sampling rate of $f_{s,ifft}$. Contiguous groups of modulation mapping-derived (e.g. QAM, QPSK, BPSK etc.) frequency domain samples are contiguously organised to form individual channels, which are separated by arbitrary numbers of null samples (i.e. frequency guard bands) to facilitate digital filtering at the receiver side. The channels are distributed in both NZs (each with a size of $f_{s,ifft}/2$) such that they are symmetric in their number of frequency domain samples across the two zones. The DMT-derived channels are created such that corresponding channels in the two NZs are conjugate symmetric, resulting in a maximum total number of n DMT channels (real). On the other hand, the corresponding groupings in the two NZs are not conjugate symmetric for the SSB-derived channels (meaning that the signals in the first and second NZs are independent of each other), leading to a maximum total number of $2n$ SSB-derived channels (complex). In this technique, analogue or

digital domain filters (for removing sidebands) or Hilbert transforms (for creating SSB signals) are not required.

To summarise, if there are multiplexed channels distributed in the positive and negative parts of the spectrum (the two NZs) and *n* is the number of multiplexed channels in the positive part of the spectrum, the maximum number of DMT channels is

$$N_{DMT} = n \; for \; n \in \mathbb{N}^{+}, \tag{5-1}$$

while the maximum number of SSB channels is

$$N_{SSB} = 2n \; for \; n \in \mathbb{N}^{+}. \tag{5-2}$$

In Figure 5-1, DMT Channel 1, SSB Channel *n* and SSB Channel 2*n* have a larger grouping of frequency domain samples compared to SSB Channel 1 and DMT Channel *n*. This means that each channel can be a grouping of a different number of frequency domain samples giving rise to a different bandwidth. However, since single IFFT processing is applied, the spacing between adjacent frequency samples (bin size) is the same. In addition, any possible combination and/ or placement of SSB- and DMT-derived channels can be employed (in this case, they are shown as interleaved). Finally, to simplify the description, a common phase for all the frequency domain samples (that make up each channel) is assumed. In reality, each sample will have its own phase as determined by the modulation mapping (real or complex) and the relative amplitudes of the In-phase and Quadrature components that make up each sample.

5.3 Hierarchical Nyquist Zone Mapping

For channels such as those shown in Figure 5-1, the mapping technique, illustrating possible mappings of channels into NZs, is shown in Figure 5-2. For ease of explanation, the number of frequency domain samples per channel is kept the same in this figure (i.e. all channels have the same bandwidth) and in all other figures/ examples in this section. The sampling rate of the ADC in this example is larger or equal to the sampling rate of the IFFT at the transmitter side but this need not be the case (this case will be discussed later in Section 5.4.5).

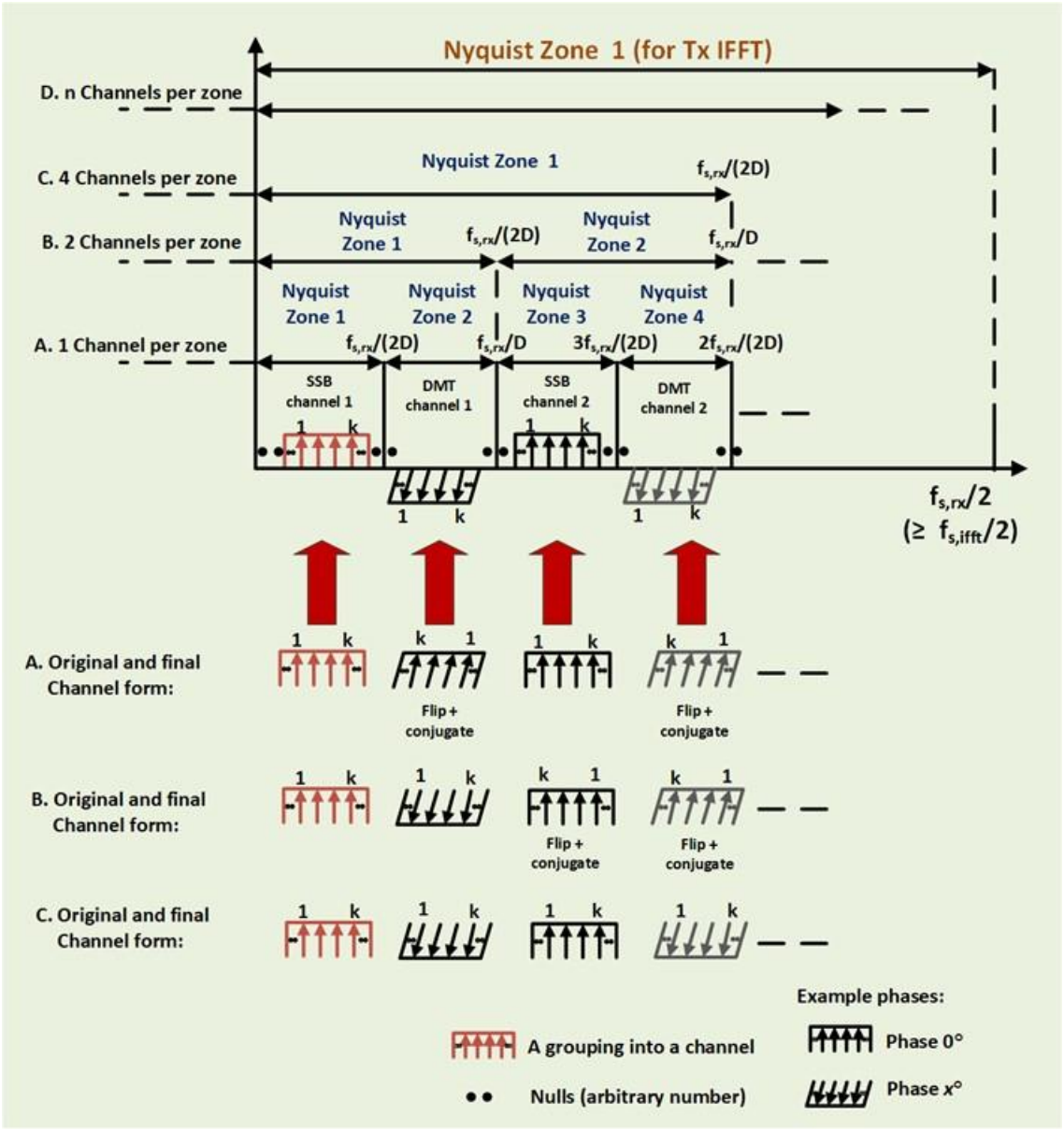

Figure 5-2 Examples of arbitrary NZ mapping of individual or multiple channels and manipulation of signals to minimize processing at the receiver.

Assuming $f_{s,rx}$ is the sampling rate of the ADC at the RRU (as shown in Figure 5-2),

$$f_{s,rx} \geq f_{s,ifft}. \tag{5-3}$$

When down-sampling is applied, the final sampling rate used at the receiver is

$$f_{s,final} = \frac{f_{s,rx}}{D} \text{for } D \in \mathbb{N}^+, \tag{5-4}$$

where *D* is the down-sampling factor. The choice of *D* depends on the number of channels within each multiplex. As a result of down-sampling

$$f_{s,final} \leq f_{s,ifft}, \tag{5-5}$$

and NZs are created with mirror images around every multiple of $f_{s,final}/2$ ($f_{s,final}/2$, $f_{s,final}$, $3f_{s,final}/2$ and so on). This means that the frequency spectrum is divided into a (theoretically) infinite number of NZs. The bandwidth of each NZ is given by

$$f_{bw,NZ} = \frac{f_{s,rx}}{2D} \text{for } D \in \mathbb{N}^{+}. \tag{5-6}$$

This can also be expressed as

$$f_{bw,NZ} = \frac{f_{s,final}}{2}. \tag{5-7}$$

Based on $f_{s,rx}$ and *D* at the receiver, channels can be grouped such that there is one channel per NZ or multiple channels per NZ, provided that the total bandwidth occupied by these channels is smaller than $f_{bw,NZ}$ (i.e. the Nyquist criterion is met). Considering only the number, *n*, of channels in the positive part of the spectrum, if *m* is the number of channels in each NZ, the number of NZs (as derived by the down-sampling process at the receiver) is given by

$$Z = \frac{n}{m} \quad \text{for } n, m \in \mathbb{N}^{+} \& \, m \leq n \ . \tag{5-8}$$

Therefore,

$$D = Z \; for \; Z \in \mathbb{N}^{+} \ . \tag{5-9}$$

Individual or multiple groups of channels that are pre-calculated to fall in even NZs are pre-processed at the transmitter so that the amount of processing required at the receiver is reduced. The pre-processing stage involves the conjugation and frequency flipping of each channel, a process that is reversed at the receiver side following the down-sampling process. This way, the channels are obtained back in their original form at the receiver.

As shown in the figure, the first NZ resulting from the original IFFT stage sampling rate at the transmitter side ($f_{s,ifft}$) has been annotated for reference at the top of the figure. For Case A, there are four channels with one channel per NZ, i.e. *m = 1*. Out of these four channels, DMT channel 1 and 2 are in even NZs and are pre-processed (conjugated and frequency domain flipped) while SSB channels 1 and 2 are not. Case B shows two channels per NZ (*m = 2*) such that DMT channel 1 and SSB channel 1 are not pre-processed while DMT channel 2 and SSB channel

2 are. Case C shows four channels per NZ (*m = 4*), with none of the channels pre-processed (the next four channels which are not shown would be pre-processed). Case D is for *n* channels per NZ (*m = n*).

5.3.1 Signal Processing at the Receiver Side

The process of filtering/ de-multiplexing the NZ mapped channels at the receiver is illustrated in Figure 5-3. Once the multiplex is digitised at the receiver via an ADC stage, individual or groups of channels are filtered digitally. When more than one channel is mapped within a NZ, a second filtering stage is required after the down-sampling stage to “select” individual channels within the NZs. At the second stage, the digital filters can be low-pass, band-pass or high-pass depending on the location of channels and channels groups within each NZ.

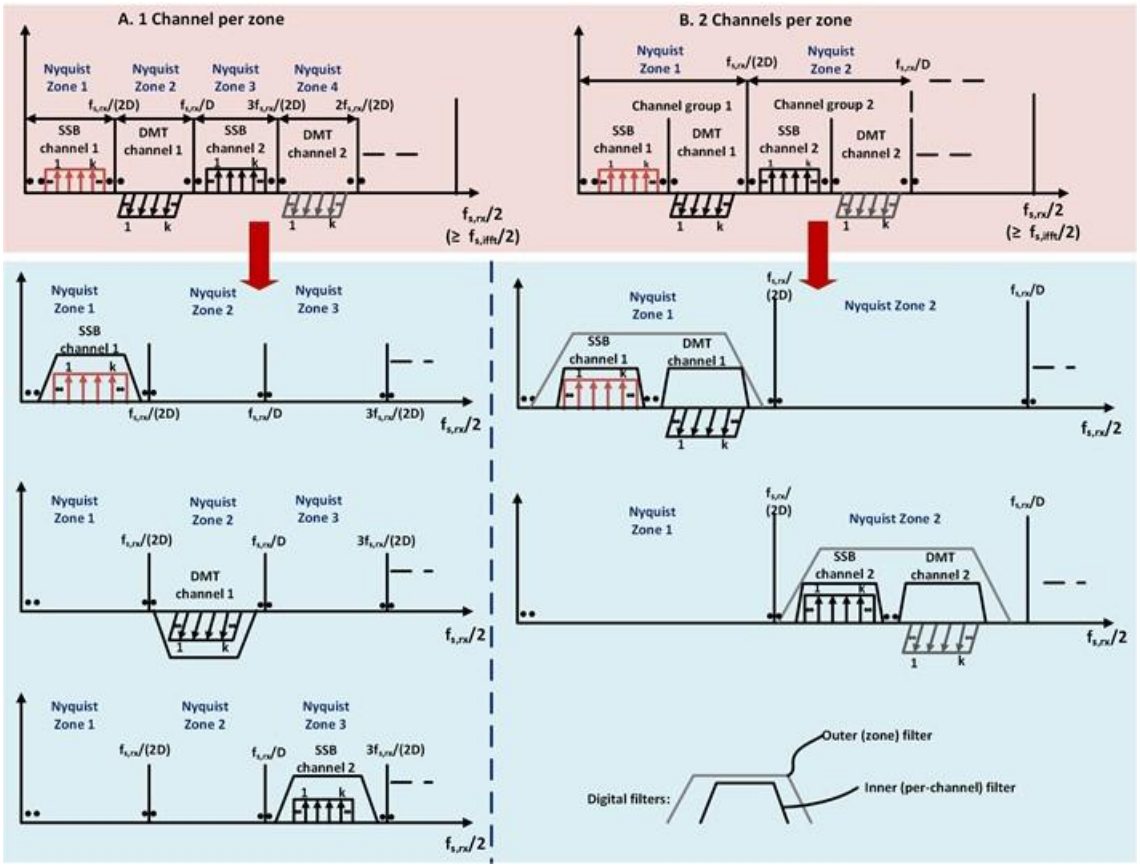

Figure 5-3 Filtering/ de-multiplexing of an individual or group of channels at the receiver side.

Following on from Cases A and B of Figure 5-2, examples of two different mappings are shown in Figure 5-3. For one channel per NZ (Case A), the filter selects the one channel while for two channels per NZ (Case B), the filter selects both channels. For *n* channels per NZ, the filter selects *n* channels.

Due to the mapping technique employed at the transmitter (described in Figure 5-2), each channel or channel group can now be down-sampled using a single down-sampling factor *D*. As explained previously, this process results in the creation of multiple NZs with a size of $f_{bw,NZ}$. Each channel or channel group can be obtained at the same IF (or at baseband) in the first NZ and conjugate symmetric copies of the same channel/s are created in each NZ around the NZ boundary (shown using dashed line annotations). It should be noted that due to the transmitter side pre-processing carried out on the channels in even NZs, the channels are obtained in the first NZ in their original form upon down-sampling. An illustration of the down-sampling technique for Cases A and B is shown in Figure 5-4.

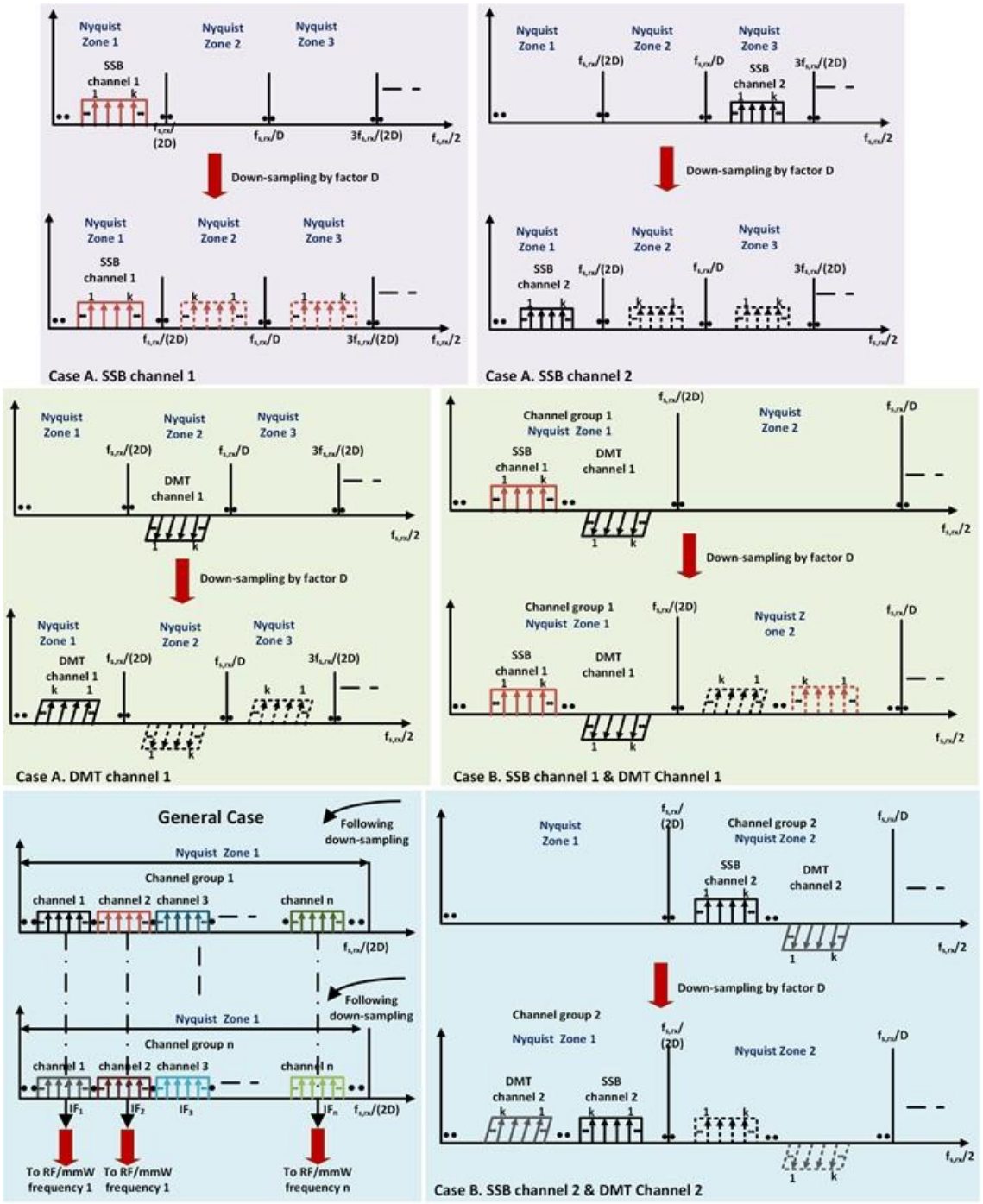

Figure 5-4 Down-sampling individual or multiple channels to the same IF at the receiver side.

For Case A in the first (top) part of the figure, SSB channel 1 is located in the first NZ when down-sampled and conjugate symmetric copies of the channel are created in all NZs. For SSB channel 2, which is in the third NZ, copies of the channel are created in the first and consecutive NZs. In the second (middle) part of the figure (for the same case), DMT channel 1 is in the second NZ

(even zone) and has thus been pre-processed. As a result of the down-sampling process, the copy of the channel created in the first NZ is obtained in the correct form.

For Case B shown in the second part of Figure 5-4, SSB channel 1 and DMT channel 1 are located in the first NZ and the down-sampling process creates copies of these channels in all NZs. For the same case at the bottom-right of the figure, SSB channel 2 and DMT channel 2 are in the second NZ are thus pre-processed. The channels are obtained in the first NZ in the correct form upon down-sampling.

This way, using systematic NZ mapping to create a multiplex, all channels and /or channel groups can be down-sampled to the same IF (or at baseband). For groups of channels shown in the General Case at the bottom-left of Figure 5-4, individual channels within a group will be in different IFs following the down-sampling process. Using a single/ common LO signal, these channels and their corresponding counterparts (originally mapped to other NZs) can then be readily up-converted to the same RF/ mmW frequency. This will be the case for all channels destined to the same RF/ mmW frequency but different from the RF/ mmW frequency that the other channels in the group are destined to, facilitating multi-RAT or heterogeneous networking. However, it has to be noted that any distribution of channels into RF/ mmW frequencies can be employed, irrespective of their relative positions within NZs. Lastly, other than DACs and quadrature mixers, minimal per-channel processing will be required using this technique (analogue/ digital up/ down-converters, filters etc. will not be required).

Summary

Figure 5-5 provides an overview of the processes of multiplexing and de-multiplexing at the transmitter and receiver, effectively summarising the concepts discussed so far in this chapter. As an example, a multiplex consisting of three channels per NZ is shown, destined for three different RF/ mmW bands. Channels of different bandwidths are multiplexed at the transmitter via a single IFFT operation with a sampling rate of $f_{s,ifft}$, such that two NZs (as derived by the IFFT process) of length $f_{s,ifft}$ /2 are created. At the receiver, the multiplex is sampled using a sampling rate of $f_{s,rx}$, which is smaller than or equal to $f_{s,ifft}$. The channels have been arranged at the transmitter such that when groups of three channels are digitally filtered at the receiver and band-pass sampled (or down-sampled) using a common sampling rate of $f_{s,rx}/D$, mirror images of these channels are created around every multiple of $f_{s,rx}/2D$ (the NZ size as derived by the receiver), including an image within the first NZ. Considering the 9 channels shown in the figure, following the band-pass sampling operation, channels 1, 6 and 7 will be at the same IF in the

first NZ while channels 3, 4 and 9 will also be at the same IF, albeit at a different one. Upon filtering, channels 1, 6 and 7 can be readily up-converted to the RF/ mmW band 1 while channels 3, 4 and 9 can be up-converted to RF/ mmW band 3.

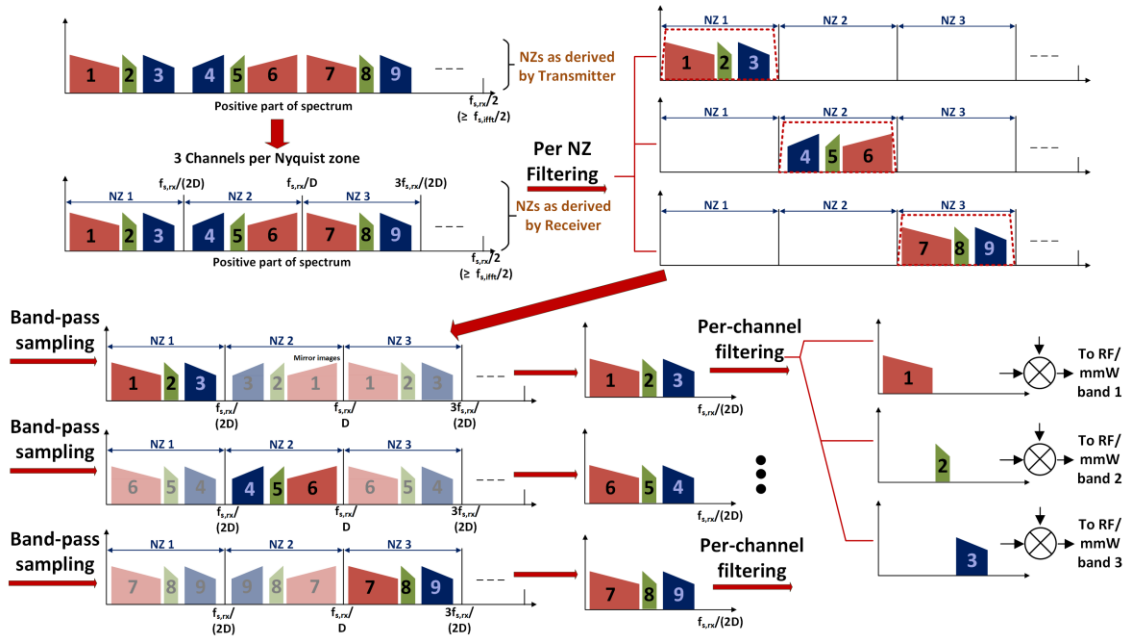

Figure 5-5 Summary of the concepts of (de-)mapping and (de-)multiplexing at the transmitter and receiver, as discussed so far.

5.3.2 Using a Bandwidth Extension Device

The techniques described in Section 5.3.1 will accommodate low cost and low sampling rate ADCs in the receiver side only if the bandwidth occupied by the multiplex is small enough to be within the analogue bandwidth specifications of the ADC. This means that there is limited flexibility in terms of the size of the multiplex and the original IF placement of the multiplex at the transmitter, such that, the highest frequency component of the multiplex exceeds the analogue bandwidth (passband) specification of the ADC at the receiver.

Figure 5-6 shows a technique using a bandwidth extension device that allows arbitrary size multiplexes placed at a high IF to be received, by frequency translating the entire multiplex to a lower IF using an intermediate down-sampling factor of D', such that

$$D' \leq D. \tag{5-10}$$

As a result, the multiplex is now within the analogue bandwidth (passband) specification of the ADC and can be received (quantized) and processed further. In this example (unlike the one described next, in Figure 5-7), the aggregate bandwidth of the multiplex is within the ADC sampling rate specifications, that is

$$f_{s,inter} \geq f_{s,rx}, \tag{5-11}$$

where $f_{s,inter}$, is the intermediate down-sampling rate, given by

$$f_{s,inter} = \frac{f'_{s,rx}}{D'}. \tag{5-12}$$

Here $f'_{s,rx}$ is the sampling rate of the bandwidth-extension device. Again, as shown previously in Figure 5-2, the signals that are mapped into even NZs based on $f'_{s,rx}$, are pre-processed (conjugated and frequency flipped). Only now, whole signal blocks are pre-processed according to their placement in even or odd bandwidth-extension device-derived NZs.

This concept will be further generalised in Section 5.4 in the context of a hierarchical technique of mappings and the creation of Super-Multiplexes.

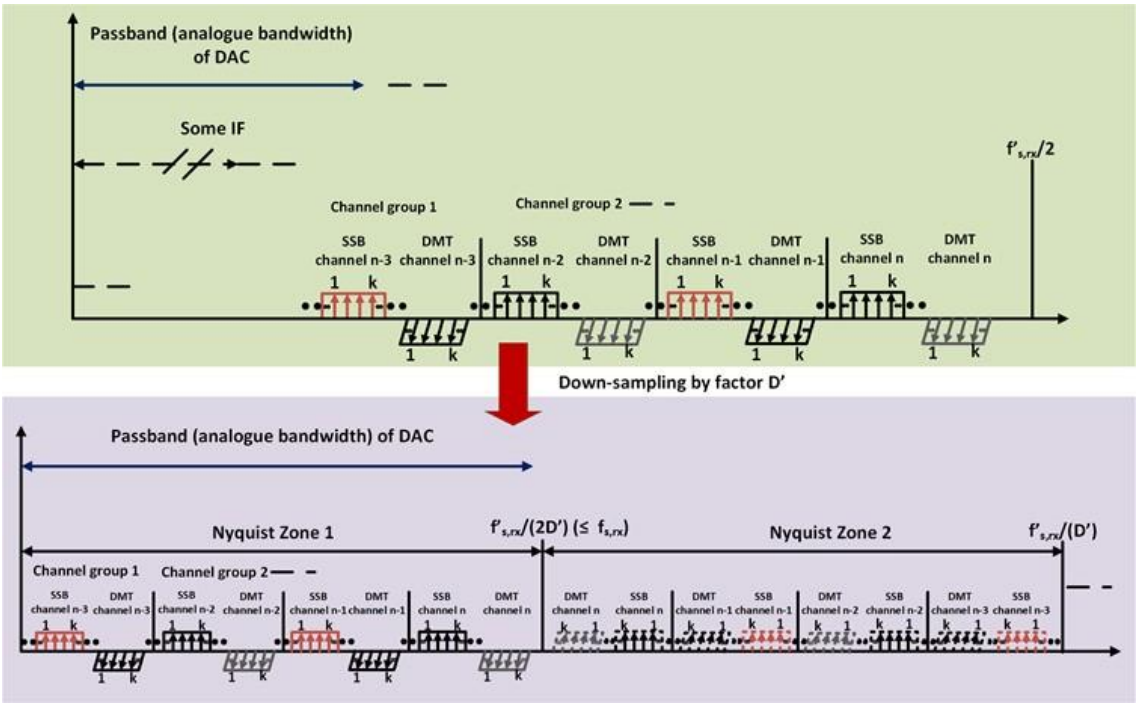

Figure 5-6 Using a bandwidth-extension device with multiplex placed at an arbitrary IF which exceeds the analogue bandwidth specification of the ADC at the receiver.

The concept described in Figure 5-6 is extended in Figure 5-7 to that of arbitrary size multiplexes with an aggregate bandwidth that exceeds the analogue bandwidth and sampling rate specification of the ADC stage at the receiver. As shown in the figure, arbitrary size channel groupings (termed "channel super-groups") are now first mapped into first-order NZs with a size

$$f'_{bw,NZ} = \frac{f'_{s,rx}}{2D'} \text{for } D' \in \mathbb{N}^+ \ , \tag{5-13}$$

where $f'_{bw,NZ}$ is half of the intermediate sampling rate and can also be expressed as

$$f'_{bw,NZ} = \frac{f_{s,inter}}{2} \ . \tag{5-14}$$

At the receiver, these groupings are filtered/de-multiplexed using analogue filters. The individual groupings are then down-sampled by an intermediate factor of *D'* by the bandwidth-extension device. This way, the channels are discretised and down-sampled down to the same IF is shown in Figure 5-7. The number of filters will depend on the number of groupings mapped into these NZs, while the size of these groupings will depend on the second-order NZs, as derived from the ADC sampling rate ($f'_{s,rx}$). However, for practical applications (number of mMIMO antennas and commercially available ADCs) their number will be limited. Once these channel groups are filtered and down-sampled to the same IF and within the analogue passband of the second ADC stage, each channel within these groups will be down-sampled to the same lower IF via the processes described in Figure 5-2 to Figure 5-4.

This concept is generalised further to the context of a hierarchical technique of mappings and the creation of Super-Multiplexes in Section 5.4.5.

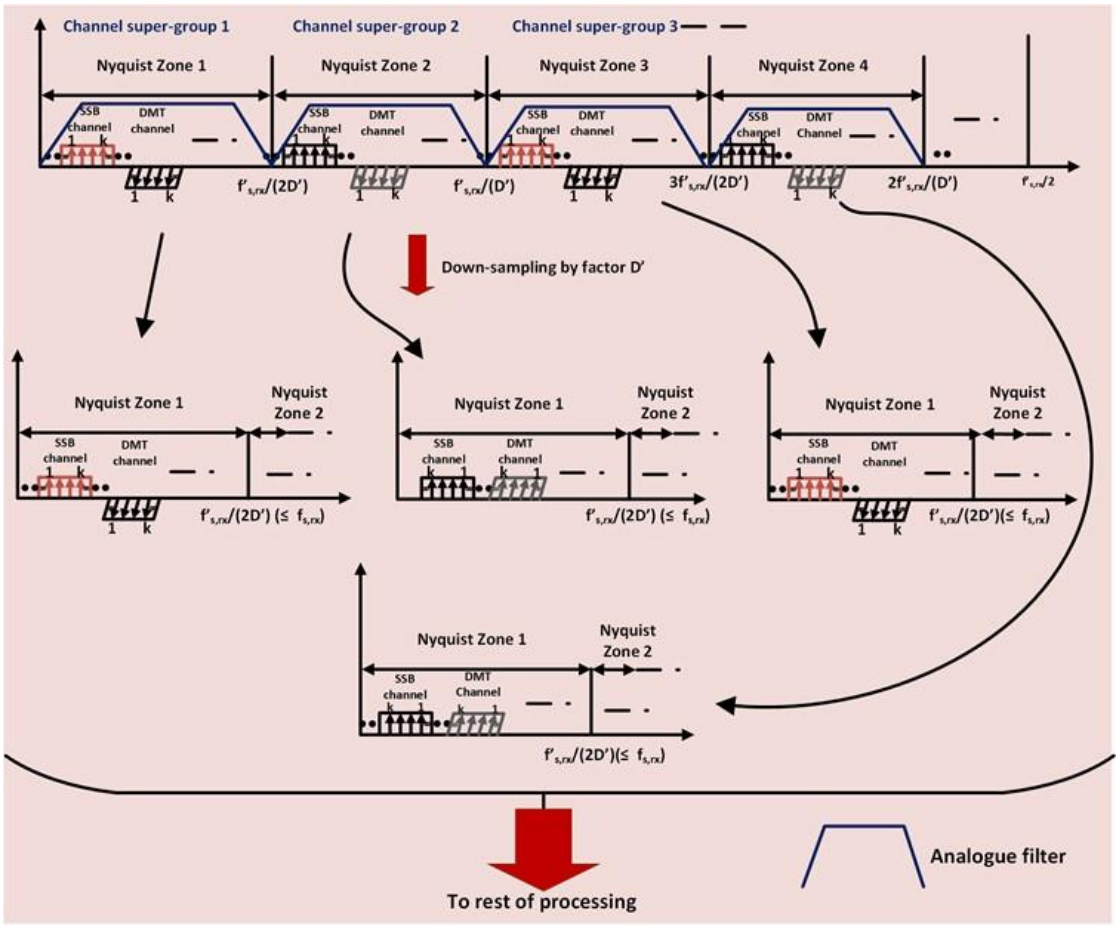

Figure 5-7 Using a bandwidth-extension device and analogue filtering with a multiplex exceeding the analogue bandwidth specification of the ADC at the receiver.

5.4 System Architecture

The NZ design and mapping hierarchy concepts of sub-multiplexes, multiplexes and super-multiplexes are discussed in the context of transmitter and receiver structures in this section.

5.4.1 Transmitter

In Figure 5-8, a concept of a transmitter architecture implementing the techniques discussed in Section 5.3 is shown.

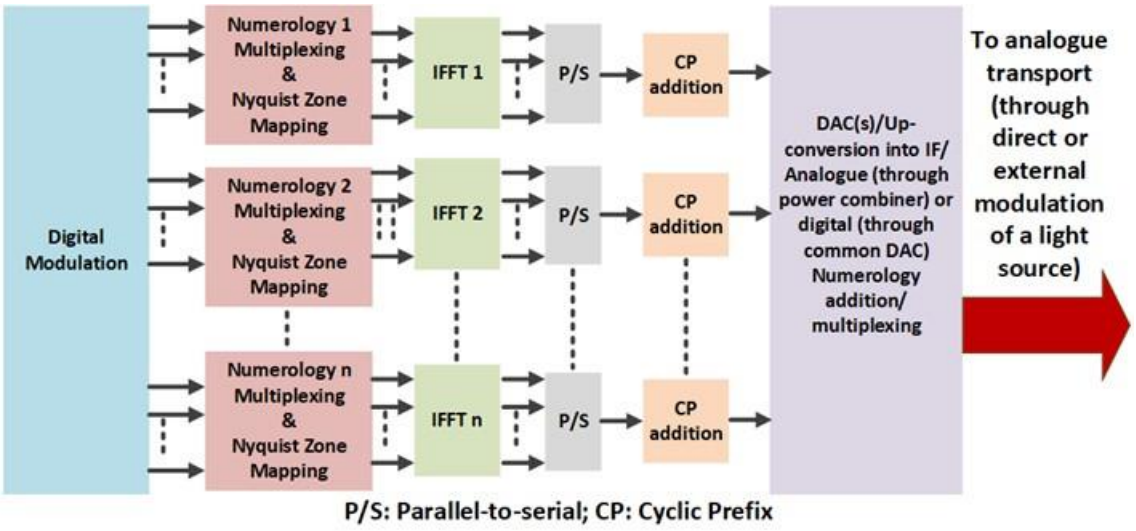

Figure 5-8 Concept of a transmitter architecture based on NZ mapping.

The digital modulation stage involves producing modulated symbols which can be real (e.g. derived from BPSK mapping) or complex (e.g. derived from QPSK, QAM mapping), or a combination of both. These symbols may be interleaved and/or cross-processed (e.g. by applying precoding) in any manner possible depending on application. For ease of explanation, these symbols or frequency domain samples will be called subcarriers from this point onwards.

In the figure, the digital modulation stage is followed by the stages of numerology multiplexing and NZ mapping and IFFT. Modulated subcarriers are grouped contiguously in the frequency domain, with arbitrary numbers of null subcarriers (frequency guard bands) to separate them, thus forming channels. Note that the index information of these null subcarriers has to be known at the receiver (for example, through control signalling). Channels with different bandwidths are created by grouping together different numbers of subcarriers but they have the same subcarrier spacing (including nulls) when they are destined for the same IFFT.

The subcarriers, which are grouped in one or more channels, are arranged in the frequency domain to fall within separate NZs. The groupings and number of NZs depend on the techniques described in Figure 5-2 to Figure 5-4. The bandwidth of these zones in the frequency domain is determined by the sampling rate to be used at the digital processing stage of the receiver. This is given by the down-sampling factor *D*, which divides the sampling rate of the ADC stage at the receiver.

The resulting groups are called Sub-Multiplexes (described in more detail in Section 5.4.3). After the IFFT operation, the Sub-Multiplex is converted to a time-domain signal, which then goes

through parallel-to-serial conversion and CP addition (or any other method of guard period insertion depending on the application). Finally, the Sub-Multiplex is converted to an analogue signal through a DAC process for subsequent transmission over a channel.

The Sub-Multiplex is combined in the digital or analogue domain with other Sub-Multiplexes that are produced by other IFFTs (corresponding to the same or different numerologies and utilising the same or different sampling rates). This gives rise to Multiplexes (described in detail in Section 5.4.4), in which unoccupied spaces created in the frequency domain of each Sub-Multiplex are used to insert one or more channels from other Sub-Multiplexes.

The Sub-Multiplexes and/ or Multiplexes can be extended to form Super-Multiplexes (discussed in detail in Section 5.4.5). A Super-Multiplex is created when a Sub-Multiplex or Multiplex's aggregate bandwidth exceeds the receiver side ADC sampling rate specification (shown in Figure 5-7). Super-Multiplexes are de-multiplexed back to Multiplexes or Sub-Multiplexes by using analogue filtering, discussed in detail in the following section.

5.4.2 Receiver

Following on from the analogue transport stage shown in Figure 5-8, a concept of the receiver side architecture (RRU) is shown in Figure 5-9.

The incoming multiplexed channels go through an analogue filtering stage consisting of a small number of filters (band-pass, low pass and/or high pass) or RF de-multiplexers that are used to filter out individual super-groups within Super-Multiplexes.

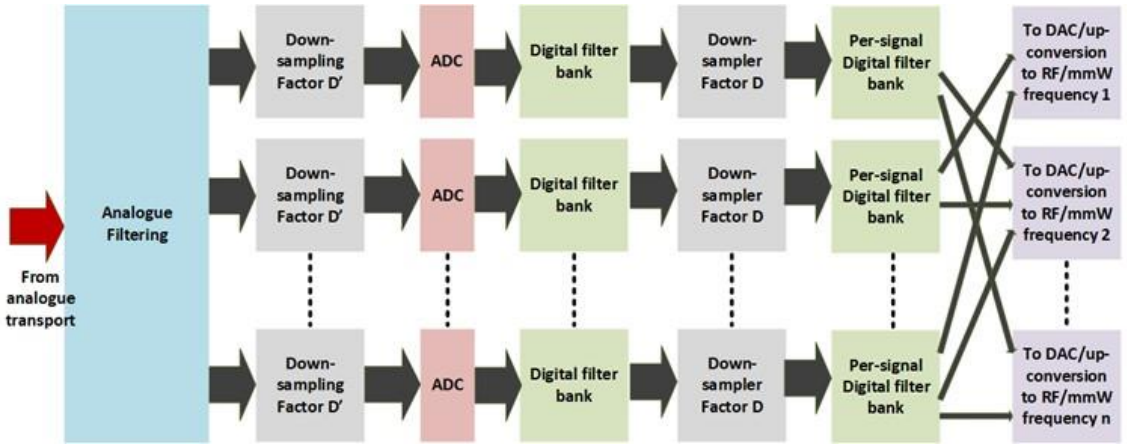

Figure 5-9 Concept of a receiver architecture based on NZ mapping.

The first down-sampling stage, using an intermediate down-sampling factor *D'*, is used to extend the capabilities of the ADC stage that follows (discussed in Section 5.3.2). Sub-Multiplexes and Multiplexes are band-pass sampled by this factor with respect to the device's base sampling rate ($f_{s,inter}$). This brings the channels down to an IF that is within the ADC's analogue bandwidth specifications. The process is similar for super-groups (derived from Super-Multiplexes), which have aggregate bandwidths exceeding the ADC's sampling rate specifications. A small count of bandwidth extension devices may be required for individual super-groups.

The resulting super-groups, Sub-Multiplexes or Multiplexes are discretised and sent to the ADC stage. After quantisation and further processing, individual channels or channel groups from Multiplexes or Sub-Multiplexes go through the first digital filter bank. Channel groups can be made up of any number of channels based on the original grouping of channels into NZs at the transmitter. If one channel is mapped into each NZ, then the digital filters in the first filter bank filter out an individual channel. If there are *n* channels per NZ, *n* channels are filtered out via each filter.

Next, each of these channels (or groups of *n* channels), which were originally occupying different parts of the frequency spectrum, are down-sampled to the same lower IF, using a down-sampling factor of *D* and the final sampling rate of $f_{s,final}$. This is followed by a second digital filter bank which filters each individual signal within channel groups occupying each NZ (Figure 5-3). In the case of one channel per NZ, this filtering stage can be used to remove additive noise. It should be noted that even though two down-sampling stages have been discussed in Section 5.3, three have been discussed here and shown in Figure 5-9 as an example. In reality, there can

be many down-sampling stages in the digital domain, with each stage having a different intermediate sampling rate. For simplicity, only one ($f_{s,inter}$) has been used in this description.

In the final stage, the individual channels are converted to analogue signals via DACs and depending on the application, the rest of the processing takes place. For example, in the case of a wireless channel with mMIMO transmission, each corresponding channel across each NZ is now present at the same frequency (IF) and can be up-converted to an RF/mmW frequency using a single LO signal (described in Figure 5-4). Similarly, other channels within the NZ (the channel group) can be up-converted to a different mmW/RF frequency whereby a different LO signal is used for these and their corresponding channels across the other NZs. This means that in the case of Sub-Multiplexes, each can be associated with a different mmW/RF frequency and a single LO signal can be used to up-convert them to the required frequency. As a result, each Sub-Multiplex can be associated with a different RAT, for example, a Wi-Fi, LTE or 5G RAT.

5.4.3 Sub-Multiplexes

The technique of creating a Sub-Multiplex is shown in detail in Figure 5-10. The single IFFT operation (*IFFT1* in this example) is used to distribute subcarriers into channels separated by nulls within the first NZ, as determined by the sampling rate ($f_{s,IFFT1}$) associated with *IFFT1*. Depending on the type of modulation (DMT or SSB), the second NZ will also be filled. In addition, as shown in the figure, at the NZ boundary on the left of an odd NZ, a large bandwidth channel is followed by a narrow bandwidth one while for an even one, a narrow bandwidth channel is followed by a large bandwidth one. This means that the order of the channels in even NZs is opposite to the order of the channels in the odd NZs, due to flipping and conjugation as discussed previously.

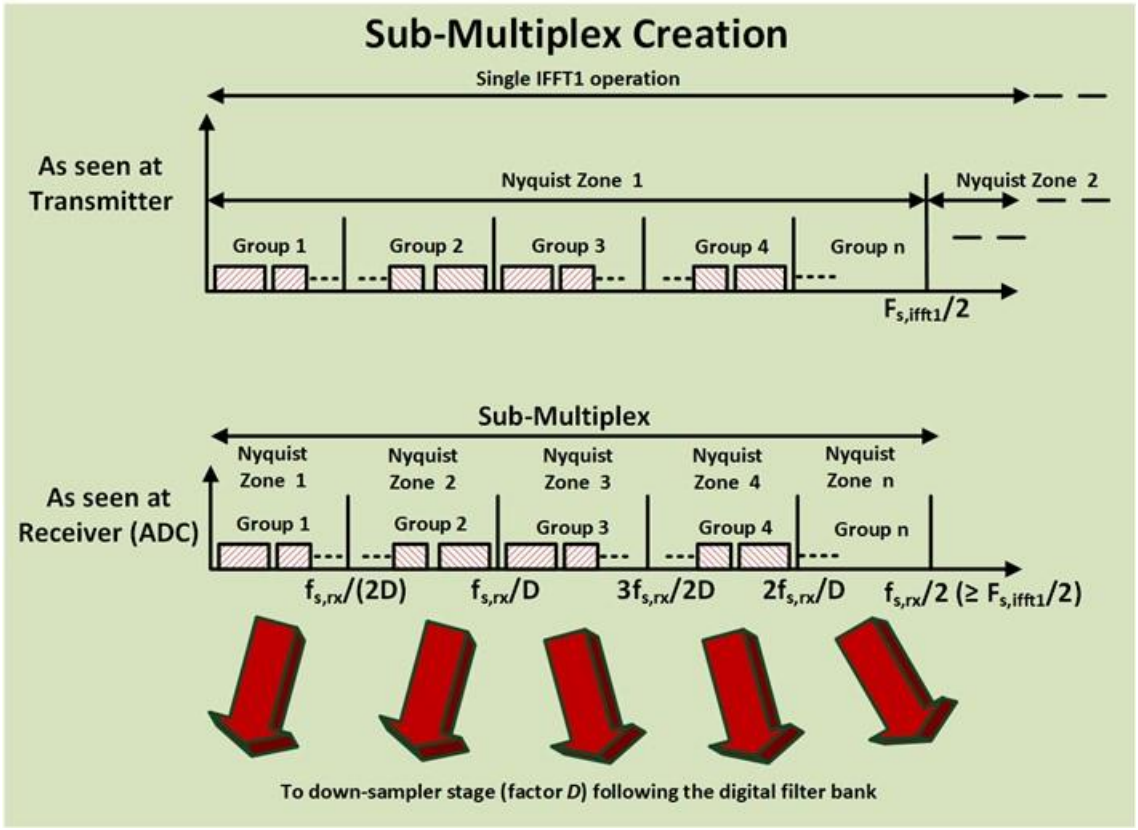

Figure 5-10 Sub-Multiplex creation, as seen from the transmitter and receiver sides of the architecture.

As explained previously, each of these channels are filtered digitally at the receiver before being sent to a down-sampling stage. Based on the sampling rate of $f_{s,final}$ used by the receiver ADCs, each of these channels is mapped into different NZs (as seen by the receiver) and down-sampled to the same IF.

5.4.4 Multiplexes

Sub-Multiplexes can be combined to form a Multiplex in the digital domain (before the DAC stage, via appropriate interpolation/ decimation) or analogue domain (after the DAC stage, via the use of RF splitters/ combiners) of the transmitter (shown in Figure 5-8). The creation of this Multiplex is shown in Figure 5-11, in which each Sub-Multiplex is associated with a given sampling rate between $f_{s,IFFT1}$ to $f_{s,IFFTn}$. These sampling rates can be related, e.g. they can be integer multiples for different 5G numerologies [49], [50]. They can also be completely

unrelated (e.g. 5G and Wi-Fi numerologies) and employ some type of filtered OFDM variant for avoiding inter-channel interference.

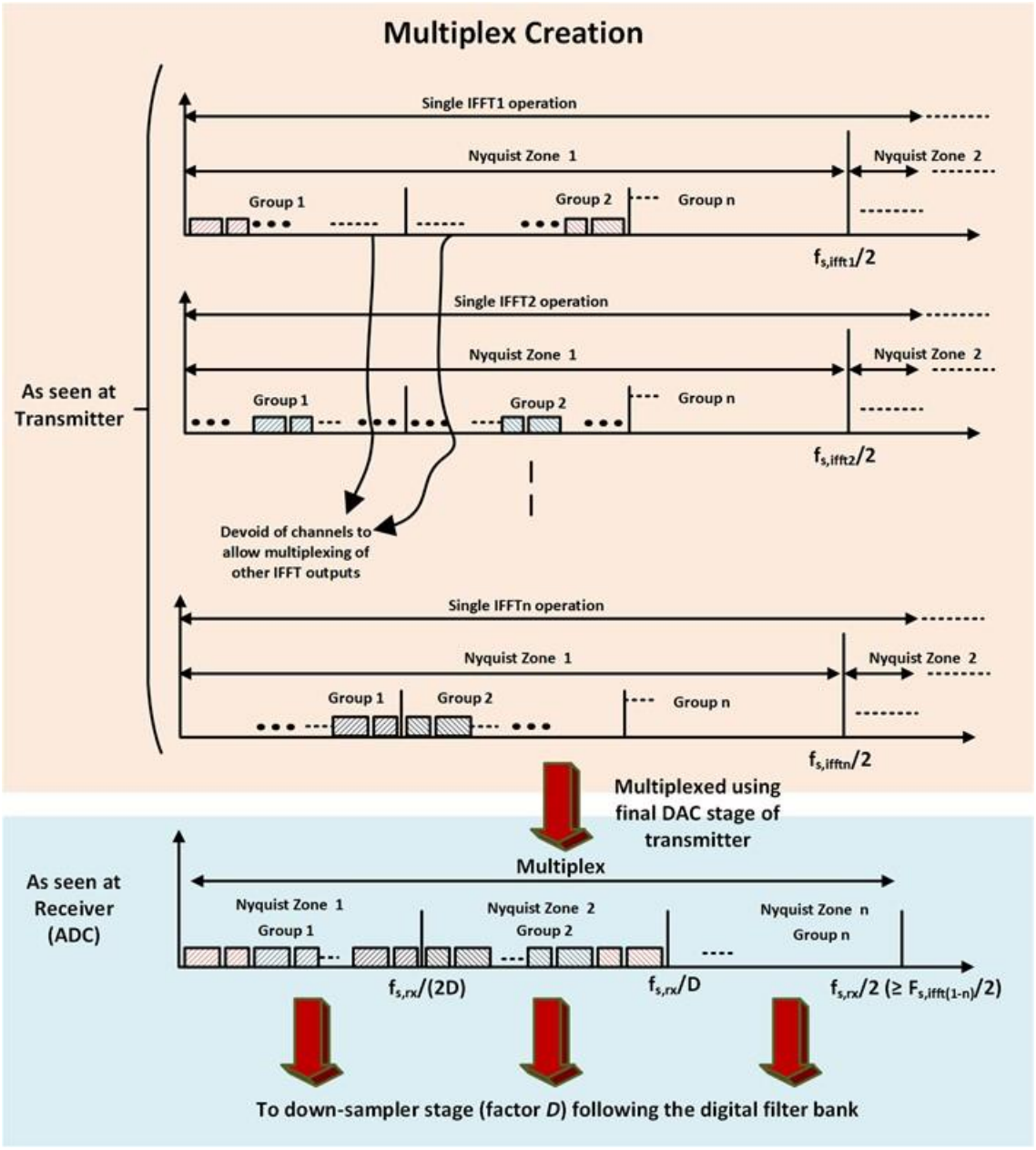

Figure 5-11 Multiplex creation, as seen from the transmitter and receiver sides of the architecture.

To facilitate the creation of the Multiplex, gaps have to be left within the IFFT-derived NZs such that channels from the different Sub-Multiplexes can be inserted into these gaps for creating

the Multiplex. This is depicted in the figure, showing that gaps are created within each Sub-Multiplex, where channels from other sub-multiplexes can be inserted.

The resulting Multiplex contains groups of channels, with channels originating from the different Sub-Multiplexes. Channels occupying the same location in each NZ can be down-sampled down to the same IF using a single down-sampling factor and associated with a common LO signal for up-conversion to an RF/mmW frequency (described in Figure 5-4).

5.4.5 Super-Multiplexes

In Figure 5-12, the technique of creating a Super-Multiplex from a single Sub-Multiplex is shown in detail. If a Sub-Multiplex has an aggregate bandwidth greater than the sampling rate specifications of the receiver ADC, a Super-Multiplex is created which is processed via a combination of analogue filtering, a bandwidth-extension device and down-sampling. Analogue filters select individual super-groups, which are then band-pass sampled down to a lower IF by an intermediate down-sampling factor of *D'*. The intermediate sampling rate of $f_{s,inter}$ places the super-groups within a frequency range $f'_{bw,NZ}$, which is within the ADC's sampling rate specifications (as described in Figure 5-7).

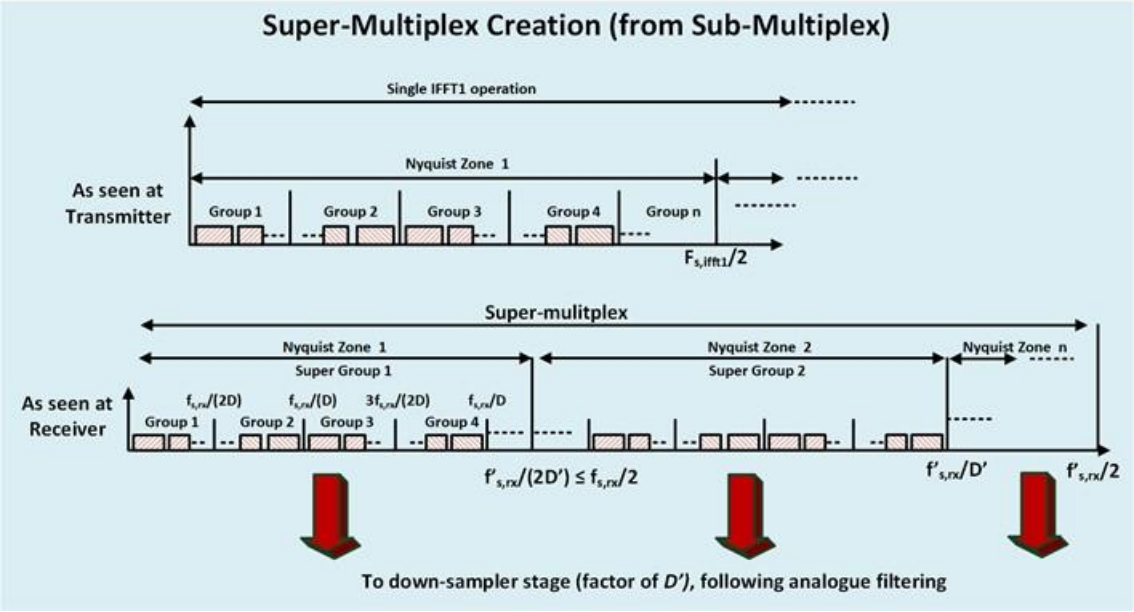

Figure 5-12 Super-Multiplex creation from a Sub-Multiplex, as seen from the transmitter and receiver sides of the architecture.

A Super-Multiplex can also be created from a single Multiplex, as shown in Figure 5-13. If a Multiplex is created such that its aggregate bandwidth is above the sampling rate specifications of the receiver ADC, it results in a Super-Multiplex which can be processed via a combination of analogue filtering, a bandwidth-extension device and down-sampling, using an intermediate factor of *D'*. Following analogue filtering, each individual super-group is band-pass sampled with a sampling rate of $f_{s,inter}$ and placed within a frequency range $f'_{bw,NZ}$ that is within the ADC's bandwidth and/or sampling rate specifications.

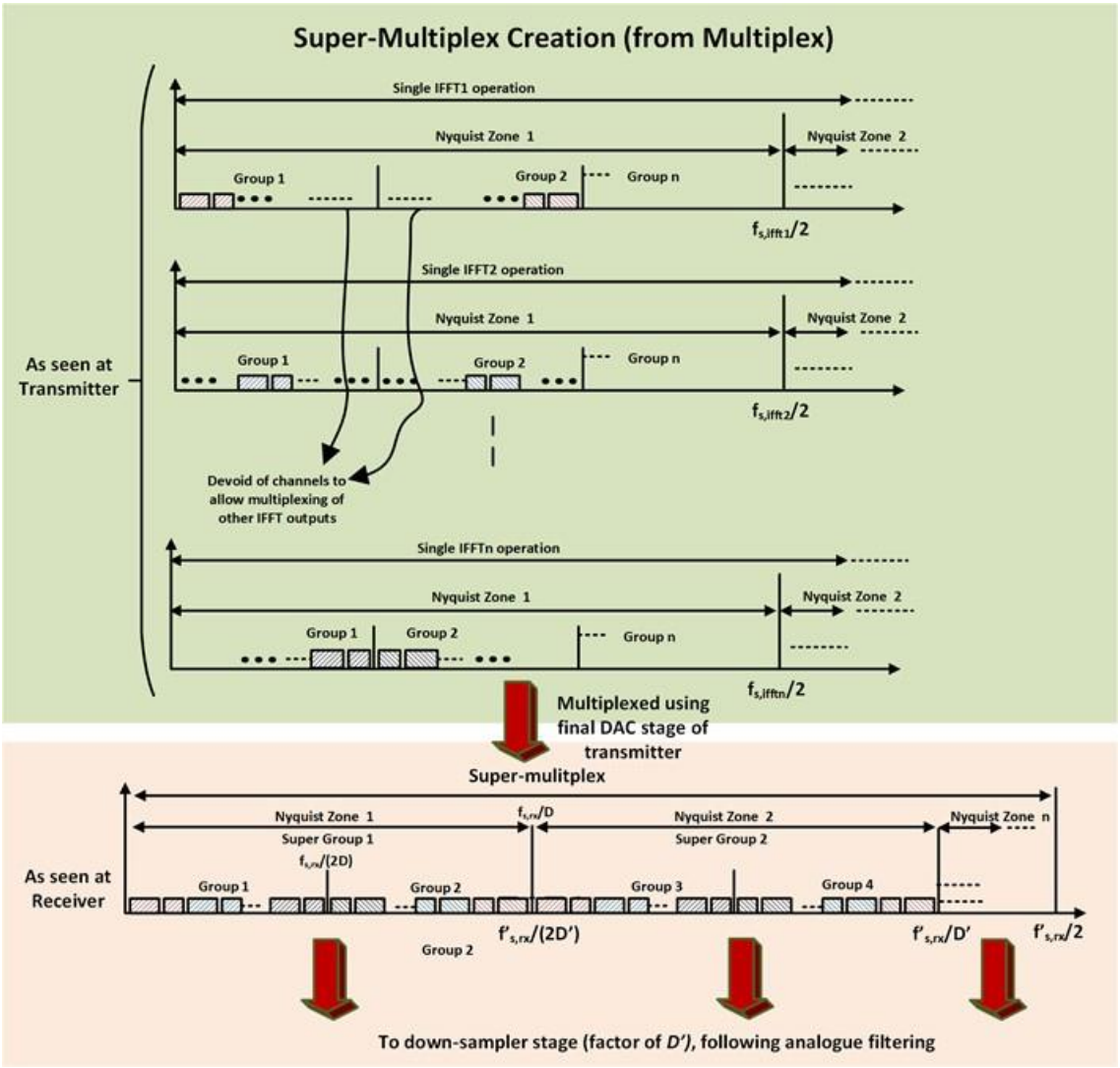

Figure 5-13 Super-Multiplex creation from a Multiplex, as seen from the transmitter and receiver sides of the architecture.

For each of the different mapping hierarchies (Sub-Multiplex, Multiplex and Super-Multiplex), channels within even NZs are frequency-domain flipped and conjugated. As discussed previously, this is done so that following the down-sampling process, the channels are "obtained" in the same general form (order of subcarriers in the frequency domain and conjugation form) that they were originally created at the transmitter. This process is optional but it reduces the amount of processing required at the receiver. For the Super-Multiplexes this process is carried out twice, once for the super-groups (these are within the first order NZs with a size of $f'_{bw,NZ}$) and once for the channel groups (these are within the second order NZs with a size of $f_{bw,NZ}$).

5.5 Summary and Conclusions

Techniques for facilitating the transport of a large number of channels in the radio access section of a mobile communication network (e.g. the fronthaul section of a cloud-radio access network (C-RAN)) have been discussed in this chapter. These techniques allow reductions in processing for heterogeneous networking (or multi-radio access technologies (multi-RATs)) and mMIMO configurations. Using single or multiple Inverse Fast Fourier Transforms (IFFTs) and additional digital processing (as well as some optional analogue processing), multiple channels can be transmitted in the form of a subcarrier multiplex. DMT and SSB modulation schemes can be used for different channels and can be integrated seamlessly within the single IFFT operation. Each of these channels or channel groups can be arranged in a hierarchical NZ mapping structure, in the form of a Sub-Multiplex, Multiplex and/ or Super-Multiplex. This allows the receiver to use digital processing (as well as some optional analogue processing) to down-sample each channel (or a group of channels) to the same IF using a single down-sampling factor, reducing analogue bandwidth and sampling rate requirements of the ADCs at the receiver. Once the channels are at the same IF, they can be readily up-converted to their respective RF or mmW channels with minimal per-signal processing.

6 Experimental Results of an Analogue Subcarrier Multiplexed Mobile Fronthaul with Digital Processing

6.1 Introduction

This chapter describes the experimental implementation of the NZ design concept discussed in Chapter 5, as well as the creation of different types of multiplexes using this approach. These multiplexed signals are part of a system that also includes analogue transport and mmW up-conversion.

The design concept of the data modulation and mmW carrier generation stages of this architecture is provided in Section 6.2. Various experimental results of digital multiplexing and analogue transport of DMT and SSB modulated signals involving a single IFFT and generic numerologies in accordance with the NZ design concept are presented in Section 6.3. Experimental results with multiplexes employing 5G numerologies are discussed in Section 6.4. This is followed by the experimental results of mmW carrier generation and mmW up-conversion of signals (selected from one of the multiplexes from a previous section) in Section 6.5. The chapter ends with summary and conclusions in Section 6.6.

6.2 Overview of Data Modulation and mm-Wave Carrier Generation

Figure 6-1 shows an overview of the hybrid multiplexing system with analogue transport and digital processing. For ease of understanding, the digital and analogue parts of the architecture are indicated using different colours.

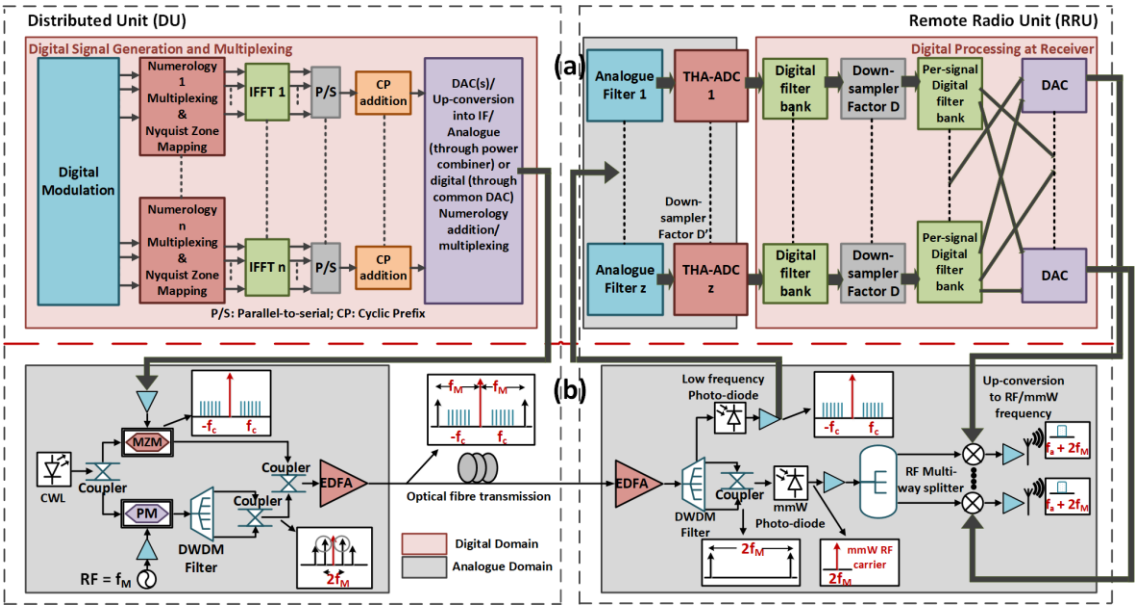

Figure 6-1 Hybrid Multiplexing System with Analogue Transport and Digital Processing. (a) Digital signal generation and subcarrier multiplexing at transmitter (DU), digital processing at receiver (RRU). (b) Data modulation and remote LO delivery via optical frequency comb generation for mmW up-conversion.

As discussed previously in Section 5.4.1, multiple signals are generated and multiplexed in the digital domain at the DU. Individual signals at different IFs are created within the same IFFT block and signals within different IFFT blocks employing different numerologies (and modulation formats, if required) can be multiplexed in the time domain (note that "time domain" here is the description for the processing following the IFFT stage). Following the IFFT stage and parallel-to-serial conversion, a CP is appended to each multiplex and the signals are sent to a DAC stage. This is shown in the digital signal generation and multiplexing stage of the DU in Figure 6-1 (a). The entire SCM multiplex, which is now a block of analogue signals, is placed at an RF frequency (f_c) and modulated onto an optical carrier using an MZM. As discussed in Chapter 5, which of the signals will populate an even or odd NZ will depend on f_c and the sampling rate used at the RRU.

As shown in Figure 6-1 (b), the optical signal from a CWL is split using an optical coupler/power divider. One part is modulated by the SCM multiplex using the MZM. The second part of the CWL signal is phase-modulated by a PM, which produces optical sidebands with a separation equal to the modulation frequency of the RF signal applied (f_M). The first order sidebands are filtered using a DWDM filter and then coupled with the data-modulated signals from the MZM. The resulting signal is optically amplified and transmitted through the optical fibre link.

At the RRU, the signals are sent to another DWDM filter, as shown in Figure 6-1 (b). The optical carrier with the data-modulated signals is filtered and sent to a low-frequency PD. Following the optical to electrical conversion, the signal multiplex is sent to *z* analogue filters/ de-multiplexers and combined Track-and-Hold Amplifier – Analogue-to-Digital converter (THA-ADC) stages . The operation of the THA within this architecture will be discussed in detail in Chapter 7.

The signals are de-multiplexed and down-sampled to the same IF through the processes described in Section 5.3. This means that signal groups are filtered in the analogue domain and band-pass-sampled to the first NZ (as derived by the THA sampling rate) by the THA-ADC stage using a common intermediate sampling rate. After that, the signal(s) in each resulting NZ are filtered using a digital filter bank and down-sampled, using a common down-sampling factor, down to the first NZ (as derived by the down-sampling factor). The resulting signals within each NZ are individually filtered, and sent to the appropriate DAC and up-conversion stages.

In the mmW generation section (Figure 6-1 (b)), the optical sidebands, separated by a frequency of $2f_M$ are detected by a mmW PD to produce a mmW beat signal. The mmW signal is then distributed (through appropriate splitters) to the up-conversion stages where the individual signals of the SCM multiplex are up-converted to a frequency of $f_a + f_M$ for mmW-mMIMO transmission, with f_a being the IF of the down-sampled signals.

6.3 Experiments at RF with DMT and SSB Modulated Multiplexes using a Single IFFT and Generic Numerologies

The processes of creating different types of digital multiplexes employing single IFFTs and generic numerologies and their analogue transport are described in detail in the following sub-sections with the help of block diagrams of the transmitter and receiver functions, as well as equations and practical values used in the experiments. Here, the term ‘generic’ has been used to mean a numerology that does not fall under specifications such as Wi-Fi, LTE, 5G etc.

6.3.1 MATLAB Transmitter and Receiver Functions for DMT and SSB Modulated Multiplexes using Single IFFTs

In this work, a MATLAB transmitter function has been used to generate different types of subcarrier multiplexes using the NZ mapping method and a single IFFT while a MATLAB receiver function has been used to de-multiplex the channels (concepts explained in Section 5.4). As it will be shown later on in Sections 6.3.3 and 6.3.4, the digital multiplexes are downloaded to the AWG, transported through the optical link and captured by an Oscilloscope for offline processing. This section provides a detailed overview of the transmitter and receiver functions with the help of block diagrams of the MATLAB code (with related equations dealt with in Section 6.3.2). These functions have been used both in experiments and in simulations.

6.3.1.1 MATLAB Transmitter Function for DMT and SSB Modulated Multiplexes

In order to generate the aforementioned multiplexes, a number of simulation parameters have to be defined by the user. These parameters are shown and described with example values in Table 6-1.

Table 6-1 MATLAB transmitter function user-defined parameters with example values

Simulation Parameter	**Parameter Description**	**Example Values**
M	Modulation level (only powers of 2, non-negative)	16
CP length	Length of cyclic prefix to be appended to multiplex as a ratio to symbol duration (non-negative)	0.125
Number of channels	Total number of channels to be multiplexed (non-negative, preferably even)	64 (SSB)/ 32 (DMT)
Channels per NZ	Number of channels in each NZ (non-negative, less than or equal to the total number of channels)	1
Per-NZ IFFT length	Sample size of each NZ when sampled by the receiver (non-negative, power of 2)	512

Number of symbols	Number of OFDM symbols in the multiplex/ per IFFT (non-negative)	10
Number of data subcarriers	An array containing the number of data subcarriers for each channel in the multiplex (non-negative, smaller than Per-NZ IFFT length)	400 (Array length: 64/ 32 for SSB/ DMT)
Number of null subcarriers	An array containing the number of null subcarriers to form gaps between channels (non-negative, smaller than Per-NZ IFFT length)	112 (Array length: 63/ 31 for SSB/ DMT)

Even though the transmitter function is highly flexible and any modulation level, number of channels etc. can be attained, in order to obtain the desired number of channels, channel bandwidths, gaps between channels, IFFT length and down-sampling rate, a number of parameters have to be carefully designed. For example, to use the IFFT algorithm, the total number of channels has to be a power of two, while to use the IDFT algorithm, the total number of channels should be even (preferably) to ensure that the decimation/ down-sampling factor at the receiver is an integer factor. For both cases, the per-NZ IFFT length should be a power of 2. In addition, the number of channels per NZ have to be less than or equal to the total number of channels and the number of data and null subcarriers (for each channel) has to be smaller than the per-NZ IFFT length. Further explanation regarding choice of number of symbols, data subcarriers and null subcarriers will be provided in Section 6.3.2.

When the MATLAB transmitter function is run, a drop-down list of sampling rates choices from 97.656250 MSps to 3.125 GSps (only multiples of 2: 97.656250 MSps, 195.3125 MSps and so on) is provided. Even though any sampling rate can be used in simulations, for simplicity, these sampling rates have been chosen as they are the ones allowed by the Oscilloscope that was used for the experimental measurements. The choice of sampling rate is very important as it also determines the passband of the digital filters that will be used in the receiver function. The equations for calculating filter passbands will been shown in Section 6.3.2. The block diagram (to be followed in the anti-clockwise direction) of the MATLAB transmitter function is shown in Figure 6-2.

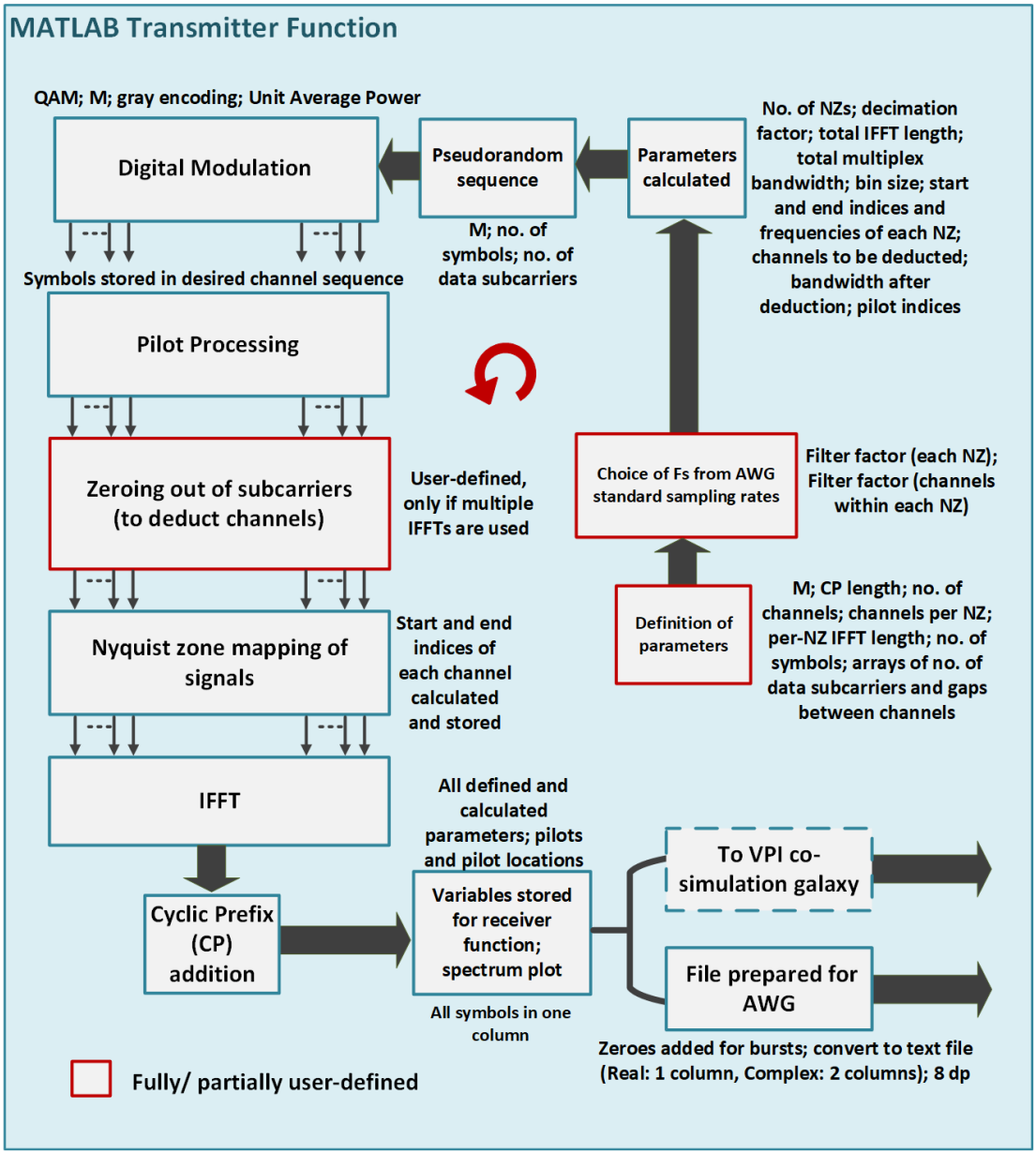

Figure 6-2 MATLAB transmitter function for DMT and SSB modulated multiplexes (anti-clockwise).

After the parameters have been defined and the sampling rate has been chosen, parameters such as number of NZs, decimation factor, total IFFT length, total multiplex bandwidth, bin size, start and end indices and boundary frequencies of each NZ, channels to be deducted and bandwidth after channel deduction are calculated. These parameters will be discussed in detail in Section 6.3.2.

Following this stage, the pseudorandom sequence is generated, based on the modulation level, number of symbols and number of data subcarriers. This is followed by QAM modulation, again

depending on modulation level. The '*qammod*' function has been used, with the '*UnitAveragePower*' argument flag set to true, which ensures that the function scales the constellation to an average power of 1 watt referenced to 1 ohm [184]. Gray encoding has been used. The modulated symbols are stored within an array structure according to the desired channel sequence for the next steps.

For the pilot processing step, three different approaches have been tested.

- **Single pilot**: a single pilot with a value normalized to the 16-QAM reference constellation used to plot the constellation diagrams is inserted within known locations in each symbol of the multiplex
- **Pilot array**: an array of pilots derived from a specific 16-QAM modulated pseudorandom sequence is inserted within known locations in each symbol of the multiplex
- **Random pilots:** data subcarriers from known locations in each symbol of the multiplex are copied and stored to be used for interpolation in the receiver

The third approach produced the best results and has thus been used in this work. The extracted pilot tones (first and last data subcarrier, as well as every 10^{th} data subcarrier of each channel) and their corresponding indices are stored to be used in the demodulation process.

The next stage involves replacing data subcarriers with null subcarriers to meet the Oscilloscope sampling rate requirements (this is discussed in Section 6.3.2). Generally, this stage does not require user intervention but if multiple IFFTs need to be combined, the user has to specify which channels need to be removed.

After this, channels are multiplexed in the desired order by taking data and null subcarriers, as well as odd and even NZs into account. For a DMT signal multiplex, channels in the "negative" part of the spectrum are conjugate symmetric with the channels in the "positive" part of the spectrum. Moreover, only the start and end indices of all the channels in the "positive" part of the spectrum are stored. For the SSB signal multiplex, the channels in the "negative" part of the spectrum are independent from those in the "positive" part of the spectrum (thus are not conjugate symmetric). The start and end indices of channels in both parts of the spectrum are stored. Channels are also conjugated and frequency domain flipped in the even NZs, as discussed in Chapter 5.

The mapped channels undergo conversion from frequency to time domain via IFFT/ IDFT (depending on the total IFFT length). This is followed by CP insertion.

Finally, all user-defined and calculated parameters are stored in a file, to be used in the receiver function. The resulting multiplexed signal, in the form of floating point numbers, is stored either in a single array (in the case of DMT modulation where the resulting signal is real), or two arrays (for the In-phase and Quadrature components in the case of SSB modulation where the resulting signal is complex)

To download the signal to the AWG, a two-column text file is created with the floating point numbers rounded to 8 decimal points. Null subcarriers are added at the beginning of the file in order to ensure that bursts of the signal (these are multiple copies of the signal repeatedly generated by the AWG) captured by the Oscilloscope can be distinguished from one another.

When simulations are instead carried out using MATLAB-VPI co-simulation, the columns of real (and imaginary) values are generated and passed to the co-simulation galaxy automatically. This will be discussed in detail in Chapter 7.

6.3.1.2 MATLAB Receiver Function for DMT and SSB Modulated Multiplexes

Following transmission through the analogue link, the Oscilloscope captures the multiplexed signal for offline processing via the MATLAB receiver function (in the case of MATLAB-VPI co-simulations, the signals are passed from a co-simulation galaxy back to MATLAB automatically). In measurements, the null subcarriers that were added to differentiate between bursts are removed and the stored variables are loaded for the demodulation process. Following these steps, the captured file undergoes time correction, which is the process of aligning the FFT window with the received symbols. The new IFFT length (corresponding to twice the per-NZ IFFT length) and sampling rate after down-sampling, as well as the start and end indices of each down-sampled channel are pre-calculated. The block diagram of the MATLAB receiver function (to be followed in the clockwise direction) for DMT and SSB modulated multiplexes is shown in Figure 6-3.

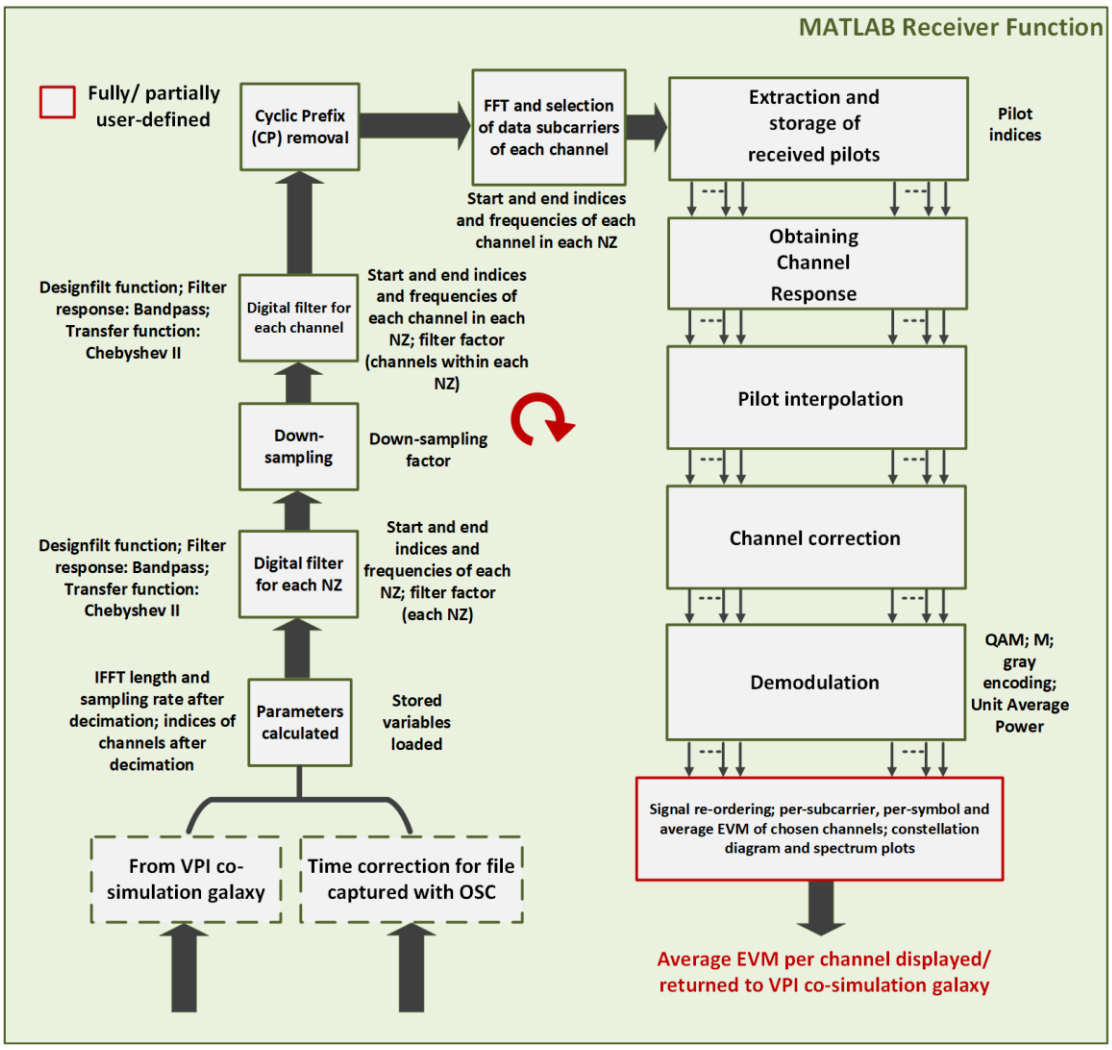

Figure 6-3 MATLAB receiver function for DMT modulated multiplexes (clockwise).

The "*Designfilt*" function in MATLAB has been used to create the digital filters to be used for filtering each channel of the multiplex. After testing a number of filter response options, an Infinite Impulse Response (IIR) band-pass filter response (Chebyshev II) was chosen for the filter per NZ and the filter per channel. The stopband and passband frequencies are calculated depending on the sampling rate, bin size, filter factor (calculated at the transmitter) and start and end frequencies (and indices) of NZs and channels.

After the stages of filtering per NZ, down-sampling and filtering per channel, the CP is removed for each channel. Following the FFT stage, the data subcarriers of each channel are extracted, using the pre-calculated indices from the beginning of the receiver function. Since the channels in even NZs have been frequency domain flipped and conjugated at the transmitter, channels in both odd and even NZs can be now directly processed in the same manner at the receiver.

Using the received pilots (with locations indicated by stored pilot location indices) the channel response is estimated, followed by pilot interpolation using a linear interpolation function. Channel correction is carried out at following this stage. Finally, the "*qamdemod*" function is used to demodulate the signal.

EVM calculations, constellation diagrams and spectrum plots are calculated/displayed for user-defined selection of channels. EVM per subcarrier, per symbol/ frame and average EVM (for all symbols) are calculated.

6.3.2 Creating a Digital Multiplex with a Single Signal per NZ using a Generic Numerology

For performance verification, initially, a generic numerology and frequency spacing is used to produce 64 SSB/32 DMT signals, with OFDM subcarrier modulation using 16-QAM. The subcarrier multiplex is generated by the MATLAB transmitter function using the NZ mapping method and a single IFFT and following analogue transmission, the multiplex is processed offline via the MATLAB receiver function. This section explains the equations that are used to create such a multiplex for both experiments and simulations, using example values to aid the explanation. Some of these values, which are user-defined, have been shown in Table 6-1. Equations for calculating some of the other parameters in the transmitter and receiver functions are also shown in this section but are not necessarily in the order of the blocks shown in Figure 6-2 and Figure 6-3.

For simplicity, the sampling rate set at the AWG (F_s) has to be a certain factor times the aggregate bandwidth of the signal. This is so that the AWG and Oscilloscope can operate at the same sampling rate and is a requirement due to the selectivity of the digital filters used by the Oscilloscope (in reality, this can be avoided by adding an extra decimation stage in the receiver function in MATLAB). Assuming that this factor is r_{OSC}, the maximum allowable signal bandwidth $F_{BW,max}$ (Hz) is

$$F_{BW,max} \leq \frac{F_S}{r_{OSC}} \ . \tag{6-1}$$

For these experiments, r_{OSC} has to be set to a value of at least 1.25.

For an F_s of 3.125 GSps (the maximum practically allowed by the AWG), $F_{BW,max} \leq 2.5$ GHz.

Also, if $N_{data,sub}$ is the total number of data subcarriers for a single signal and the per-NZ IFFT length is $N_{IFFT,NZ}$, then

$$N_{data,sub} \leq \frac{N_{IFFT,NZ}}{r_{OSC}} \ , \tag{6-2}$$

and from (6-1)

$$\frac{F_S}{F_{BW,max}} = \frac{N_{IFFT,NZ}}{N_{data,sub}} \geq r_{OSC} \ . \tag{6-3}$$

As shown in Table 6-1, the per-NZ IFFT length corresponds to the size of each NZ when sampled by the receiver.

Keeping these equations in mind, in order to down-sample and up-convert each of the multiplexed signals to mmW frequencies, which will involve reintroducing the signal/s extracted from the multiplex to the AWG (this will be discussed in detail in Section 6.5), a sufficient gap needs to be maintained between the signals. Again, this is done to maintain the bandwidth to sampling rate ratio of 1.25. Potentially, this gap can become arbitrarily small if digital filters with sufficient selectivity can be used at the RRU.

The gap between signals is created by introducing null subcarriers (subcarriers which are not modulated with data). The number of null subcarriers, $N_{null,sub}$, between signals can be calculated by

$$N_{null,sub} = N_{IFFT,NZ} - N_{data,sub} \ . \tag{6-4}$$

Using (6-2) and (6-4), for $N_{IFFT,NZ}$ = 512, $N_{data,sub}$ = 400 is chosen. $N_{null,sub}$ = 112 and r_{OSC} = 1.28, which meets the requirement of (6-1).

If $N_{IFFT,total}$ is the total IFFT length taking the per-NZ IFFT length and number of multiplexed signals into account, for a DMT multiplex

$$N_{IFFT,total} = 2 \times \left[\left(N_{mux,DMT} \times N_{data,sub}\right) + \left(N_{mux,DMT} \times N_{null,sub}\right)\right] \ , \tag{6-5}$$

with the number of signals in the DMT multiplex ($N_{mux,DMT}$) given by

$$N_{mux,DMT} = \frac{N_{IFFT,total}}{N_{IFFT,NZ} \times 2} \ . \tag{6-6}$$

In the case of SSB signals, $N_{IFFT,total}$ can be calculated from

$$N_{IFFT,total} = \left[\left(N_{mux,SSB} \times N_{data,sub}\right) + \left(N_{mux,SSB} \times N_{null,sub}\right)\right] \ , \tag{6-7}$$

where the number of signals in the SSB multiplex ($N_{mux,SSB}$) is given by

$$N_{mux,SSB} = \frac{N_{IFFT,total}}{N_{IFFT,NZ}} \quad . \tag{6-8}$$

Taking into acount available AWG sampling rates, $N_{mux,DMT}$ = 32 and $N_{mux,SSB}$ = 64 are chosen as a good balance between per-signal bandwidth and the number of signals for mMIMO applications. Thus, using (6-5) and (6-7), $N_{IFFT,total}$ = 32768, which is calculated by the MATLAB transmitter function to be the nearest power of 2 value for the given per-NZ IFFT length and number of signals. If the IDFT algorithm is used instead, an even number, preferably a multiple of 10, has to be chosen such that the down-sampling factor used at the receiver is an integer value. Considering the same per-NZ IFFT length of 512, and the use of the IDFT algorithm, the number of signals in the DMT multiplex may be increased to 35 for a possible IDFT length of 35840.

The method of multiplexing and the parameters discussed so far are shown in Figure 6-4.

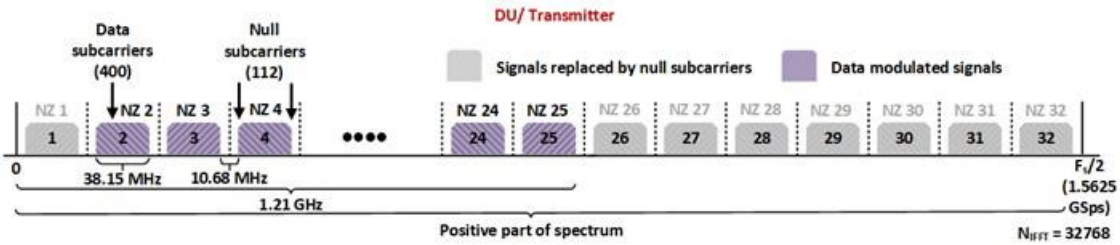

Figure 6-4 Multiplexing 32 DMT/ 64 SSB signals using NZ mapping design and a single IFFT at the transmitter.

For DMT, there are 32 different signals (one in each NZ), (32 signals in the "positive" part of the spectrum, with their 32 conjugated counterparts in the "negative" part of the spectrum). In the case of SSB, there can be up to 64 signals within the same IFFT length (32 in the "positive" part of the spectrum and 32 more in the "negative" part of the spectrum).

The bandwidth of the signals and the frequency gaps shown in Figure 6-4, are calculated using the subcarrier spacing or bin size, δf, given by

$$\delta f = \frac{F_S}{N_{IFFT,total}} \quad . \tag{6-9}$$

Thus, the bandwidth per signal, $F_{BW,sig}$, is given by

$$F_{BW,sig} = \delta f \times N_{data,sub} \ , \tag{6-10}$$

and the bandwidth occupied by the frequency gap between each signal, $F_{BW,gap}$, can be calculated by

$$F_{BW,gap} = \delta f \times N_{null,sub} \ . \tag{6-11}$$

The aggregate bandwidth occupied by the DMT multiplex can be calculated from

$$BW_{total} = 2 \times \left\{ \left(F_{BW,sig} \times N_{mux,DMT} \right) + \left[F_{BW,gap} \times \left(N_{mux,DMT} - 1 \right) \right] \right\} \ , \tag{6-12}$$

while the bandwidth occupied by the SSB multiplex can be calculated from

$$BW_{total} = \left(F_{BW,sig} \times N_{mux,SSB} \right) + \left[F_{BW,gap} \times \left(N_{mux,SSB} - 1 \right) \right] \ . \tag{6-13}$$

The bandwidth occupied is the same for both types of multiplexes as the number of independent SSB signals is twice that of the DMT signals.

For F_s = 3.125 GSps and $N_{IFFT,total}$ = 32768, the bin size can be calculated from (6-9) to be 95.37 kHz. As show in Figure 6-4, the bandwidth per signal and the frequency gap between signals are 38.15 MHz and 10.68 MHz respectively (using (6-10) and (6-11)). Using (6-12) or (6-13), the total bandwidth occupied by the multiplex is 3.1 GHz. This results in an r_{OSC} of 1.01, which is clearly much lower than the required bandwidth to sampling rate ratio of 1.25.

To ensure that the generated multiplexed signal meets this requirement, 14 out of 64 SSB signals or 7 out of 32 DMT signals (7 in each of the “positive” and “negative” part of the spectrum) are replaced by null subcarriers. This is shown in Figure 6-4. For simplicity, the first NZ of the digital multiplex is also left void of a signal. As a result, a total of 48 SSB signals (24 DMT signals) are transmitted. This is also shown in the figure, albeit for the positive spectrum only.

Using (6-12) or (6-13) and taking the gap in the first Nyquist zone into account (97.66 MHz), as well as the signals replaced by null subcarriers, if $N_{mux,DMT}$ is replaced by $N_{finalmux,DMT}$ = 24 and $N_{mux,SSB}$ is replaced by $N_{finalmux,SSB}$ = 48, the new total bandwidth occupied by the SSB/ DMT multiplex is 2.42 GHz, resulting in an r_{OSC} of 1.29.

Assuming that the modulation level of each OFDM subcarrier is *M*, using solely DMT modulation, the aggregate data rate can be calculated from

$$R_{DMT} = N_{finalmux,DMT} \times F_{BW,sig} \times \log_2 M \ , \tag{6-14}$$

while the aggregate data rate of the SSB multiplex can be calculated from

$$R_{SSB} = N_{finalmux,SSB} \times F_{BW,sig} \times \log_2 M \ . \quad (6\text{-}15)$$

Since 16-QAM subcarrier modulation is used in this case, *M = 16*. Using (6-14) and (6-15), the maximum aggregate data rate of the DMT multiplex is 3.66 Gbps, while that of the SSB multiplex it is 7.32 Gbps.

At the RRU, the multiplex is captured via an Oscilloscope using the same sampling rate that was used to generate it at the AWG (F_s). It then undergoes offline processing in MATLAB in the manner described in Section 5.3.

The de-multiplexing process at the receiver via the MATLAB receiver function is illustrated in Figure 6-5. The figure shows an example of how Signal 2, which is the first signal of the multiplex (from an even NZ) and Signal 25, which is the last signal of the multiplex (and in an odd NZ), are de-multiplexed at the RRU. Each of the signals in the positive part of the spectrum is filtered using a digital filter, after which it is down-sampled to the same centre frequency in the first NZ. The down-sampling process results in aliasing whereby mirror images of the filtered signal within the first and every other NZ of the spectrum are created, allowing a copy of the signal to be obtained from the first NZ. This down-sampling frequency used at the receiver is pre-determined and is what governs the mapping of the signals in the multiplex created at the transmitter and the size of each NZ.

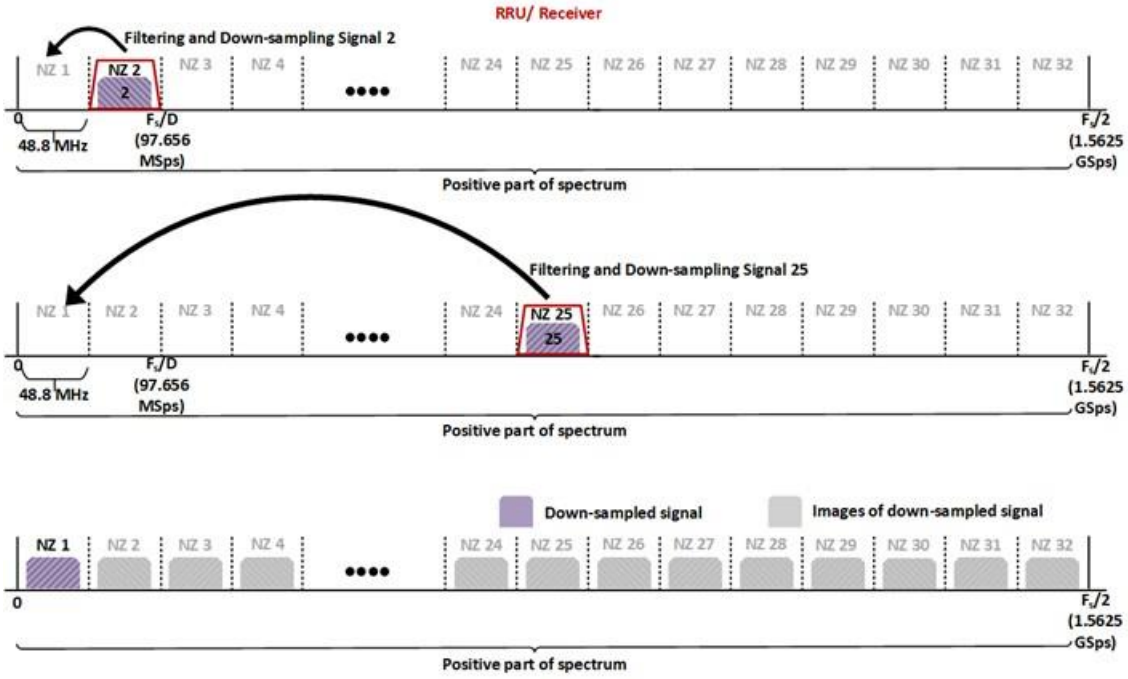

Figure 6-5 De-multiplexing 24 DMT/ 48 SSB signals at the receiver.

Using Equation (6-16), which is similar to (5-4) from Section 5.3 (in this case, $F_{s,down} = F_{s,final}$ and $F_{s,osc} = F_{s,rx}$), the down-sampling or final sampling rate used in the MATLAB receive function can be calculated to be

$$F_{s,down} = \frac{F_{s,osc}}{D} \text{for } D \in \mathbb{N}^+ \ , \tag{6-16}$$

with D, the decimation/ down-sampling factor, equal to the number of NZs.

Therefore, if N_{NZ} is the number of NZs

$$N_{NZ} = D \ . \tag{6-17}$$

If $N_{sigs,NZ}$ is considered to be the number of DMT signals per NZ, D can also be written as

$$D = \frac{N_{mux,DMT}}{N_{sigs,NZ}} \ , \tag{6-18}$$

and for SSB signals

$$D = \frac{N_{mux,SSB}}{2 \times N_{sigs,NZ}} \ . \tag{6-19}$$

Using (6-18) and (6-19), $N_{sigs,NZ} = 1$ in this case. Therefore, D is also equal to the number of signals (in the positive part of the spectrum).

In this case, $F_s = F_{s,OSC}$ as the sampling rate used to capture the multiplex in the Oscilloscope is the same as the one used to generate the multiplex at the AWG. For the DMT multiplex, if $F_{s,OSC}$ = 3.125 GSps and $D = 32$ (as there are 32 NZs for 32 DMT signals, regardless of the number of signals removed to stay within r_{OSC}), the final sampling rate following down-sampling is 97.656 MSps. This sampling rate is the same for the SSB multiplex as there are 32 signals in the "positive" part of the spectrum and 32 more signals in the "negative" part of the spectrum. From (6-11), the bandwidth of each NZ can be calculated to be 48.8 MHz.

Additional Formulae

- *CP addition and total number of transmitted samples*

The final IFFT length with CP is given by

$$N_{TotalIFFT,CP} = N_{IFFT,total} + (N_{IFFT,total} \times l_{CP}) \ , \tag{6-20}$$

where is the l_{CP} is the CP length. The CP length used in this work is 0.125, as shown in Table 6-1. For $N_{IFFT,total}$ = 32768, the $N_{TotalIFFT,CP}$ can be calculated to be 36864. Note that at the receiver/ RRU side, due to the processes of per-channel digital filtering and down-sampling, each individual channel will have its own decimated and appropriately sized CP and can thus be directly processed for transmission over the wireless channel.

The total number of samples, $N_{samples,total}$, transmitted in simulations and measurements can be calculated by

$$N_{samples,total} = N_{TotalIFFT,CP} \times N_{sym} \ , \tag{6-21}$$

Where N_{sym}, which is equal to 10, is the number of OFDM symbols. $N_{samples,total}$, can thus be calculated to be 368640.

The AWG has a maximum waveform (memory) length of 32 MSamples [185] while the Oscilloscope has a maximum waveform length of 62 MSamples [186]. The duration of the burst has to be such that at least two full bursts are captured at the Oscilloscope. The maximum waveform length for the Oscilloscope corresponds to a length of time, $t_{samples,max}$, of 625µs for a sampling rate of 100 GSps, which has been used in all experiments in this chapter. If a sampling rate, F_s, of 3.125 GSps is used, time duration of the signal, $t_{samples}$, is given by

$$t_{samples} = N_{samples,total} \ / \ F_s \ . \tag{6-22}$$

The time duration of the signal can be calculated to be 117.96μs. The number of bursts, N_{burst}, is given by

$$N_{burst} = \frac{t_{samples,max}}{t_{samples}} \ , \tag{6-23}$$

which is 5.3 bursts for 368640 samples and a sampling rate of 3.125 GSps.

- *Filter factors, channel index and passband calculation*

Once the sampling rate from the drop-down menu of the transmitter function is chosen, the 'Filter Factor' for each per-NZ filter and for each per-channel filter (for each channel within each NZ) is calculated. This factor is used to scale the passbands of these digital filters used in the receiver function, according to the chosen sampling rate and the different frequencies at which the multiplexed channels are located. This way, the passbands do not have to be changed manually every time a multiplex with different parameters (different sampling rate, channel bandwidth or number of channels) is created. The filter factor for each NZ, is given by

$$filtfactor_{NZ} = 10^{-2} \ / \ (2^{p}) \ \ , \tag{6-24}$$

while the factor for each channel in each NZ (only used when multiple channels reside within an NZ) is given by

$$filtfactor_{channel} = (10^{-2} \ / \ (0.2^{p})) - \ 0.001 \ \ . \tag{6-25}$$

In both these formulae, *p* is a factor that changes for each sampling rate. For a sampling rate of 3.125 GSps, this factor is 1 (it is 0 for 1.5625 GSps, -1 for 781.25 MSps and so on).

The start and end indices of each NZ can be calculated using a simple conditional loop and the per-NZ IFFT length

$$NZ_{start} = \ NZ_{start} + \ 1 \ , \tag{6-26}$$

and

$$NZ_{end} = \ NZ_{end} - 1 \ , \tag{6-27}$$

in which the initial value of NZ_{start} is 1 and the initial value of NZ_{end} is the per-NZ IFFT length. At the end of the first loop, NZ_{start} and NZ_{end} are updated to 513 and 1023, respectively and then to

1025 and 1535 and so on till NZ_{end} is (($N_{IFFT,total}$ /2)-2). Similar methods with number of data and null subcarriers are used to calculate start and end indices of each down-sampled channel.

The frequencies corresponding to these indices are calculated by simply using the bin-size parameter. Using Channel 2 from Figure 6-5 as an example, the passbands and stopbands of the filter per NZ can be calculated as follows

$$StopFreq1 = NZ_{start} * \delta f \ , \tag{6-28}$$

$$PassFreq1 = StopFreq1 + [StopFreq1 \times filtfactor_{NZ} \times (NZ_{start1}/NZ_{start}] \ , \tag{6-29}$$

$$StopFreq2 = NZ_{end} * \delta f \ , \tag{6-30}$$

$$PassFreq2 = StopFreq2 - [StopFreq2 \times filtfactor_{NZ} \times (NZ_{start1}/NZ_{end}] \ , \tag{6-31}$$

in which NZ_{start1} is the first start index (2) in the first NZ of the multiplex (all indices are calculated relative to this index). For Channel 2 in NZ 2, the start and end indices used for the filter are 513 and 1023 respectively. Using the previously calculated bin size of 95.367 kHz and (6-28) – (6-31), the values of StopFreq1, PassFreq1, StopFreq2 and PassFreq2 are 48.923 MHz, 48.924 MHz, 97.561 MHz and 97.560 MHz, respectively.

A similar method is used for the per-channel filters. Most of these calculations are carried out in the transmitter function, to reduce the amount of processing required in the receiver function.

6.3.3 Back-to-back Measurements at RF employing a Digital Multiplex with a Single Signal per NZ, a Generic Numerology and Different Subcarrier Modulation Formats

Figure 6-6 shows the experimental setup for b2b measurements using a subcarrier multiplex comprising 48 SSB/ 24 DMT signals (as discussed in the previous section), each with a bandwidth of 38.15 MHz (sampling rate of 3.125 GSps). The setup involves creating the multiplex in the digital domain using the MATLAB transmitter function and downloading it to the AWG. After analogue transmission via a short length of RF cable, the signals are captured using the Oscilloscope and de-multiplexed in MATLAB.

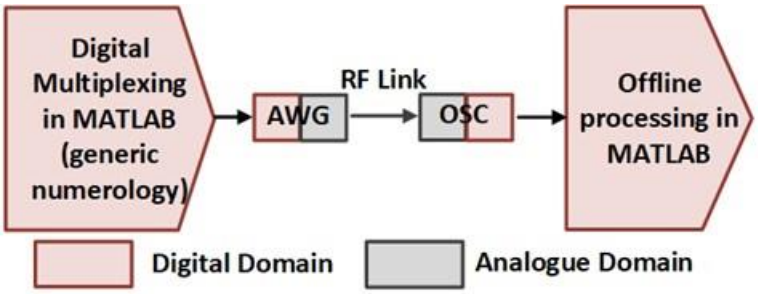

Figure 6-6 Back-to-back measurement setup.

Three different subcarrier modulation formats have been used for the back-to-back measurements. The results for Signals 2, 11, 18 and 25 of the multiplex for 16-QAM, 64-QAM and 256-QAM subcarrier modulation are shown in Figure 6-7, Figure 6-8 and Figure 6-9, respectively. Since the signal in the first NZ has been removed, Signal 2 is the first signal of the multiplex while Signal 25 is the last signal of the multiplex and Signals 11 and 18 have been chosen to represent the middle region of the multiplex.

As seen from the three figures, the range of EVMs for 16-QAM subcarrier modulation is from 3.5% to 4.7%, for 64-QAM subcarrier modulation it is from 3.9% to 5% and finally for 256-QAM, it is from 3% to 4%. For 16-QAM and 64-QAM, EVM performance is well within the 3GPP specification limits [74] of 12.5% for 16-QAM and 8% for 64-QAM but for 256-QAM, the specification limit of 3.5% is exceeded. The EVM performance of 256-QAM is better than that of 16-QAM and 64-QAM. Note that as these signals have the same power, there is no particular reason behind this observed behaviour (EVM given as a percentage of the rms value of the constellation is independent of modulation level). Thus, it can be attributed to stochastic symbol variations originating from the different seed values used in the pseudo-random symbol generation.

As a result, for the experimental results shown in Section 6.3.4 and elsewhere, 16-QAM subcarrier modulation has been used. However, most of the results are also valid for 64-QAM subcarrier modulation.

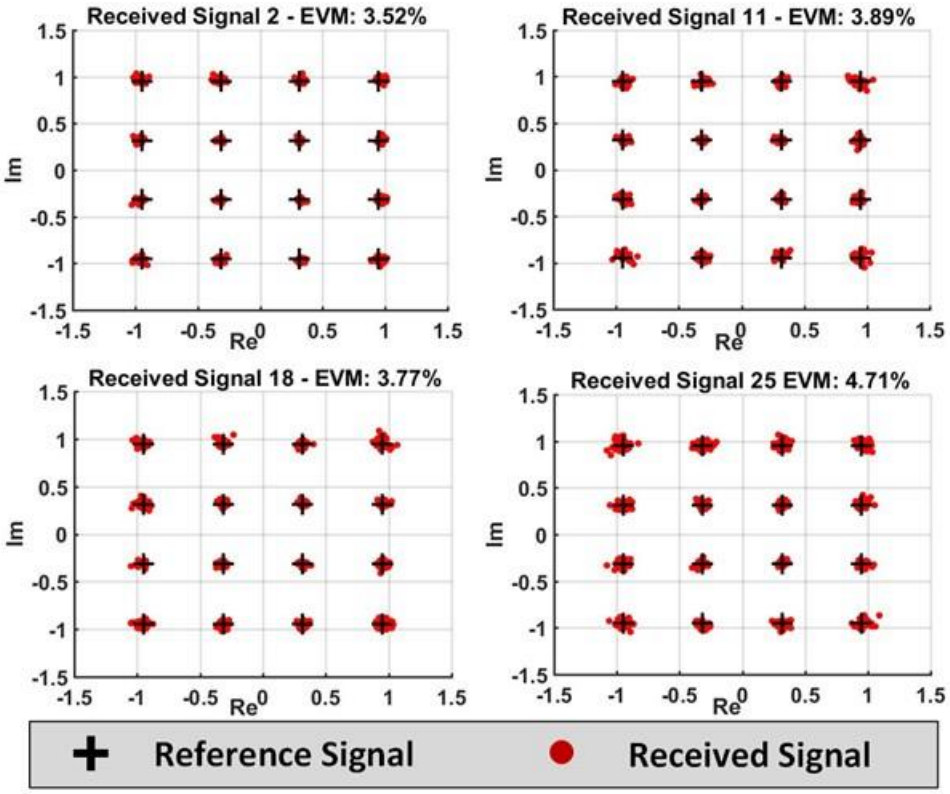

Figure 6-7 Back-to-back measurement results with 16-QAM subcarrier modulation.

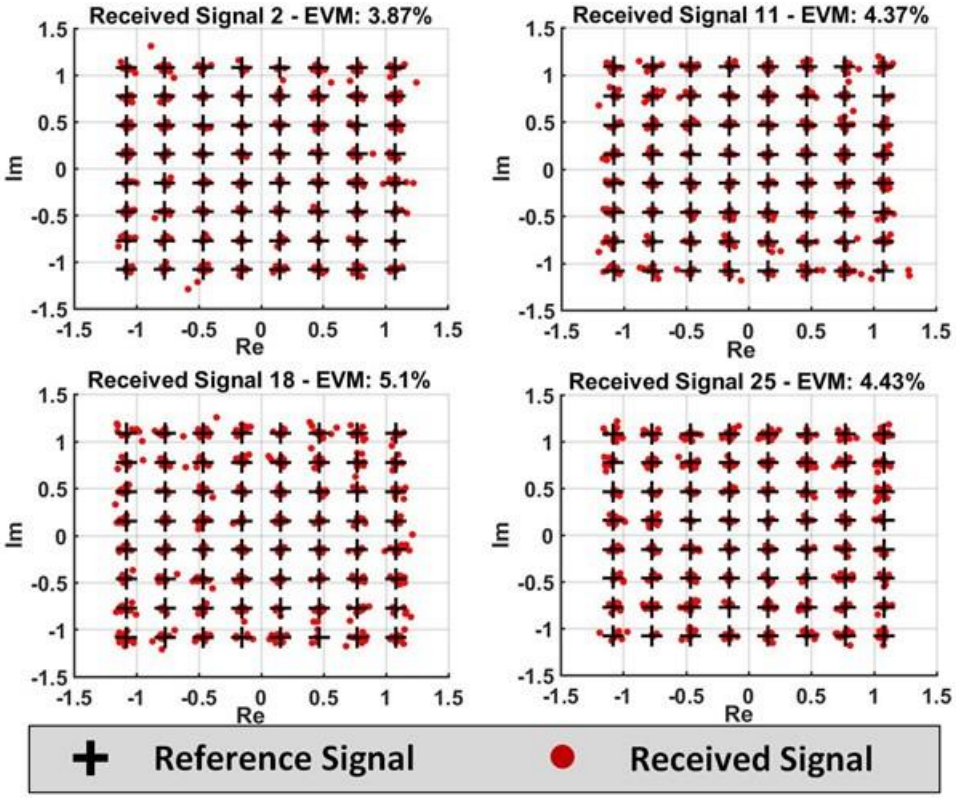

Figure 6-8 Back-to-back measurement results with 64-QAM subcarrier modulation.

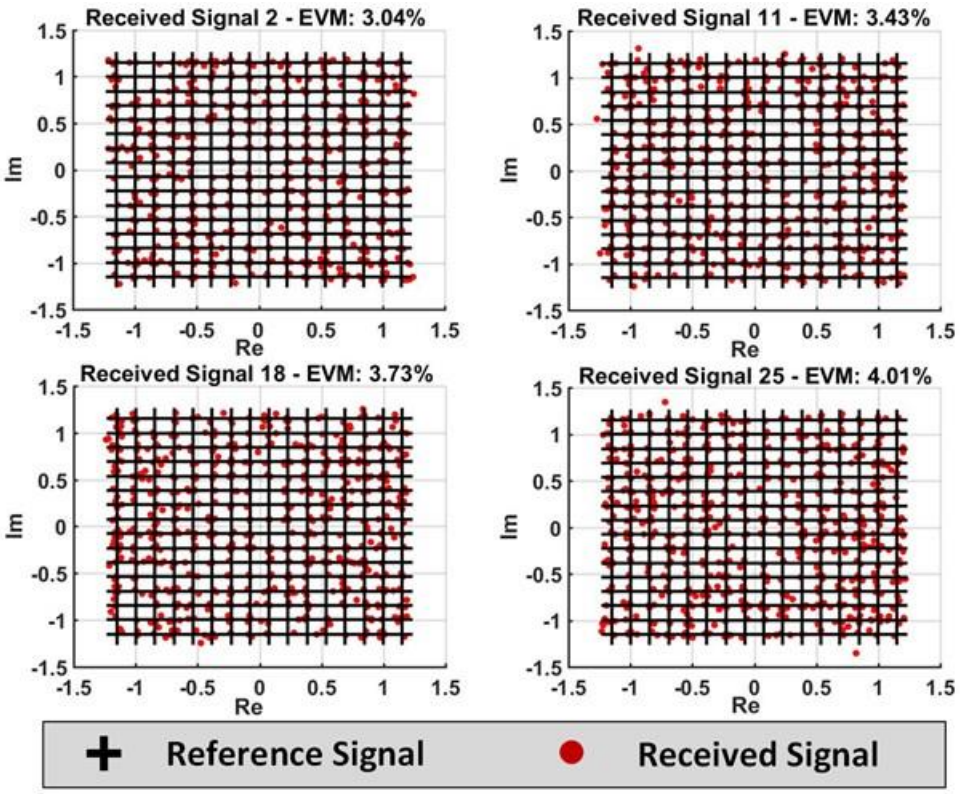

Figure 6-9 Back-to-back measurement results with 256-QAM subcarrier modulation.

6.3.4 External IM-DD Experiments at RF employing a Digital Multiplex with a Single Signal per NZ and a Generic Numerology

Due to equipment limitations, some modifications have been made in the experimental setup compared to the concept diagram shown in Figure 6-1. Separate fibres have been used for the signal multiplexes and the sidebands for mmW up-conversion (thus, the DWDM filter in the RRU in Figure 6-1 was not required). Only one EDFA has been used and due to power limitations in the setup, the RF multi-way splitter was not used. Lastly, the functions of the THA-ADC have been performed by a real-time oscilloscope.

Figure 6-10 illustrates the experimental setup while the outputs at different stages of the experimental setup (points A – C) are shown in Figure 6-11 and are discussed next.

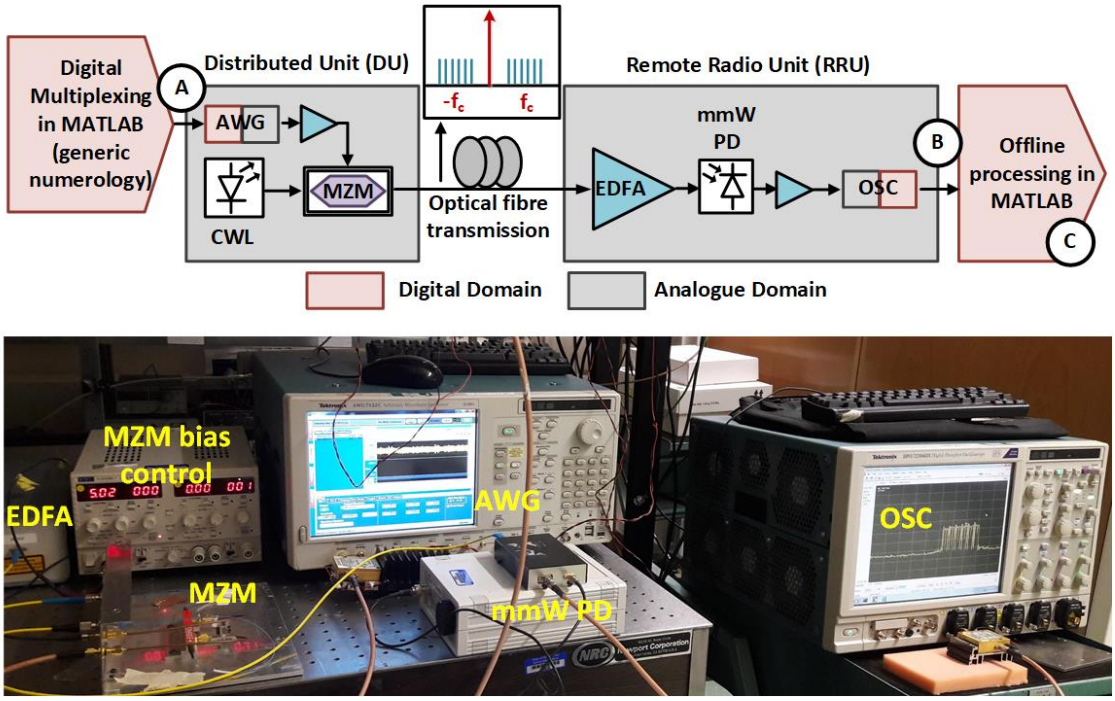

Figure 6-10 External IM-DD experiments (Top: schematic; Bottom: actual laboratory testbed) at RF with DMT and SSB modulated multiplexes using a single IFFT and generic numerologies (device models and parameters shown in Table 6-2).

In these experiments, the same multiplex that was used for the b2b measurements is used. The resulting spectrum is shown in Figure 6-11 A. The multiplex is downloaded to the AWG, which up-converts it to an RF frequency (f_c) of 1.5625 GHz. The optical carrier from the CWL is intensity modulated by the up-converted multiplex, with an MZM biased at an optimum working point between quadrature and null [109].

The devices and the parameters used in the experimental setup are shown in Table 6-2.

Table 6-2 Devices and parameters used in External IM-DD digital SCM experiments at RF

Type of Device	**Device Model and Parameters**
Continuous Wave External Cavity Laser (CWL)	Agilent 8164A Lightwave Measurement System
	Wavelength used: 1554.6nm, max. 5 dBm optical power
Arbitrary Waveform	Tektronix AWG7122C Arbitrary Waveform Generator 12 GS/s; 3-dB bandwidth: 6 GHz (but poor frequency response beyond 4

Generator (AWG)	GHz)
	Maximum sampling rate that can be set for user-defined signals: 3.125 GS/s (used in most experiments), due to only standard sampling rates supported by the Oscilloscope (when capturing signals); Output power: 1 V p-p (max.)
RF Amplifier (after AWG)	SHF 824; Frequency range: 30 kHz - 30 GHz; Gain: 17 dB (typical); DC bias: +13 V; Noise figure: 3dB
Mach-Zehnder Modulator (MZM)	EOSPACE AX-OK5-10-PFU-PFUP-UL-S Single-arm MZM; 3 dB bandwidth: 10 GHz; Loss: 6.5 dB
	Accompanied by PL303QMD-P Quad Mode Dual Power Supply 30 V 3A/6A; Bias set: 5.5 V
Erbium Doped Fiber Amplifier (EDFA)	EFA 2020 Fiber Amplifier; Gain: 37 dB (-40 dBm input power); Noise figure: 6 dB
mmW Photodiode (PD)	U2T XPV2140R-VF-VP Ultrafast Photodetector; Responsivity: 0.7 A/W; 3 dB bandwidth: 45 GHz (max.); Wavelength range: 1480-1620nm; Accompanied by PPS Photodetector Power Supply
RF Amplifier (before Oscilloscope)	SHF 100 AP; Frequency range: 50 kHz - 20 GHz; Gain: 19 dB (typical); DC Bias: +9 V; Noise figure: 5.5 dB
Oscilloscope (OSC)	Tektronix DPO72304DX Digital Phosphor Oscilloscope; Bandwidth: 23 GHz; Maximum Sampling Rate: 100 GS/s

After transmission over a short length (1 metre) of optical fibre and amplification via an EDFA, the resulting spectrum (one-sided) at the output of the photodiode at the RRU after RF amplification is shown in Figure 6-11 B. The roll-off at higher frequencies is a result of the AWG's sinc-type amplitude response [163]. The multiplexed signals are captured by the Oscilloscope and processed offline by a MATLAB receive function. The constellation diagrams of Signals 2, 11, 18 and 25 of the multiplex (similar to those shown in the b2b measurement results) are shown in Figure 6-11 C. The range of EVM results is from 4% for signals at lower frequencies to 7% for signals closer to 4 GHz, showing EVM performance well within the 3GPP specification limit of

12.5% for 16-QAM. The worse performance for the signals at higher frequencies is a result of the AWG's amplitude response.

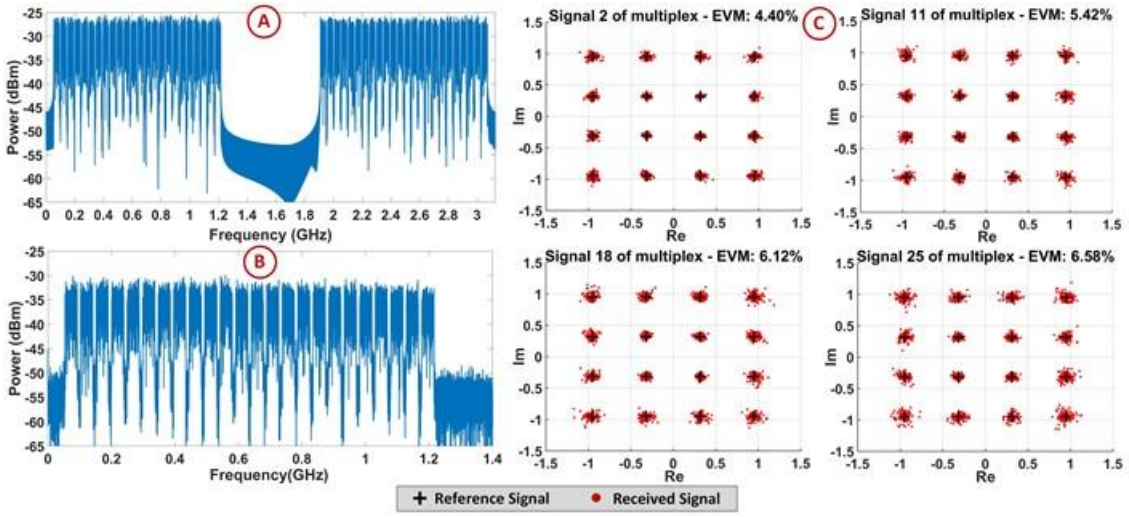

Figure 6-11 A. Transmit spectrum of 64 SSB/DMT signal multiplex as seen in MATLAB; B. Received spectrum (one-sided) at the oscilloscope; C. EVM/ constellation diagrams of Signals 2, 11, 18 and 25 of multiplex (corresponding to points A, B and C of Figure 6-10).

The EVM (% rms) for each signal in the multiplex versus the MZM bias voltage, which has been varied from 1 V to 6.5 V, is shown in Figure 6-12. The performance of each signal is different at each bias point but the best overall performance is at a bias point of 5.54 V. This can be seen more clearly from the Average EVM (% rms) trace (black dashed line).

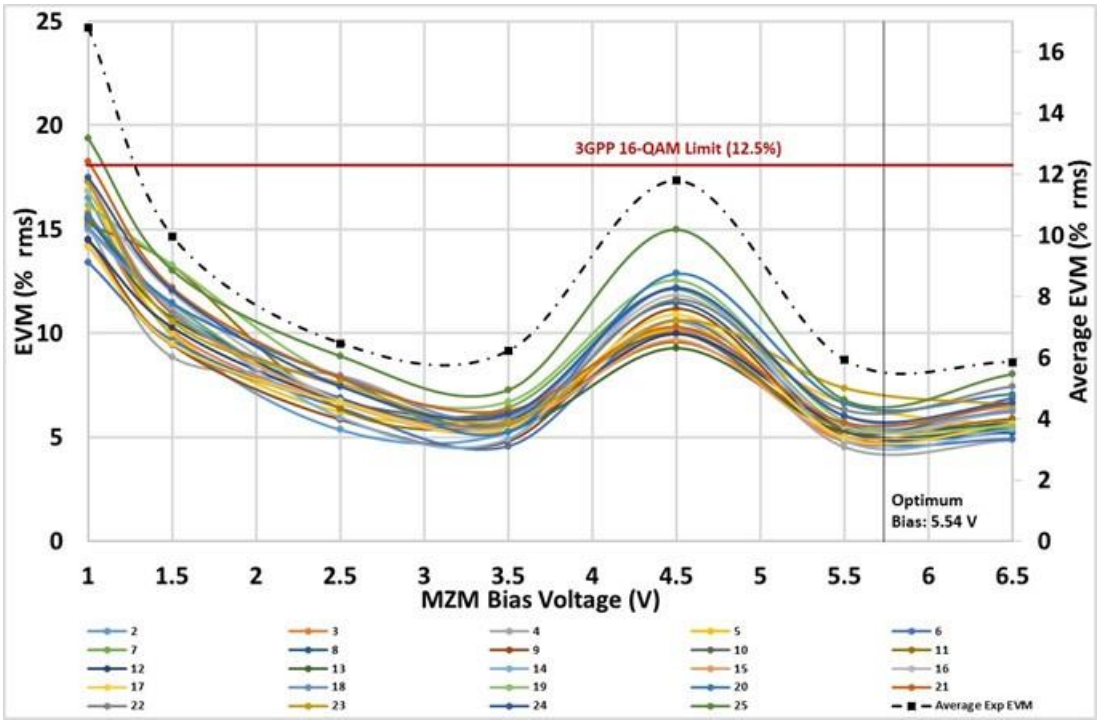

Figure 6-12 EVM and Average EVM (% rms) vs MZM Bias Voltage for all signals in the multiplex. Note that the lines between measurement points are only for an aid for viewing the results and do not represent predicted trends.

The mmW up-conversion of selected signals of this multiplex is demonstrated later in Section 6.5.

6.3.5 Further Experiments at RF employing Digital Multiplexes and Generic Numerologies

This section and its sub-sections discuss different types of experiments conducted at RF frequencies using digital multiplexes employing generic numerologies.

6.3.5.1 Experiments with Variable Sampling Rates, Signal Bandwidths and Number of Signals

The number of signals, signal bandwidth and sampling rates have been varied for digital multiplexes employing a generic numerology and a single IFFT, in order to examine the effects

of these variations on the performance of the multiplexed signals via the experimental setup shown in Figure 6-10. Considering only the positive part of the spectrum, 32 DMT/ SSB signals were multiplexed using 450 and 250 data subcarriers (24 and 25 signals were transmitted respectively to maintain the bandwidth to sampling rate ratio) and 16 signals were multiplexed using 950 and 850 data subcarriers (11 were transmitted to maintain the bandwidth to sampling rate ratio). The per-NZ IFFT length for the 32-signal multiplex is 512 while that of the 16-signal multiplex is 1024, resulting in a total IFFT length of 32768 for all the multiplexes. For simplicity, the terms "32-signal multiplex" and "16-signal multiplex" have been used in the rest of the figures in this section.

Three different sampling rates (3.125 GSps, 1.5625 GSps and 781.25 MSps) have been used for all these multiplexes. Table 6-3 shows a summary of all the parameters, along with the bandwidth per signal, aggregate bandwidth occupied by the multiplex and the data rates of each SSB multiplex (the data rate for the DMT multiplex is half that of the SSB multiplex). Figure 6-13 shows how the signals are mapped in these different multiplexes for any chosen sampling rate. The multiplexes are created using the same techniques shown in Section 6.3.2, albeit using different numbers of signals, data subcarriers and null subcarriers.

Table 6-3 Parameters used for measurements with different numbers of signals, data subcarrier and sampling rates

Number of DMT/ SSB Signals Multiplexed	**Number of DMT/ SSB Signals Transmitted**	**Number of Data Subcarriers**	**Bandwidth per Signal/ Total Bandwidth/ Data Rates for different Sampling Rates (SSB); Total IFFT Length: 32768**		
			3.125 GSps (Bin Size: 95.4 kHz)	**1.5625 GSps (Bin Size: 47.7 kHz)**	**781.25 MSps (Bin Size: 23.8 kHz)**
32 / 64	24/ 48	450	42.9 MHz/ 2.44 GHz/ 8.24 GSps	21.45 MHz/ 1.22 GHz/ 4.12 GSps	10.73 MHz/ 610 MHz/ 2.06 GSps
	25/ 50	250	23.8 MHz/ 2.5 GHz/ 4.77 GSps	11.9 MHz/ 1.25 GHz/ 2.39 GSps	5.95 MHz/ 625 MHz/ 1.2 GSps

16/ 32	11/ 22	950	90.6 MHz/ 2.34 GHz/ 7.97 GSps	45.3 MHz/ 1.17 GHz/ 3.99 GSps	22.7 MHz/ 585 MHz/ 1.99 GSps
	11/ 22	850	81.1 MHz/ 2.33 GHz/ 7.13 GSps	40.6 MHz/ 1.17 GHz/ 3.57 GSps	20.3 MHz/ 585 MHz/ 1.77 GSps

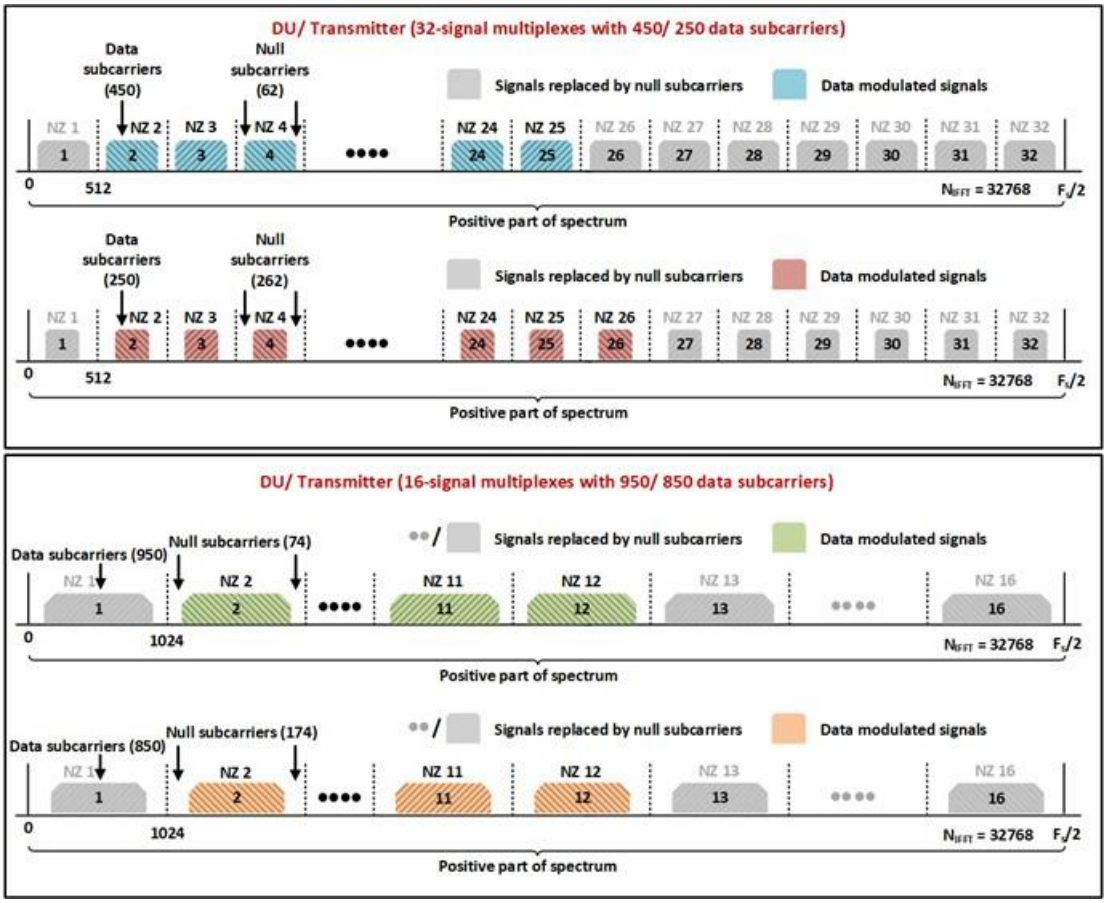

Figure 6-13 Multiplexing 32 DMT/ 64 SSB and 16 DMT/ 32 SSB signals using NZ mapping design, variable signal bandwidths and a single IFFT at the DU/ Transmitter (positive part of spectrum).

Figure 6-14 shows the EVM (% rms) versus the signal number for the 32-signal multiplex (again, only the positive part of the spectrum is considered in these results). The EVM performance of the multiplex employing 250 data subcarriers is better than that of the multiplex employing 450 data subcarriers for 1.5625 GSps and 3.125 GSps. The EVM performances of both multiplexes employing a sampling rate of 781.25 MSps are worse than those with the higher sampling rates.

The overall EVM range is from 4% to 10% (4% to 8% for sampling rates of 1.5625 GSps and 3.125 GSps), with the signals at higher frequencies having worse EVM performance.

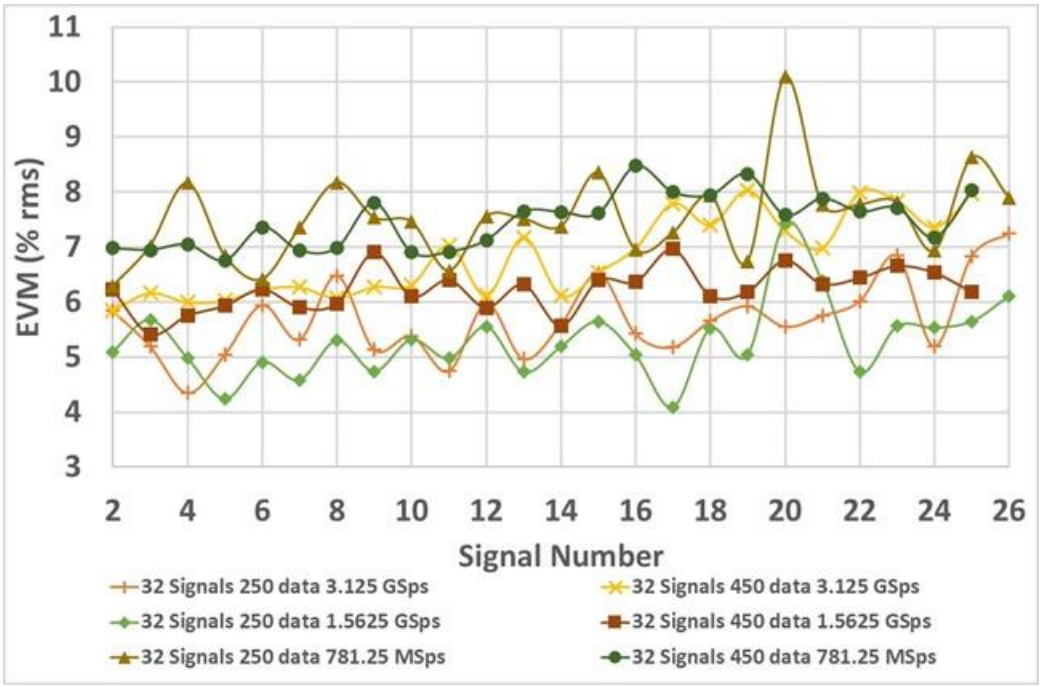

Figure 6-14 EVM (% rms) results of 32 DMT/ 64 SSB signal multiplex employing different numbers of data subcarriers and sampling rates (only positive part of spectrum). Note that the lines between measurement points are only for an aid for viewing the results and do not represent predicted trends.

Figure 6-15 shows the EVM (% rms) versus the signal number for the 16-signal multiplex. The EVM performance of the multiplexes employing 1.5625 GSps is better than that of the multiplexes employing 3.125 GSps. Again, the EVM performances of both multiplexes employing a sampling rate of 781.25 MSps are much worse than those with the higher sampling rates. The overall EVM range is from 5.5% to 9.8% (5.5% to 7.6% for sampling rates of 1.5625 GSps and 3.125 GSps), with the signals at higher frequencies having worse EVM performance.

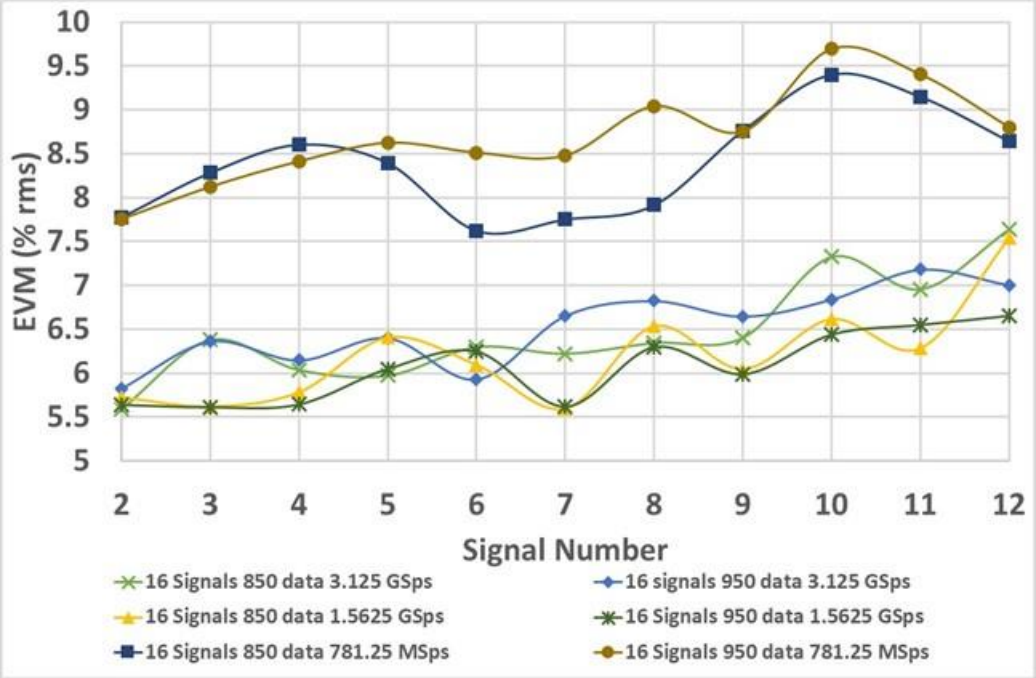

Figure 6-15 EVM (% rms) results of 16 DMT/ 32 SSB signal multiplex employing different numbers of data subcarriers and sampling rates (only positive part of spectrum). Note that the lines between measurement points are only for an aid for viewing the results and do not represent predicted trends.

Finally, Figure 6-16 shows the average EVM (% rms) versus the number of data subcarriers for different numbers of signals and different sampling rates (again, only the positive part of the spectrum is considered in these results). This average EVM takes all the signals into account (24/ 25 for the 32-signal multiplex and 11 for the 16-signal multiplex in the positive part of the spectrum).

The EVM performance of the multiplexes employing 1.5625 GSps (with 850 and 950 data subcarriers) is better than that of the multiplexes employing 3.125 GSps. Moreover, for both of these sampling rates, the EVM performance of the 32-signal multiplex employing the 450 data subcarriers seem to have worse EVM performance compared to the 16-signal multiplex with 950 data subcarriers, possibly due to the smaller gaps used between the signals for the 450 data subcarrier multiplex. Again, the average EVM is much higher for all the multiplexes using a sampling rate of 781.25 MSps. The figure also shows that while the multiplexes employing 1.5625 GSps and 3.125 GSps show a similar trend, this is not the case for 781.25 MSps multiplex. Multiplexes with a smaller number of signals and larger signal bandwidths have a much higher average EVM for a sampling rate of 781.25 MSps, compared to 3.125 GSps and 1.5625 GSps.

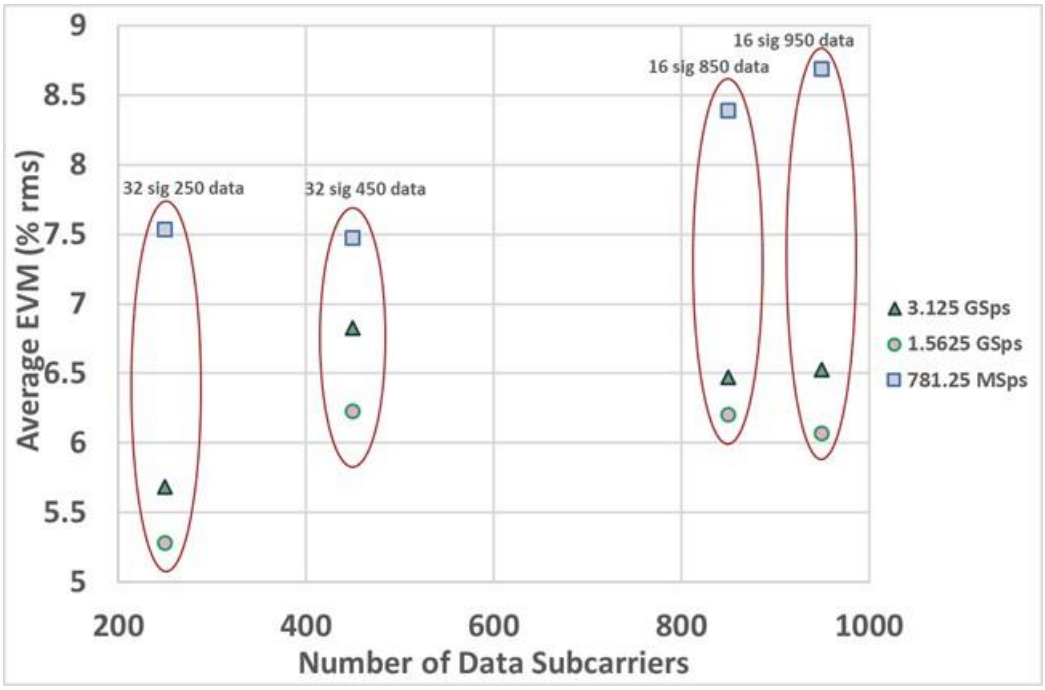

Figure 6-16 Average EVM (% rms) results of 16 DMT/ 32 SSB and 32 DMT/ 64 SSB signal multiplexes for different sampling rates versus different number of data subcarriers (only positive part of spectrum).

6.3.5.2 Experiments with a DFB Laser (direct IM-DD)

For a low cost alternative to external modulation via an MZM, experiments with digitally multiplexed DMT and SSB modulated signals using a single IFFT and generic numerologies have also been carried out using direct modulation via a DFB Laser. The experimental setup for direct IM-DD is shown in Figure 6-17.

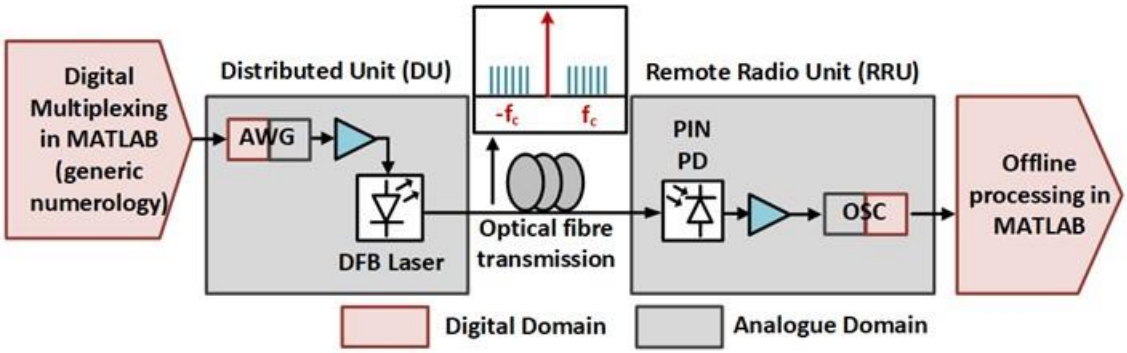

Figure 6-17 Direct IM-DD experiments at RF using a DFB laser with DMT and SSB modulated multiplexes using a single IFFT and generic numerologies

The setup consists of a Teradian DFB Laser and an Appointech PIN Photodiode (these device parameters are summarised in the Appendix, Table 9-1). A 32 DMT/ 64 SSB signal multiplex with 16-QAM subcarrier modulation and 450 data subcarriers (shown in Figure 6-13) is used in these experiments. As with all experiments so far, a carrier frequency of 1.5625 GHz has been used. Figure 6-18 shows the spectrum of the signals captured by the oscilloscope after transmission via the link.

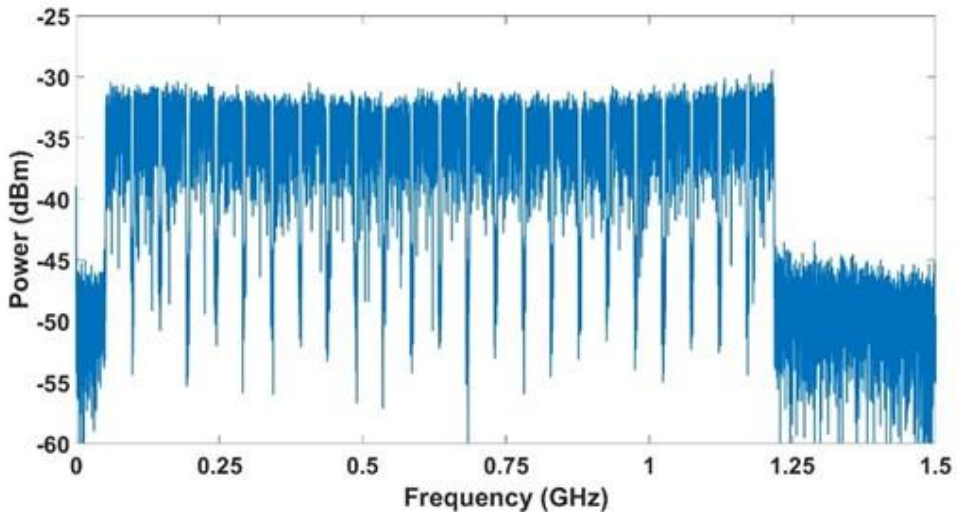

Figure 6-18 Received spectrum (one-sided) at the oscilloscope for direct IM-DD.

Figure 6-19 shows the spectra and EVM/ Constellation diagrams of Signals 2, 10, 17 and 25 of the multiplex. Signal 2 is the first signal of the multiplex while Signal 25 is the last signal of the multiplex and Signals 10 and 17 have been chosen to represent the middle region of the

multiplex. As shown in the figure, the EVM performance (from 6.2% to 9.2%) is slightly worse compared to external IM-DD due to the frequency response and higher noise floor of direct IM-DD.

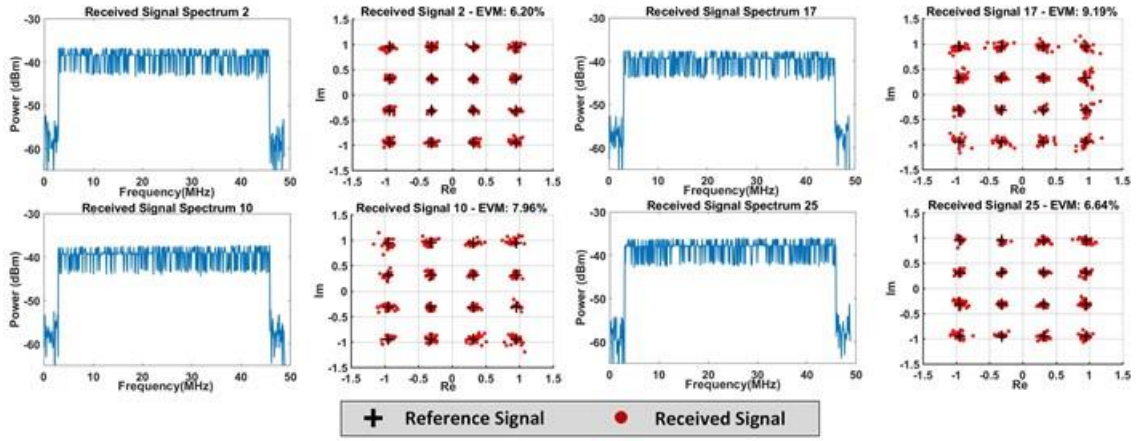

Figure 6-19 Spectra and EVM/ constellation diagrams of Signals 2, 10, 17 and 25 of multiplex for direct IM-DD.

6.4 Experiments at RF with DMT and SSB Modulated Multiplexes and 5G Numerology

6.4.1 Multiplexes with Two Different Bandwidths and 5G Numerologies

External IM-DD experiments have been carried out with mixed bandwidth signals by combining two different signal sets (produced from two different IFFTs), employing different 5G numerologies. These results do not consider mmW up-conversion and are obtained using the same experimental setup as shown in Figure 6-10, albeit with some changes in the digital multiplexing and de-multiplexing stages. The modified experimental setup is shown in Figure 6-20. .

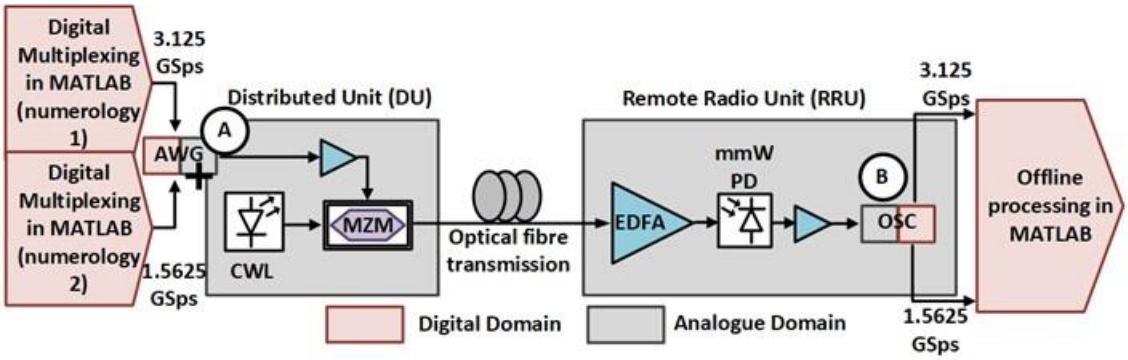

Figure 6-20 External IM-DD experimental setup for experiments at RF with DMT and SSB Modulated Multiplexes using 5G Numerology.

As shown in the figure, multiplexes or signal sets employing two different numerologies are created via the MATLAB transmit function at the DU. These multiplexes denoted Signal Set 1 (employing 5G numerology 1) and Signal Set 2 (employing 5G numerology 2) from here onwards, are downloaded to the AWG. Signal Set 1 has a sampling rate ($F_{s,num1}$) of 3.125 GSps while Signal Set 2 has a sampling rate ($F_{s,num2}$) of 1.5625 GSps. The two signal sets are combined using the multicarrier modulation option of the AWG, i.e. in the digital domain. This block of multiplexed signals is then modulated onto a carrier frequency f_c (which is the same as the one used in Section 6.3.4) using an MZM. Once the signals are detected by the PD at the receiver, they are captured twice by the Oscilloscope, once using $F_{s,num1}$ and the second time using $F_{s,num2}$. The reason for this will be explained later on in this section.

In order to demonstrate a general use case, two signal sets are multiplexed by mapping one signal from each numerology to each NZ, resulting in two signals per NZ when the multiplexes are combined. This NZ corresponds to the larger of the per-signal IFFT lengths of the two signal sets. The mapping of signals using two different numerologies is shown in Figure 6-21. Again, for ease of explanation, only the positive part of the spectrum is shown for each signal set.

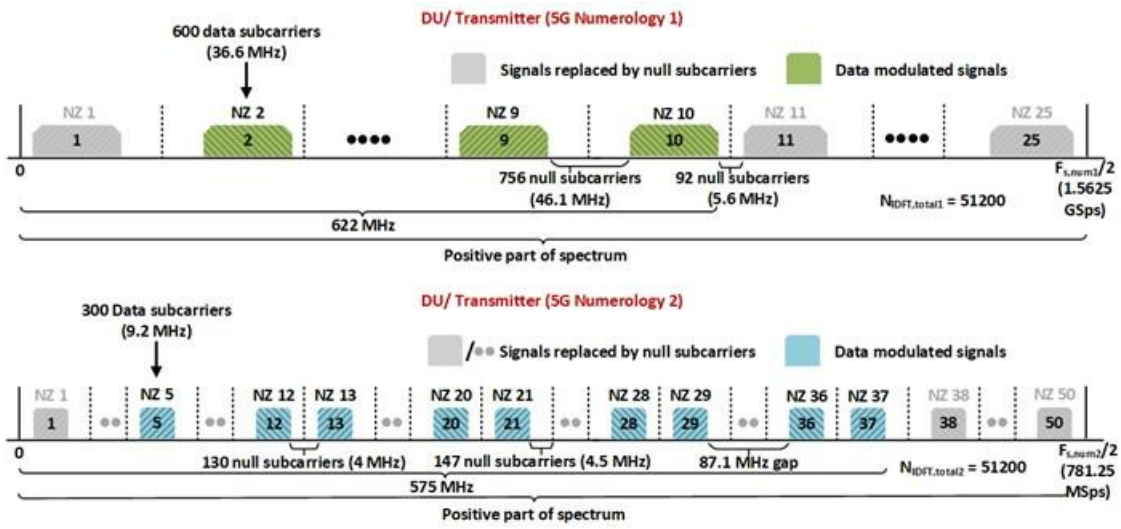

Figure 6-21 Mapping signals at the DU/ Transmitter using two different 5G numerologies

Signals employing the first numerology (Signal Set 1) are made up of 600 data subcarriers each, corresponding to a per-NZ IFFT length of 1024 at the RRU. Since the oscilloscope allows only particular sampling rates, 50 SSB signals/ 25 DMT signals are multiplexed and a non-power of 2 IFFT length ($N_{IDFT,total1}$) of 51200 is used to obtain a frequency bin size, δf_1, given by

$$\delta f_1 = \frac{F_{s,num1}}{N_{IDFT,total1}} \ . \tag{6-32}$$

The result is a bin size of 61.035 kHz for Signal Set 1 (close in value to the 5G frequency bin size of 60 kHz). It should be noted that when using a non-power of 2 IDFT, it is preferable to choose a value that is easily divisible by 2 by the decimation factor to be used at the RRU.

In order to accommodate signals from the second signal set, signals in this set are not positioned at the centre of each NZ, as shown in Figure 6-21. This results in two different gaps between signals in an even NZ and an odd NZ (46.1 MHz and 5.6 MHz) due to the different distribution of null subcarriers between signals. The bandwidth of each signal is 36.6 MHz, which corresponds to a 40 MHz 5G signal. Signal Set 1 occupies a total bandwidth of 1.244 GHz (2x622 MHz, including both the "positive" and "negative" side spectra).

Signals of the second numerology (Signal Set 2) are made up of 300 data subcarriers each, corresponding to a per-NZ IFFT length of 512 at the RRU. A total of 100 SSB/50 DMT signals are multiplexed, resulting in a total IFFT length ($N_{IDFT,total2}$) of 51200 and a bin size, δf_2, given by

$$\delta f_2 = \frac{F_{s,num2}}{N_{IDFT,total2}} \ . \tag{6-33}$$

This results in a bin size of 30.518 kHz, (close in value to the 5G frequency bin size of 30 kHz). The bandwidth per signal can be calculated to be 9.2 MHz, which corresponds to 10 MHz 5G signals. Again, there are variable gaps of 4 MHz and 9 MHz between signals in even and odd NZs. Signal Set 2 occupies an aggregate bandwidth of 1.15 GHz (2x575 MHz).

The sampling rate used by the first signal set is twice that of the sampling rate used by the second signal set. This results in four NZs in the second signal set corresponding to one NZ in the first signal set. Appropriate gaps in the frequency domain are thus created in the second signal set as well (such as the 87.1 MHz gaps shown in Figure 6-21) allowing for the two signal sets to be combined and aiding the filtering process at the receiver. Moreover, null subcarriers to maintain the bandwidth to sampling rate ratio of the oscilloscope, taking the different sampling rates into account, replace data subcarriers from both multiplexes. A total of 36 SSB signals (18 from each set) are transmitted and as 16-QAM subcarrier modulation is used, the resulting aggregate data rate is 3.3 Gbps (for SSB modulation).

The ability to multiplex signals using this technique in a spectrally efficient manner is demonstrated in Figure 6-22 by the narrow gaps between the signals: 11.8 MHz between a wide bandwidth (from Signal Set 1) and narrow bandwidth signal (from Signal Set 2), 5.3 MHz between two wide bandwidth signals and 3.7 MHz between two narrow bandwidth signals.

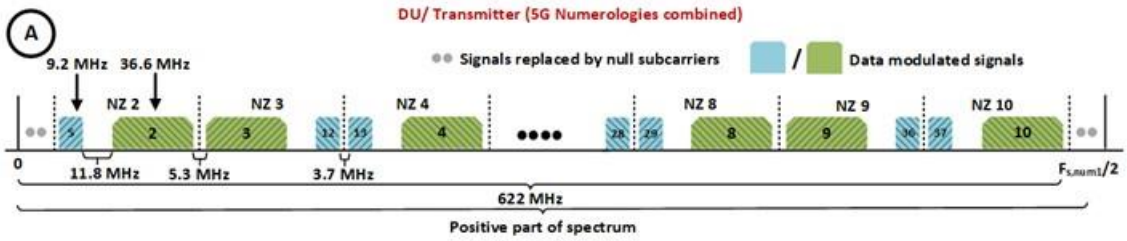

Figure 6-22 Signal sets with different 5G numerologies combined at the DU/ Transmitter.

Figure 6-23 shows the positive-sided spectra of the received signals from the oscilloscope (Point B of Figure 6-20). As mentioned earlier, the signals are captured once using a sampling rate ($F_{s,num1}$) of 3.125 GSps and a second time using a sampling rate ($F_{s,num2}$) of 1.5625 GSps. Using the MATLAB receive function, the first capture is down-sampled using a factor of D_1. This is equal to the number of multiplexed signals in Signal Set 1 in the positive part of the spectrum (D_1 = 25). The sampling rate ($F_{s,down1}$) at the receiver for Signal Set 1 can be calculated from

$$F_{s,down1} = \frac{F_{s,num1}}{D_1} \text{for } D_1 \in \mathbb{N}^+ \ , \tag{6-34}$$

while the sampling rate ($F_{s,down2}$) at the receiver for Signal Set 2 can be calculated from

$$F_{s,down2} = \frac{F_{s,num2}}{D_2} \text{for } D_2 \in \mathbb{N}^+ \ , \tag{6-35}$$

where $D_2 = 50$ (number of signals in the positive spectrum of Signal Set 2). The down-sampling rates of Signal Set 1 and 2 are thus 125 MSps and 31.25 MSps, respectively.

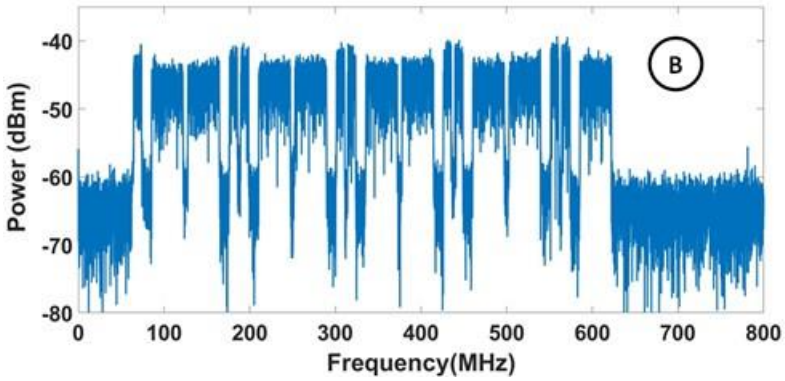

Figure 6-23 Received 36-signal multiplex with mixed bandwidth signals employing 5G numerology (positive side of spectrum) (Point B of Figure 6-20).

Figure 6-24 shows the received signal spectra and constellation diagrams (with annotated EVM % rms) of selected signals from the two signal sets. Signals 2 (EVM of 5.19%) and 10 (EVM of 6.34%) have been chosen from Signal Set 1 while Signals 5 (EVM of 5.88%) and 37 (EVM of 5.89%) have been chosen from Signal Set 2. This has been done to provide an overview of achieved EVM performance for the two signal sets as the chosen signals are the first and last channels from each signal set.

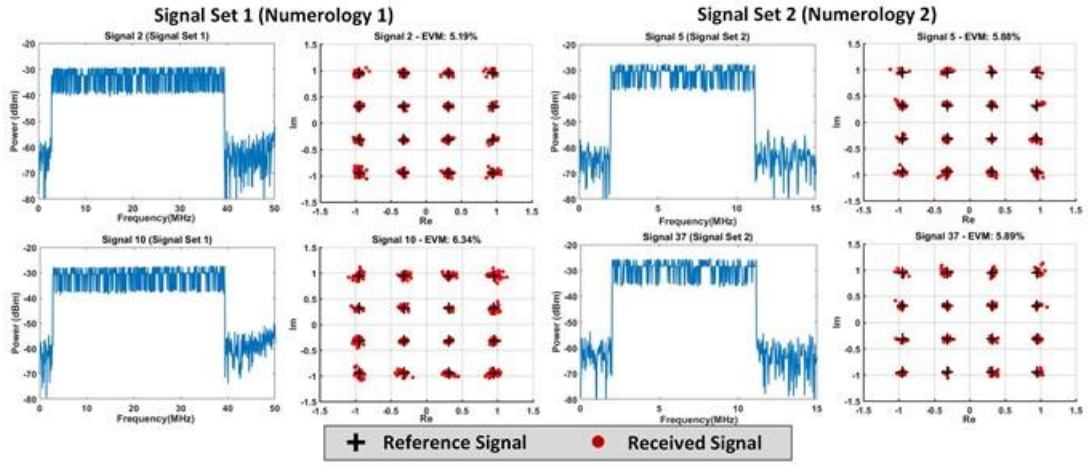

Figure 6-24 Received signal spectra and constellation diagrams (with EVM % rms) of selected signals from Signal Sets 1 and 2 employing different 5G numerologies.

6.4.2 Multiplexes with One 5G Numerology and Two Different Bandwidths

Signals employing a single 5G numerology (via a single IFFT) but with different bandwidths can be mapped within one NZ. Figure 6-25 shows how this can be achieved using a single IFFT.

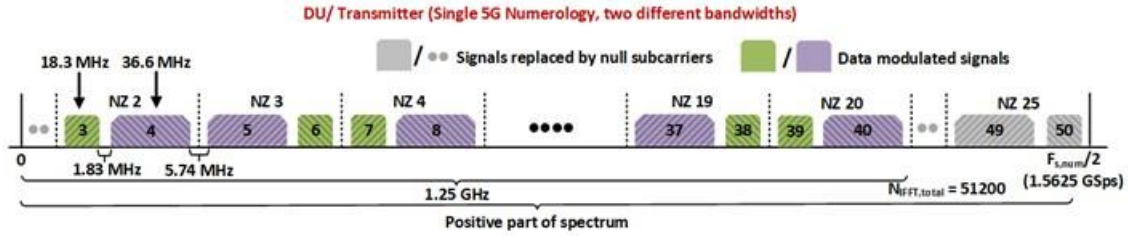

Figure 6-25 38-signal (positive part of the spectrum) mixed bandwidth multiplex employing a single 5G numerology

In the figure, 76 signals (38 in the positive part of the spectrum) out of 100 signals (24 deducted to maintain the bandwidth to sampling rate ratio) are multiplexed within a total IFFT length ($N_{IFFT,total}$) of 51200 and total bandwidth of 2.5 GHz (2x1.25 GHz). A sampling rate (denoted by $F_{s,num}$) of 3.125 GSps leads to a frequency bin size of 61.035 kHz. 300 and 600 data subcarriers are accommodated within each NZ (having per-NZ IFFT length of 1024), resulting in 18.3 MHz

and 36.6 MHz signals, respectively. Using (5-16) to (5-19), since $N_{mux,DMT}$ = 50 and $N_{sigs,NZ}$ = 2 in this case, D can be calculated to be 25 and $F_{s,down}$ is 125MSps.

Considering that there are 38 signals of each bandwidth and that 16-QAM subcarrier modulation is used, the aggregate data rate is 8.3 GSps. Figure 6-26 shows the performance of selected signals from the multiplex following the analogue radio-over-fibre transport at RF using the same experimental setup shown in Figure 6-10.

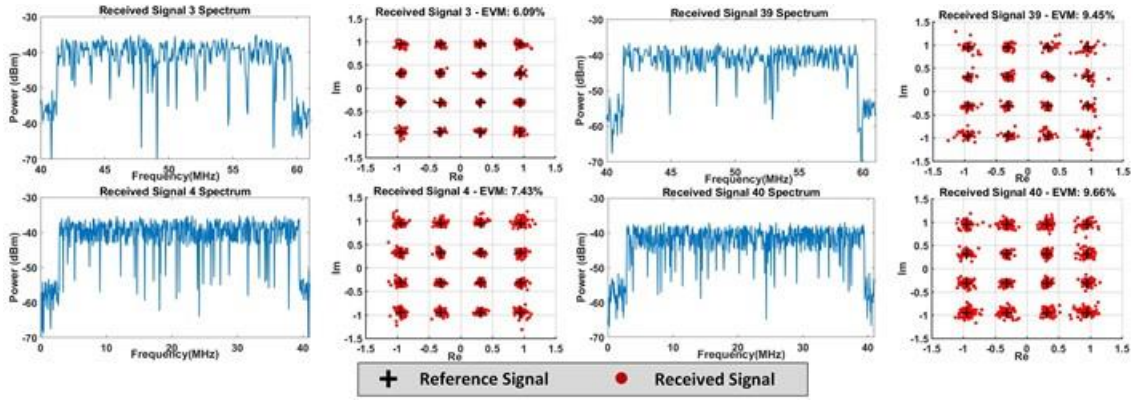

Figure 6-26 Received signal spectra and constellation diagrams (with % rms EVM) of selected signals from different bandwidth signals employing a single 5G numerology.

The EVM performance of Signals 3 and 4, which are the first two signals of the multiplex (in the second NZ) and Signals 39 and 40, which are the last two signals of the multiplex (in the 20th NZ) have been shown in Figure 6-26. The range of EVM (% rms) of the narrower bandwidth signals is from 6% to 9.5% while the EVM (% rms) of the wider bandwidth signals is from 7.4% to 9.7%. The higher EVM (compared to the previous mixed numerology multiplex) can be attributed to poor AWG response at high frequencies, as this multiplex has a higher aggregate bandwidth. Moreover, this multiplex consists of very narrow gaps between signals, e.g. 1.83 MHz between a narrow bandwidth and wide bandwidth signal and 5.74 MHz between two wide bandwidth signals.

6.5 mm-Wave Up-conversion Experiments for Massive MIMO Applications

The experimental setup used for mmW carrier generation and up-conversion is shown in Figure 6-27. Signals extracted from the multiplex that was discussed in Sections 6.3.2 and 6.3.4 with 32 DMT/ 64 SSB signals and employing a generic numerology have been used in these mmW experiments.

The optical carrier from the CWL is split into two parts by a 3-dB optical coupler. One part is modulated by a phase modulator, which receives an RF signal of f_M. This results in phase-modulated sidebands which are 25.5 GHz apart, since f_M = 25.5 GHz.

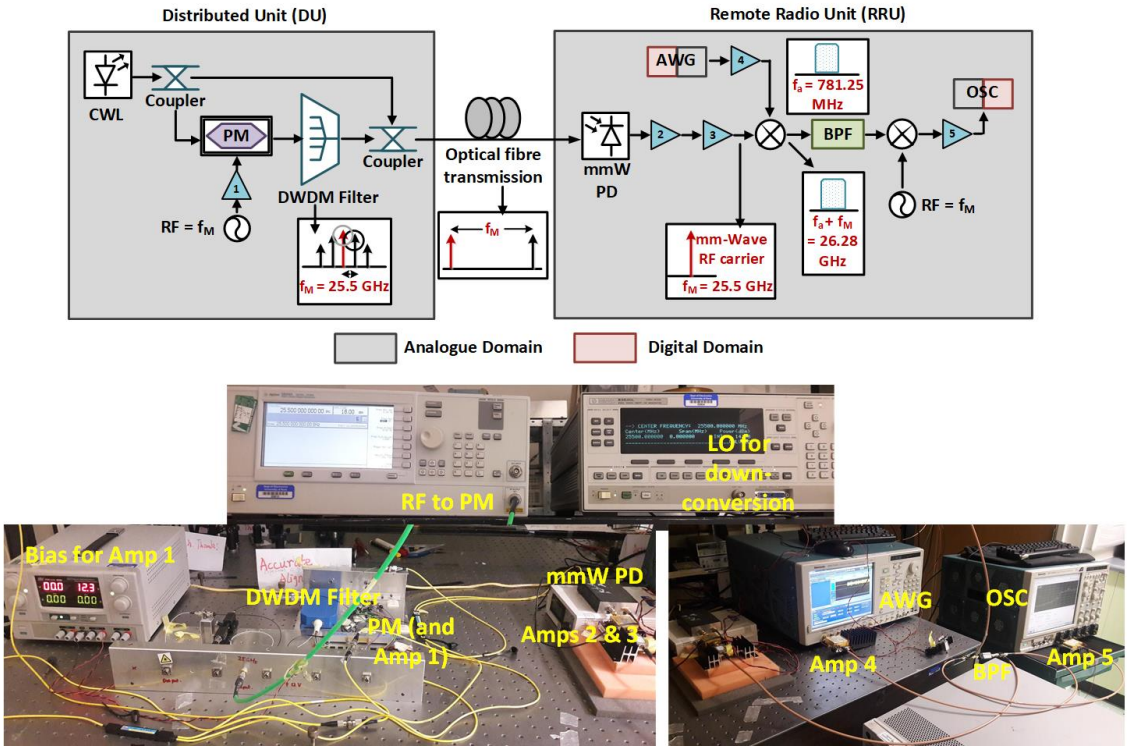

Figure 6-27 Experimental setup (Top: schematic; Bottom: actual laboratory testbed) for mmW carrier generation and up-conversion (device models and parameters shown in Table 6-4).

Table 6-4 Devices and parameters used in digital SCM mmW experiments

Type of Device	Device Model and Parameters
The CWL, mmW PD and RF amplifiers 4 and 5 (after the AWG and before the OSC, respectively) used in these experiments are the same as those shown in Table 6-2.	
Optical Phase Modulator (PM)	Sumitomo T.PM 1.5 – 40; RF range: 1.5 GHz – 40 GHz; Loss: 6 dB
RF Amplifier 1	Norden Millimeter N07-1593; Frequency range: 22.5 GHz – 35 GHz; Gain: 20 dB; Noise figure: 8 dB
Dense Wavelength Division Multiplexing (DWDM) Filter	Kylia 192.672-193.047 THz; 25 GHz; Loss: 6dB
RF Amplifier 2	Quinstar QLW-24403536-JO; Gain: 35 dB; Frequency Range: 24-40 GHz; DC Bias: +12 V; Noise figure: 3.5 dB
RF Amplifier 3	Norden Millimeter N07-1726; Frequency range: 24 GHz – 26 GHz; Gain: 30dB; DC Bias: +12 V; Noise figure: 8dB
RF Band-pass Filter (BPF)	K&L Microwave, Centre frequency: 26.25 GHz; 3-dB bandwidth: 300 MHz, Loss: 1 dB
Mixers (2)	Marki Microwave M20250; Frequency range: LO/RF 2 GHz – 50 GHz, IF 0.4 – 50 GHz; Loss: 8 dB@25 GHz

The parameters shown in Table 6-2 and Table 6-4 will also be used later in Chapter 7 for modelling the measurement setups in the simulation environment.

As shown in the figure, the first order 25.5 GHz sideband is filtered using a 25-GHz DWDM filter and coupled with the other part of the optical carrier. After transmission via a short length of optical fibre, the optical carrier and 25.5 GHz sideband beat at the mmW photo-diode to produce a 25.5 GHz mmW carrier. The resulting spectrum, after amplification via RF amplifiers 2 and 3, is shown in Figure 6-28.

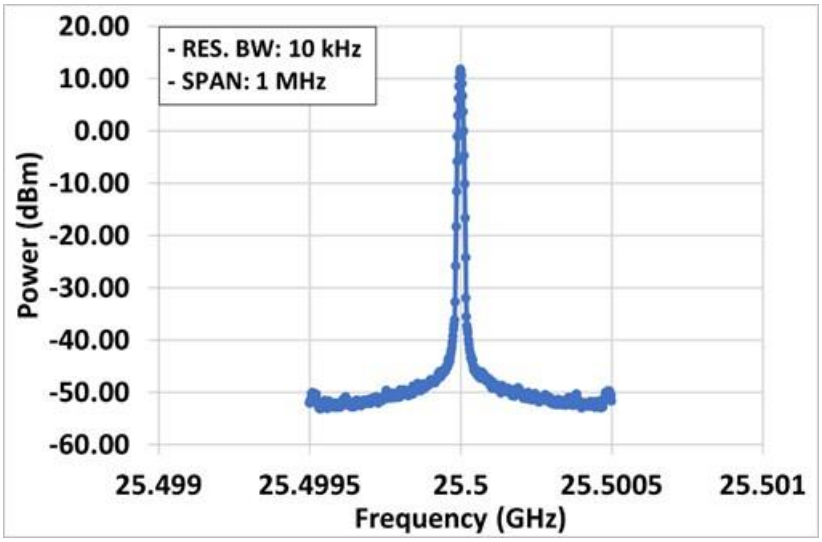

Figure 6-28 25.5 GHz mmW carrier (Resolution bandwidth: 10 kHz, Span: 1 MHz).

Out of the multiplexed signals discussed in Sections 6.3.2 and 6.3.4, the first and last signals in the positive spectrum of the multiplex (signals 2 and 25) are chosen for mmW up-conversion and are extracted and downloaded back to the AWG. Each signal is then regenerated at an arbitrary IF (f_a = 781.25 MHz), using a sampling rate of approximately 97.66 MSps (i.e. the original F_s has been decimated by a factor of 32).

The remotely delivered mmW carrier is used to up-convert the digitally processed signals. Double sidebands are produced due to the mmW up-conversion and a narrowband band-pass filter centered at 26.25 GHz is used to filter out the required upper sideband (at 26.28 GHz). Note that this filtering stage can be avoided by employing a mmW quadrature mixer.

Finally, following transmission over a short-length co-axial cable, the signals are down-converted and recaptured with the real-time oscilloscope for performance evaluation. The received spectra and the constellations (following OFDM demodulation) corresponding to Signals 2 and 25 are shown in Figure 6-29. The EVM for Signals 2 and 25 are 8.8% and 8.5% respectively and are again well within 3GPP limits [74]. Compared to the 25 GHz analogue SCM measurement results shown in Table 4-4, the EVM performance shown here is worse. However, the analogue SCM measurements consisted of up to four 76 MHz channels occupying a bandwidth of 810 MHz (with 160 MHz being the smallest gap between channels) while these measurements are for up to 48 channels occupying a bandwidth of 2.42 GHz, with a per channel bandwidth of 38.15 MHz and a gap of 10.68 MHz between channels.

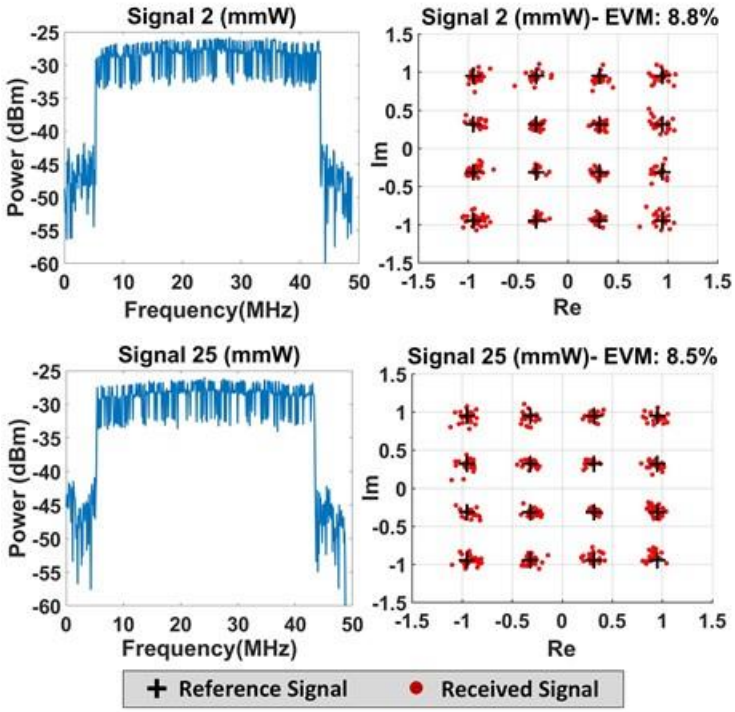

Figure 6-29 Received spectra and EVM/ constellation diagrams of down-converted Signals 2 (top) and 25 (bottom) following de-multiplexing, down-sampling and up-conversion to the same mmW frequency at the RRU.

6.6 Summary and Conclusions

This chapter discusses the creation of different types of multiplexes in a MATLAB transmitter function using the NZ design approach and the experiments conducted using these multiplexes. DMT and SSB modulated signals with 16-QAM, 64-QAM and 256-QAM subcarrier modulation have been used while large multiplexes have been demonstrated with signals with the same or different bandwidths and variable frequency gaps between signals within a single IFFT. These multiplexes have been created using the same, generic numerology or using different 5G numerologies (produced by separate IFFTs). Experimental results with these multiplexes at microwave frequencies over a radio-over-fibre link employing external modulation and direct detection are well within 3GPP limits for 16-QAM subcarrier modulation (some results are also valid for 64-QAM subcarrier modulation).

Finally, at the receiver, mmW up-conversion of the de-multiplexed signals also show EVM performance to be within 3GPP limits for 16-QAM subcarrier modulation.

7 Co-Simulations of an Analogue Subcarrier Multiplexed Mobile Fronthaul with Digital Processing

7.1 Introduction

This chapter discusses in detail the simulation models with digital SCM at RF and mmW frequencies, conducted in VPI^{TM}. Individual components (such as MZM, PM, RF amplifiers etc.) have already been modelled in VPI (shown previously in Chapter 4) and matched to experimental characterisation measurements.

The chapter includes results of MATLAB-VPI co-simulations, in which multiplexes are created in MATLAB and then processed once again in MATLAB after transmission via the analogue optical link modelled in VPI. Simulation runs (signal generation, transmission through optical link models and signal reception), employ a "single button" control through VPI.

The chapter begins with an introduction on the MATLAB-VPI co-simulation environment in Section 7.2. This is followed in Section 7.3 by MATLAB-VPI co-simulation results matched to measurement results shown in Chapter 6, which employ DMT/ SSB modulated multiplexes with generic and 5G numerologies, a single IFFT and NZ mapping design.

Performance predictions employing a THA and very large multiplexes are presented in Section 7.4, including mmW carrier generation and up-conversion of channels extracted from the multiplex. It is shown that for very large multiplexes, the use of a THA at the receiver can relax the analogue bandwidth specifications of ADCs.

The chapter ends with summary and conclusions in Section 7.5.

7.2 The MATLAB – VPI Co-Simulation Environment

In the simulations that will be presented here, digitally multiplexed channels at the transmitter side are prepared in MATLAB and passed from the MATLAB transmitter function to VPI (as shown in Figure 6-2). After transmission through the VPI model of the optical link, the channels are de-multiplexed once again at the receiver side in the MATLAB receiver function (as shown

in Figure 6-3). The modules used and the sampling rate calculations required for MATLAB – VPI co-simulations are presented in this section.

7.2.1 MATLAB – VPI Co-Simulation Modules

The "*CoSimInterface*" block inside the Co-simulation galaxy shown in Figure 7-1 runs the MATLAB transmitter function (*.m file, MATLAB Ver. 9.1.0, R2016b*) [187], [188] for signal generation when the VPI co-simulation is run. It then passes the array of signal amplitudes returned by the script to the "*CoSimOutputMxFlt*" block, which declares a matrix floating point output port for a co-simulation module. For complex signals (such as SSB), there two output separate output blocks for I and Q data streams while for real signals (such as DMT), there is only one output block. This type of galaxy has been used in the transmitter side for all co-simulations discussed in this chapter.

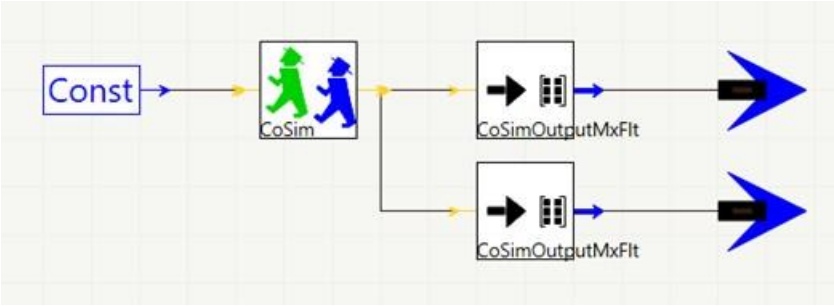

Figure 7-1 Inside the co-simulation galaxy used in the transmitter side in VPI.

Inside the *CoSimInterface* block shown in Figure 7-2, the "*InterfaceType*" has to be set to "Matlab" to specify the co-simulation interface being used. "*RunCommand*" triggers the function or MATLAB script for signal generation (the function returns the I and Q data streams to "*txRoutput*" and "*txIoutput*", respectively, which also have to be specified in the *CoSimOutputMxFlt* blocks). "*Path*" specifies the directory in the local file system where the interface script or code resides.

Name:	Value
General	
InterfaceType	Matlab
LogicalInformation	Yes
Path	X:\
InitCommand	
RunCommand	[txRoutput,txIoutput] = TxXDMTsignalsMAT32;
WrapupCommand	
ShareInterface	On

Figure 7-2 Parameters set in the transmitter side CoSimInterface module.

The Co-simulation galaxy is followed by two additional blocks. The first one is the "*UnPk_M*" block, which reads the floating-point matrix and outputs it row by row. This is followed by "*PackBlockEl*", which serves as an interface to signal processing modules and converts floating-point inputs to electrical blocks/ samples using a specified sampling rate.

At the receiver side, the In-phase and Quadrature phase data streams are separated by a quadrature demodulator. The two streams pass through separate "*UnpackBlockEl*" modules, which convert the electrical blocks/ samples to floating-point outputs using a specified sampling rate. These blocks are followed by separate "*Pack_M*" blocks, which produces a matrix with floating-point entries constructed from floating-point input values. These values are passed to the MATLAB receiver function using the "*CoSimInputMxFlt*" block, which declares a matrix floating point input port for a co-simulation module. The *CoSimInterface* block inside the Co-simulation galaxy shown below in Figure 7-3 runs the MATLAB receiver code. The EVM of the de-multiplexed channels is returned by the MATLAB code to VPI via the *CoSimOutputMxFlt* block.

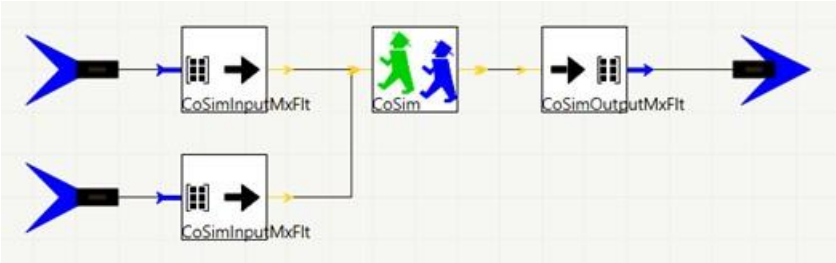

Figure 7-3 Inside the co-simulation galaxy used in the receiver side in VPI.

The parameters set inside the *CoSimInterface* block on the receiver side are shown in Figure 7-4. The MATLAB receiver function arguments "*rxRinput*" and "*rxIinput*" are specified in the *CoSimInputMxFlt* blocks while the matrix containing the EVM values of all de-multiplexed channels is returned from MATLAB through "*rxoutput*".

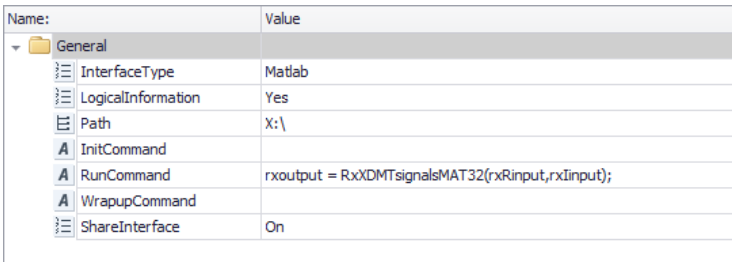

Figure 7-4 Parameters set in the receiver side CoSimInterface module.

7.2.2 Key MATLAB – VPI Frequency Conversions

Previously, in Section 6.3.2, sampling rate calculations required for experiments were discussed in detail using actual values for a 32 DMT/ 64 SSB channel multiplex using a single IFFT and a generic numerology. If the same example values are used for simulations, the sampling rate (F_s) in VPI or "*SampleRateDefault*" will be 3.125 GSps and the total IFFT length of the multiplex ($N_{IFFT,total}$) will be 32768. As a result, the frequency bin size can be calculated from (6-9) to be 95.27 kHz. If a cyclic prefix with a length of 0.125 is included, $N_{TotalIFFT,CP}$ is 36864.

The choice of time window (denoted by t_W) in VPI determines the speed of the simulation. If the time window and sampling rate are chosen incorrectly in VPI, the simulation may not run properly or produce undesired results. An important simulation parameter is the samples per block, which determines whether the simulator will truncate samples provided by MATLAB. Samples per block, denoted by S_{block}, is given by

$$S_{block} = F_s \times t_W \ . \tag{7-1}$$

This also determines the resolution of spectral analysis or the resolution bandwidth, δ_{f_res}, which is given by

$$\delta_{f\_res} = \frac{1}{t_W} \ . \tag{7-2}$$

The speed of the simulation is also determined by this parameter, with larger blocks giving faster simulation times.

For this work, choosing a ratio to be equal to $N_{TotalIFFT,CP}$ results in block-based processing, with each block corresponding to one OFDM symbol (or frame, as it is referred to in previous chapters). As a result, for the 32 DMT/ 64 SSB channel multiplex, the following global parameters have been chosen for the co-simulation:

- *TimeWindow* = 36864/3.125e9 seconds
- *GreatestPrimeFactor* = -1
- *BoundaryConditions* = Periodic
- *SampleRateDefault/ BitRateDefault* = 3.125e9 bit/s

Therefore, *TimeWindow x SampleRateDefault* = 36864. This is the size of each time domain OFDM symbol being transmitted and for 10 OFDM symbols (368640 data points), the simulator will propagate 10 blocks. As discussed in Section 4.4.2.3, a *GreatestPrimeFactor* of -1 has been chosen to disable the parameter so that the simulation runs correctly even if any of the symbol rates being used in the simulation are not powers of 2 (different sampling rates are being used throughout the simulation, as discussed in the next section) [165]. *BoundaryConditions* has been set to periodic since periodic signals are being simulated.

The *UnPk_M* and *Pack_M* modules at the transmitter and receiver sides, respectively require $N_{TotalIFFT,CP}$ while the *PackBlockEl* and *UnpackBlockEl* modules at the transmitter and receiver sides, respectively require F_s.

Now that the values of important parameters have been established, the MATLAB – VPI co-simulation results will be discussed in detail.

7.3 Co-Simulation Results at RF of DMT and SSB Modulated Multiplexes with Generic and 5G Numerologies

7.3.1 Generic Numerology

The experimental setup shown in Figure 6-10 has been modelled in a MATLAB- VPI co-simulation environment. As in the experimental process described in Section 6.3.4, 24 DMT/ 48 SSB

channels with 16-QAM subcarrier modulation (one channel per NZ, single IFFT) have been generated in MATLAB and passed through the modelled architecture in VPI, before being sent to the receiver function in MATLAB for digital processing. The parameters used to set up the co-simulation have already been shown in Table 6-2 and the global parameters have been set according to Section 7.2.2. Devices such as the CWL, MZM, RF amplifiers etc. used in the co-simulation have already been modelled in Section 4.4. The transmitter side/ DU of the MATLAB-VPI co-simulation is shown in Figure 7-5.

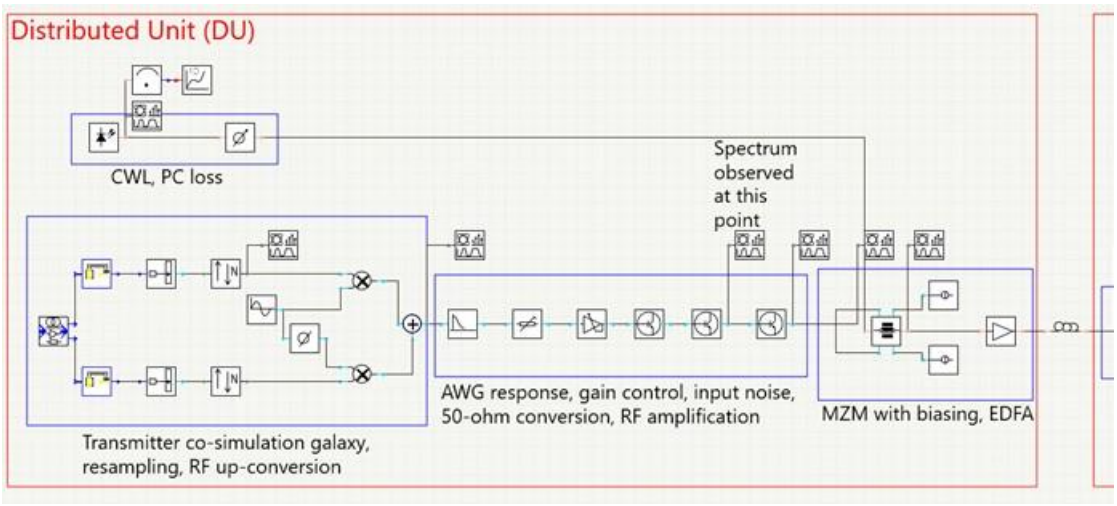

Figure 7-5 MATLAB-VPI co-simulation of the DU for external IM-DD at RF with DMT and SSB modulated multiplexes using a single IFFT and generic numerologies (one channel per NZ).

In the figure, the co-simulation module and RF up-conversion stages have been set up as discussed in Section 7.2.1. As in experiments, an RF frequency of 1.5625 GHz has been used. The "*Resample*" module modifies the sampling rate and centre frequency of the sampled band signals [166] and has been used to multiply 3.125 Gbps by 80 times. This is done to match the sampling rate of the CWL, such that the sampling rates at the RF and optical inputs of the MZM are the same.

In order to match the observed spectra and the EVM performance in experiments, the AWG response has been modelled in the co-simulations using a low-pass RF filter (*Transfer function: Chebyshev II; 3-dB bandwidth: 2.8 GHz; Stopband: 3 GHz; Filter order: 3*). This is followed by the gain control, input noise and 50-ohm conversion modules. The spectrum after 50-ohm conversion is shown in Figure 7-6. After this stage, the multiplex is amplified and modulated onto the optical carrier via the MZM.

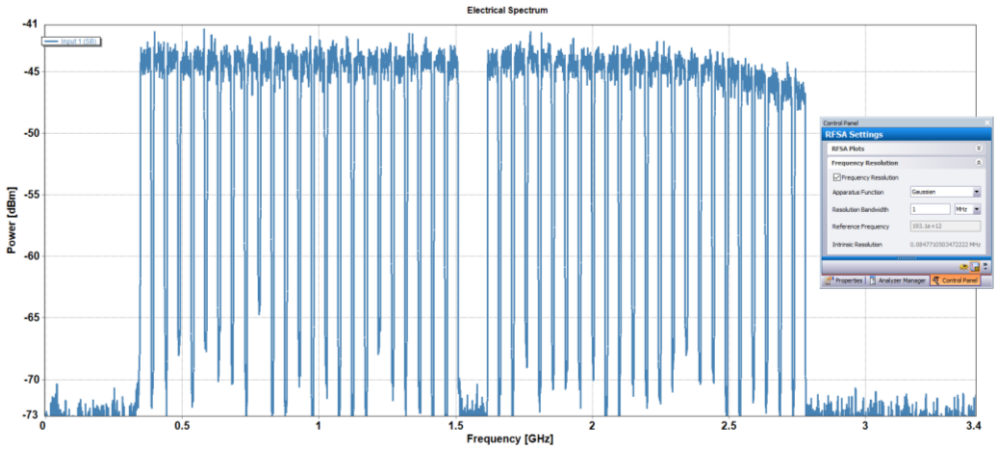

Figure 7-6 24 DMT/ 48 SSB channels after 50-ohm conversion (Res. BW: 1 MHz).

The MATLAB-VPI co-simulation of the RRU is shown in Figure 7-7. The multiplex is detected by the mmW PD at the RRU. Cable losses and receiver noise are modelled after the RF amplification stage. The multiplex undergoes RF down-conversion and the resampling modules readjust the sampling rate of the In-phase and Quadrature phase data streams to match the global parameters. Finally, the multiplex is sent to the MATLAB receiver function via the co-simulation galaxy, as discussed in Section 7.2.1

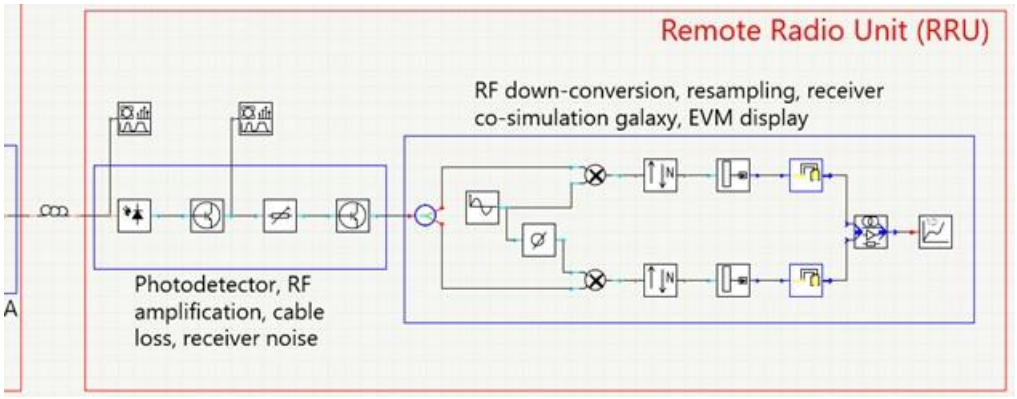

Figure 7-7 MATLAB-VPI co-simulation of the RRU for external IM-DD at RF with DMT and SSB modulated multiplexes using a single IFFT and generic numerologies (one channel per NZ).

For model validation, a comparison between measured and modelled average EVM (% rms) of all signals in the positive part of the multiplex versus the MZM bias voltage is shown in Figure 7-8. Note that the experimental work generally used a bias of 5.54 V, where the match between simulation and experiment is particularly good.

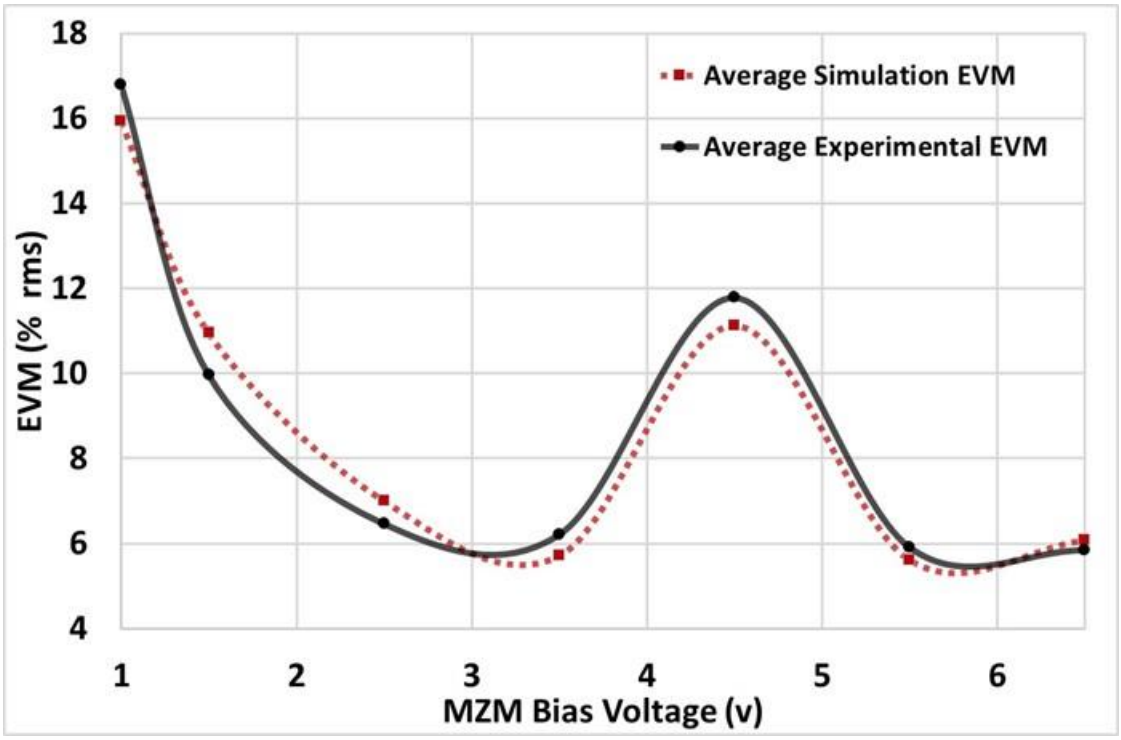

Figure 7-8 Modelled and experimental MZM bias sweeps versus average EVM (% rms) for all signals (RF only).

7.3.2 5G Numerology

Experimental results with multiplexes employing two different bandwidths and 5G numerologies were discussed in detail in Section 6.4.1. Two channel sets are multiplexed by mapping one channel from each numerology to each NZ, resulting in two channels per NZ when the multiplexes are added. This NZ size corresponds to the larger of the per-NZ IFFT lengths of the two signal sets.

The same DU and RRU models discussed in Section 7.3.1 are used for this co-simulation as well, with slight changes to accommodate the two channel sets generated via separate IFFTs. The $N_{TotalIDFT,CP}$ is 57600 for this co-simulation. Multiplexes or channel sets employing two different numerologies are generated via the MATLAB transmitter function. These multiplexes, denoted Channel Set 1 (employing 5G numerology 1) and Channel Set 2 (employing 5G numerology 2), are sent via two different co-simulation galaxies to the MATLAB-VPI co-simulation. As with experiments, Channel Set 1 has a sampling rate, of 3.125 GSps while Channel Set 2 has a sampling rate of 1.5625 GSps. This block of multiplexed channels is then modulated onto a carrier frequency of 1.5625 GHz using an MZM.

The MATLAB-VPI co-simulation is run twice, once by setting the sampling rate to 3.125 GSps and the second time to 1.5625 GSps in the global parameters and the *UnpackBlockEl* module. Figure 7-9 shows an EVM comparison between measured and simulated results for the two Channel sets respectively. The EVMs for Channel Set 1 in simulations and experiments are between 5 – 6.5% while the EVMs for Channel Set 2 are between 5 – 8%. The measured and simulated EVMs for both channel sets are very close on average, and well within specification limits. Channel Set 2 has worse EVM performance, as it has slightly lower transmit power compared to Channel Set 1.

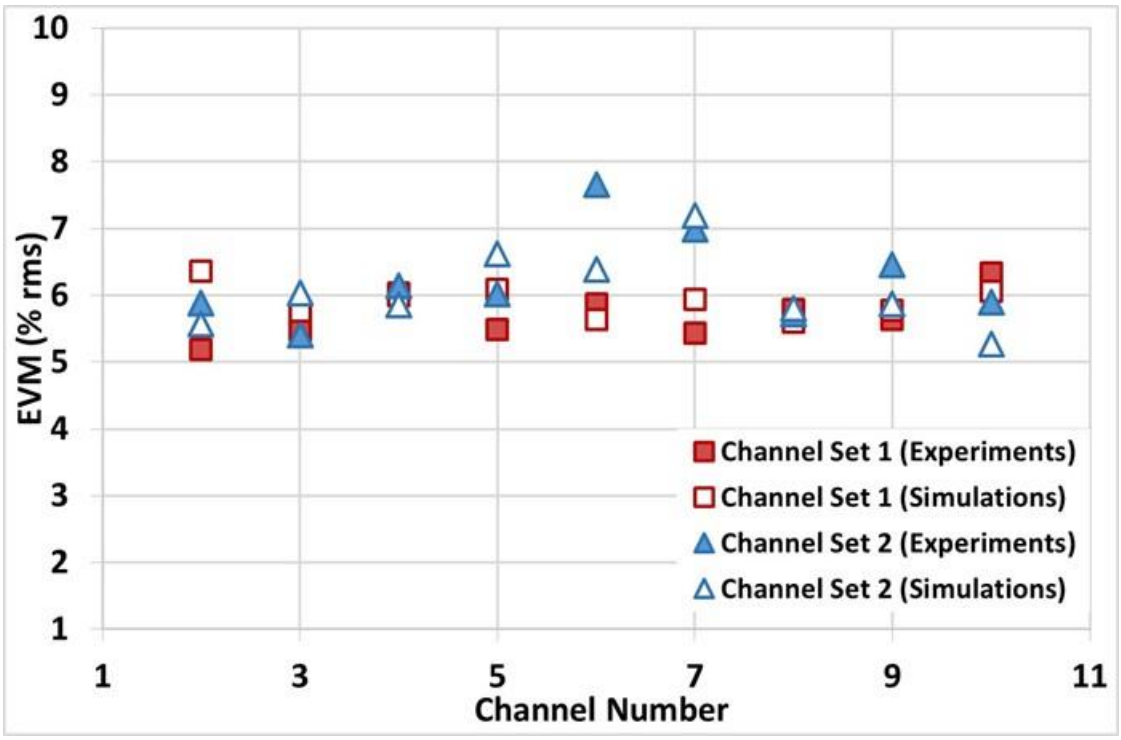

Figure 7-9 Modelled and experimental EVM (% rms) of signals in Channel Sets 1 and 2, employing 5G numerologies (positive side of spectrum).

7.4 Performance Predictions with a THA

The use of a THA in the case of very large multiplexes or "super-multiplexes" has been discussed in Sections 5.3.2 and 6.2. This section presents the scenarios in which a THA can be used, as well as performance predictions with a THA in the co-simulation environment. It also extends the

predictions with the THA to include co-simulation results of mmW carrier generation and up-conversion.

7.4.1 Use of THA in the receiver chain and extension to a mapping hierarchy

Receiving even larger multiplexes using the digital techniques described so far would ultimately require an RRU ADC with a large analogue bandwidth and sampling rate. This will happen for cases in which

- Multiplexes are of aggregate bandwidths exceeding the ADC's sampling rate specifications
- Multiplexes occupy sufficiently low aggregate bandwidths but are placed at an RF such that their highest frequency component exceeds the ADC's analogue bandwidth. Note that flexibility in the RF placement of the multiplex can be beneficial in certain optical network scenarios, e.g. in the case of certain analogue fibre communication links in which external or direct modulation of a light source at a low IF may result in detrimental performance in the form of inter-mixing and inter-modulation distortion [29], [30], [31].

Moreover, both of these conditions may be present at the same time. Such cases, as well as a technique to mitigate them using a THA, are depicted conceptually in Figure 7-10.

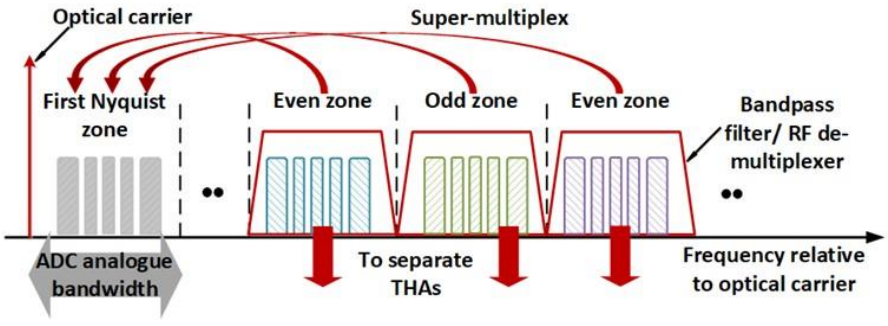

Figure 7-10 Extending to a mapping hierarchy with super-multiplexes by employing a small number (dependent on ADC specifications and for practical mMIMO applications) of analogue filters with multiple THAs for very large aggregate bandwidths.

The THA samples the received multiplex but does not quantize it. The resulting discrete-time signal is quantized by the ADC stage that follows. Larger bandwidth multiplexes are broken up into smaller blocks, e.g. 4 blocks of 32 or 64 channels each. These multiplexes are termed “super-multiplexes” as they lead to a mapping hierarchy. Now, instead of mapping individual channels or channel groups into NZs, at the transmitter, entire multiplexes are first mapped into NZs dependent on the sampling rates of the THA and front-end ADC at the receiver. As before, channel blocks that are mapped in even NZs are frequency domain flipped and conjugated. At the receiver, each of these channel blocks is filtered using analogue filters/de-multiplexers and then sent to a THA, to be down-sampled to an IF (this can be the same for all blocks). This process requires the addition of analogue filters, but for a wide range of mMIMO applications, and assuming sampling rates of commercially available ADCs, the required number of filters will be small.

As explained previously in Section 5.4.2, after an intermediate down-sampling stage for each block, each channel is filtered and down-sampled using a final sampling rate. Thus, THAs offer flexibility in RF placement of the multiplex and flexibility of design for the creation of even larger multiplexes (or super-multiplexes), that are not limited by ADC sampling rate and/or analogue bandwidth constraints. The THA offers high frequency linearity and in effect improves the analogue bandwidth of the ADC.

The combined THA-ADC stage has been modelled in VPI by an analogue low-pass filter, a down-sampler and an ADC, with the main model parameters shown in Figure 7-11 (extracted from [182]). This stage follows the photodetector, as in the overview shown in Section 6.2, and an analogue band-pass filter (or RF de-multiplexer stage, for multiple signal blocks). The THA has an analogue bandwidth of 18 GHz while the ADC has a resolution of 12 bits, Full Scale Range (FSR) of 1V and sampling rate of 3.93 GSps.

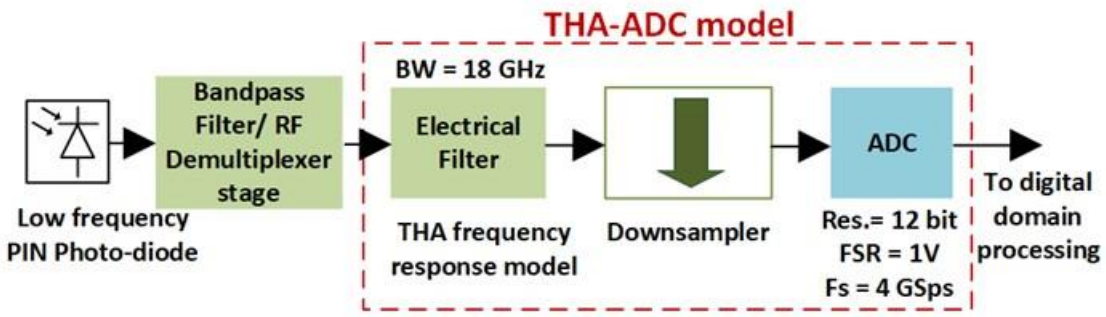

Figure 7-11 Modelled frontend section of the RRU. The THA frequency response is modelled with an electrical filter prior to the down-sampler block (THA frequency response model adapted from [182].

7.4.2 Simulation Setup and Performance Predictions

The simulation model discussed in Section 7.3 is now extended to include two THAs for two blocks of mixed bandwidth channels (i.e. a super-multiplex), to demonstrate how a very large number of channels occupying a large analogue bandwidth can be down-sampled using a much smaller sampling rate at the receiver.

Four sets of SSB modulated channels (Channel Sets 1, 2, 3 and 4) employing different 5G numerologies are up-converted to an RF frequency of 7.86 GHz. A block of 60 channels is placed at approx. 5.9 GHz while a second block of channels is placed at approx. 9.8 GHz, resulting in 120 channels in total within a bandwidth of 7.86 GHz. A gap in the frequency domain is used between the two blocks to facilitate analogue filtering. Each of these blocks contain 30 channels of 18 MHz bandwidth (30 kHz subcarrier spacing) and 30 more channels of 72 MHz bandwidth (60 kHz subcarrier spacing). Channel Sets 1 and 3 have a bin size of 30 kHz while channel sets 2 and 4 have a bin size of 60 kHz. The MATLAB-VPI co-simulation model of the DU is shown in Figure 7-12.

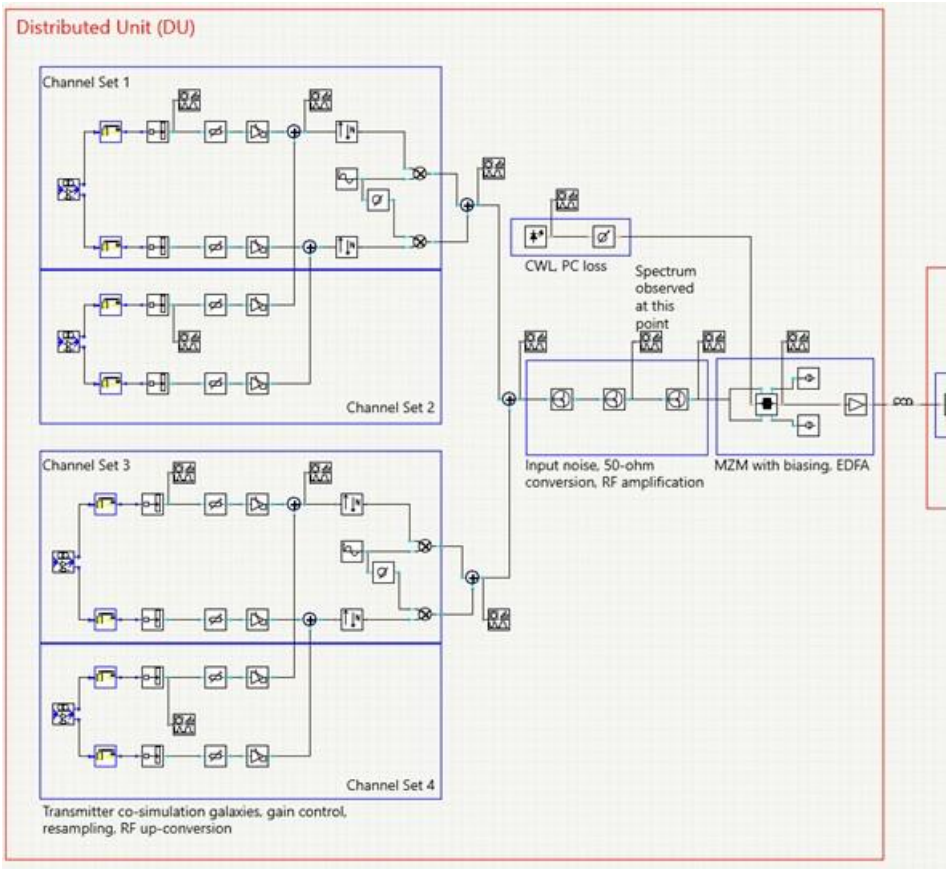

Figure 7-12 MATLAB-VPI co-simulation model of the DU for performance predictions with a THA.

The resulting multiplex after 50-ohm conversion is shown in Figure 7-13. According to the sampling rate used at the RRU of 3.93 GSps, the first block is in an odd Nyquist zone while the second block is in an even zone and has thus been frequency domain flipped and conjugated. Since this is a performance prediction in a simulation environment with a much higher multiplex bandwidth than what is allowed by the AWG used in measurements, the AWG response and Oscilloscope sampling rate ratio have not been taken into account.

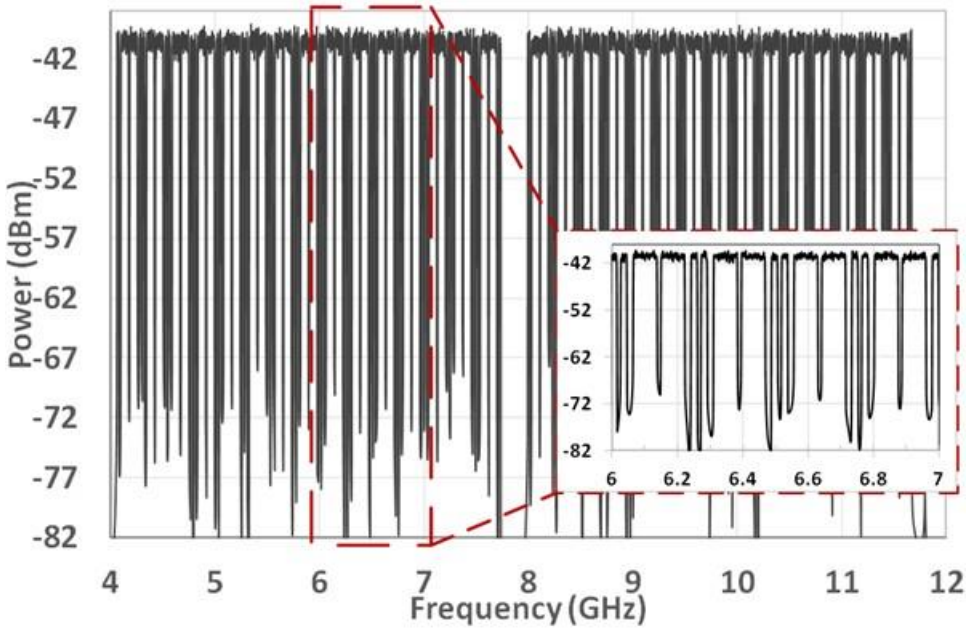

Figure 7-13 120-channel super-multiplex of mixed bandwidth channels, with 18 MHz and 72 MHz bandwidth and 30 kHz and 60 kHz subcarrier spacing (5G numerologies).

At the receiver, each of these blocks is filtered with a Chebyshev II band-pass filter and down-sampled using different THAs but with the same sampling rate of 3.93 GSps. The down-sampled blocks are then sent to the MATLAB receiver function for de-multiplexing and further processing. The MATLAB-VPI co-simulation model of the RRU is shown in Figure 7-14. For simplicity, only one filter and THA-ADC stage is shown as only the centre frequency of the filter has to be changed for each block.

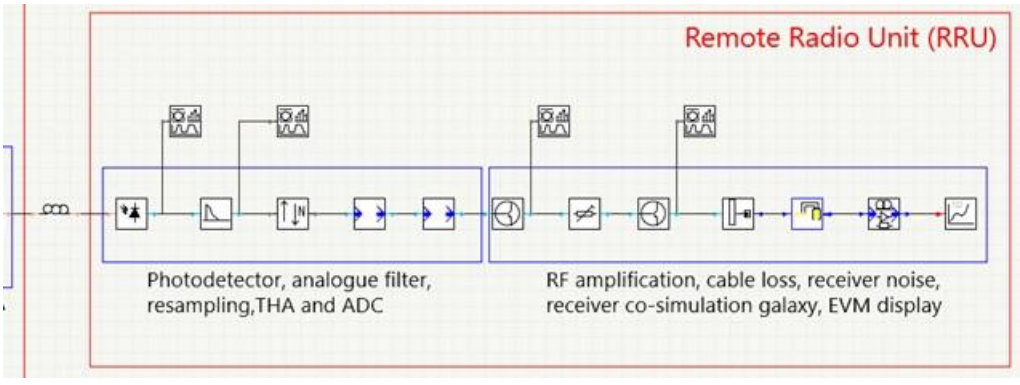

Figure 7-14 MATLAB-VPI co-simulation of the RRU for performance predictions with a THA.

The received spectra, constellation diagrams and EVMs of Channel 1 of the first channel set (18 MHz bandwidth) in the first block and Channel 60 of the second channel set (72 MHz bandwidth) in the second block are shown in Figure 7-15. Channel 1 is chosen as it is the first 18 MHz channel of the 120-channel multiplex and Channel 60 is chosen as it is the last 72 MHz channel. An average EVM within the range of 5 % - 7% has been obtained for all channels in both channel sets in the two blocks. Since 16-QAM subcarrier modulation has been used, the aggregate data rate is 21.6 Gbps. Channels at the edge of the filter passband (e.g. Channel 60 shown in Figure 7-15) show some filtering roll-off effects in their amplitude response but these can be minimized with further filtering optimization.

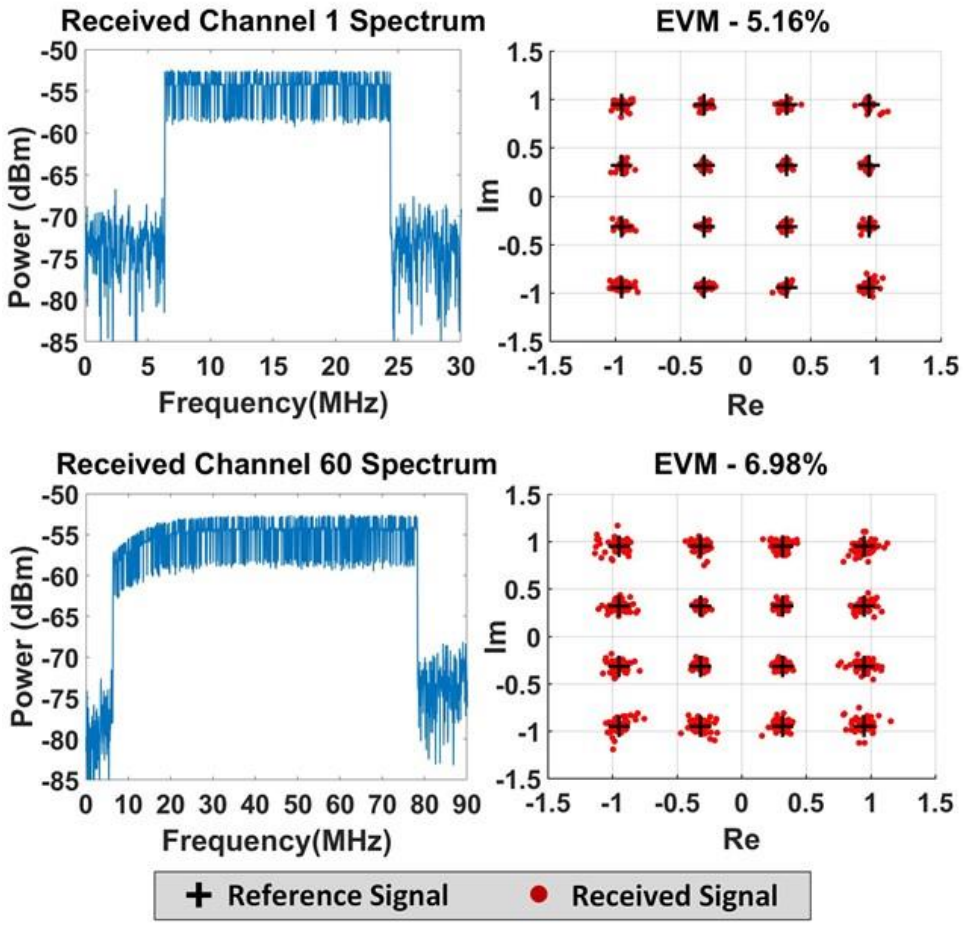

Figure 7-15 Top: Received channel spectrum, EVM and constellation diagram of Channel 1 (18 MHz) of the first channel set. Bottom: Received channel spectrum, EVM and constellation diagram of Channel 60 (72 MHz) of the second channel set.

7.4.3 Performance predictions of mm-Wave Up-conversion for Massive MIMO Applications

In this section, the performance predictions with a THA have been extended to include mmW carrier generation and up-conversion using a 240-channel super-multiplex with mixed channel bandwidths employing 5G numerologies and different modulation levels (e.g. for mMIMO applications such as full-digital beamforming). To exhibit the versatility of the architecture, the super-multiplex has been generated using a combination of single and multiple IFFTs and with multiple channels in each NZ. This co-simulation is based on the concept of the hybrid architecture discussed in Section 6.2.

The VPI co-simulation model of the DU is shown in Figure 7-16. The output of the CWL is split into two parts, with one part used for data modulation via an MZM and the other part used to produce phase-modulated sidebands. The sidebands are 30 GHz apart and the first order sidebands are filtered using a 25-GHz DWDM filter. The filtered sidebands and data modulated optical carrier are combined, amplified by EDFA1 and transmitted to the RRU via optical fibre. The components that have already been modelled in previous simulations (along with their corresponding losses, noise etc.) have been reused in this model of the DU. The only differences are the use of higher RF amplification, higher optical output power of the CWL (7.61 dBm) and a different MZM bias point (closer to the quadrature point).

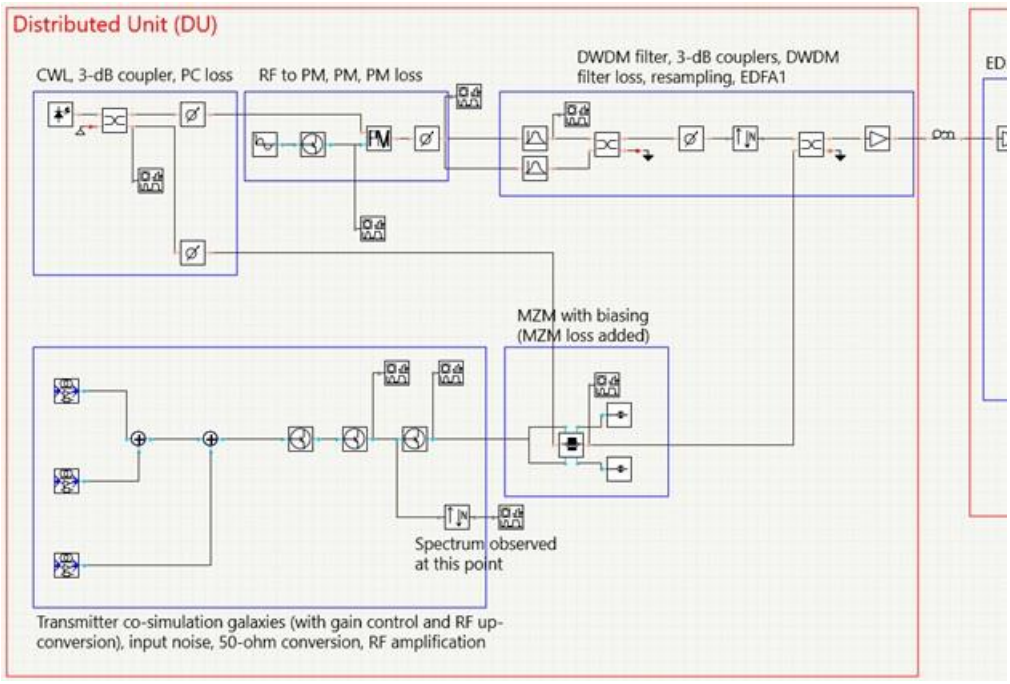

Figure 7-16 MATLAB-VPI co-simulation model of the DU for performance predictions with a THA and mmW up-conversion.

The spectrum of the multiplexed channels after 50-ohm conversion (at the point indicated in Figure 7-16) is shown in Figure 7-17. Since different types of multiplexes are used in this model, a number of MATLAB transmitter functions are required to generate them. These functions, run by different co-simulation galaxies, are encapsulated within the three co-simulation galaxies shown in the figure. The first two co-simulation galaxies resemble the one shown in Figure 7-12, with the first galaxy generating Channel Sets 1 and 3 and the second galaxy generating Channel Sets 2 and 4 (utilising separate IFFTs). The third co-simulation galaxy generates two more mixed bandwidth multiplexes using a single IFFT. The first four channel sets use a subcarrier modulation of 64-QAM while the final two channel sets (5 and 6) use a subcarrier modulation of 16-QAM. The channel bandwidths in the first four channel sets are 72 MHz and 18 MHz (similar to the multiplex shown in Figure 7-13) while the channel bandwidths in the final two channel sets are 60 MHz and 12 MHz (for a bin size of 60 kHz). The total bandwidth occupied by this super-multiplex is approximately 15.5 GHz while the aggregate data rate is 49.7 Gbps (32.4 Gbps (Channel sets 1 - 4) + 17.3 Gbps (Channel sets 5 - 6)).

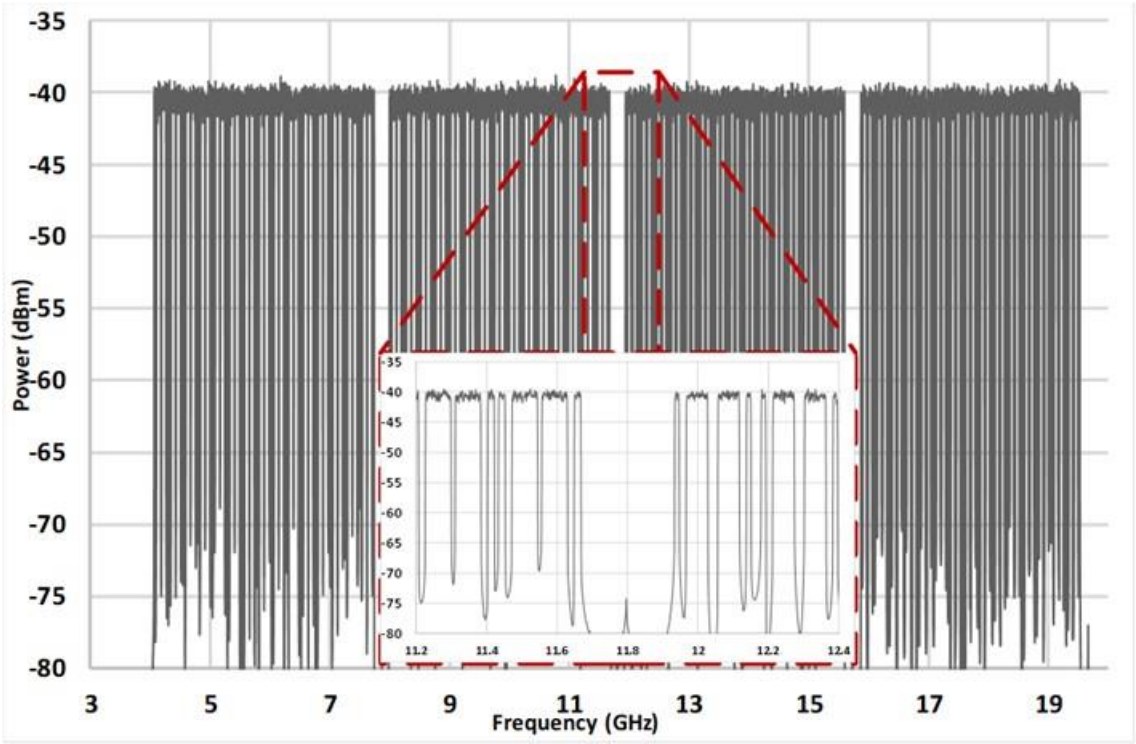

Figure 7-17 Spectrum of 240-channel multiplex after 50-ohm conversion at DU.

The RRU side of the VPI model is shown in Figure 7-18. The received signal is amplified by EDFA2 and the spectrum at this point is shown in Figure 7-19 (indicated in Figure 7-18). The first order sidebands from the PM and the optical carrier are filtered by a DWDM filter, combined and after photo-detection, a 60 GHz carrier signal is generated. The optical carrier with the data modulated signals are detected by another photodiode and the desired set of channels are filtered using an RF band-pass filter. After undergoing the THA-ADC stage using an intermediate sampling rate of 3.93 GSps, as explained in Section 7.4.2, the channels are de-multiplexed in the MATLAB receiver function corresponding to the filtered multiplex. A single channel of the channel set is extracted and returned to VPI via the same co-simulation galaxy. This channel is up-converted to frequency of 60.8 GHz, down-converted and sent back to a MATLAB receiver function for performance evaluation.

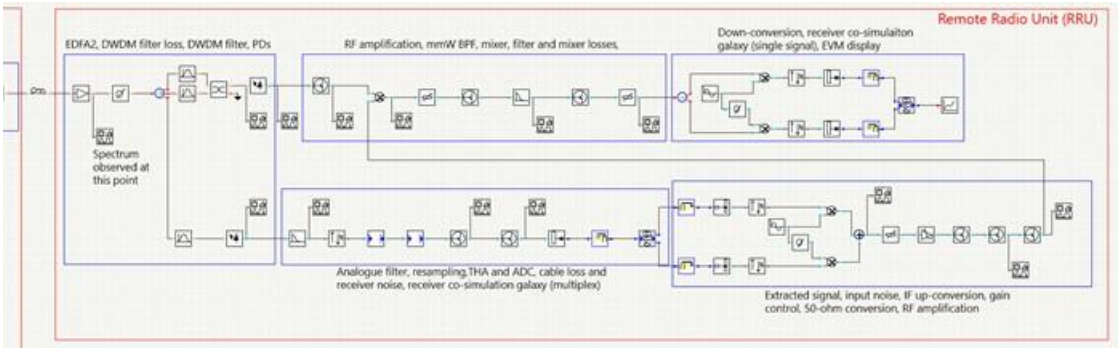

Figure 7-18 MATLAB-VPI co-simulation of the RRU for performance predictions with a THA and mmW up-conversion.

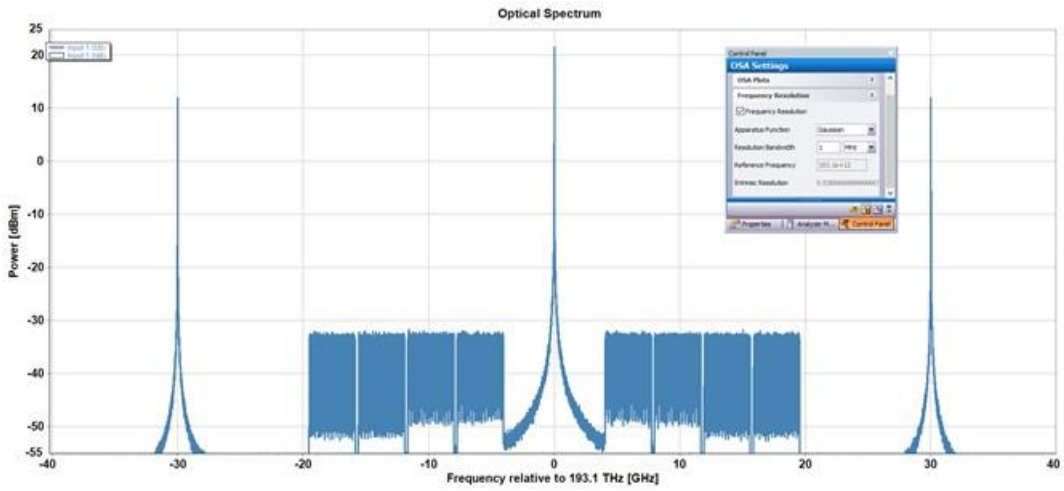

Figure 7-19 Spectrum after second EDFA at the RRU.

Most of the parameters that have been used for the model of the RRU have been reused from previous simulations, albeit for some changes. EDFA2 has been replaced by the default VPI model as the output power of the EDFAs used so far had been limited to match experimental results. RF amplification has been increased. The bandwidth of the THA has been increased slightly to accommodate the larger multiplex (THAs with larger analogue bandwidths are commercially available). Moreover, the bandwidth of the optical filter used to filter the data modulated optical carrier has been increased to accommodate the much higher bandwidth occupied by the multiplex. This means that in a practical system, an optical filter with a wide bandwidth has to be used separately to filter the data modulated carrier.

The spectra, EVM and constellation diagrams of Channel 1 (Channel Set 1) and Channel 239 (Channel Set 6) are shown in Figure 7-20. Channel 1 is from an odd NZ while Channel 239 is from an even NZ. These channels have undergone mmW up-conversion.

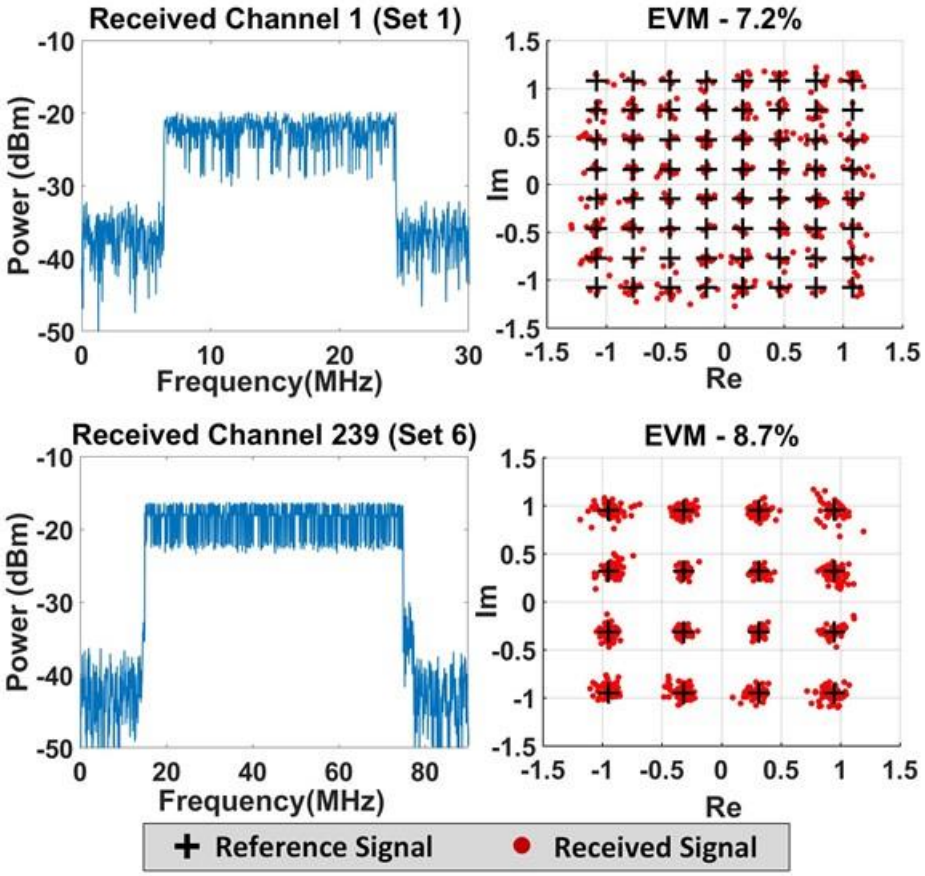

Figure 7-20 Top: Received channel spectrum, EVM and constellation diagram of Channel 1 (18 MHz) of the first channel set with 64-QAM subcarrier modulation. Bottom: Received channel spectrum, EVM and constellation diagram of Channel 239 (60 MHz) of the sixth channel set with 16-QAM subcarrier modulation.

7.5 Summary and Conclusions

In this chapter, the process of setting up a MATLAB-VPI co-simulation environment has been explained in detail and a good match between measurement and co-simulation results employing generic and 5G numerologies, single and multiple IFFTs and mixed channel bandwidths has been shown. Different types of DMT/ SSB modulated multiplexes have been created in a MATLAB transmitter function using the NZ design approach, transmitted through a

VPI co-simulation environment and then processed in a MATLAB receiver function much like the experimental results shown in the preceding chapter.

Furthermore, the problem of very large multiplexes requiring equally large sampling rates at the RRU has been addressed. A solution to this problem has been presented in the form of predictions in a simulation environment using a THA. Performance predictions with a model of this device in a MATLAB-VPI co-simulation environment exhibit promising results. Finally, the performance predictions have been extended to the proposed hybrid concept, involving digital processing and analogue transport for a heterogeneous 5G mobile fronthaul. The results show the feasibility of extending the NZ mapping method to a hierarchical structure for mMIMO applications, thus employing receivers with arbitrarily low sampling rates and analogue bandwidth specifications.

8 Conclusions and Future Work

8.1 Conclusions

The aims of 5G include very high bit-rates (eMBB), very low latency (URLLC) and massive machine connectivity (mMTC). The 5G air interface will include new sub-6GHz and mmW frequency bands, as well as LTE bands, in order to accommodate a large number of high bandwidth signals employing different numerologies. Moreover, the air interface will support several different 5G radio technologies and services.

Currently the fronthaul section of the RAN employs sampled radio waveform transport using industry standard specifications such as CPRI. Increased signal bandwidths and the widespread adoption of mMIMO techniques in 5G, will result in very high data rates making this type of transport impractical. Although functional splitting can alleviate some of the data rate constraints, it can also impair joint processing of signals due to increased latency. Analogue transport does not suffer from these limitations but is susceptible to noise, non-linearity and poor dynamic range. In addition, analogue multiplexing techniques lack flexibility and scalability, especially at millimetre wave frequencies. As a result, analogue transport schemes coupled with digital aggregation/ de-aggregation (SCM in the digital domain) has been actively studied in the last few years for the 5G mobile fronthaul.

In Chapter 4, investigations via measurement and simulation for analogue SCM at microwave and mmW frequencies (25 GHz and 60 GHz) were reported. Experimental results were discussed, employing a limited number of variable wide bandwidth channels for back-to-back, directly modulated IM-DD and externally modulated IM-DD links at microwave frequencies, and for externally modulated IM-DD at mmW frequencies. The mmW measurement setups were modelled in a VPI^{TM} simulator, in order to study the system in more detail and to determine the causes of the system performance limitations, with a very good match between measurement and simulation. It was observed that at mmW frequencies, it became progressively more difficult to scale the architecture due to a lack of flexibility, (e.g. changes in channel bandwidths or carrier frequencies required changes in RF filters being used in the setup) and increased complexity (e.g. mMIMO deployment required mmW up-conversion of each channel to the same carrier frequency at the RRU). Measurement results employing up to four channels with bandwidths of 76 MHz, 152 MHz and 305 MHz and data rates up to 2.13 Gbps, exhibited EVM

performance within 3GPP specifications. Higher data rates (higher number of multiplexed channels) and spectral efficiency could not be attained mainly due to limitations in analogue filtering.

The concept of a flexible mapping method for subcarrier multiplexing a large number of signals in the digital domain was discussed in Chapter 5. The concept allows multiple channels to be aggregated in the digital domain in order to create multiplexes of variable sizes, without the need for analogue/ digital domain up-converters, combiners etc. Channels with variable bandwidths employing DMT and SSB modulation are multiplexed efficiently using a single IFFT. Systematic mapping of individual channels or groups of channels into RRU-derived NZs is accomplished using a hierarchical NZ mapping structure. Channels or channel groups are mapped into NZs by using, for example, a single IFFT (for a single 5G numerology) or multiple IFFTs (for multiple 5G numerologies). At the RRU, the multiplexed channels are de-aggregated and transmitted at their respective RF/ mmW frequencies. Minimal per-channel digital domain processing is employed in this process, as a result of the original mapping into NZs at the DU. The mapping technique allows, e.g. channels employing the same numerology to be down-converted to the same IF, without the need for additional mixers in the analogue or digital domain. In order to transport even larger multiplexes and/ or channel bandwidths, beyond the analogue bandwidth specifications of the ADCs at the RRU, the use of a bandwidth-extension device such as a THA is proposed, thus relaxing the analogue bandwidth requirements of the ADCs. The THA leads to a mapping hierarchy and allows the architecture to scale for much larger multiplexes. The method presented here for creating the digitally multiplexed signals can be part of mMIMO and HetNet implementations, in the future 5G (and beyond) analogue mobile fronthaul.

Chapter 6 presented the proposed architecture that employed the techniques discussed in Chapter 5, which involve channel aggregation/ de-aggregation in the digital domain, combined with analogue transport and up-conversion to mmW frequencies. It also described the process of multiplexing/ de-multiplexing using MATLAB transmitter/ receiver functions (based on the NZ mapping approach discussed in the previous chapter), as well as the various calculations related to this process. Measurement results at microwave frequencies were presented, using different types of multiplexes created in MATLAB. DMT and SSB modulated signals employing different subcarrier modulation formats were used to multiplex large numbers of channels with the same or different bandwidths and variable gaps between channels. These multiplexes were created using the same, generic numerology (generated using a single IFFT) or using different 5G

numerologies (generated using separate IFFTs). At the receiver, the channels were de-multiplexed using digital domain processing. With gaps between channels as narrow as 1.83 MHz and aggregate data rates as high as 8.3 Gbps (with 76 mixed-bandwidth channels employing 16-QAM subcarrier modulation), good spectral efficiency and high data rates were demonstrated (higher data rates could not be achieved due to equipment limitations).

The EVM performance at microwave frequencies over a radio-over-fibre link employing external modulation and direct detection was well within LTE/ 5G EVM specifications for 16-QAM (with some of the results within EVM specifications for 64-QAM subcarrier modulation as well). Experiments involving mmW up-conversion using a remotely optically delivered mmW carrier also exhibited EVM performance for 16-QAM subcarrier modulation that was within LTE/ 5G 3GPP specifications.

Finally, in Chapter 7, a MATLAB-VPI co-simulation environment was presented, through which different types of DMT/ SSB modulated multiplexes were transmitted, much like with the measurement setup in Chapter 6. A good match between measurement and co-simulation results involving generic and 5G numerologies, single and multiple IFFTs and mixed channel bandwidths was shown. Moreover, for performance predictions, the NZ mapping hierarchy was extended to even larger multiplexes by introducing a model of a THA in co-simulation for a densely-packed 120-channel multiplex (occupying a bandwidth of approx. 8 GHz) and 240-channel multiplex (occupying a total bandwidth of approx. 16 GHz). By using a limited number of RF bandpass filters to filter groups of channels and THAs at the RRU, the channels were de-aggregated in the digital domain using an RRU ADC intermediate sampling rate of only 3.93 GSps. Channels selected from the multiplex were up-converted to 60 GHz via a remotely delivered carrier. An aggregate data rate of 49.7 Gbps was achieved for the 240-channel multiplex, using mixed bandwidths, numerologies and subcarrier modulation (16-QAM and 64-QAM).

The measurement and simulation results have shown the feasibility of using hierarchical NZ mapping to aggregate/ de-aggregate very large numbers of signals in the digital domain, for a flexible, scalable, dynamic and versatile analogue 5G mobile fronthaul. LTE and 5G signals can be presented at their respective frequencies for heterogeneous and mMIMO applications, employing receivers with arbitrary low sampling rates and analogue bandwidth specifications.

8.2 Future Work

A number of extensions to the work that has been presented in this thesis are discussed and elaborated in this section. These extensions are discussed in short term to longer term ordering.

- ***Complexity estimations with different use cases***: The digital aggregation/ de-aggregation technique presented in this work employs a single IFFT and NZ mapping to multiplex all channels (for the same numerology) at the transmitter, coupled with digital band-pass filtering and band-pass sampling at the receiver for the de-multiplexing process. The overall complexity of the architecture will be determined by a number of factors, including bandwidth of signals, size of multiplexes, use of a THA (with some analogue processing), sampling rates in ADCs and filter selectivities as well as number of IFFTs and their length. Different use cases can be analysed in terms of complexity, the aim being to see how complexity scales under more or less demanding use cases and how the flexibility of the system and achieved spectral efficiencies can alleviate potential complexity constraints.

- ***Incorporation of other 5G waveform candidates***: 5G waveform candidates such as F-OFDM and RB-F-OFDM are characterised by very low spectral leakage [47] due to transmit and receive filtering. Thus, multiplexes can be created employing such filtered variants for higher spectral efficiency and can be used for performance comparison with the CP-OFDM multiplexes presented in this work (e.g. in terms of how close the channels can be, and performance under non-linearity constraints). Normally, processing for filtered OFDM variants is carried out for a single signal. Modifying this type of processing so that filtering is applied to an entire multiplex in the way that it is created in this work will be an interesting approach that can reduce the amount of processing required per channel.

- ***Non-linearity analysis and pre-distortion***: Non-linearity analysis, as well as different non-linearity compensation schemes for digital channel aggregation systems have been presented in [13], [189], [152], [190], with channel bandwidths of up to 500 MHz and multiplexes with up to 72 channels. Non-linearity analysis can be carried out for the multiplexing technique presented in this work. The multiplexing technique presented

here employs large IFFTs, which can result in multiplexed signals with high PAPR. An analysis of distortion effects caused by this approach within a direct or external IM-DD link will therefore be of interest. Furthermore, simple and flexible Digital Pre-distortion (DPD) schemes can be used for non-linearity compensation at the transmitter side. Pre-distortion analysis can include multiplexes created using CP-OFDM, F-OFDM and RB-F-OFDM and other filtered variants and comparisons among achieved performances.

- ***Analogue fronthauls with network slicing:*** Digital multiplexing techniques are promising, but must be as flexible and scalable as possible to operate within a dynamic next generation mobile network (5G and beyond) that includes different numerologies and bandwidths, multiple antenna techniques and heterogeneous networking. Flexibility is of prime importance in such a network, requiring the SCM transport architecture to be able to dynamically adapt to accommodate such differing use cases. The SCM approach presented in this work is very flexible and could thus be employed within an architecture that is dynamically adjustable, for example one employing orchestration and network slicing approaches in the future 5G analogue fronthaul. This development would be inherently novel as the focus of current network slicing approaches is on digital fronthaul applications. Specifically, through Software Defined Radio (SDR) techniques within such an orchestration and network slicing environment a number of control elements (these receive instructions from the orchestrator and adjust parameters accordingly) may be distributed within the fronthaul as shown in Figure 8-1 among Stages A – E. The orchestrator can be used to adjust the sampling rate, down-sampling factor, digital filter parameters etc. of RRUs in a dynamic/ semi-dynamic manner using SDR approaches. Furthermore, NZs become “resources”, which, based on network-wide conditions and as directed by the orchestrator, are resized and adjusted to fulfil user requirements (e.g. throughput, throughput enhancement through MIMO). The resources are dynamically adjustable, meaning that they can be created, adjusted and removed according to demand. Some of these adjustments can be the mapping of channels and/ or super groups of channels with varying bandwidths and sizes into Sub-Multiplexes, Multiplexes and Super-Multiplexes (these were described at a conceptual level in Section 5.4; an experimental demonstration of a Multiplex was shown in Section 6.4.1 with two different 5G numerologies; a simulation-based demonstration for a Super-Multiplex was carried out in Section 7.4) at the transmitter side. These are associated directly with sampling rates and down-sampling factors available at the

receiver, which are also adjusted dynamically. This way, the network can utilise available processing resources more efficiently and reduce energy consumption.

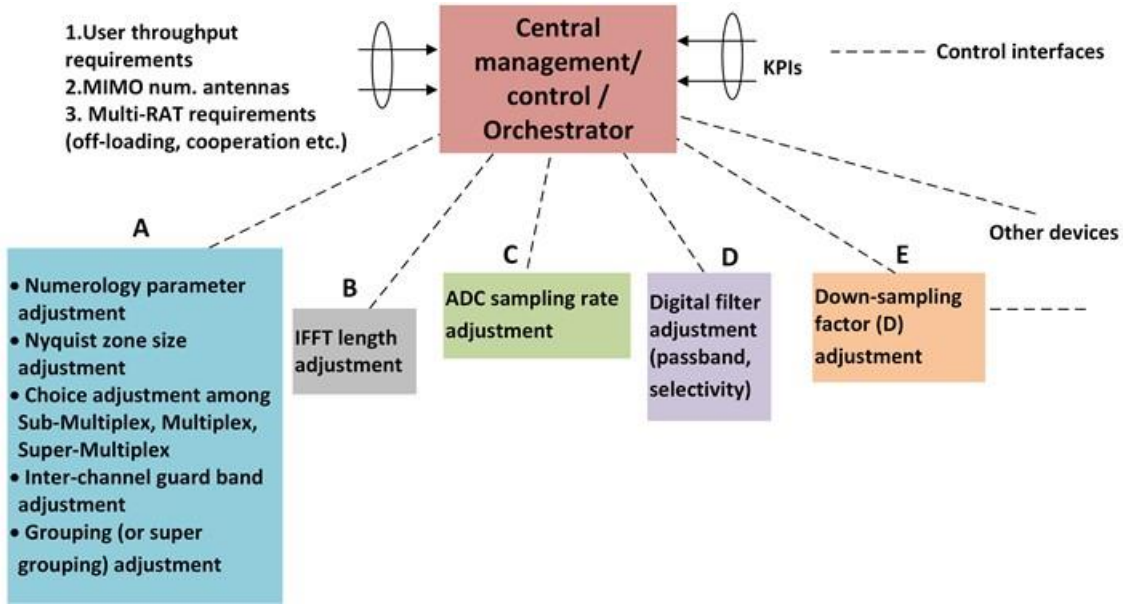

Figure 8-1 Application of technique within an analogue fronthaul with network slicing.

References

[1] NGMN Alliance, “NGMN 5G White Paper,” 17 February 2015. [Online]. Available: https://www.ngmn.org/fileadmin/ngmn/content/images/news/ngmn_news/NGMN_5G_White_Paper_V1_0.pdf. [Accessed 5 February 2019].

[2] METIS, “Deliverable D1.1: Scenarios, requirements and KPIs for 5G mobile and wireless system,” 29 April 2013. [Online]. Available: https://cordis.europa.eu/docs/projects/cnect/9/317669/080/deliverables/001-METISD11v1pdf.pdf. [Accessed 27 February 2019].

[3] Ofcom, “Enabling 5G in the UK,” 9 March 2018. [Online]. Available: https://www.ofcom.org.uk/__data/assets/pdf_file/0022/111883/enabling-5g-uk.pdf. [Accessed 7 March 2019].

[4] M. Steeg, N. J. Gomes, A. A. Juarez, M. Kościesza, M. Lange, Y. Leiba, H. Mano, H. Murata, M. Szczęsny and A. Stöhr, “Public Field Trial of a Multi-RAT (60 GHz 5G/ LTE/WiFi) Mobile Network,” *IEEE Wireless Communications,* vol. 25, no. 5, pp. 38-46, 2018.

[5] N. J. Gomes, P. Chanclou, P. Turnbull, A. Magee and V. Jungickel, “Fronthaul Evolution: From CPRI to Ethernet,” *Optical Fiber Technology,* vol. 26, no. Part A, pp. 50-58, 2015.

[6] T. Pfeiffer, “Next Generation Mobile Fronthaul and Midhaul Architectures [Invited],” *Journal of Optical Communications and Networking,* vol. 7, no. 11, pp. B38-B45, 2015.

[7] 3GPP Technical Specification Group Radio Access Network, “Study on New Radio Access Technology: Radio Access Architecture and Interfaces (Release 14), TR 38.801, V14.0.0,” March 2017. [Online]. Available: http://www.3gpp.org/DynaReport/38-series.htm. [Accessed 3 March 2019].

[8] N. J. Gomes, P. P. Monteiro and A. Gameiro, Next Generation Wireless Communications Using Radio over Fiber, West Sussex, United Kingdom: Wiley, 2012, pp. 3, 61-89, 162.

[9] F. A. Gutierrez, E. P. Martin, P. Perry, A. D. Ellis, P. M. Anandarajah and L. P. Barry, “WDM Orthogonal Subcarrier Multiplexing,” *Journal of Lightwave Technology,* vol. 34, no. 8, pp. 1815-1823, 2016.

[10] P. Assimakopoulos, A. Nkansah, N. J. Gomes and D. Wake, “Multi-channel signal transmission through radio over fiber architecture,” in *IEEE GLOBECOM Workshops (GC Wkshps)*, Houston, TX, USA, 2011.

[11] W. H. Chen and W. I. Way, “Multichannel Single-Sideband SCM/DWDM Transmission Systems,” *Journal of Lightwave Technology,* vol. 22, no. 7, pp. 1679-1693, 2004.

[12] ITU-T - Telecommunication Standardization Sector of International Telecommunication Union, “Series G Supplement 55: Radio-over-fibre (RoF) technologies and their applications,” July 2015. [Online]. Available: https://www.itu.int/rec/dologin_pub.asp?lang=e&id=T-REC-G.Sup55-201507-I!!PDF-E&type=items. [Accessed 4 March 2019].

[13] P. Li, W. Pan, L. Huang, X. Zou, Y. Pan, Q. Zhou, Y.-W. Chen, P.-C. Peng, S. Liu, S. Shen and G.-K. Chang, “Multi-IF-Over-Fiber Based Mobile Fronthaul With Blind Linearization and Flexible Dispersion Induced Bandwidth Penalty Mitigation,” *Journal of Lightwave Technology,* vol. 37, no. 4, pp. 1424-1433, 2019.

[14] P. T. Dat, A. Kanno, N. Yamamoto and T. Kawanishi, “190-Gb/s CPRI-Equivalent Rate Fiber-Wireless Mobile Fronthaul for Simultaneous Transmission of LTE-A and F-OFDM Signals,” in *European Confernce and Exhibition on Optical Communications (ECOC)*, Düsseldorf, Germany, 2016.

[15] P. T. Dat, A. Kanno, N. Yamamoto and T. Kawanishi, “Simultaneous Transmission of MultiRATs and Mobile Fronthaul in the MMW Bands over an IFoF System,” in *Optical Fiber Communications Conference and Exhibition (OFC)*, Los Angeles, CA, USA, 2017.

[16] Z. Dong, H.-C. Chien, J. Yu, Z. Jia, J. Zhang, L. Cheng and G.-K. Chang, “A bandwidth-efficient coherent ultra-dense WDM-PON based on Nyquist independent-sideband modulation,” in *The European Conference on Optical Communication (ECOC)*, Cannes, France, 2014.

[17] S. Ishimura, A. Bekkali, K. Tanaka, K. Nishimura and M. Suzuki, “1.032-Tb/s CPRI-Equivalent Rate IF-Over-Fiber Transmission Using a Parallel IM/ PM Transmitter for High-Capacity Mobile Fronthaul Links,” *Journal of Lightwave Technology,* vol. 36, no. 8, pp. 1478-1484, 2018.

[18] L. Cheng, X. Liu, N. Chard, F. Effenberger and G. Chang, “Experimental Demonstration of Sub-Nyquist Sampling for Bandwidth-and-Hardware-Efficient Mobile Fronthaul Supporting 128x128 MIMO with 100 MHz OFDM signals,” in *Optical Fiber Communication Conference (OFC)*, California, 2016.

[19] R. G. Vaughan, N. L. Scott and D. R. White, “The Theory of Bandpass Sampling,” *IEEE Transactions on Signal Processing,* vol. 39, no. 9, pp. 1973-1984, 1991.

[20] Y. Yang, C. Lim and A. Nirmalathas, “A full-duplex digitized RoF system for millimeter-wave OFDM transmission,” in *European Conference and Exhibition on Optical Communications (ECOC)*, Amsterdam, Netherlands, 2012.

[21] Y. Yang, C. Lim and A. Nirmalathas, “Investigation on Transport Schemes for Efficient High-Frequency Broadband OFDM Transmission in Fibre-Wireless Links,” *Journal of Lightwave Technology,* vol. 32, no. 2, pp. 267-274, 2014.

[22] S. T. Le, K. Schuh, M. Chagnon, F. Buchali and H. Buelow, “1.53-Tbps CPRI-Equivalent Data Rate Transmission with Kramers-Kronig Receiver for Mobile Fronthaul Links,” in *European Conference on Optical Communication (ECOC)*, Rome, Italy, 2018.

[23] J. E. S. James, “Optical phase modulator and sideband filtering millimetre-wave generation for radio over fibre systems, Ph.D dissertation,” EDA, University of Kent, Canterbury, 2011.

[24] C.-Y. Li, H.-S. Su, C.-H. Chang, H.-H. Lu, P.-Y. Wu, C.-Y. Chen and C.-L. Ying, “Generation and Transmission of BB/MW/MMW Signals by Cascading PM and MZM,” *Journal of Lightwave Technology,* vol. 30, no. 3, pp. 298-303, 2012.

[25] K. A. Mekonnen, E. Tangdiongga and T. Koonen, “High-Capacity Dynamic Indoor All-Optical-Wireless Communication System Backed up with Millimeter-wave Radio Techniques,” *Journal of Lightwave Technology,* vol. 36, no. 19, pp. 4460-4467, 2018.

[26] J. Vucic, C. Kottke, S. Nerreter, K. Langer and W. J. Walewski, “513 Mbit/s Visible Light Communications Link Based on DMT-Modulation of a White LED,” *Journal of Lightwave Technology,* vol. 28, no. 24, pp. 3512-3518, 2010.

[27] Radiocommunication Sector of International Telecommunication Union (ITU-R), “Report ITU-R BT. 2254: Frequency and network planning aspects of DVB-T2,” September 2012. [Online]. Available: https://www.itu.int/dms_pub/itu-r/opb/rep/R-REP-BT.2254-2012-PDF-E.pdf. [Accessed 11 March 2019].

[28] X. Liu, H. Zeng, N. Chand and F. Effenberger, “Efficient mobile fronthaul via DSP-based channel aggregation,” *Journal of Lightwave Technology,* vol. 34, no. 6, pp. 1556-1564, 2016.

[29] M. Sung, S.-H. Cho, J. Kim, J. K. Lee, J. H. Lee and H. S. Chung, “Demonstration of IFoF-Based Mobile Fronthaul in 5G Prototype With 28-GHz Millimeter Wave,” *Journal of Lightwave Technology,* vol. 36, no. 2, pp. 601-609, 2018.

[30] G. Vedala, M. A. Hameed and R. Hui, “Digital Compensation of SSBI in Direct Detection Multicarrier System with SOA Nonlinearities,” *IEEE Photonics Technology Letters,* vol. 29, no. 4, pp. 369-372, 2017.

[31] M. Xu, J.-H. Yan, J. Zhang, F. Lu, J. Wang, L. Cheng, D. Guidotti and G.-K. Chang, “Bidirectional fiber-wireless access technology for 5G mobile spectral aggregation and cell densification,” *IEEE/ OSA Journal of Optical Communications and Networking,* vol. 8, no. 12, pp. 104-110, 2016.

[32] Y. Yang, C. Lim and A. Nirmalathas, “Bandwidth Improvement of Digitized RoF System Using Track-and-Hold Amplifier,” in *IEEE International Topical Meeting on Microwave Photonics*, Noordwijk, Netherlands, 2012.

[33] C. P. Liu and A. Seeds, “Transmission of Wireless MIMO-Type Signals Over a Single Optical Fiber Without WDM,” *IEEE Transactions on Microwave Theory and Techniques,* vol. 58, no. 11, pp. 3094-3102, 2010.

[34] R. Hui, K. Kaje and A. Fumagalli, “Digital-Analog Hybrid SCM for Fine-Granularity Circuit-Switched Optical Networks,” in *International Conference on Transparent Optical Networks*, Trento, Italy, 2016.

[35] Qualcomm, “Making 5G NR a reality,” December 2016. [Online]. Available: https://www.qualcomm.com/media/documents/files/whitepaper-making-5g-nr-a-reality.pdf. [Accessed 7 March 2019].

[36] Institute of Electrical and Electronics Engineers (IEEE), “IEEE 5G and Beyond Technology Roadmap White Paper,” 2019. [Online]. Available: https://futurenetworks.ieee.org/images/files/pdf/ieee-5g-roadmap-white-paper.pdf. [Accessed 26 February 2019].

[37] Cisco, “Cisco Visual Networking Index: Forecast and Trends, 2017-2022,” 26 November 2018. [Online]. Available: https://www.cisco.com/c/en/us/solutions/collateral/service-provider/visual-networking-index-vni/white-paper-c11-741490.pdf. [Accessed 26 February 2019].

[38] GSMA, “5G Spectrum: GSMA Public Policy Question,” November 2018. [Online]. Available: https://www.gsma.com/spectrum/wp-content/uploads/2018/11/5G-Spectrum-Positions.pdf. [Accessed 27 February 2019].

[39] E. Björnson, E. G. Larsson and T. L. Marzetta, “Massive MIMO: Ten Myths and One Critical Question,” *IEEE Communications Magazine,* vol. 54, no. 2, pp. 114-123, 2016.

[40] E. Björnson, L. V. d. Perre, S. Buzzi and E. G. Larsson, “Massive MIMO in Sub-6 GHz and mmWave: Physical, Practical and Use-Case Differences,” *IEEE Wireless Communications,* pp. 2-10, 2019.

[41] Ericsson, “Advanced antenna systems for 5G networks,” November 2018. [Online]. Available: https://www.ericsson.com/assets/local/publications/white-papers/10201407_wp_advanced_antenna_system_nov18_181115.pdf. [Accessed 27 February 2019].

[42] S. Kutty and D. Sen, “Beamforming for Millimeter Wave Communications: An Inclusive Survey,” *IEEE Communications Surverys and Tutorials,* vol. 18, no. 2, pp. 949-972, 2016.

[43] J. Ghosh and S. D. Roy, “The Implications of Cognitive Femtocell Based Spectrum Allocation over Macrocell Networks,” *Wireless Personal Communications,* vol. 92, no. 3, pp. 1125-1143, 2017.

[44] Anritsu, “5G - New Waveform Signal Analysis,” 2016. [Online]. Available: https://dl.cdn-anritsu.com/ja-jp/test-measurement/reffiles/About-Anritsu/R_D/Technical/91/91-04-5g-2.pdf. [Accessed 28 February 2019].

[45] Rohde and Schwarz, “5G Waveform Candidates,” 10 June 2016. [Online]. Available: https://www.rohde-schwarz.com/nl/applications/5g-waveform-candidates-application-note_56280-267585.html. [Accessed 12 March 2019].

[46] X. Zhang, L. Chen, J. Qiu and J. Abdoli, “On the Waveform for 5G,” *IEEE Communications Magazine,* vol. 54, no. 11, pp. 74-80, 2016.

[47] Y. Liu, X. Chen, Z. Zhong, B. Ai, D. Miao, Z. Zhao, J. Sun, Y. Teng and H. Guan, “Waveform Design for 5G Networks: Analysis and Comparison,” *IEEE Access,* vol. 5, pp. 19282-19292, 2017.

[48] Q. Zheng, F. Wang, X. Chen, Y. Liu, D. Miao and Z. Zhao, “Comparison of 5G Waveform Candidates in High Speed Scenario,” in *General Assembly and Scientific Symposium of the International Union of Radio Science (URSI GASS)*, Montreal, QC, Canada, 2017.

[49] National Instruments, “5G New Radio: Introduction to the Physical Layer [White Paper],” 2018. [Online]. Available: http://download.ni.com/evaluation/rf/5G_New_Radio_WP.pdf. [Accessed 28 February 2019].

[50] Keysight Technologies, “Understanding the 5G NR Physical Layer,” 1 November 2017. [Online]. Available: https://www.keysight.com/upload/cmc_upload/All/Understanding_the_5G_NR_Physical_Layer.pdf. [Accessed 28 February 2019].

[51] A. A. Zaidi, R. Baldemair, H. Tulberg, H. Björkegren, L. Sundström, J. Medbo, C. Kilinc and I. Da Silva, “Waveform and Numerology to Support 5G Services and Requirements,” *IEEE Communications Magazine,* vol. 54, no. 11, pp. 90-98, 2016.

[52] M. Alard and R. Lassalle, “Principles of modulation and channel coding for digital broadcasting for mobile receivers,” *EBU Technical Review,* no. 224, pp. 168-190, 1987.

[53] J. Armstrong, “OFDM for Optical Communications,” *Journal of Lightwave Technology,* vol. 27, no. 3, pp. 189-204, 2009.

[54] S. B. Weinstein, “The history of orthogonal frequency-division multiplexing [History of Communications],” *IEEE Communications Magazine,* vol. 47, no. 11, pp. 26-35, 2009.

[55] LAN/MAN Standards Committee of the IEEE Computer Society, “Part 11: Wireless LAN Medium Access Control (MAC) and Physical Layer (PHY) specifications: High-speed Physical Layer in the 5GHz Band,” The Institute of Electrical and Electronics Engineers, NY, USA, 1999.

[56] R. V. Nee, V. K. Jones, G. Awater, A. V. Zelst, J. Gardner and G. Steele, “The 802.11n MIMO-OFDM Standard for Wireless LAN and Beyond,” *Wireless Personal Communications,* vol. 37, no. 3-4, pp. 445-453, 2006.

[57] T. Hwang, C. Yang, G. Wu, S. Li and G. Y. Li, “OFDM and Its Wireless Applications: A Survey,” *IEEE Transactions on Vehicular Technology,* vol. 58, no. 4, pp. 1673-1694, 2009.

[58] P. Assimakopoulos, “Nonlinear effects in OFDM signal transmission over radio over fibre links, Ph.D dissertation,” EDA, University of Kent, Canterbury, 2012.

[59] A. Goldsmith, “Multicarrier Modulation,” in *Wireless Communications*, New York, Cambridge University Press, 2005, pp. 374-401.

[60] J. Tellado, Multicarrier modulation with low par: applications to DSL and wireless, Boston, Mass.: Kluwer Academic Publishers, 2000.

[61] A. M. Khalid, G. Cossu, R. Corsini, P. Choudhury and E. Ciaramella, “1-Gb/s Transmission Over a Phosphorescent White LED by Using Rate-Adaptive Discrete Multitone Modulation,” *IEEE Photonics Journal,* vol. 4, no. 5, pp. 1464-1473, 2012.

[62] J. M. Cioffi, “A Multicarrier Primer,” June 2008. [Online]. Available: https://web.stanford.edu/group/cioffi/documents/multicarrier.pdf. [Accessed 15 February 2019].

[63] S. C. J. Lee, “Discrete Multitone Modulation for Short-Range Optical Communications, Ph.D dissertation,” Dept. Elect. Eng Eindhoven: Technische Universiteit, Eindhoven, Netherlands, 2009.

[64] Y. S. Cho, J. Kim, W. Y. Yang and C. G. Kang, MIMO-OFDM Wireless Communications with MATLAB, Clementi Loop, Singapore: IEEE Press, John Wiley & Sons (Asia) Pte Ltd, 2010, pp. 121-135.

[65] P. Golden, H. Dedieu and K. Jacobsen, Fundamentals of DSL technology, Boca Raton, FL: Auerbach Publications, 2006.

[66] Meyer, Charles J, Senior Applications Engineer, Boonton Electronics, “Measuring the Peak-to-Average Power of Digitally Modulated Signals [Application Note],” Boonton Electronics Corporation, Parsippany, NJ, USA, 1993.

[67] J. K. Cavers, “An analysis of pilot symbol assisted modulation for Rayleigh fading channels,” *IEE Transactions on Vehicular Technology,* vol. 40, no. 4, pp. 686-693, 1991.

[68] S. Coleri, M. Ergen, A. Puri and A. Bahai, “Channel Estimation Techniques Based on Pilot Arrangement in OFDM Systems,” *IEEE Transactions on Broadcasting,* vol. 48, no. 3, pp. 223-229, 2002.

[69] M. Sliskovic, “Carrier and sampling frequency offset estimation and correction in multicarrier systems,” *Global Telecommunications Conference,* vol. 1, pp. 285-289, 2001.

[70] M. Sandell, J. J. Van de Beek and P. O. Borjesson, “Timing and frequency synchronization in OFDM systems using the cyclic prefix,” in *International Symposium on Sychronization*, Essen, Germany, 1995.

[71] S. G. Wilson, R. Shang and R. He, “Frame Synchronization for OFDM Using Cyclic Prefix and Pilot Carriers,” in *IEEE Military Communications Conference*, Baltimore, MD, USA, 2017.

[72] J. James, P. Shen, A. Nkansah, X. Liang and N. J. Gomes, “Nonlinearity and Noise Effects in Multi-Level Signal Millimeter-Wave Over Fiber Transmission Using Single and Dual Wavelength Modulation,” *IEEE Transactions on Microwave Theory and Techniques,* vol. 58, no. 11, pp. 3189-3198, 2010.

[73] IEEE Computer Society and the IEEE Microwave Theory and Techniques Society, “IEEE Standard for Local and metropolitan area networks. Part 16: Air Interface for Fixed Broadband Access Systems, IEEE 802.16,” IEEE LAN/MAN Standards Committee, NY, USA, 2009.

[74] 3GPP Technical Specification Group Radio Access Network, “Base Station (BS) radio transmission and reception (Release 15), NR, TS 38.104, V15.0.0,” December 2017. [Online]. Available: http://www.3gpp.org/DynaReport/38-series.htm. [Accessed 8 December 2018].

[75] M. Vigilante, E. McCune and P. Reynaert, “To EVM or Two EVMs?: An Answer to the Question,” *IEEE Solid-State Circuits Society,* vol. 9, no. 3, pp. 36-39, 2017.

[76] B. Cutler, “Effects of Physical Layer Impairments on OFDM Systems,” *RF Design,* vol. 25, pp. 36-45, 2002.

[77] W. Kester and J. Bryant, “Sampled Data Systems,” in *Mixed-signal and DSP Design Techniques (Analog Devices)*, Massachusetts, Newnes/Elsevier, 2003, pp. 15-21.

[78] Texas Instruments, “Why Oversample when Under-sampling can do the Job? (Application Report),” July 2013. [Online]. Available: http://www.ti.com/lit/an/slaa594a/slaa594a.pdf. [Accessed 4 January 2019].

[79] G. Hill, “The Benefits of Undersampling,” *Electronic Design,* pp. 69-79, 1994.

[80] Silicon Laboratories, “AN118: Improving ADC Resolution by Oversampling and Averaging,” 2013. [Online]. Available: https://www.silabs.com/documents/public/application-notes/an118.pdf. [Accessed 23 February 2019].

[81] Texas Instruments Europe, “Oversampling Techniques using the TMS320C24x Family,” June 1998. [Online]. Available: http://www.ti.com/lit/an/spra461/spra461.pdf. [Accessed 23 February 2019].

[82] C. Baack, G. Elze, G. Großkopf, F. Kraus, W. Krick and L. Küller, “Analogue optical transmission of 26 t.v. channels,” *Electronics Letters,* vol. 15, no. 10, pp. 300-301, 1979.

[83] T. E. Darcie, “Subcarrier Multiplexing for Multiple-Access Lightwave Networks,” *Journal of Lightwave Technology,* vol. 5, no. 8, pp. 1103-1110, 1987.

[84] W. I. Way, “Subcarrier Multiplexed Lightwave System Design Considerations For Subscriber Loop Applications,” *Journal of Lightwave Technology,* vol. 7, no. 11, pp. 1806-1818, 1989.

[85] D. Wake, A. Nkansah and N. J. Gomes, “Radio Over Fiber Link Design for Next Generation Wireless Systems,” *Journal of Lightwave Technology,* vol. 28, no. 16, pp. 2456-2464, 2010.

[86] A. E. Aighobahi, P. Assimakopoulos and N. J. Gomes, “Experimental Analysis of Single and Multiple Antenna Units in Uplink of Radio-over-Fiber Distributed Antenna System,” in *International Topical Meeting on Microwave Photonics (MWP)*, Paphos, Cyprus, 2015.

[87] C. H. Cox, III, Analog Optical Links: Theory and Practice, New York, USA: Cambridge University Press, 2004.

[88] G. Keiser, Optical Fiber Communications, Singapore: McGraw-Hill, 2000.

[89] Common Public Radio Interface (CPRI), “Interface Specification, CPRI Specification V7.0,” October 2015. [Online]. Available: http://www.cpri.info/spec.html. [Accessed 8 January 2019].

[90] D. Wake, A. Nkansah, N. J. Gomes, G. d. Valicourt, R. Brenot, M. Violas, Z. Liu, F. Ferreira and S. Pato, “A Comparison of Radio Over Fiber Link Types for the Support of Wideband Radio Channels,” *Journal of Lightwave Technology,* vol. 28, no. 16, pp. 2416-2422, 2010.

[91] G. E. Betts, C. H. Cox III and K. G. Ray, “20 GHz optical analog link using an external modulator,” *IEEE Photonic Technology Letters,* vol. 2, no. 12, pp. 923-925, 1990.

[92] B. G. Kim, S. H. Bae and Y. C. Chung, “RoF-Based Mobile Fronthaul Networks Implemented by Using DML and EML for 5G Wireless Communication Systems,” *Journal of Lightwave Technology,* vol. 36, no. 14, pp. 2874-2881, 2018.

[93] M. C. R. Medeiros, R. Avo, P. Laurencio, N. S. Correia, A. Barradas, H. J. A. d. Silva, I. Darwazeh, J. E. Mitchell and P. M. N. Monteiro, “Radio over fiber access network architecture employing reflective semiconductor optical amplifiers,” in *ICTON Mediterranean Winter Conference*, Sousse, Tunisia, 2008.

[94] X. Yu, T. B. Gibbon and I. T. Monroy, “Bidirectional Radio-over-Fiber System with Phase-Modulation Downlink and RF Oscillator-Free Uplink Using a Reflective SOA,” *IEEE Photonics Technology Letters,* vol. 20, no. 24, pp. 2180-2182, 2008.

[95] D. Zibar, K. J. Larsen and I. T. Monroy, “Digital Coherent Receiver for Subcarrier Multiplexed Phase-Modulated Radio-over-Fibre Signals,” *Electronics Letters,* vol. 45, no. 11, pp. 563-564, 2009.

[96] A. Caballero, D. Zibar and I. T. Monroy, “Performance Evaluation of Digital Coherent Receivers for Phase-Modulated Radio-over-Fiber Links,” *Journal of Lightwave Technology,* vol. 29, no. 21, pp. 3282-3292, 2011.

[97] V. J. Urick, F. Bucholtz, P. S. Devgan, J. D. McKinney and K. J. Williams, “Phase Modulation with Interferometric Detection as an Alternative to Intensity Modulation with Direct Detection for Analog-Photonic Links,” *IEEE Transactions on Microwave Theory and Techniques,* vol. 55, no. 9, pp. 1978-1985, 2007.

[98] A. K. M. Lam, M. Fairburn and N. A. F. Jaegar, “Wide-Band Electrooptic Intensity Modulator Frequency Response Measurement Using an Optical Heterodyne Down-Conversion Technique,” *IEEE Transactions on Microwave Theory and Techniques,* vol. 54, no. 1, pp. 240-246, 2006.

[99] M. Maafa, “Frequency Doubling of RF-Over-Fiber Signal Based on Mach Zehnder Modulator [MSc Thesis],” Rochester Institute of Technology Scholar Works, Rochester, New York, 2016.

[100] Z. Chen, J. Dai, Y. Zhou, F. Yin, T. Zhang, L. Jianqiang, Y. Dai and K. Xu, “Frequency quadrupling microwave signal generation based on an optoelectronic oscillator with low phase noise,” in *International Topical Meeting on Microwave Photonics (MWP)*, Beijing, China, 2017.

[101] C. H. Cox, III, E. I. Ackerman, G. E. Betts and J. L. Prince, “Limits on the Performance of RF-Over-Fiber LInks and Their Impact on Device Design,” *IEEE Transactions on Microwave Theory and Techniques,* vol. 54, no. 2, pp. 906-920, 2006.

[102] F. . A. Gutiérrez, P. Perry, F. Smyth, A. D. Ellis and L. P. Barry, “Optimum Bias Point in Broadband Subcarrier Multiplexing with Optical IQ Modulators,” *Journal of Lightwave Technology,* vol. 33, no. 1, pp. 258-266, 2015.

[103] K.-i. Kitayama, “Highly Spectrum Efficient OFDM/PDM Wireless Networks by Using Optical SSB Modulation,” *Journal of Lightwave Technology,* vol. 16, no. 6, pp. 969-, 1998.

[104] G. H. Smith, D. Novak and Z. Ahmed, “Overcoming Chromatic-Dispersion Effects in Fiber-Wireless Systems Incorporating External Modulators,” *IEEE Transactions on Microwave Theory and Techniques,* vol. 45, no. 8, pp. 1410-1415, 1997.

[105] A. Loayssa, C. Lim, A. Nirmalathas and D. Benito, “Optical Single-Sideband Modulator for Broad-Band Subcarrier Multiplexing Systems,” *IEEE Photonics Technology Letters,* vol. 15, no. 2, pp. 311-313, 2003.

[106] Y. Tian, K.-L. Lee, C. Lim and A. Nirmalathas, “60 GHz Analog Radio-Over-Fiber Fronthaul Investigations,” *Journal of Lightwave Technology,* vol. 35, no. 19, pp. 4304-4310, 2017.

[107] V. Torres-Company and A. M. Weiner, “Optical frequency comb technology for ultra-broadband radio-frequency photonics,” *Laser and Photonics Reviews,* vol. 8, no. 3, pp. 368-393, 2014.

[108] P. Assimakopoulos , J. Zou, K. Habel, J.-P. Elbers, V. Jungnickel and N. J. Gomes, “A Converged Evolved Ethernet Fronthaul for the 5G Era,” *IEEE Journal on Selected Areas in Communications,* vol. 36, no. 11, pp. 2528-2536, 2018.

[109] N. J. Gomes, P. Assimakopoulos, M. K. Al-Hares, U. Habib and S. Noor, “The New Flexible Mobile Fronthaul: Digital or Analog, or Both?,” in *International Conference on Transparent Optical Networks (ICTON)*, Trento, 2016.

[110] B. Bertenyi, R. Burbidge, G. Masini, S. Sirotkin and Y. Gao, “NG Radio Access Network (NG-RAN),” *Journal of ICT Standardization,* vol. 6, no. Combined Special Issue 1 & 2, pp. 59-76, 2018.

[111] N. J. Gomes and P. Assimakopoulos, “Optical Fronthaul Options for Meeting 5G Requirements,” in *International Conference on Transparent Optical Networks (ICTON)*, Bucharest, Romania, 2018.

[112] Nokia Bell Labs, “Carrier Aggregation and Dual Connectivity,” August 2017. [Online]. Available: https://www.its.bldrdoc.gov/media/66437/ratasuk_isart2017.pdf. [Accessed 2 March 2019].

[113] J. Zhang, Q. Zeng, T. Mahmoodi, A. Georgakopoulos and P. Demestichas, “LTE Small Cell Enhancement by Dual Connectivity [White Paper],” *Wireless World Research Forum,* no. 15, pp. 1-20, November 2014.

[114] H.-S. Jo, Y. J. Sang, P. Xia and J. G. Andrews, “Heterogeneous Cellular Networks with Flexible Cell Association: A Comprehensive Downlink SINR Analysis,” *IEEE Transactions on Wireless Communications,* vol. 11, no. 10, pp. 3484-3495, 2012.

[115] A. Bonfante, L. G. Giordano, D. Lopez-Perez, A. Garcia-Rodriguez, G. Geraci, P. Baracca, M. M. Butt, M. Dzaferagic and N. Marchetti, “Performance of Massive MIMO Self-Backhauling for Ultra-Dense Small Cell Deployments,” in *IEEE Global Communications Conference (GLOBECOM)*, Abu Dhabi, United Arab Emirates, 2018.

[116] X. Wang, E. Turgut and M. C. Gursoy, “Coverage in Downlink Heterogeneous mmWave Cellular Networks with User-Centric Small Cell Deployment,” *IEEE Vehicular Technology Society,* pp. 1-19, 2019.

[117] M. A. Abyaneh, B. Huyart and J.-C. Cousin, “Carrier Aggregation of Three OFDM Signals Using a Single Oscillator and I/Q Modulator,” *IEEE Transactions on Microwave Theory and Techniques,* vol. 65, no. 9, pp. 3351-3359, 2017.

[118] N. J. Gomes, P. Sehier, H. Thomas, P. Chanclou, B. Li, D. Münch, P. Assimakopoulos, S. Dixit and V. Jungnickel, “Boosting 5G Through Ethernet: How Evolved Fronthaul Can Take Next-Generation Mobile to the Next Level,” *IEEE Vehicular Technology Magazine,* vol. 13, no. 1, pp. 74-84, 2018.

[119] C. Ranaweera, E. Wong, A. Nirmalathas , C. Jayasundara and C. Lim, “5G C-RAN With Optical Fronthaul: An Analysis From a Development Perspective,” *Journal of Lightwave Technology,* vol. 36, no. 11, pp. 2059-2068, 2018.

[120] S. Rangan, T. S. Rappaport and E. Erkip, “Millimeter-Wave Cellular Wireless Networks: Potentials and Challenges,” *Proceedings of the IEEE,* vol. 102, no. 3, pp. 366-385, 2014.

[121] F. Boccardi, R. W. Heath Jr., A. Lozano, T. L. Marzetta and P. Popovski, “Five disruptive technology directions for 5G,” *IEEE Communications Magazine,* vol. 52, no. 2, pp. 74-80, 2014.

[122] J. G. Andrews, S. Buzzi, W. Choi, S. V. Hanly, A. Lozano, A. C. K. Soong and J. C. Zhang, “What Will 5G Be?,” *IEEE Journal of Selected Areas in Communications,* vol. 32, no. 6, pp. 1065-1082, 2014.

[123] U. Gliese, S. Norskov and T. N. Nielsen, “Chromatic dispersion in fiber-optic microwave and millimter-wave links,” *IEEE Transactions on Microwave Theory and Techniques,* vol. 44, no. 10, pp. 1716-1724, 1996.

[124] C. Lim, A. Nirmalathas, M. Bakaul, K.-L. Lee, D. Novak and R. Waterhouse, “Mitigation strategy for transmission impairments in millimeter-wave radio-over-fiber networks [Invited],” *Journal of Optical Network,* vol. 8, no. 2, pp. 201-214, 2009.

[125] A. Seeds, “Microwave Photonics,” *IEEE Transactions on Microwave Theory and Techniques,* vol. 50, no. 3, pp. 877-887, 2002.

[126] X. Huang and R. Kohno, “60-GHz Ultra-WideBand Radio-Over-Fiber System Employing SCM/WDM,” in *IEEE International Conference of Ultra-Wideband (ICUWB)*, Sydney, NSW, Australia, 2013.

[127] J. Maeda, T. Katoh and S. Ebisawa, “Effect of Fiber Dispersion on Subcarrier QAM Signal in Radio-Over-Fiber Transmission,” *Journal of Lightwave Technology,* vol. 30, no. 16, pp. 2625-2632, 2012.

[128] Y. Tian, K.-L. Lee, C. Lim and A. Nirmalathas, “Experimental comparison of DSB-SC & OSSB based 60 GHz radio-over-fiber fronthaul links,” in *IEEE International Topical Meeting on Microwave Photonics*, Long Beach, CA, USA, 2016.

[129] M. Weiß, M. Huchard, A. Stöhr, B. Charbonnier, S. Fedderwitz and D. S. Jäger, “60-GHz Photonic Millimeter-Wave Link for Short- to Medium-Range Wireless Transmission Up to 12.5 Gb/s,” *Journal of Lightwave Technology,* vol. 26, no. 15, pp. 2424-2429, 2008.

[130] X. Li, J. Yu and G.-K. Chang, “Frequency-Quadrupling Vector mm-Wave Signal Generation by Only One Single-Drive MZM,” *IEEE Photonics Technology Letters,* vol. 28, no. 12, pp. 1302-1305, 2016.

[131] M. Ogusu, K. Inagaki, Y. Mizuguchi and T. Ohira, “Multiplexing of Millimeter-Wave Signals for Fiber-Radio Links by Direct Modulation of Two-Mode Locked Fabry–Pérot Laser,” *IEEE Transactions on Microwave Theory and Techniques,* vol. 52, no. 2, pp. 498-507, 2004.

[132] P. T. Dat, A. Kanno, N. Yamamoto and T. Kawanishi, “Simultaneous Transmission of 4G LTE-A and Wideband MMW OFDM Signals over FIber Links,” in *IEEE International Topical Meeting on Microwave Photonics (MWP)*, Long Beach, CA, USA, 2016.

[133] L. Roselli, V. Borgioni, F. Zepparelli, F. Ambrosi, M. Comez, P. Faccin and A. Casini, “Analog Laser Predistortion for Multiservice Radio-Over-Fiber Systems,” *Journal of Lightwave Technology,* vol. 21, no. 5, pp. 1211-1223, 2003.

[134] D.-K. G. Pham, G. Gagnon, F. Gagnon, G. Kaddoum, C. Jabbour and P. Desgreys, “FFT-Based Limited Subband Digital Predistortion Technique for Ultra Wideband 5G Systems,” in *IEEE International New Circuits and Systems Conference (NEWCAS)*, Montreal, QC, Canada, 2018.

[135] B. Hraimel, X. Zhang and K. Wu, “Photonic Down-Conversion of Millimeter Wave Multiband Orthogonal Frequency Division Multiplexing Ultra-Wideband Using Four Wave Mixing in an Electro-Absorption Modulator,” *Journal of Lightwave Technology,* vol. 28, no. 13, pp. 1987-1993, 2010.

[136] D.-H. Jeon, H.-D. Jung and S.-K. Han, “Mitigation of Dispersion-Induced Effects Using SOA in Analog Optical Transmission,” *IEEE Photonics Technology Letters,* vol. 14, no. 8, pp. 1166-1168, 2002.

[137] N. Cheng and L. Zhou, “Efficient mobile fronthaul for 24×20MHz LTE signals using self-seeded RSOA with adaptive crosstalk cancellation,” in *European Conference on Optical Communication (ECOC)*, Valencia, Spain, 2015.

[138] Y. Zhao, X. Pang, L. Deng, M. B. Othman, X. Yu, X. Zheng, H. Zhang and I. T. Monroy, “Experimental Demonstration of 5-Gb/s Polarization-Multiplexed Fiber-Wireless MIMO Systems,” in *International Topical Meeting on Microwave Photonics jointly held with the Asia-Pacific Microwave Photonics Conference*, Singapore, 2011.

[139] X. Li, Y. Xu and J. Yu, “Over 100-Gb/s V-Band Single-Carrier PDM-64QAM Fiber-Wireless-Integration System,” *IEEE Photonics Journal,* vol. 8, no. 5, 2016.

[140] R. Puerta, J. Yu, X. Li, Y. Xu, J. J. V. Olmos and I. T. Monroy, “Single-Carrier Dual-Polarization 328-Gb/s Wireless Transmission in a D-Band Millimeter Wave 2 × 2 MU-MIMO Radio-Over-Fiber System,” *Journal of Lightwave Technology,* vol. 36, no. 2, pp. 587-593, 2018.

[141] C. P. Liu and A. Seeds, “Transmission of MIMO radio signals over fibre using a novel phase quadrature double sideband frequency translation technique,” in *IEEE Int. Microw. Photon. Top. Meeting*, Gold Coast, Australia, 2008.

[142] ITU-T - Telecommunication Standardization Sector of International Telecommunication Union , “Recommendation ITU-T G.694.1: Spectral grids for WDM applications: DWDM Frequency Grid,” 13 February 2012. [Online]. Available: https://www.itu.int/rec/T-REC-G.694.1-201202-I/en. [Accessed 12 February 2019].

[143] A. Hraghi, M. E. Chaibi, M. Menif and D. Erasme, “Demonstration of 16QAM-OFDM UDWDM Transmission Using a Tunable Optical Flat Comb Source,” *Journal of Lightwave Technology,* vol. 35, no. 2, pp. 238-245, 2017.

[144] J. D. Reis, A. Shahpari, R. Ferreira, S. Ziaie, D. M. Neves, M. Lima and A. L. Teixeira, “Terabit+ (192 × 10 Gb/s) Nyquist Shaped UDWDM Coherent PON with Upstream and Downstream over a 12.8 nm Band,” *Journal of Lightwave Technology,* vol. 32, no. 4, pp. 729-735, 2014.

[145] M. Zhu, F. Li, F. Lu, J. Yu, C. Su, G. Gu and G.-K. Chang, “Wavelength Resource Sharing in Bidirectional Optical Mobile Fronthaul,” *Journal of Lightwave Technology,* vol. 33, no. 15, pp. 3182-3188, 2015.

[146] P. J. Pinzon, C. Vazquez, I. Perez and J. M. S. Pena, “Synthesis of asymmetric flat-top birefringent interleaver based on digital filter design and genetic algorithm,” *IEEE Photonics Journal,* vol. 5, no. 1, pp. 1496-1502, 2013.

[147] M. Bakaul, A. Nirmalathas and C. Lim, “Multifunctional WDM optical interface for millimter-wave fiber-radio antenna base station,” *Journal of Lightwave Technology,* vol. 23, no. 3, pp. 1210-1218, 2005.

[148] C. Hullin, B. Neyret, J. M. Delavaux, G. C. Wilson and C. Bethea, “DWDM/SCM bi-directional interleaved transmission of 64-QAM using electro absorption modulated laser transmitters,” in *Optical Fiber Communication Conference and Exhibit. Technical Digest Postconference Edition*, Anaheim, CA, USA, 2001.

[149] V. Torres-Company, D. E. Leaird and A. M. Weiner, “Optical Frequency Comb Shaping for Simultaneous Complex Multi-tap Microwave Photonic Filtering and Downconversion Sampling,” in *IEEE International Topical Meeting on Microwave Photonics (MWP)*, Noordwijk, Netherlands, 2012.

[150] A. Kanno, P. T. Dat, N. Sekine, I. Hosako, N. Yamamoto, Y. Yoshida, K.-i. Kitayama and T. Kawanishi, “Seamless Fiber-Wireless Bridge in the Millimeter-and-Terahertz-Wave Bands,” *Journal of Lightwave Technology,* vol. 34, no. 20, pp. 4794-4801, 2016.

[151] C. Lim, Y. Tian, C. Ranaweera, A. Nirmalathas, E. Wong and K.-L. Lee, “Evolution of Radio-over-Fiber Technology,” *Journal of Lightwave Technology,* 2018.

[152] N. Argyris, G. Giannoulis, K. Kanta, N. Iliadis, C. Vagionas, S. Papaioannou, G. Kalfas, D. Apostolopoulos, C. Caillaud, H. Debrégeas, N. Pleros and H. Avramopoulos, “A 5G mmWave Fiber-Wireless IFoF Analog Mobile Fronthaul link with up to 24 Gb/s Multi-band Wireless Capacity,” *Journal of Lightwave Technology,* pp. 1-9, 2019.

[153] N. Shibata, T. Murakami, K. Ishihara, T. Kobayashi, J.-i. Kani, J. Terada, M. Mizoguchi, Y. Miyamoto and N. Yoshimoto, “256-QAM 8 Wireless Signal Transmission with DSP-Assisted Analog RoF for Mobile Front-Haul in LTE-B,” in *OptoElectronics and Communication Conference and Australian Conference on Optical Fibre Technology*, Melbourne, Australia, 2014.

[154] Z. Tayq, L. A. Neto, F. Saliou, C. A. Berthelemot, J. Gomes, T. Haustein, M. Lacouche, J. Plumecoq, L. Bellot and P. Chanclou, “Real Time Demonstration of Fronthaul Transport over a Mix of Analog and Digital RoF,” in *International Conference on Transparent Optical Networks (ICTON)*, Girona, Spain, 2017.

[155] C. Browning, A. Gazman, N. Abrams, K. Bergman and L. P. Barry, “256/ 64 QAM Multicarrier Analog Radio-over-Fiber Modulation using a Linear Differential Drive Silicon Mach-Zehnder Modulator,” in *IEEE International Topical Meeting on Microwave Photonics*, Toulouse, France, 2018.

[156] P. Torres-Ferrera, S. Straullu, S. Abrate and R. Gaudino, “Upstream and Downstream Analysis of an Optical Fronthaul System Based on DSP-Assisted Channel Aggregation,” *IEEE/OSA Journal of Optical Communications and Networking,* vol. 12, no. 9, pp. 1191-1201, 2017.

[157] M. Sung, C. Han, S.-H. Cho, H. S. Chung, S. M. Kim and H. J. Lee, “Bandwidth efficient transmission of 96 LTE-A signals with 118-Gb/s CPRI-equivalent rate using 2-GHz frequency span and intermixing mitigation for mobile fronthaul,” in *International Conference on Information and Communication Technology Convergence*, Jeju, South Korea, 2016.

[158] M. Befekadu, P. Torres-Ferrera and R. Gaudino, “DSP-Assisted Channel Aggregation Options for Next-Generation Mobile Fronthauling,” in *International Conference of Transparent Optical Networks (ICTON)*, Bucharest, Romania, 2018.

[159] X. Li, X. Xiao, Y. Xu, K. Wang, L. Zhao, J. Xiao and J. Yu, “Real-time demonstration of over 20Gbps V- and W-band wireless transmission capacity in one OFDM-RoF system,” in *Optical Fiber Communications Conference and Exhibition (OFC)*, Los Angeles, CA, USA, 2017.

[160] A. Bekkali, T. Kobayashi, K. Nishimura, N. Shibgaki, K. Kashima and Y. Sato, “Millimeter-Wave-Based Fiber-Wireless Bridge System for 8K UHD Video Streaming and Gigabit Ethernet Data Connectivity,” *Journal of Lightwave Technology,* vol. 36, no. 18, pp. 3988-, 2018.

[161] P. T. Dat, A. Kanno, N. Yamamoto and T. Kawanishi, “Seamless Convergence of Fiber and Wireless Systems for 5G and Beyond Networks,” *Journal of Lightwave Technology,* vol. 37, no. 2, pp. 592-605, 2019.

[162] Tektronix, “RFXpress RFX100 Advanced RF/IF/IQ Waveform Creation and Editing Software for the AWG70000, AWG5000 & AWG7000 Series Signal Generators Quick Start User Manual,” 2004. [Online]. Available: https://download.tek.com/manual/RFXpress-RFX100-Quick-Start-User-Manual_0.pdf. [Accessed 5 February 2019].

[163] Tektronix, “Understanding AWG70000A Series Frequency Response and DAC Performance (Application Note),” 2013. [Online]. Available: https://www.tek.com/document/application-note/understanding-awg70000a-series-frequency-response-and-dac-performance. [Accessed 8 December 2018].

[164] VPI Photonics Design Automation, “VPI Photonics Design Automation,” SaM Solutions, [Online]. Available: https://www.vpiphotonics.com/index.php. [Accessed 08 May 2019].

[165] VPIphotonics Design Automation, “VPIphotonics Design Suite Simulation Guide,” 2017.

[166] VPIphotonics, “VPIphotonics Module Reference,” 2019.

[167] VPIphotonics, “Tx_El-OFDM, VPIphotonics Module Reference,” 2019.

[168] VPIphotonics, “Rx_El-OFDM_BER, VPIphotonics Module Reference,” 2019.

[169] VPIphotonics, “ModulatorDiffMZ_DSM, VPIphotonics Module Reference,” 2019.

[170] China Telecom, “China Telecom 5G Technology White Paper,” June 2018. [Online]. Available: http://www.chinatelecom.com.cn/2018/ct5g/201806/P020180626325685163826.pdf. [Accessed 5 February 2019].

[171] J. Zhang, M. Xu, J. Wang, F. Lu, L. Cheng, H. Cho, K. Ying, J. Yu and G.-K. Chang, “Full-Duplex Quasi-Gapless Carrier Aggregation Using FBMC in Centralized Radio-Over-Fiber Heterogeneous Networks,” *Journal of Lightwave Technology,* vol. 35, no. 4, pp. 989-996, 2017.

[172] C. P. Tsekrekos, T. Kuri and K.-i. Kitayama, “Distribution of Millimeter-Wave and Baseband Services Over an Integrated Reconfigurable Access Network Platform,” *Journal of Lightwave Technology,* vol. 28, no. 19, pp. 2783-2790, 2010.

[173] T. Rahman, D. Rafique, B. Spinnler, S. Calabrò, E. d. Man, U. Feiste, A. Napoli, M. Bohn, G. Khanna, N. Hanik, E. Pincemin, C. L. Bouëtté, J. Jauffrit , S. Bordais, C. André , C. Dourthe , B. Raguénès, C. . M. Okonkwo, A. M. J. Koonen and H. d. Waardt, “Long-Haul Transmission of PM-16QAM-, PM-32QAM-, and PM-64QAM-Based Terabit Superchannels Over a Field Deployed Legacy Fiber,” *Journal of Lightwave Technology,* vol. 34, no. 13, pp. 3071-3079, 2016.

[174] I. N. Cano, J. C. Velásquez, V. Polo and J. Prat, “Bidirectional Real-Time DSP-less Heterodyne UDWDM-PON,” in *International Conference on Transparent Optical Networks*, Girona, Catalonia, Spain, 2017.

[175] M. Luo, . T. Zeng, L. Yi, J. Li, X. Li, Q. Yang and L. Xue, “Demonstration of 10-Gb/s, 5-GHz Spaced Coherent UDWDM-PON with Digital Signal Processing in Real-Time,” in *Optical Fiber Communications Conference and Exposition (OFC)*, San Diego, CA, USA, 2018.

[176] A. Stöhr, N. Gomes, A. A. Juarez, M. Kościesza, M. Lange, Y. Leiba, H. Mano, H. Murata, M. Steeg and M. Szczęsny, “Multi RAT (WiFi/LTE/5G) Mobile Network Featuring RoF Fronthaul, 60 GHz Beam-Switching and Mobile IP,” in *European Conference on Optical Communication (ECOC)*, Rome, Italy, 2018.

[177] C. Wang, N. Gomes and H. Toda, “European Horizon 2020 Programme Project: RAPID - Report on photonic processing of mm-wave signals,” 2016.

[178] U. Habib, M. Steeg, A. Stöhr and N. J. Gomes, “Radio-over-Fiber-supported Millimeter-wave Multiuser Transmission with Low-Complexity Antenna Units,” in *International Topical Meeting on Microwave Photonics (MWP)*, Toulouse, France, 2018.

[179] L. Yigal, “European Horizon 2020 Programme Project: RAPID - Subsystem and component specifications,” 2015.

[180] Y. Onishi, N. Nagatani, H. Toda and T. Kawanishi, “Suppression of Optical Spectrum Fluctuations by Stabilizing Fiber Loop Length in Optical Comb Generator Using an Optical SSB Modulator,” in *International Topical Meeting on Microwave Photonics (MWP)*, Paphos, Cyprus, 2015.

[181] A. J. Coulson, R. G. Vaughan and M. A. Poletti, “A. J. Coulson, R. G. Vaughan, M. A. Poletti, “Frequency-shifting using Bandpass Sampling,” *IEEE Transactions on Signal Processing,* vol. 42, no. 6, pp. 1556-1559, 1994.

[182] Analog Devices, “DC – 18 GHz, Ultra-Wideband, Dual Rank 4 GSPS Track-and-Hold Amplifier HMC1061LC5 (Datasheet),” February 2017. [Online]. Available: http://www.analog.com/media/en/technical-documentation/data-sheets/hmc1061.pdf. [Accessed 4 January 2019].

[183] T. M. Comberiate, R. L. Schmid, J. E. Hodkin, M. D. Sharp and J. A. Nanzer, “A Bandpass Sampling Receiver for Wide-Bandwidth, Spectrally-Sparse Waveforms for High-Accuracy Range Measurements,” *IEEE Microwave and Wireless Components Letters,* vol. 27, no. 1, pp. 88-90, 2017.

[184] Mathworks, “Documentation R2018b: qammod,” 2019. [Online]. Available: https://uk.mathworks.com/help/comm/ref/qammod.html. [Accessed 6 February 2019].

[185] Tektronix, “Arbitrary Waveform Generators AWG7000 Series Datasheet,” 19 November 2010. [Online]. Available: https://www.testwall.com/wp-content/uploads/2016/03/TEK-awg7122c.pdf. [Accessed 6 February 2019].

[186] Tektronix, “Digital and Mixed Signal Oscilloscopes MSO/DPO70000 Series Datasheet,” 28 January 2016. [Online]. Available: https://gomeasure.dk/wp-content/uploads/2017/03/MSO-DPO70000.pdf. [Accessed 6 February 2019].

[187] VPIphotonics Design Automation, “VPIphotonics Design Suite Developer Guide,” 2017.

[188] VPIphotonics Design Automation, “VPIphotonics Design Suite Release Notes,” 2017.

[189] J. Zhang, J. Wang, M. Xu, F. Lu, L. Chen, J. Yu and G.-K. Chang, “Memory-Polynomial Digital Pre-distortion for Linearity Improvement of Directly-Modulated Multi-IF-over-Fiber LTE Mobile Fronthaul,” in *Optical Fiber Communications Conference and Exhibition (OFC)*, Anaheim, CA, USA, 2016.

[190] C. Han, M. Sung, S.-H. Cho, H. S. Chung, S. M. Kim and J. H. Lee, “Performance Improvement of Multi-IFoF-Based Mobile Fronthaul Using Dispersion-Induced Distortin Mitigation with IF Optimization,” *Journal of Lightwave Technology,* vol. 34, no. 20, pp. 4772-4778, 2016.

9 Appendix

Table 9-1 Devices and their parameters used in back-to-back, direct IM-DD and external IM-DD analogue SCM measurements at RF

Type of Device	Devices and their Parameters
Continuous Wave External Cavity Laser (CWL)	Agilent 8164A Lightwave Measurement System
	Wavelength used: 1554.6nm, max. 5 dBm optical power
Distributed Feedback (DFB) Laser	Teradian 10mW (10dBm), 3-dB bandwidth: approx. 4 GHz
Arbitrary Waveform Generator (AWG)	Tektronix AWG7122C Arbitrary Waveform Generator 12 GS/s; 3-dB bandwidth: 6 GHz (but poor frequency response beyond 4 GHz); 2-channel
	Maximum sampling rate that can be set for user-defined signals: 3.125 GS/s, due to only standard sampling rates supported by the Oscilloscope (when capturing signals); Output power: 1 V p-p (max.)
2-way splitters (2) (used only in Figure 4-1)	Mini-Circuits 2-way ZX10-2-442+ power splitter/ combiner; Frequency Range: 1550 - 4400 MHz; Power rating: 1.5 W/ 32 dBm; Insertion loss: 3.0dB + 1.0dB (minimum) and 3.0dB+2.1dB (maximum); Isolation: 16 dB
RF Amplifier A (after AWG)	SHF 824; Frequency range: 30 kHz - 30 GHz; Gain: 17 dB (typical); DC bias: +13 V; Noise figure: 3dB
4-way power divider/ combiner	MECA 4-way, 804-S-1.900-M01; SMA Female power divider/ combiner; Frequency Range: 0.8-3.0 GHz; Power rating: 20 W/ 43 dBm; Insertion loss: 6.02dB + 0.8dB (minimum) and 6.02dB+1dB (maximum); Isolation between channels 1 and 4: 35 dB
BPF1	Cascaded Minicircuits VLF-1800+ Low Pass Filter DC - 1800 MHz

	and Minicircuits VHF-1500+ High Pass Filter 1700 MHz - 4500 MHz; 3-dB bandwidth = 1.5 GHz - 2.15 GHz (650 MHz); Insertion loss = 1.5 dB
BPF2	Cascaded Minicircuits VHF-1500+ High Pass Filter 1700 MHz - 4500 MHz and Minicircuits High Pass Filter (ZFHP-2100-S+) 2500 MHz - 6800 MHz; Cutoff frequency = 2.12; Insertion loss = 2 dB
Mach-Zehnder Modulator (MZM)	EOSPACE AX-OK5-10-PFU-PFUP-UL-S Single-arm MZM; 3 dB bandwidth: 10 GHz; Loss: 6.5 dB
	Accompanied by PL303QMD-P Quad Mode Dual Power Supply 30 V 3A/6A; Bias set: 5.5 V
Erbium Doped Fiber Amplifier (EDFA1)	EFA 2020 Fiber Amplifier; Gain: 37 dB (-40 dBm input power); Noise figure: 6 dB
Erbium Doped Fiber Amplifier (EDFA2)	(In-house) FITEL FOL 1402PLF-617-1461 Pump Laser Diode Module, 22 dBM (max. output power)
mmW Photodiode (PD)	U2T XPV2140R-VF-VP Ultrafast Photodetector; Responsivity: 0.7 A/W; 3 dB bandwidth: 45 GHz (max.); Wavelength range: 1480-1620nm; Accompanied by PPS Photodetector Power Supply
PIN Photodiode (PD)	Appointech InGaAs PIN photodiode, 3-dB bandwidth: 4.3 GHz, Responsivity: 1 A/W
RF Amplifier B (before Oscilloscope)	SHF 100 AP; Frequency range: 50 kHz - 20 GHz; Gain: 19 dB (typical); DC Bias: +9 V; Noise figure: 5.5 dB
Oscilloscope (OSC)	Tektronix DPO72304DX Digital Phosphor Oscilloscope; Bandwidth: 23 GHz; Maximum Sampling Rate: 100 GS/s; 4-channel

Table 9-2 Devices and their parameters used in analogue SCM mmW experiments

Type of Device	Devices and their Parameters
The CWL, AWG, 4-way power combiner/ splitter, BPF1, BPF2, MZM and OSC from Table 9-1 have been re-used in these experiments. Some other devices have been re-used as well but have been renumbered	
Optical Phase Modulator (PM)	Sumitomo T.PM 1.5 – 40; RF range: 1.5 GHz – 40 GHz; Loss: 6.5 dB
Dense Wavelength Division Multiplexing (DWDM) Filter	Kylia 192.672-193.047 THz; 25 GHz; Loss: 6dB
Band-pass Filter (25GHz BPF)	K&L Microwave; Centre frequency: 25 GHz; 3-dB bandwidth: 1 GHz, Insertion loss: 1 dB
Band-pass Filter (2.45 GHz)	RFLambda RFCF2400 Cavity Filter; 3-dB bandwidth = 2.37 to 2.53 GHz (160 MHz); Insertion loss = 0.385 dB
Mixers (2)	Marki Microwave M20250 Triple Balanced RF Mixer; Frequency range: LO/RF 2 GHz – 50 GHz, IF 0.4 – 50 GHz; Loss: 8 dB@25 GHz and 15 dB @ 60 GHz
RF Amplifier 1	SHF 824; Frequency range: 30 kHz - 30 GHz; Gain: 17 dB (typical); DC bias: +13 V; Noise figure: 3dB
RF Amplifier 2	Norden Millimeter N07-1593; Frequency range: 22.5 GHz – 35 GHz; Gain: 20 dB; Noise figure: 8 dB
RF Amplifier 3	Quinstar mmwave power amplifier QPI-V02030-C1 (50GHz-75Ghz range; Gain: 30dB gain; Noise figure: 5 dB
RF Amplifier 4	Quinstar QLW-24403536-JO; Gain: 35 dB; Frequency Range: 24-40 GHz; DC Bias: +12 V; Noise figure: 3.5 dB
RF Amplifier 5	SHF 100 AP; Frequency range: 50 kHz - 20 GHz; Gain: 19 dB (typical); DC Bias: +9 V; Noise figure: 5.5 dB
RF Amplifier 6	Mini-circuits ZX60-2522M+; Frequency range: 0.5 to 2.5 GHz; Gain: 20 dB (typical); DC Bias: +5V; Noise figure: 3 dB
RF Amplifier 7	Norden Millimeter N07-1725; Frequency range: 24 GHz – 26 GHz; Gain: 30dB; DC Bias: +12 V; Noise figure: 3dB
Erbium Doped Fiber Amplifier (EDFA1)	EFA 2020 Fiber Amplifier; Gain: 37 dB (-40 dBm input power); Noise figure: 6 dB
Erbium Doped Fiber Amplifier (EDFA2)	(In-house) FITEL FOL 1402PLF-617-1461 Pump Laser Diode Module, 22 dBM (max. output power)

mmW Photodiode (mmW PD1)	Finisar U2T XPDV3120R-VF-FP Ultrafast Photodetector; Responsivity: 0.5 A/W; 3 dB bandwidth: 70 GHz (typ.); Wavelength range: 1480-1620nm; Accompanied by PPS Photodetector Power Supply
mmW Photodiode (mmW PD2)	Finisar U2T XPV2140R-VF-VP Ultrafast Photodetector; Responsivity: 0.7 A/W; 3 dB bandwidth: 45 GHz (max.); Wavelength range: 1480-1620nm; Accompanied by PPS Photodetector Power Supply
3-dB Optical Couplers	FOCI Fiber Optic Communications C-WS Singlemode Wideband Couplers
Polarisation Controllers	PolaRITE™ Polarization Controllers
Antennas	FMI standard gain horn antenna 20240 (17.6 – 26.7 GHz); mid-band gain: 20 dB